AD-A098 057 ADVISORY GROUP FOR AEROSPACE RESEARCH AND DEVELOPMENT--ETC F/G 20/4
BOUNDARY LAYER EFFECTS ON UNSTEADY AIRLOADS.(U)
FEB 81
UNCLASSIFIED AGARD-CP-296 NL

1 OF 2
AD A
098057

LEVEL

0

AGARD-CP-296

GARD-CP-296

AD A098057

AGARD

ADVISORY GROUP FOR AEROSPACE RESEARCH & DEVELOPMENT

7 RUE ANCELLE 92200 NEUILLY SUR SEINE FRANCE

AGARD CONFERENCE PROCEEDINGS No. 296

Boundary Layer Effects on Unsteady Airloads

DTIC
ELECT
S APR 22 1981 D
D

DISTRIBUTION STATEMENT A
Approved for public release;
Distribution Unlimited

NORTH ATLANTIC TREATY ORGANIZATION

DISTRIBUTION AND AVAILABILITY
ON BACK COVER

81 4 21 078

14) AGARD-CP-296

NORTH ATLANTIC TREATY ORGANIZATION

ADVISORY GROUP FOR AEROSPACE RESEARCH AND DEVELOPMENT

(ORGANISATION DU TRAITE DE L'ATLANTIQUE NORD)

[illegible]

9

AGARD Conference Proceedings No.296

11)

BOUNDARY LAYER EFFECTS ON UNSTEADY AIRLOADS

Accession For
NTIS GRA&I ☒
DTIC TAB ☐
Unannounced ☐
Justification
per title on file
By
Distribution/
Availability Codes
Dist | Avail and/or Special
A

[illegible]

Papers presented at the 51st Meeting of the AGARD Structures and Materials Panel
held in Aix-en-Provence, France on 14 19 September 1980.

[illegible]

THE MISSION OF AGARD

The mission of AGARD is to bring together the leading personalities of the NATO nations in the fields of science and technology relating to aerospace for the following purposes:

- Exchanging of scientific and technical information;
- Continuously stimulating advances in the aerospace sciences relevant to strengthening the common defence posture;
- Improving the co-operation among member nations in aerospace research and development;
- Providing scientific and technical advice and assistance to the North Atlantic Military Committee in the field of aerospace research and development;
- Rendering scientific and technical assistance, as requested, to other NATO bodies and to member nations in connection with research and development problems in the aerospace field;
- Providing assistance to member nations for the purpose of increasing their scientific and technical potential;
- Recommending effective ways for the member nations to use their research and development capabilities for the common benefit of the NATO community.

The highest authority within AGARD is the National Delegates Board consisting of officially appointed senior representatives from each member nation. The mission of AGARD is carried out through the Panels which are composed of experts appointed by the National Delegates, the Consultant and Exchange Programme and the Aerospace Applications Studies Programme. The results of AGARD work are reported to the member nations and the NATO Authorities through the AGARD series of publications of which this is one.

Participation in AGARD activities is by invitation only and is normally limited to citizens of the NATO nations.

The content of this publication has been reproduced
directly from material supplied by AGARD or the authors.

Published February 1981

Copyright © AGARD 1981
All Rights Reserved

ISBN 92-835-0281-7

Printed by Technical Editing and Reproduction Ltd
Harford House, 7–9 Charlotte St, London, W1P 1HD

PREFACE

At its Fall 1980 meeting in Aix en Provence, France, the AGARD Structures and Materials Panel (SMP) held a Specialists' Meeting on "Boundary Layer Effects in Unsteady Airloads".

The meeting was conceived, organized and chaired by Dr Gabriel Coupry of France. It was a fitting finale to his term as Chairman of the Subcommittee on Aeroelasticity as he moved to his new post of Chairman of the entire SMP.

Mr Walter J.Mykytow of the United States also played a prominent role in the meeting. He compiled and edited the comments of the Recorders, added his own comments from many years as an outstanding aeroelastician, and prepared the Summary paper.

I am sure that all the Members of the Subcommittee on Aeroelasticity join me in dedicating this report to Dr Coupry and Mr Mykytow in appreciation for their many years of leadership in aeroelasticity.

JJOlsen

JAMES J.OLSEN
Chairman, Subcommittee
on Aeroelasticity

CONTENTS

Page

PREFACE
by J.J.Olsen iii

Reference

SESSION I – PREDICTION METHODS AND COMPARISON WITH EXPERIMENTS – Part 1

INTRODUCTORY REMARKS ON BOUNDARY LAYER EFFECTS ON UNSTEADY AIRLOADS
by H.Zimmermann I

AN ASSESSMENT OF THEORETICAL MODELS FOR VISCOUS AND TRANSONIC FLOW
by E.H.Dowell, M.H.Williams and M.R.Chi 1

OSCILLATING SUPERCRITICAL AIRFOILS IN THE TRANSONIC REGIME WITH VISCOUS INTERACTIONS
by D.P.Rizzetta and H.Yoshihara 2

METHODES DE CALCUL DES COUCHES LIMITES INSTATIONNAIRES
par J.Cousteix, R.Houdeville et J.Javelle 3

VISCOUS EFFECTS ON UNSTEADY AIRLOADS OF OSCILLATING CONFIGURATIONS
by W.Geissler 4

SESSION II – PREDICTION METHODS AND COMPARISON WITH EXPERIMENTS – Part 2

SOME REMARKS ON BOUNDARY LAYER EFFECTS ON UNSTEADY AIRLOADS
by R.Houwink 5

PRISE EN COMPTE D'EFFETS DE COUCHE LIMITE INSTATIONNAIRE DANS UN CALCUL BIDIMENSIONNEL TRANSSONIQUE
par M.Couston, J.J.Angélini, J.C. Le Balleur et P.Girodroux-Lavigne 6

EXPERIMENTAL FLUTTER AT HIGH SUBSONIC SPEEDS AND ITS THEORETICAL PREDICTION TAKING INTO ACCOUNT WING THICKNESS AND REYNOLDS NUMBER
by H.C.Garner, B.W.Payne with J.C.A.Baldock 7

ANALYSIS OF TURBULENT FLOW ABOUT AN ISOLATED AIRFOIL USING A TIME-DEPENDENT NAVIER-STOKES PROCEDURE
by S.J.Shamroth and H.J.Gibeling 8

SESSION III – EXPERIMENTAL STUDIES

EXPERIMENTAL STUDIES OF SCALE EFFECTS ON OSCILLATING AIRFOILS AT TRANSONIC SPEEDS
by S.S.Davis 9

SOME REMARKS ON THE UNSTEADY AIRLOADS ON OSCILLATING CONTROL SURFACES IN SUBSONIC FLOW
by H.Försching 10

OSCILLATORY FLOWS FROM SHOCK-INDUCED SEPARATIONS ON BICONVEX AEROFOILS OF VARYING THICKNESS IN VENTILATED WIND TUNNELS
by D.G.Mabey 11

EXPERIMENTS ON A TURBULENT UNSTEADY BOUNDARY LAYER WITH SEPARATION
by S. De Ponte and A.Baron 12

DISCUSSION SUMMARY
by W.J.Mykytow D

INTRODUCTORY REMARKS ON BOUNDARY LAYER EFFECTS ON UNSTEADY AIRLOADS

by
Helmut Zimmermann
Vereinigte Flugtechnische Werke GmbH, D-2800 Bremen,
Germany

For a long time flutter calculations for aircraft were performed satisfactorily by using unsteady airloads which were derived from thin-wing theory. For flutter cases involving control surface motion, and for even more complicated control-surface-tab systems, however, it turned out that the theoretical values for the coefficients of hinge moment n_c, lift k_c, and moment m_c due to control surface motion had to be corrected with the aid of more or less suitable experimental values. The theoretical value for the hinge moment n_c, as well as the force k_c, were too large in comparison with their corresponding measured values (Fig. 1). This discrepancy was ascribed to the fact that the theory neglected airfoil thickness and boundary layer effects.

With the emergence of the "advanced wing" designed to produce its optimum performance in the transonic speed range, the "thin-airfoil forces" are, strictly speaking, no longer appropriate for flutter calculations in this speed range. The "transonic dip" in the flutter speed which occurs here is not predicted by linear theory. The reason that they continue to be applied to flutter investigations is not only that linear theory has been developed to the point of being able to handle a large number of aircraft configurations, but also because of the difficulties in theoretically predicting steady and unsteady air forces for the transonic range with sufficient accuracy and industrially suitable methods.

Whereas in linear wing theory the unsteady pressure distribution may be treated independently of the steady pressure distribution - which properly reflects the physical situation in the subsonic range - there exists a strong interaction between steady and unsteady pressure in the transonic range, i. e. the unsteady pressure distribution, apart from its Mach dependence, depends on the profile, its mean incidence, and its mean flap angle. During the last few years a number of unsteady pressure distributions have been measured in wind tunnels on conventional and advanced airfoil profiles for the transonic speed range. Furthermore numerical methods, mostly of the Finite Difference kind, were developed to solve the partial differential equations governing inviscid transonic flow, the equations being the Euler equations, the full-potential equation, or the small perturbation equation, depending on the degree of simplification. These methods take into account profile thickness as well as shock wave effects. If no provisions are made in these calculations for boundary layer effects, then the following discrepancies between calculated and measured pressure distributions are likely to arise.

The inclusion of profile thickness effects already in the subsonic range leads to an overestimate of the unsteady wing derivatives k_a, k_b, m_a, m_b, k_c and m_c, whose values (Fig. 1, Fig. 2) deviate further from measured ones than those obtained by thin-wing theory. Only the hinge moment coefficient is improved by thickness effects. For the transonic speed range the numerical methods mentioned above are capable of predicting shocks in the pressure distributions, at least qualitatively, whereas the thin-airfoil theory makes no provision at all for the existence of imbedded shocks.

Because of this the numerical methods for solving the transonic equations are basically superior to the methods of thin-wing theory. The size and the location of the shock, however, are not predicted correctly by inviscid theory, and wing derivatives are even more overestimated than those for the subsonic range, (Fig. 3). The main reason for the discrepancy between measured and calculated pressure is evidently due to the omission of boundary layer effects, bringing us to the topic of our meeting.

Most comparisons between experimental and calculated values have shown that the influence of viscosity on steady and unsteady pressure is not negligible for transonic flow, and for rear loaded profiles. This is not surprising since there would be no lift on an airfoil in a frictionless flow. The fact that most theories for frictionless flows are so successful in predicting lift depends on the Kutta condition which effectively replaces the physical influence of friction in inviscid flow. One cannot, of course, expect that a single condition like that is capable of modelling all viscous effects in a flow that is as complex as the transonic one.

If one starts with a comparison of calculated and measured steady transonic pressure distributions for an airfoil, it turns out the calculated shock is larger and is located farther downstream than the measured one, if the FD equations were set up in conservation form, meaning that the requirement of conservation of mass was satisfied across the shock. If conservation of mass is neglected the shock moves upstream and becomes smaller and thus shows a better agreement with measured values, (Fig. 4). One physical explanation would be as follows: if the numerical procedure does not automatically satisfy the continuity equation across the shock, mass is in general produced behind the shock. This can be interpreted as a thickening of the profile behind the shock, thus producing a forward shift and a decrease of the shock in the same way as a thickening of the boundary layer behind the shock. A similar result can be produced, as Yoshihara and Magnus have shown by a "viscous ramp" behind the shock, whose inclination and height can be deduced from measured shock values such that calculated shock values match the measured ones.

In these considerations the boundary layer is assumed to be adequately represented by its displacement thickness on the airfoil. Is this approach to the problem correct? What really happens in the flow in the vicinity of an airfoil? Because of the no-slip condition at the airfoil boundary and because of viscosity vortices are generated which are transported by convection and diffusion into the flow region around the airfoil and into its wake. For unseperated flows with large Reynolds numbers - which are going to be looked at here - vortices are distributed by diffusion only a short distance from the airfoil wall, before they are swept away by the flow. Outside of this distance, and outside of the wake there are no vortices, i. e. the flow there becomes potential flow. The region around the airfoil in which vortices occur are the boundary layer, and a relatively thin wake. With the exception of the wake which is treated somewhat differently, the following iterative method for calculating pressure distributions is in principle possible:

(1) Calculation of pressure distribution over the original or thickened profile

(2) Calculation of the boundary layer thickness produced by the previously calculated pressure distribution

(3) Addition of the boundary layer thickness to the profile

This approach of changing the profile by adding the boundary layer thickness presupposes that the pressure across the boundary layer does not vary appreciable. This condition, however, is not satisfied for transonic flows in the vicinity of the shock and the wake, and is especially pronounced for supercritical profiles. For this case the boundary layer equations must be extended to include the pressure gradient normal to the boundary layer. This implies furthermore that the pressure distribution calculated for the thickened profile by potential theory cannot be applied to the real profile without some recalculation.

For the purpose of the applications considered here the boundary layer may always be assumed to be turbulent except for the nose region and the very thin laminar sublayer. A deterministic description of the processes within the boundary layer is not possible. It consists of eddies which have a micro- and a macrostructure. The physical relations in viscous flow are described by a balance of vortex production, their diffusion, convection, and dissipation.

The mean values of the flow quantities satisfy the Reynolds-averaged Navier-Stokes equations, if the velocity fluctuations are represented by shear stresses similar to those in laminar flow. The resulting viscosity depends on time and spatial coordinates, and is much larger than the one defined for laminar flow. To determine these shear stresses the turbulence is represented by various models. With the aid of these turbulence models the mean square values and the cross-correlation factors of the velocity fluctuations are related to the mean flow values. Since the Navier-Stokes equations contain only the mean values of the velocities and shear stresses, the relations between shear stress and velocity furnished by the turbulence models close the system of Navier-Stokes equations.

The turbulence is described by "eddy viscosity" models of different levels of sophistication, such as

(1) algebraic relations derived from the mixing-length hypothesis

(2) the so-called $k-\varepsilon$ model which employs two additional differential equations describing the turbulence energy k and the dissipation ε .

Since, as mentioned above, viscous flow is confined to a thin boundary layer and wake for high Reynolds numbers, the Navier-Stokes equations supplemented by the equations derived from the turbulence models can be simplified to the boundary layer equations. In these equations the change in pressure across the boundary layer is usually neglected. If the turbulence is described by an algebraic equation the boundary layer equations can be solved by integral procedures. For more complicated turbulence models finite-difference methods are used for the solution.

For the purpose of modeling and solving boundary layer problems, which may also be applied to the wake, a number of methods are available in the literature. There also exist a number of solutions of the closed Reynolds-averaged Navier-Stokes equations for the entire space.

Some of the publications are associated with persons who present papers at this meeting, making it superfluous to enter into details or to quote publications.

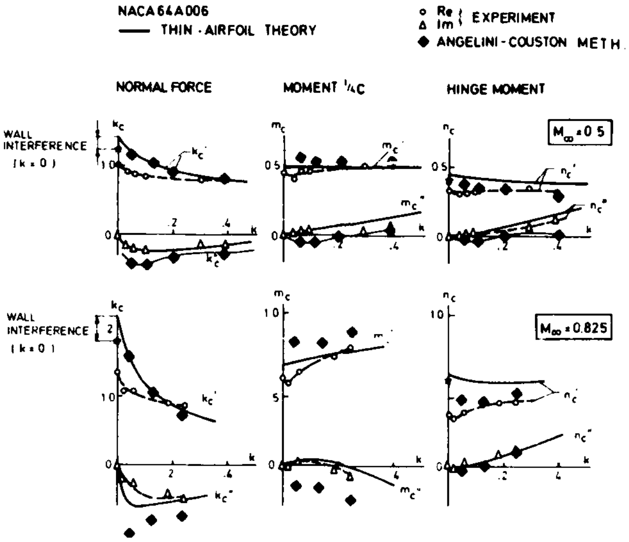

FIG.1 UNSTEADY AERODYNAMIC COEFFICIENTS AS A FUNCTION OF REDUCED FREQUENCY IN SUBCRITICAL FLOW

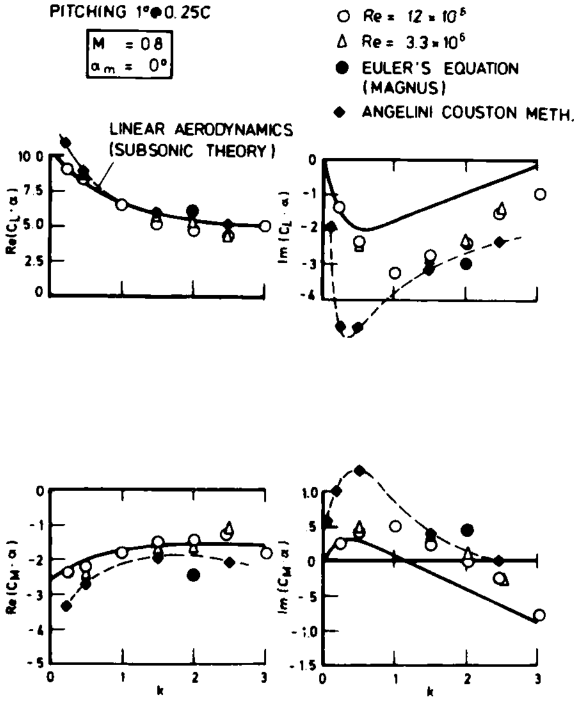

FIG 2 AERODYNAMIC TRANSFER FUNCTION FOR TRANSONIC FLOW

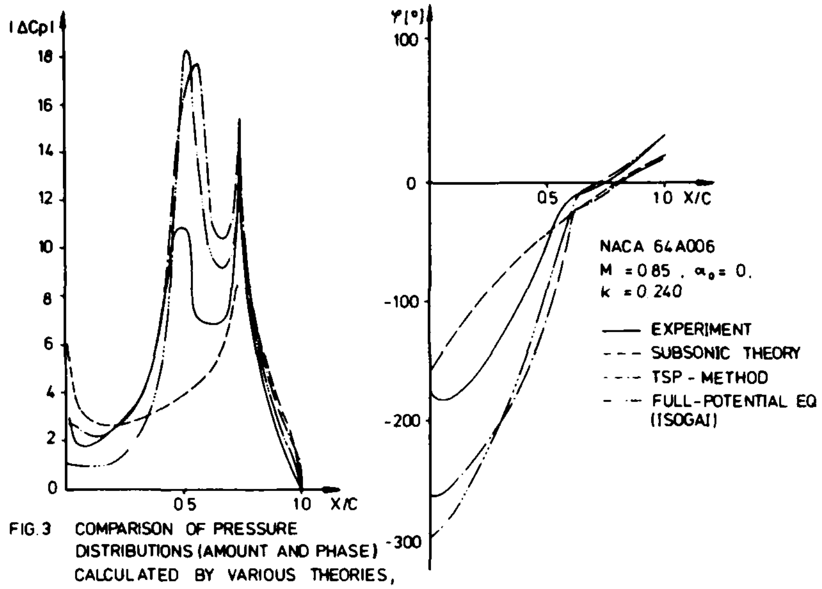

FIG.3 COMPARISON OF PRESSURE DISTRIBUTIONS (AMOUNT AND PHASE) CALCULATED BY VARIOUS THEORIES, WITH EXPERIMENTAL VALUES

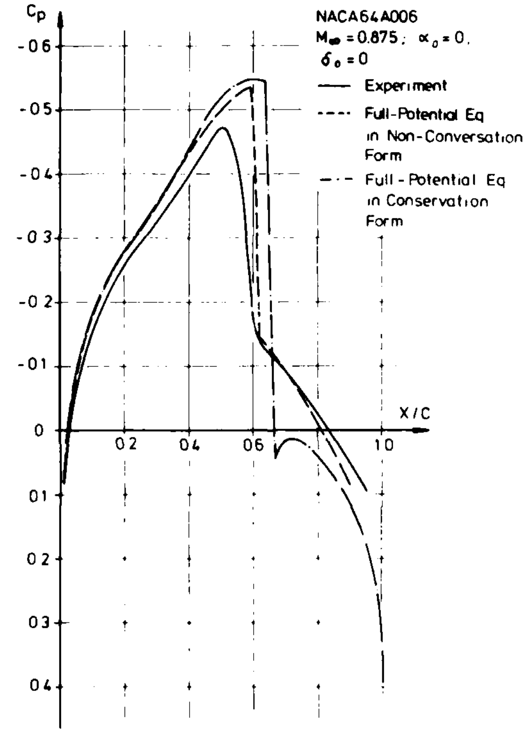

FIG 4 COMPARISON OF STEADY TRANSONIC PRESSURE DISTRIBUTIONS CALCULATED BY THE FULL - POTENTIAL EQUATIONS WITH AND WITHOUT MASS CONSERVATION

AN ASSESSMENT OF THEORETICAL MODELS FOR VISCOUS AND TRANSONIC FLOW

Earl H. Dowell
Professor

Marc H. Williams
Research Staff

Princeton University
Princeton, N. J. 08544
USA

M. Ray Chi

General Electric Company
Evendale, Ohio 45215
USA

SUMMARY

Some current and proposed methods of treating viscous and transonic effects in theoretical aerodynamic models suitable for aeroelastic applications are reviewed critically. Where possible, theoretical results of such models are compared with experiment. Topics discussed include shear flow models (Princeton), simplified models for treating separation (Sisto, Princeton, Chi), classical linear theory, a local linearization theory, a transonic linear theory (Eckhaus-Williams), a transonic nonlinear (small disturbance) theory (LTRAN2), the experiment of Davis, and the experiment of Tijdeman. It is concluded that (1) shear flow models, which have proven very accurate in taking into account boundary layer effects for panel flutter, are likely to be less so for lifting surface flutter; (2) an extremely simple model of separation shows promise, (3) for many applications in transonic flow, transonic linear theory will be adequate; (4) as the reduced frequency, k, increases nonlinear effects decrease; (5) the concept of an aerodynamic transfer function remains useful even in the transonic regime; (6) for the transonic regime a composite aerodynamic representation in k using various aerodynamic models may be extremely useful.

LIST OF SYMBOLS

a	one half of peak-to-peak displacement of wavy wall; also plate length
b	plate width
C_L, C_M	lift, moment coefficients
C_{L_α}, C_{M_α}	lift, moment curve slope
C_{M_F}	flap hinge moment
C_p, $\bar{C}_p$	pressure coefficients
c	airfoil chord
c_F	flap chord
d	stagger distance
h	plate thickness; also vertical distance between two neighboring blades
K	$(\gamma+1)\ M_\infty^2\tau/\beta^3)$
k	$\omega c/U_\infty$; reduced frequency
M	Mach number
N	exponent in power law for boundary layer velocity profile
p	perturbation pressure
s	blade pitch (leading edge distance) for cascade; also $(\beta^2 tU_\infty/c)/M_\infty^2$
t	time
U, W	flow velocity components
x, z	spatial coordinates
x_{PCH}	pitching axis location

---

*The work described here was supported by the NASA Ames, Langley, and Lewis Research Centers and also the Pratt and Whitney Corporation.

x_s	shock location
α	wavenumber; ; 2π divided by wavelength
α_{CH}	$\pi/2 - \gamma$
α_i	mean incidence angle
α_o, α_1	mean angle of attack; dynamic angle of attack
β	$(1 - M_\infty^2)^{1/2}$
δ	boundary layer thickness
$\Delta(\ )$	denotes change in quantity
γ	ratios of specific heats
λ	staffer angle (NASA convention)
λ_F^*	a non-dimensionless dynamic pressure above which flutter occurs; see Ref. I-4
μ	air/plate mass ratio; see Ref. I-4
ν	$k\ M_\infty^2/\beta^2$
ϕ	phase angle
σ	inter-blade phase angle
τ	pitch to chord ratio for cascade, s/c; also thickness ratio of airfoil
ω	frequency

Subscripts

∞	freestream
L	local; also lift
M	moment
max	maximum
pot	potential
+, -	upper, lower
0, 1	mean, dynamic
TE	trailing edge

Superscripts

c	where shock first forms
sc	where shock reaches the trailing edge

INTRODUCTION

The paper rather naturally divides into three parts. Part I considers shear flow models as a possible inviscid representation of the effects of the boundary layer on unsteady airfoil aerodynamics, Part II considers a highly simplified, again inviscid, model of separation and its effects on unsteady aerodynamics, and Part III considers the inviscid, transonic problem.

Some recommendations for further work are made, combining the various models discussed in Parts I, II and III.

Because of the range of topics treated, the paper is of necessity concise. The authors will be content if the reader retains the essence of the conclusions and is encouraged to consult the principal original sources.

PART I - SHEAR FLOW MODELS FOR BOUNDARY LAYERS

In Ref. I-1 a general theory of planar disturbances in inviscid parallel shear flows, analogous to thin-wing theory in potential flows, has been developed. Integral relations between surface pressure and deformation are obtained that are similar to, and can be solved by the same numerical methods as, those of linear potential flow theory. Computed results are shown that illustrate the effects of a model turbulent boundary layer on various lifting and nonlifting surfaces, including an elastic panel in low supersonic flow and an airfoil control surface in subsonic flow.

The physical model employed is that of a small (linearized) perturbation about a mean flow which is strongly non-uniform normal to the aerodynamic surface and weakly nonuniform parallel to the surface. Hence the mean flow is typically that of a turbulent boundary layer and is taken from measurement (or, in principal, from a solution to the Navier-Stokes equations). In the equations for the perturbation per se, however, the direct effects of viscosity are ignored. That is to say it simply, the Reynolds number is finite in the mean flow equations but infinite in the perturbation equations. There is a Reynolds number effect (though weak) in the latter, however, by virtue of the appearance of (known) coefficients which are properties of the mean flow. Typically an N power law velocity profile is used to describe the mean flow.

For the full theory the reader is referred to Refs. I-1 and II-2. Here we focus on results from the model and assess their meaning. Of course, a strong motivation behind using such a model is its relative simplicity. Indeed, with the fundamental theory which has been developed, numerical calculations to obtain solutions are no more difficult than those for classical linear, potential flow theory.

Results will be discussed for three physical situations, for all of which corresponding experimental data are available.

- steady flow over a wavy wall at transonic Mach numbers
- flutter of a plate at low supersonic Mach numbers
- hinge moment on a NACA64A006 airfoil at high subsonic Mach numbers.

In Fig. I-1 the perturbation pressure, p, on a wavy wall is shown for several subsonic freestream Mach numbers, M_∞, as a function of boundary layer thickness δ. $2\pi/\alpha$ is the wall wavelength, 2a the peak-to-peak wall displacement and p_{pot} the corresponding wall pressure as determined by classical, linear, potential flow theory. In Fig. I-2 results of this type are compared to the experimental data of Ref. I-3. The agreement is excellent. In Figs. I-3 and I-4, a similar comparison is made for $M_\infty = 1.1$. For $M_\infty > 1$, there is a spatial phase shift between wall pressure and wall displacement as shown in Fig. I-4. For $M_\infty < 1$ there is no such shift. Again the agreement between theory and experiment is excellent. Perhaps this is not surprising since the ratio, $\alpha\delta/2\pi$, boundary layer thickness to wall wavelength, is smaller than one and hence a (nearly) parallel shear flow model would appear appropriate. Even so the closeness of the agreement for $\alpha\delta$ as large as four is most encouraging.

Consider now a similar, but more complex, flow, i.e., the unsteady flow over an oscillating plate. Here the comparison is less direct (for the aerodynamicist). Flutter boundaries are considered wherein the shear flow model has been used in the theoretical calculations[I-4]. In Fig. I-5, the dynamic pressure at which flutter occurs, λ_F^*, is shown vs. Mach number for two values of boundary layer thickness to length of the elastic plate, δ/a.

The experimental results for $\delta/a = 0$ are obtained by extrapolation of data. Considering the complexity of the physical situation, which includes the dynamics of the elastic plate as well as those of the fluid, the agreement between theory and experiment is remarkably satisfying.

Now we shall turn to a lifting problem, namely the flow over a control surface. Although the model may be used for overall pitching of an airfoil, for example, the control surface problem is more appropriate physically because it more nearly meets the criterion fundamental to the validity of the shear flow model[I-1] of a slowly varying boundary layer thickness over the length of the control surface. Indeed the shorter the control surface chord to total airfoil chord the better one may expect the shear flow model to be, at least as long as the control surface chord remains much larger than the laminar sublayer thickness of the boundary layer.

In Fig. I-6 static hinge moment for a NACA64A006 airfoil with a twenty-five percent trailing edge chord is shown. The experimental results are from Ref. I-5. Theoretical results are shown for various boundary layer to airfoil chord ratios, δ/c. The exact δ/c is not known, but is probably near .05. The agreement is not quantitative; all one can say is that the shear layer model provides a correction of the correct sign and magnitude. Clearly, above the airfoil critical Mach number, transonic thickness effects dominate which are not presently taken into account by the shear flow model.

The conclusions to be drawn are more or less clear.

- Where aerodynamic surface profile thickness effects are small and the boundary layer thickness is small compared to the characteristic wavelength dimension of the aerodynamic surface, the shear flow model works very well.
- Where aerodynamic profile thickness effects are important, the shear flow model does less well as expected.
- A useful line of research would be to combine shear flow and profile thickness effects into a single aerodynamic model. This is possible within the framework of transonic linear theory using the method of matched asymptotic expansions on the aerodynamic Green's function. There is an analogy to the procedure already used to obtain a composite aerodynamic kernel function for unsteady, shear flows by combining the kernel function for a steady, shear flow with that for an unsteady, potential flow[I-1].

PART II - A SIMPLIFIED MODEL FOR SEPARATED FLOWS

A two-dimensional small perturbation theory has been developed by Sisto[II-1,II-2], Dowell[II-3], Williams[II-3], Chi[II-4] and others to take into account the effects of airfoil self-induced flow separation and fluid compressibility on unsteady aerodynamic forces due to the blade vibration of (an isolated airfoil or) a rectilinear stalled cascade. Here we closely follow Chi's discussion[II-4]. The steady mean flow is assumed to be subsonic and separates at an identical and fixed point along the airfoil chords. A kernel (Green's) function approach is employed to solve the problem for a given cavitation distribution in the separated flow region. Calculated results for lift and moment coefficients show reasonably good correlation with other theory and experimental results. Also application of the aerodynamic model to flutter prediction of a representative fan stage shows qualitative agreement with measurements, whereas the classical attached flow aerodynamic model fails to predict any flutter at all.

The basic flow model is shown in Fig. II-1. The distinction between this model and the classical attached flow model is that in the separated flow region on the airfoil the pressure is given (for example, the local pressure is assumed equal to the freestream pressure) and the downwash on the airfoil in the separated flow region is an unknown to be determined. Elsewhere on the airfoil, as in classical attached flow, the downwash is known and the pressure is to be determined. As a result of the relatively simple flow model, a kernel (Green's) function approach similar to, but more general than, its classical nonstalled (non-separated) counterpart is developed. Because of its elliptic nature, the complex mixed boundary value problem is transformed into two Fredholm integral equations. A standard collocation method is used to solve the two resultant integral equations. The solution of one integral equation yields the upwash distribution in the separated flow region. With the complete upwash information now known, the other integral equation is solved for the pressure differential across the airfoil^{II-4}.

Fig. II-2 shows the aerodynamic damping in pitch versus the reduced frequency based on the airfoil full-chord and upstream flow velocity at zero Mach number. Relevant cascade parameters are stagger angle of 45°, solidity of 1, and inter-blade phase angle of 180°. All blades are at a mean angle of attack of 15° and the mean flow separates at the leading edge. Airfoil thickness ratio is 4%. The top surface of each blade was a circular arc and the lower surface a flat plate. These parameters were chosen to match Yashima and Tanaka's experiment^{II-5} in which an 11-blade linear cascade was forced to pitch about the quarter chord in a water tunnel at a Reynolds number of approximately $.5 \times 10^5$. Flow visualization confirmed leading-edge flow separation occurred at a mean angle of 15°. Yashima and Tanaka's theoretical results, based upon a free-streamline theory in incompressible flow with leading edge separation, showed torsional instabilities in the relatively low frequency range. The present theory agrees reasonably well with their experimental data. It is noted that classical attached flow theory does not predict torsional instability for these parameters.

Results have also been obtained for compressible flow over cascades and for flutter prediction of the F100 engine^{II-4}. The latter is encouraging in that the separated flow model appears to describe the essence of the flutter mechanism where, by contrast, the attached flow model failed to predict any flutter whatsoever.

PART III - NONLINEAR EFFECTS IN UNSTEADY TRANSONIC AERODYNAMICS

The aeroelastician uses linear dynamic system theory for most aeroelastic analysis. The motivation for doing so is clear. Extensive experience, understanding, and effective computational/experimental procedures have been developed for linear systems. By contrast, although nonlinear methods of analysis and experimentation are available, the results are far more expensive to obtain and also more difficult to interpret. Hence linear models, where applicable, are very powerful, relatively simple, and extremely valuable. Thus it is highly important to determine the domain of validity of any linear model. For example, in panel flutter or control surface flutter, it is known that structural nonlinearities may be important. Here our concern is with possible aerodynamic nonlinearities in transonic flow. Of course, aerodynamic nonlinearities may arise in other flow regimes, however it is transonic flow where they tend to be most important. Indeed it is sometimes said that the transonic flow regime is inherently nonlinear. Unqualified, this statement is incorrect. At any Mach number for any airfoil, if the angle of attack is sufficiently small, the aerodynamic forces and shock motion will be linear in the angle of attack. Moreover as the frequency of the angle of attack motion increases, the range over which linear behavior persists increases. It is our purpose here to study when linear or nonlinear behavior occurs using as our principal analytical method the low frequency, transonic small disturbance (LTRAN2) procedure of Ballhaus and Goorjian$^{III-1,III-2}$. Any other present or future nonlinear aerodynamic method could (and should) be used for similar purposes.

In this respect it is of interest to display the results of Figs. III-1a and III-1b, which show lift and pitching moment divided by angle of attack for a NACA 64A010 airfoil at $M_\infty = .8$ for various reduced frequencies. The mean steady angle of attack is $\alpha_0 = 0°$, and the dynamic angle of attack is $\alpha_1 = 1.0°$. Results from several theories and one experiment^{III-3} are shown. Except for flow separation, not accounted for by current inviscid transonic aerodynamic methods, Davis^{III-3} observed no significant nonlinearities in α_1 in his experiment. The various theoretical methods whose results are shown are

- classical theory (i.e., the airfoil thickness is set to zero and the mean flow is uniform everywhere)
- Williams' theory$^{III-4,III-5}$ (linear in α_1; theoretical or experimental data are used to locate the steady state shock and its strength which are determined by (α_0 and) the airfoil profile; the flow ahead and behind the shock is taken as uniform in the current version of the method, but the shock moves as α_1 varies
- LTRAN2$^{III-1,III-2}$ (nonlinear in (both α_0 and) α_1; transonic small disturbance theory; low frequency). See Yang^{III-4} for these specific results
- TRACI (nominally the same as LTRAN2, but linear in α_1 with a less satisfactory treatment of the shock). See Yang^{III-6} for these specific results.
- Magnus^{III-7} (solution of the complete, nonlinear, inviscid Euler equations; non-potentials).

Also shown is a steady flow result provided by Bland^{III-8} using the well known steady flow method of Bauer, Garabedian and Korn^{III-9}. These results, though only for one Mach number and one airfoil, remind one that what constitutes a best theory depends upon the particular flow conditions, common deficiencies of all available theories, e.g., omission of viscosity, and the eye of the beholder. See Williams^{III-5} for other comparisons of his method and LTRAN2 with Tijdeman's experiments^{III-10}. It should be noted that comparisons of theory with experiment for chordwise pressure distributions show the clear superiority of Williams' theory and LTRAN2 over classical theory. See Williams III-5.

The point of view taken here is that of the aeroelastician or dynamicist and the questions pursued are correspondingly posed. Before beginning it will be helpful to make certain basic distinctions from the dynamicist's perspective and to discuss in particular the shock and its motion which is sometimes a source of confusion. It is a consequence of any consistent linearization of unsteady transonic small disturbance aerodynamic theory in the dynamic angle of attack that a concentrated force (sometimes called a shock doublet) will appear at the location of the steady state shock$^{III-4,III-5}$. The strength of this force is equal to the steady state shock pressure jump and its width is proportional to the dynamic angle of attack. By contrast elsewhere on the airfoil chord (away from the shock doublet whose center is at the steady state shock location) the pressure magnitudes (in a transonic linear theory) are proportional to the dynamic angle of attack and become smaller in proportion as the dynamic angle of attack is smaller. Of course this latter behavior is also true in classical theory as well. The most important (though not the only) distinction between classical, linear theory and transonic, linear theory is the presence of the shock and its motion.

The behavior described above is also seen in a nonlinear dynamic theory as well, when the dynamic angle of attack becomes small. Consider Fig. III-2 which was obtained using LTRAN2. It shows the chordwise differential (lower surface minus upper) pressure distribution for a NACA64A006 airfoil at $M_\infty = .86$ for several angles of attack. Here, for simplicity, the reduced frequency is set to zero so there is no distinction (numerically) between steady and dynamic angle of attack. As may be seen for small angles of attack, say $\alpha = .125^\circ$, $.25^\circ$, the pressure distribution has a shock doublet centered at the mean (angle of attack) shock location, $x_s/c = .584$. The width of the shock doublet is indicated by the vertical lines, the forward one is at the lower surface shock location and the rearward one at the upper surface shock location. The shock doublet width is proportional to α for the smaller α; however as α increases to 1° the lower surface shock disappears while the upper surface shock moves to the trailing edge and remains there. Also for the smaller α the shock doublet magnitude is essentially equal to the pressure jump through the shock at $\alpha = 0^\circ$, i.e., .43. Away from the shock doublet, the pressures are proportional to α for small α. Finally note a matter of practical importance. For small α as the shock doublet width narrows, any finite difference scheme nonlinear in α will have a resolution problem as $\alpha \to o$. By contrast a method a priori linearized in α avoids this difficulty as it computes the shock motion explicity, e.g., see Williams$^{III-4,III-5}$.

We now turn to the five major issues which are listed below. These issues are first addressed for one airfoil, NACA64A006, at one Mach number, .86, which is pitching about its leading edge. Subsequently other Mach numbers are considered. For a more complete account of the present work, including a study of the MRB-A3 supercritical airfoil, see Ref. III-11. The present calculations were carried out using a grid mesh of 113 x 97.

NACA64A006 AIRFOIL AT $M_\infty = .86$ PITCHING ABOUT ITS LEADING EDGE

The following principal issues were studied^{III-11}.

- EFFECT OF DYNAMIC ANGLE OF ATTACK @ VARIOUS REDUCED FREQUENCIES ON DYNAMIC FORCES AND SHOCK MOTION
- BOUNDARY FOR LINEAR/NONLINEAR BEHAVIOR
- EFFECT OF REDUCED FREQUENCY AND DYNAMIC AMPLITUDE ON AERODYNAMIC TRANSFER FUNCTIONS
- EFFECT OF DYNAMIC ANGLE OF ATTACK ON STEADY STATE FORCES AND SHOCK DISPLACEMENT
- EFFECT OF STEADY STATE ANGLE OF ATTACK ON DYNAMIC FORCES AND SHOCK MOTION

• EFFECT OF DYNAMIC ANGLE OF ATTACK AT VARIOUS REDUCED FREQUENCIES ON DYNAMIC FORCES AND SHOCK MOTION

It is desired to assess at what dynamic amplitude nonlinear effects become important and to determine the relative linear vs. nonlinear behavior of lift, pitching moment and shock motion. Note that the total lift (moment, shock motion) is characterized by $C_L = C_{L_o} + C_{L_1}$ where C_{L_o} is defined to be the lift due to α_o and C_{L_1} that due to α_1 for a given α_o. In classical linear theory (but not transonic linear theory) C_{L_1} is independent of α_o.

In Figs. III-3 and III-4 lift, pitching moment and shock displacement amplitudes are shown as a function of dynamic amplitude, α_1, for reduced frequencies of $k = 0$, and .2. Lift and moment coefficient have their usual definitions and the moment is about the mid-chord. The shock displacement is normalized by the airfoil chord. For $k \neq 0$ phases are also presented for lift and pitching moment. The shock motion phase was also computed, however it tended to be less accurately determined^{III-11}. Since it is not needed for our present purposes, it is not shown.

It is seen that lift tends to remain linear to higher dynamic amplitudes than moment which in turn tends to remain linear to higher amplitudes than shock motion. Moreover the larger the reduced frequency the greater the range of linear behavior. Phase information generally, though not universally, is a more sensitive indicator of departure from linearity than lift, moment or shock amplitude information.

• BOUNDARY FOR LINEAR/NONLINEAR BEHAVIOR

It is highly desirable to provide a criterion by which the aeroelastician may assess when a linear dynamical theory may be used.

Fig. III-5 has been constructed from Figs. III-3 and other similar results[III-11] by identifying the k,α_1 combinations for which the pitching moment deviates by 5% in amplitude or phase from linearity. As expected at higher k, the pitching moment remains linear to larger α_1.

Although Fig. III-5 provides very useful information, it requires a nonlinear dynamical theory to construct it. The question arises, is there a similar, but perhaps more conservative, criterion which may be used with a linear dynamical theory. The answer is provided by the shock motion. In Fig. III-6 a similar boundary to that shown in Fig. III-5 is constructed (again from the information provided by Figs. III-3 and III-4) based upon shock motion rather than pitching moment. It is observed in Figs III-3 and III-4 that for shock displacement amplitudes of less than 5% the shock motion (as well as lift and pitching moment) behave in a linear fashion. Hence a 5% shock motion boundary is shown in Fig. III-6. Note that this boundary could be constructed from a linear dynamical theory. A second boundary (less conservative) based upon the first detectable deviation of shock motion from linearity is also shown. Finally, the boundary from Figs. III-5 is shown for reference. These results are consistent with those of Ballhaus and Goorjian[III-1,III-2] who also suggested that shock motions of less than 5% chord correspond to linear behavior.

Thus it is concluded that a simple criterion for departure from nonlinearity based upon shock motion may be used. It can be evaluated by a linear dynamical theory in principle (which enhances its practical utility), although the present results were obtained using a nonlinear, dynamical theory.

• EFFECT OF REDUCED FREQUENCY AND DYNAMIC AMPLITUDE ON AERODYNAMIC TRANSFER FUNCTIONS

We wish to determine when linear aerodynamic transfer functions are adequate and, when they are not, provide information for characterizing nonlinear aerodynamic transfer (describing) functions. To fully accomplish this purpose requires aeroelastic studies using the present (or similar) aerodynamic data. Here only the aerodynamic aspects are considered.

The aerodynamic transfer functions C_{L_1}/α_1, C_{M_1}/α_1, $\Delta x_{s_1}/\alpha_1$ are plotted in Figs. III-7 - III-9 vs. k for α_1 = .25, .5 and 1. As expected for k → .3, the aerodynamic transfer functions are independent of α_1, but for k → 0 they become discernible functions of α_1.

For $k \geq .2$, linear aerodynamic transfer functions may be used with good accuracy. For k → 0 aerodynamic describing functions may be constructed and may be required in aeroelastic anslyses.

• EFFECT OF DYNAMIC ANGLE OF ATTACK ON MEAN, STEADY STATE FORCES AND SHOCK DISPLACEMENT

Tentatively it is concluded that the effect of dynamic angle of attack on mean, steady state forces and shock displacement is small. For more detailed discussion of this issue, see Ref. III-11.

• EFFECT OF STEADY STATE ANGLE OF ATTACK ON DYNAMIC FORCES AND SHOCK MOTION

Next consider the effect of various steady flow fields on dynamic aerodynamic forces. From a dynamics point of view, changing steady state angle of attack, α_0, is in many ways analogous to changing the airfoil profile or flow Mach number.

Fig. III-10 displays amplitude and phase of the dynamic lift, moment and shock motions vs. α_0 for one reduced frequency, .2, and one dynamic angle of attack, $\alpha_1 = .5^\circ$. α_0 = .25 → .5 is a rough boundary between modest and substantial effects. Clearly the effect of mean angle of attack, α_0, on the dynamic aerodynamic forces can be substantial, comparable to the effect of airfoil profile or Mach number. This, of course, does not mean, necessarily, that there are nonlinear dynamic effects. It does suggest that the characterization of the steady flow about the airfoil is important in assessing its dynamic aerodynamic forces, be the latter linear or nonlinear in α_1.

• MACH NUMBER TRENDS

Mach number is one of the most important parameters in transonic flow. Here its effects are studied systematically for the NACA64A006 airfoil. We note that a similarity rule holds for low frequency, transonic flow which gives the following results for any family of airfoils,

$$C_p = \frac{\tau}{\beta}\,\bar{C}_p\,(x/c,s;\ K,\ \nu,\ \alpha/\tau)$$

where $\bar{C}_p$ is a universal function of its arguments and

$$\beta \equiv (1 - M_\infty^2)^{1/2}, \quad \nu \equiv \frac{k\,M_\infty^2}{\beta^2}$$

$$K \equiv \frac{(\gamma+1)\,M_\infty^2\tau}{\beta^3}, \quad s \equiv \frac{\beta^2 t U_\infty/c}{M_\infty^2}$$

$\tau \equiv$ thickness ratio of airfoil

$\alpha \equiv$ angle of attack

Hence the results for this airfoil may be used to obtain results for any other airfoil of the same family, in particular, the 64A010.

- FLOW AT ZERO ANGLE OF ATTACK

It is instructive to consider first the flow over the airfoil at zero angle of attack. In particular, in Fig. III-11a,b,c the shock position, the maximum local Mach number (which occurs slightly ahead of the shock), and the shock strength (pressure jump across the shock) are shown as a function of freestream Mach number. These are determined approximately but consistently, by using the following definitions

. The shock is located where the local Mach number is unity.
. The pressure jump is from the pressure maximum just ahead of the shock to the pressure at the first subsonic mesh point behind the shock.

Note that the critical Mach number where the shock first appears is $M_\infty^c = .824$. The shock position at $M_\infty = .84$ is $x_{s_o} = .48$ and it increases monotonically with M_∞, reaching the trailing edge at $M_\infty^{sc} = .92$. We shall call the latter the supercritical Mach number. As we shall see M_∞^c and M_∞^{sc} bound the essentially transonic Mach number range for this airfoil.

Also shown for reference are results from the full potential theory method of Bauer, Garabedian and Korn[III-9] as obtained by Bland[III-11]. Relative to LTRAN2, these results give a higher maximum local Mach number, a smaller pressure jump and a more forward shock location.

- FLOW AT ANGLE OF ATTACK

In Fig. III-12a,b,c the lift, pitching moment (about midchord) and shock displacement (of the upper surface shock) are presented vs. angle of attack, for steady flow, $k = 0$. Note the behavior of $M_\infty = .88$, .9 is nonlinear at much lower angles of attack than for $M_\infty = .86$, .92. For $M_\infty < .86$ or $> .92$ the behavior is linear to even larger angles of attack. Also note that the values of C_{L_o}, C_{M_o} and Δx_{s_o} are much larger for $M_\infty = .88$, .90. Indeed it is probably that at these Mach numbers even the nonlinear transonic small disturbance theory is inadequate except possibly at very small angles of attack.

In Fig. III-13a,b,c the corresponding differential pressure distributions are shown for $M_\infty = .86$, .88, .92. See Ref. III-11 for $M_\infty = .8$, .84, .9. The angle of attack was held constant at .25°. This is slightly outside the linear range at $M_\infty = .88$ and well outside it as $M_\infty = .9$; for other M the behavior is linear at $\alpha_o = .25^o$.

To avoid confusion in the subsequent discussion, let us define the following:

. ΔC_p jump across the shock ≡ pressure jump across the shock at $\alpha_o = 0^o$ -- This is the pressure difference from ahead of the shock to behind the shock on the same surface (upper or lower).
. ΔC_p ≡ differential pressure -- This is the pressure difference between the lower surface and the upper surface. It is zero for $\alpha_o = 0^o$, of course, when the airfoil profile is symmetric.

Linear transonic theory says the differential pressure, ΔC_p, near the shock for any α_o should be equal in magnitude to the pressure jump across the shock at $\alpha_o = 0^o$. Note that linear transonic theory gives a reasonable value for the peak level of ΔC_p in the vicinity of the shock even for $M_\infty = .88$ (and .9). However at the latter Mach number, the shock displacement appears too large. See Fig. III-13.

Also shown in Fig. III-13 is the differential pressure obtained using the supersonic Mach number just ahead of the shock and invoking classical supersonic theory via local linearization. For $M_\infty = .92$ reasonable results are obtained ahead of the shock, which is at the trailing edge, and hence everywhere on the airfoil except near the leading edge. For lower Mach numbers only a rough estimate is given by this approximation for ΔC_p ahead of the shock. For $M_\infty \geq .92$ local linearization is a useful tool, i.e., once the shock has reached the trailing edge. See subsequent discussion on this point also.

- LINEAR/NONLINEAR BEHAVIOR

Using results such as those shown in Fig. III-12 and invoking the 5% shock displacement criterion, a linear/nonlinear boundary may be constructed. Of course, as the shock reaches very near the trailing edge, the 5% criterion would need to be modified. Results are shown in Fig. III-14 for $k = 0$ and .2. Note that for steady flow ($k = 0$) the angle of attack must be very small when $M_\infty = .88$ and .9 for linear behavior to occur. However as we have seen before, the 5% shock displacement criterion is conservative. That is lift and moment tend to remain linear in α to higher α than this criterion would suggest. Nevertheless the trend should not change using any other reasonable criterion. By contrast for $k = .2$ the linear region is much enlarged. For $M_\infty < M_\infty^c$ or $M_\infty > M_\infty^{sc}$ the linear region is for all practical purposes unbounded. In practice, in this region, other physical effects, e.g., viscosity, are likely to come into play before inviscid, small disturbance, transonic theory nonlinearities become important.

One very interesting and perhaps surprising result is that at $M = .88$ and .9 for $k = .2$ a mean, steady offset in C_L, C_M and Δx_s is obtained as well as the usual harmonic result[III-11]. However, the harmonic component is linear in the range shown in Fig. III-14 despite this steady component. That is, the 5% criterion is applied to the harmonic component of shock displacement.

Of course, this mean, steady component is not explainable by any strictly linear theory. Whether it is an artifact of LTRAN2 or is physically meaningful is a reasonable question. The authors are inclined toward the latter view, but the question deserves further study. If these results are accepted, to use the language of the dynamicist, the flow apparently bifurcates at some Mach numbers. Albeit the new equilibrium states exist only over a small range of Mach number.

It is interesting to speculate further as to whether such possible bifurcations can be related to such qualitative physical phenomena as buffet or shock induced (as contrasted with natural) separation. However much further study is required to address such issues. See Ref. III-11 for the relevant numerical results and further discussion.

- AERODYNAMIC TRANSFER FUNCTIONS

In the linear region it is of interest to display aerodynamic transfer functions vs. Mach number. Perhaps the most familiar of these is lift curve slope, C_{L_1}/α_1. Its amplitude is shown in Fig. III-15a from LTRAN2 for $k = 0$. Also shown are results from full potential theory, classical subsonic theory and local linearization. The latter is shown for $M_\infty > M_\infty^{sc}$, i.e., the shock is at the trailing edge. It uses the local trailing edge supersonic Mach number in classical (supersonic) theory. One concludes that for $M_\infty < M_\infty^c$, classical subsonic theory gives reasonable results, and for $M_\infty > M_\infty^{sc}$ local linearization gives reasonable results. For $M_\infty^c < M_\infty < M_\infty^{sc}$, LTRAN2 gives markedly different results although it likely fails for $M_\infty = .88$, $.90$. Note the difference between transonic small disturbance theory (LTRAN2) which falls well off scale at $M_\infty = .88$ and $.9$ and full potential theory (Bauer, Garabedian and Korn).

In Fig. III-15b results are shown for $k = .2$. For reference the LTRAN2 results for $k = 0$ are also shown. Again it is seen that the classical subsonic theory and local linearization theory give reasonable results (better than for $k = 0$) for $M_\infty < M_\infty^c$ and $M_\infty > M_\infty^{sc}$ respectively. Moreover LTRAN2 appears to give reasonable results over the entire Mach number range though there is no better theory to validate it. Note that from $M_\infty = .9$ to $.92$ there is a somewhat abrupt change. This is probably associated with the change from a flow with a mean, steady offset to one which behaves very much like classical flow with a local (trailing edge) supersonic Mach number.

In Fig. III-15c the phase of the lift curve slope is shown. Perhaps surprisingly, classical subsonic theory and local linearization do rather well. Note the abrupt change in phase as the shock reaches the trailing edge. Recall the corresponding variation of lift amplitudes in Fig. III-15b.

Similar results (not shown) were obtained for pitching moment.

CONCLUSIONS

The specific conclusions to be drawn from this inviscid transonic study are:

- For $M_\infty < M_\infty^c$, i.e., where no shock exists, the aerodynamic forces are linear over a substantial range of angle of attack. This is also true for $M_\infty > M^{sc}$, i.e., where the shock has moved to the trailing edge. For $M_\infty^c < M_\infty < M^{sc}$ a boundary of linear/nonlinear behavior may be constructed which shows the angle of attack must be quite small for linear behavior to occur for steady flow However the region of linear behavior increases substantially for unsteady flow.

- In the range, $M_\infty^c < M_\infty < M_\infty^{sc}$, transonic small disturbance theory (LTRAN2) appears to fail for steady flow for some narrow band of M_∞ where it substantially overestimates the shock displacement. The corresponding results from full potential theory (Bauer, Garabedian and Korn) appear reasonable. It should be noted that the region of linear behavior as predicted by Bauer, Garabedian and Korn would be substantially larger than that predicted by LTRAN2 for steady flow.

- Classical subsonic theory and local linearization are useful tools for unsteady flows provided their limitations are recognized. Indeed in an effort to close the prediction Mach number gap in and near the range $M_\infty^c < M_\infty < M^{sc}$ and to provide the aeroelastician with practical working methods, it is likely that all existing methods will need to be employed in their respective domains of validity. The use of full potential theory to establish these domains for steady flow (and provide conservative estimates of these domains for unsteady flow) appears to be a useful approach.

- Aerodynamic transfer functions are expected to retain their utility even when nonlinear dynamic effects are important. This is for several reasons including,

  (1) nonlinear effects diminish with increasing frequency,

  (2) at high frequencies classical linear theory is expected to be reasonably accurate and indeed most inviscid theories will approach classical theory as the frequency becomes large[III-4,III-5],

  (3) the above suggests that several theories may be used to provide a composite aerodynamic representation in the frequency domain. For example, one might use Bauer, Garabedian and Korn for $k = 0$, LTRAN2 for $k = .05 \rightarrow .2$, Williams for $k = .2 \rightarrow 1.0$ and classical theory (which Williams' theory smoothly approaches) for $k > 1.0$.

- No transonic method can be expected to give useful information to the aeroelastician unless the mean steady flow it predicts and uses is accurate. Hence it is highly desirable to be able to input directly the best steady flow information which is available including that from experiment. The latter would include implicitly viscosity effects on the mean steady flow; in particular it would place the mean shock in the correct position.

The reader may wish to consult the lucid survey article by Tijdeman and Seebass[III-12] to provide a context in which to evaluate the present results and conclusions.

CONCLUDING REMARKS

Here we emphasize some of the broad conclusions to be drawn from the discussion in this paper.

- A shear flow model has been shown to be extraordinarily successful in accounting for the effect of a boundary layer over a wavy wall (including the transonic range). It also predicts very well the boundary layer effect on a fluttering plate (the dynamic, aeroelastic counterpart of the static, aerodynamic wavy wall problem). On theoretical grounds and also based upon limited experimental evidence, the shear flow model is expected to be less successful for lifting airfoils. However it still appears to give qualitatively correct results. It is noted that for the lifting problem there are no experimental data comparable to the definitive sets available for the wavy wall and plate flutter problems

- A simple separated flow model based upon a dynamic perturbation about a known steady flow with a fixed separation point shows considerable promise in predicting measured unsteady aerodynamic forces and flutter data. The theory includes the effects of compressibility, but in its present form is not a transonic model per se.

- A boundary demarcating linear from nonlinear behavior can be determined for inviscid, transonic flow which provides useful guidance to the aeroelastician in selecting analytical/experimental approaches for flutter and dynamic response work. In its simplest form this boundary employs a criterion based upon shock motion as a percentage of airfoil chord.

- A similarity law for low frequency transonic small disturbance theory is available which reduces the number of aerodynamic computations required and generalizes results for one airfoil to an entire family.

- Although two-dimensional flows have been treated here, the general concepts and approach should be useful for three-dimensional flows. In particular one expects the effect of three-dimensionality to increase the region of linear behavior and to reduce the Mach number predictability gap for transonic flows. For example, the accuracies of transonic small disturbance theory, local linearization and classical theory should be enhanced by three-dimensional effects.

- It should be possible, within the framework of a linear dynamic theory about a nontrivial mean flow, to account for shear layer and separation effects as modeled in Parts I and II in the transonic flow regime, as discussed in Part III.

- Aeroelastic studies using the aerodynamic methodology employed here should be a fruitful area of future work.

REFERENCES FOR PART I

I-1 M. H. Williams, M. R. Chi, S. C. Ventres and E. H. Dowell, "Aerodynamic Effects of Inviscid Parallel Shear Flows", AIAA Journal, Vol. 15, No. 8, August 1977, pp. 1159-1166.

I-2 M. H. Williams, "General Theory of Thin Wings in Inviscid Parallel Shear Flows", Princeton University AMS Report No. 1269, March 1976.

I-3 L. Muhlstein and R. G. Beranek, "Experimental Investigation of the Influence of the Turbulent Boundary Layer on the Pressure Distribution Over a Rigid Two-Dimensional Wavy Wall", NASA TN-D-6477, August 1971.

I-4 E. H. Dowell, "Generalized Aerodynamic Forces on a Flexible Plate Undergoing Transient Motion in a Shear Flow with an Application to Panel Flutter", AIAA Journal, Vol. 9, May 1971, pp. 834-841.

I-5 H. Tijdeman, "High Subsonic and Transonic Effects in Unsteady Aerodynamics", NLR TR 75079 U, May 1975, National Aerospace Laboratory, Netherlands.

REFERENCES FOR PART II

II-1 F. Sisto, "Stall Flutter in Cascade", J. Aero. Sciences, September 1953, pp. 598-604.

II-2 P. V. K. Perumal, "Thin Airfoil in Eddy-Array and Part-Stalled Oscillating Cascade", Ph.D. Thesis, Stevens Institute of Technology, 1975.

II-3 E. H. Dowell, "A Simplified Theory of Oscillating Airfoils in Transonic Flow: Review and Extension", AIAA Paper 77-445, AIAA Dynamics Specialist Conference, San Diego, CA., March 1977.

II-4 M. R. Chi, "Unsteady Aerodynamics in Stalled Cascade and Stall Flutter Prediction", ASME 80-C2-1, ASME Aerospace Conference, Century II, San Francisco, CA., August 1980

II-5 S. Yashima and H. Tanaka, "Torsional Flutter in Stalled Cascade", ASME Paper 77-GT-72, 1977.

REFERENCES FOR PART III

III-1 W. F. Ballhaus and P. M. Goorjian, "Implicit Finite Difference Computations of Unsteady Transonic Flows about Airfoils", AIAA Journal, Vol. 15, No. 12, December 1977, pp. 1728-1735.

III-2 W. F. Ballhaus and P. M. Goorjian, "Efficient Solution of Unsteady Transonic Flows about Airfoils", Paper No. 14, AGARD Conference Proceedings No. 226, Unsteady Airload in Separated and Transonic Flows, 1978.

III-3 S. S. Davis and G. Malcolm, "Experiments in Unsteady Transonic Flow", AIAA Paper 79-0769, Presented at the AIAA/ASME/AHS/ASCE 20th Structures, Structural Dynamics and Materials Conference, St. Louis, Missouri, April 4-6, 1979.

III-4 M. H. Williams, "The Linearization of Transonic Flows Containing Shocks", AIAA Journal, Vol. 17, No. 4, April 1979, pp. 394-397.

III-5 M. H. Williams, "Unsteady Thin Airfoil Theory for Transonic Flows with Embedded Shocks", AIAA Journal, Vol. 18, No. 6, June 1980, pp. 615-624. Also see "Unsteady Airloads in Supercritical Transonic Flows", AIAA Paper No. 79-0767, presented at the 20th SDM Meeting, St. Louis, Mo., April 1979.

III-6 T. Y. Yang, A. G. Stritz, P. Guruswamy, "Flutter Analysis of Two-Dimensional and Two-Degree-of-Freedom Airfoils in Small-Disturbance Unsteady Transonic Flow", AFFDL-TR-78-202, December 1978.

III-7 R. J. Magnus and H. Yoshihara, "Calculations of Transonic Flow Over an Oscillating Airfoil", AIAA Paper 75-98, January 1975.

III-8 S. R. Bland, personal communication.

III-9 F. Bauer, P. Garabedian and D. Korn, "Supercritical Wing Sections", Lecture Notes in Economics and Mathematical Systems 66, Springer-Verlay, 1972.

III-10 H. Tijdeman and P. Schippers, "Results of Pressure Measurements on an Airfoil with Oscillating Flow in Two-Dimensional High Subsonic and Transonic Flow", NLR TR-730780, National Aerospace Laboratory, the NETHERLANDS, July 13, 1973.

III-11 E. H. Dowell, M. H. Williams and S. R. Bland, "Nonlinear Effects in Unsteady Transonic Aerodynamics", proposed NASA TP.

III-12 H. Tijdeman and R. Seebass, "Transonic Flow Past Oscillating Airfoils", Annual Review of Fluid Mechanics, Vol. 12, 1980, pp. 181-222.

ACKNOWLEDGEMENT

The first author would like to thank Wilmer H. Reed, E. Carson Yates, Jr., Robert M. Bennett and Samuel R. Bland of the Aeroelasticity Branch, NASA Langley Research Center for their kind hospitality and useful technical discussions of transonic flow. In particular, Dr. Bennett is responsible for making LTRAN2 operational at Langley and he and Dr. Bland were most generous in sharing their knowledge of unsteady transonic aerodynamics.

NOTE ADDED IN PROOF:

It should be noted that the full potential result shown in Fig. III-15a was obtained using a non-conservative finite difference scheme. More recent full potential results obtained using a conservative finite difference scheme are essentially identical to those of transonic small disturbance theory using a conservative finite difference scheme (LTRAN2). Hence the differences shown in Fig. III-15a should be attributed to the distinction between conservative and non-conservative finite differences and not to the distinction between small disturbance and full potential theory. To the extent the non-conservative finite difference method may be said to have some form of numerical (as opposed to physical) viscosity, the differences may be attributed to the qualitative distinction between inviscid and viscous flow.

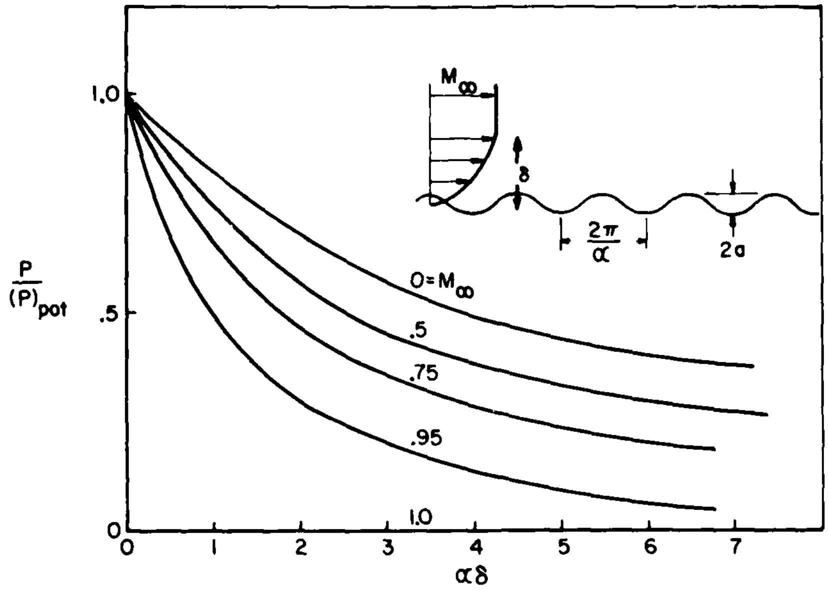

Fig.I-1 Subsonic wavy wall pressure

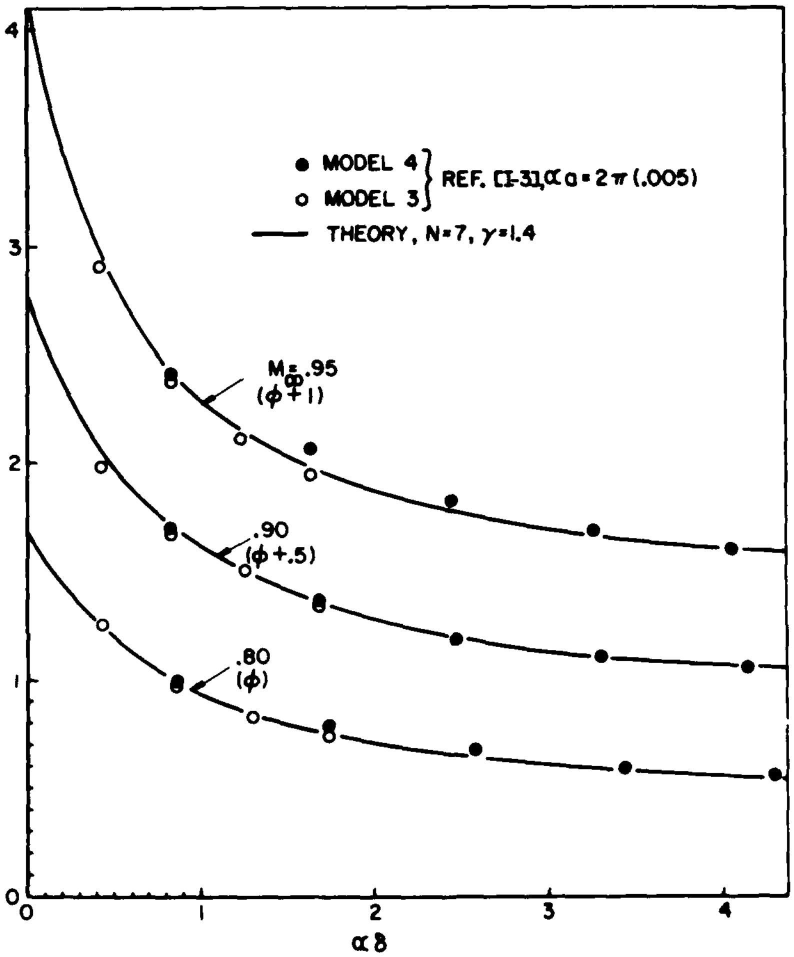

Fig.I-2 Comparison of theory and experiment Subsonic wavy wall pressure
$\phi = |C_p|/(2\alpha a)$

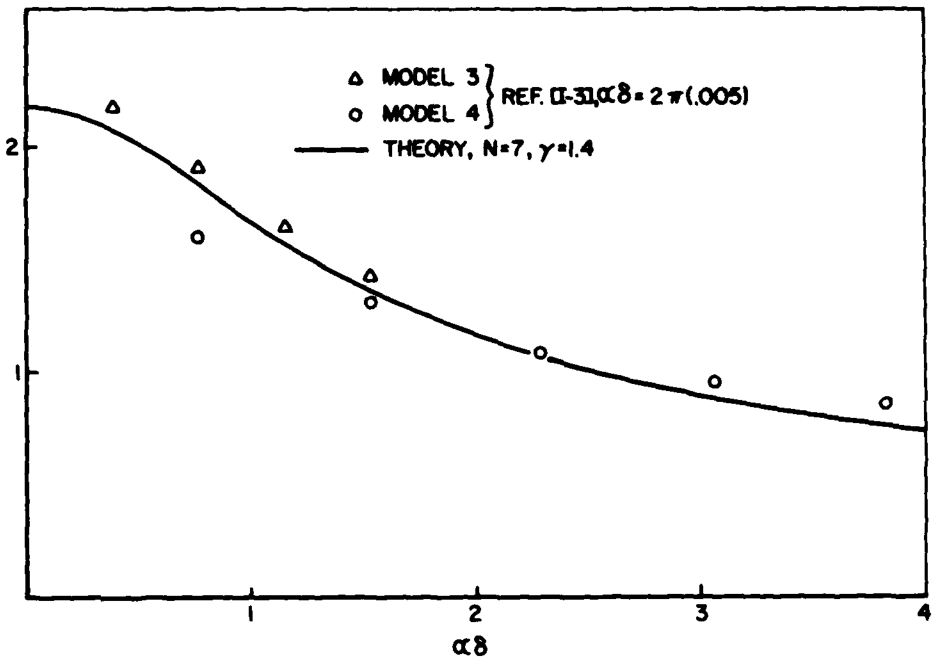

Fig.1-3 Wavy wall pressure, $M_\infty = 1.1$, magnitude

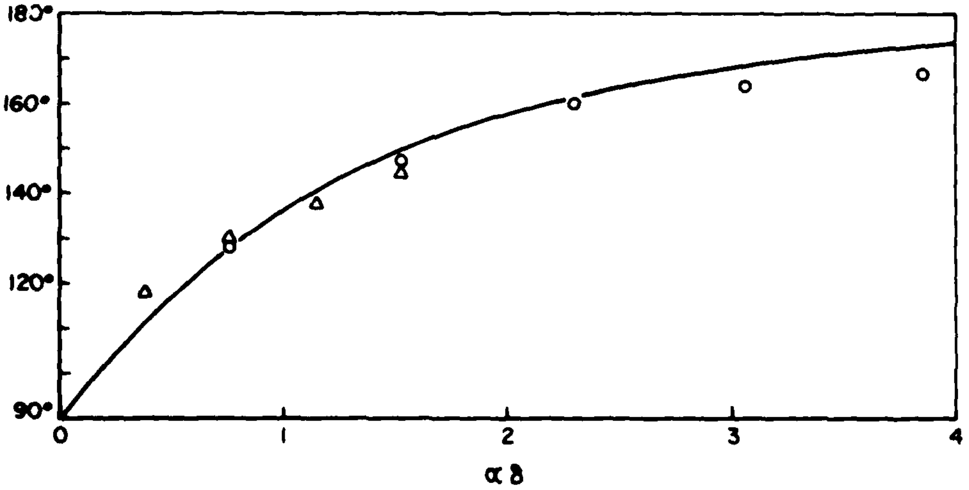

Fig.1-4 Wavy wall pressure, $M_\infty = 1.1$, phase

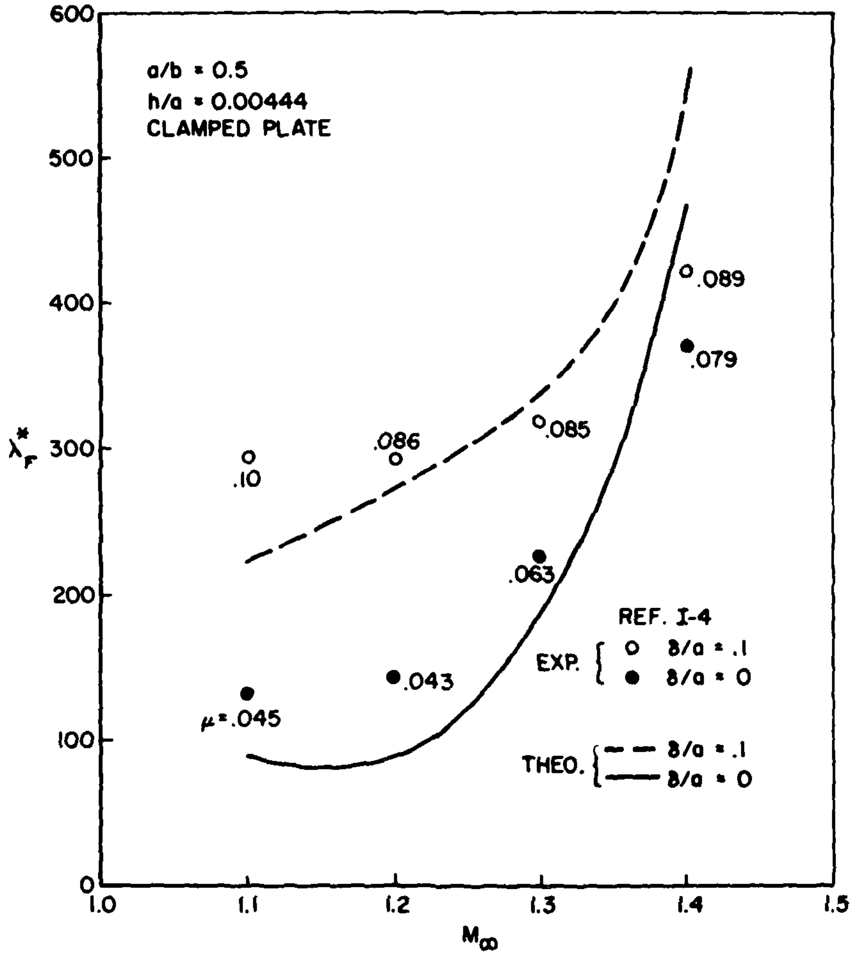

Fig.I-5 Panel flutter dynamic pressure vs. Mach number

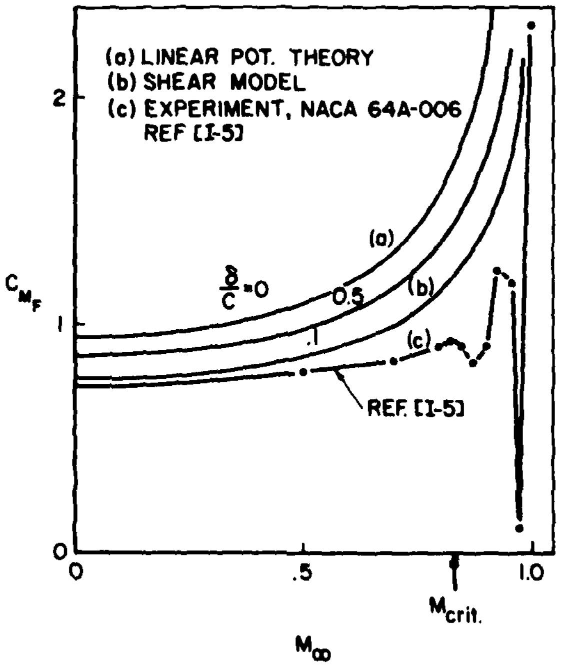

Fig.I-6 Static hinge moment, $c_{F/c}$ .25

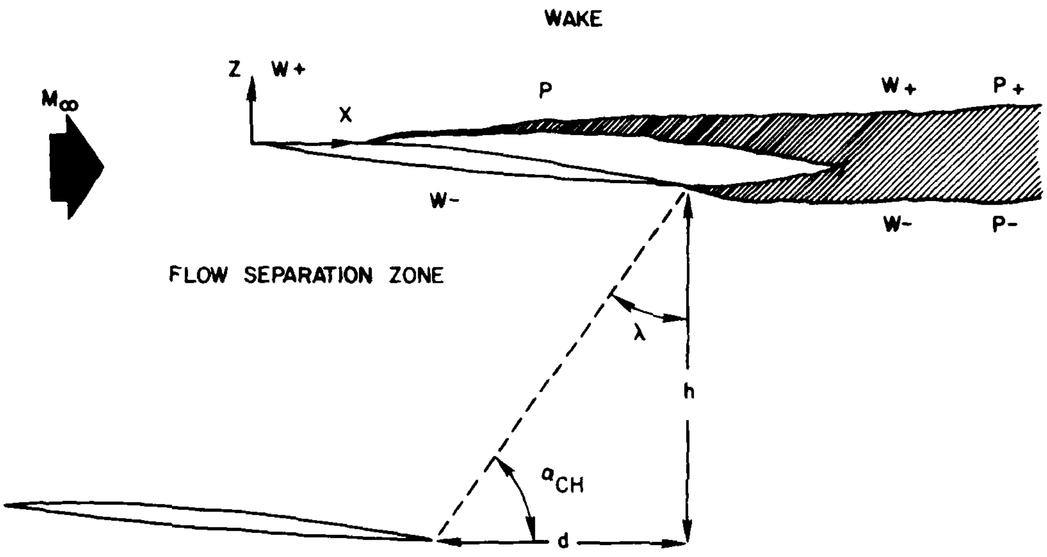
WAKE
Z
W+
X
P
W+
P+
M_∞
W-
W-
P-
FLOW SEPARATION ZONE
λ
h
α_{CH}
d

Fig.II-1 Cascade geometry

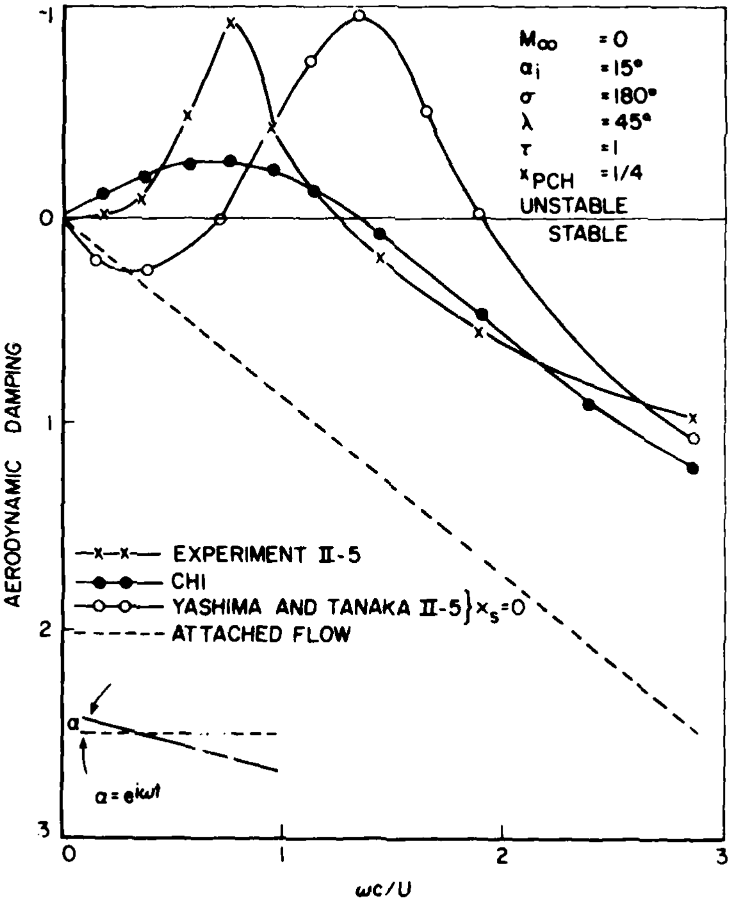

Fig.II-2 Aerodynamic damping in pitch vs. reduced frequency

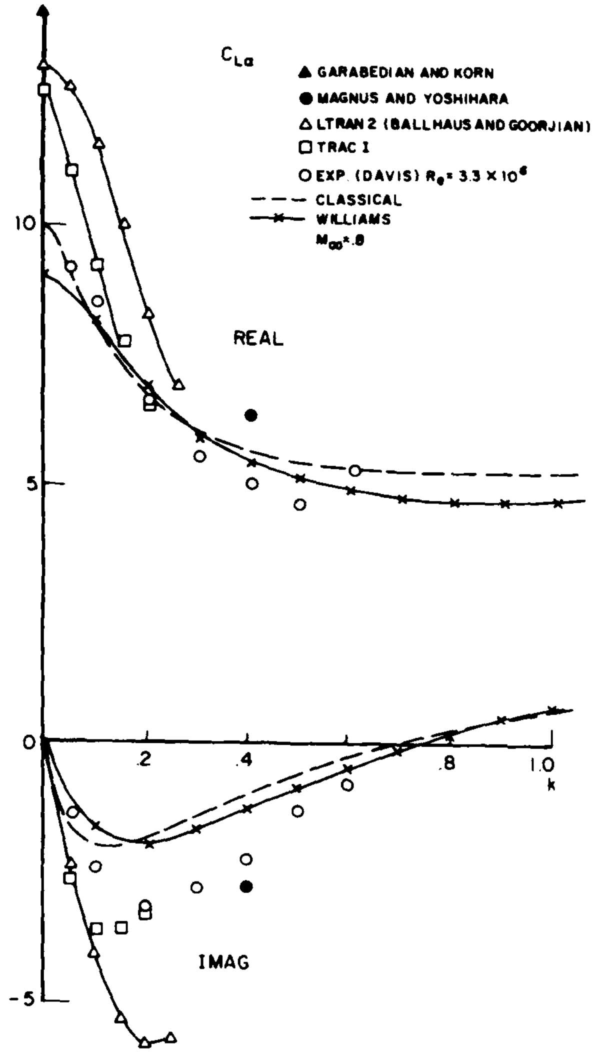

Fig.III-1(a) Comparison of several theories with experiment. Pitch about quarter chord

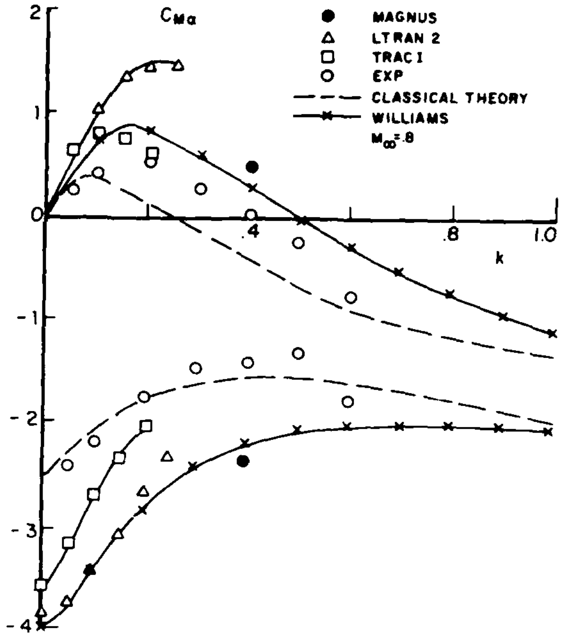

Fig.III-1(b) Comparison of several theories with experiment: Moment about leading edge. Pitch about quarter chord

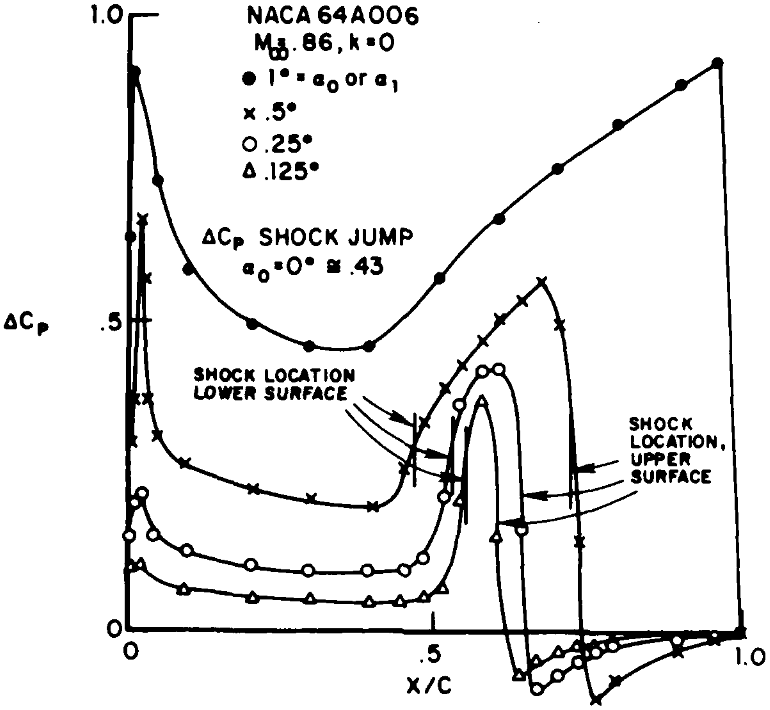

Fig.III-2 Differential pressure distribution

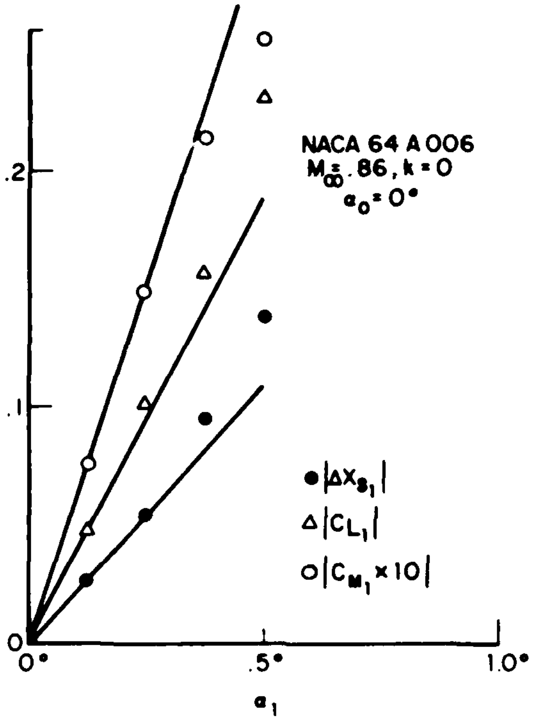

Fig.III-3 Effect of dynamic angle of attack on dynamic forces and shock motions: Amplitudes

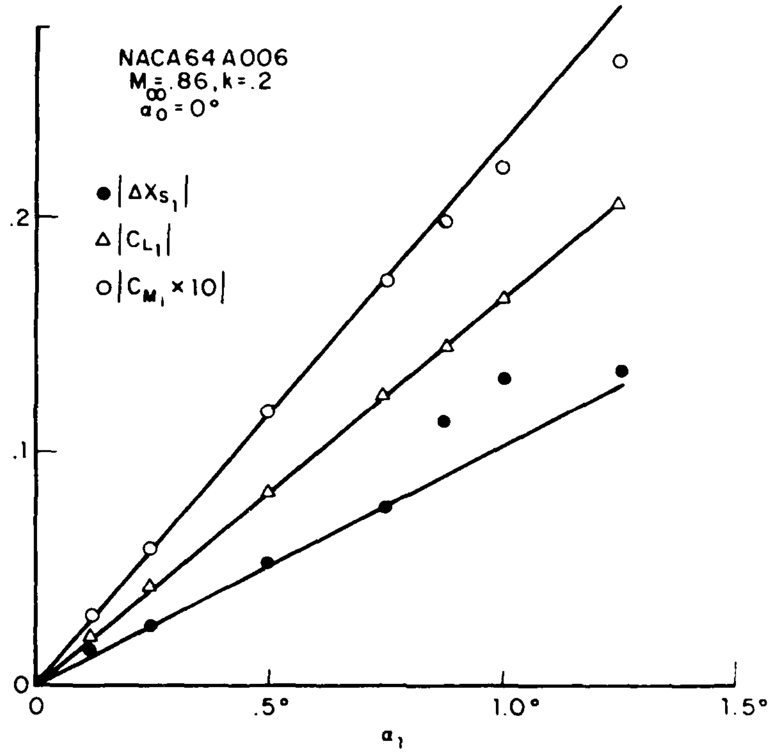

Fig.III-4(a) Effect of dynamic angle of attack on dynamic forces and shock motion: Amplitudes

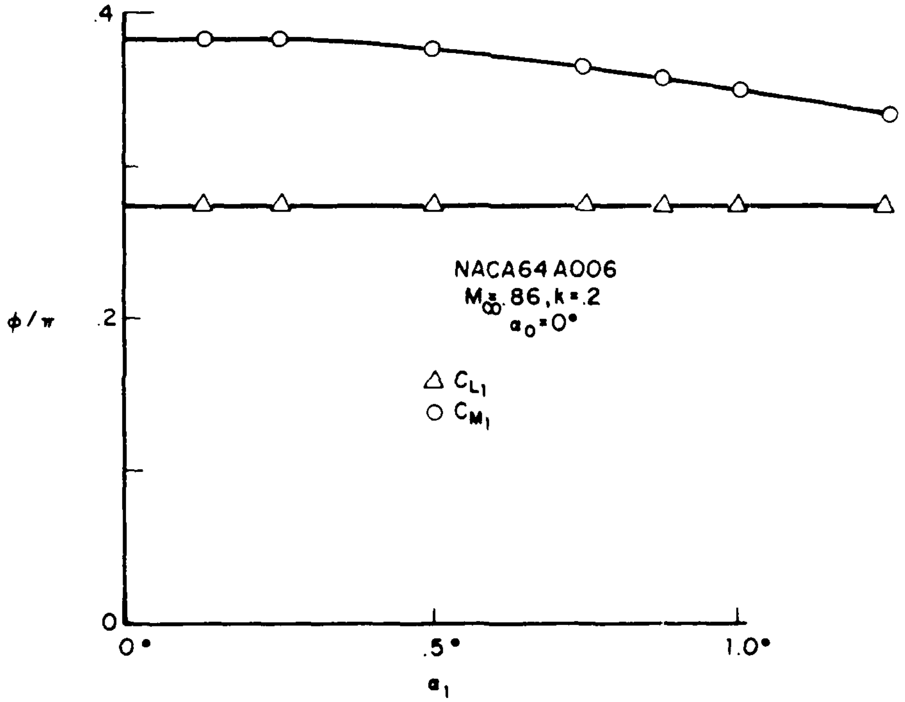

Fig.III-4(b) Effect of dynamic angle of attack on dynamic forces and shock motion: Phases

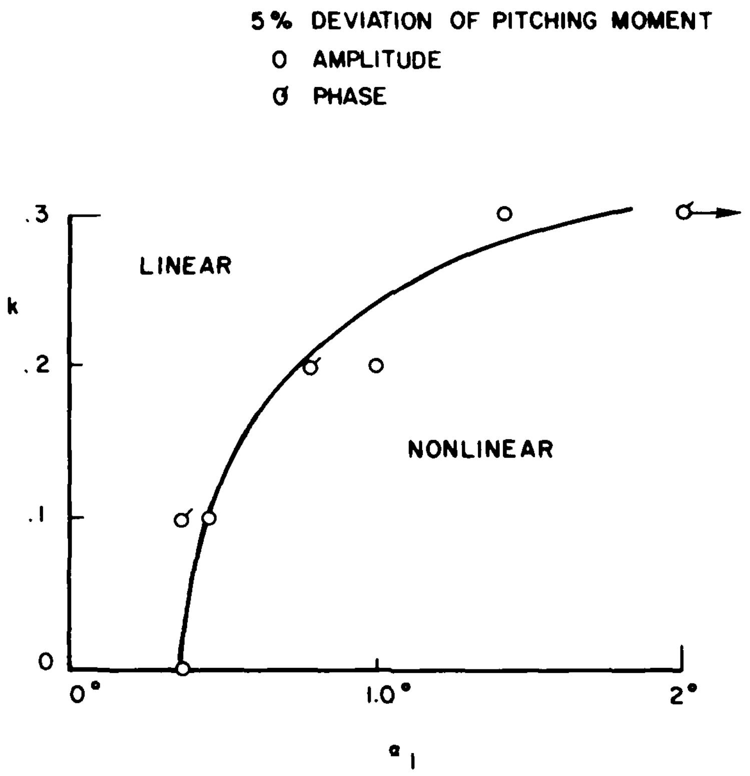

Fig.III-5 Boundary for linear vs. nonlinear behavior

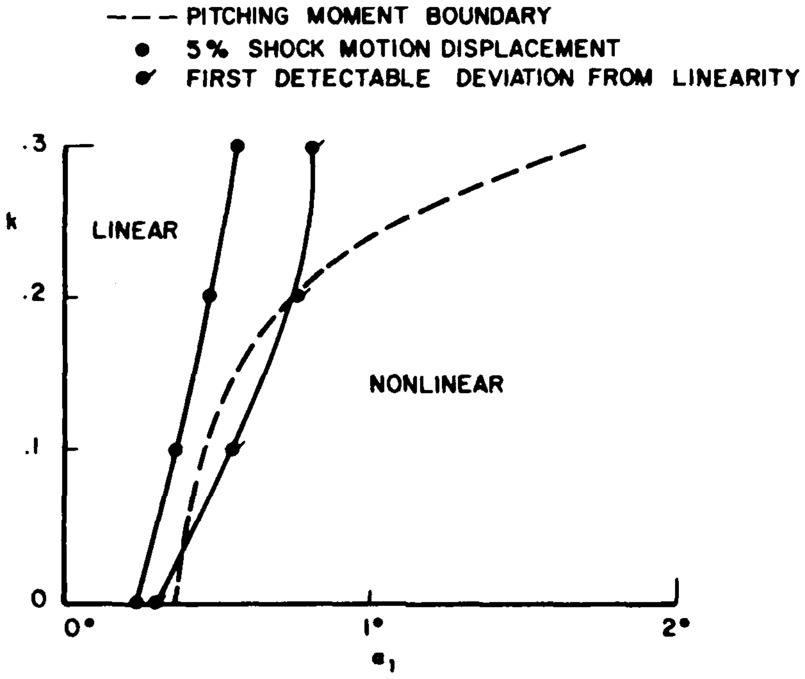

Fig.III-6 Conservative boundary for linear vs. nonlinear behavior based upon shock motion amplitude

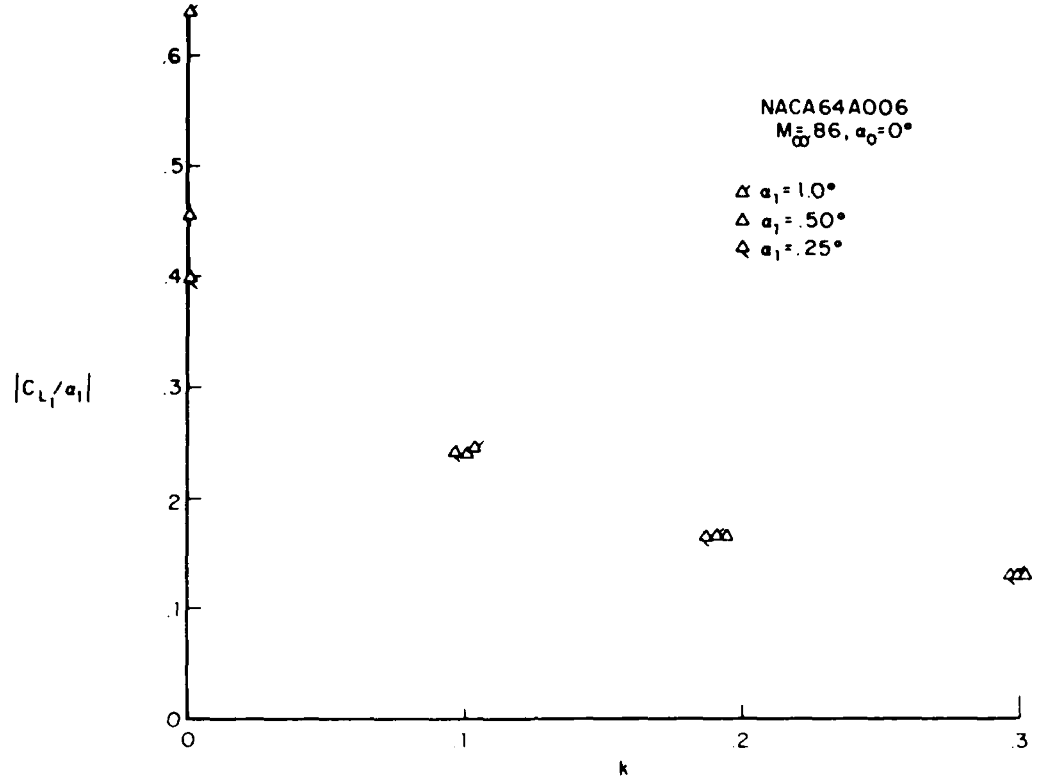

Fig.III-7(a) Effect of reduced frequency and dynamic amplitude on lift transfer function: Amplitudes

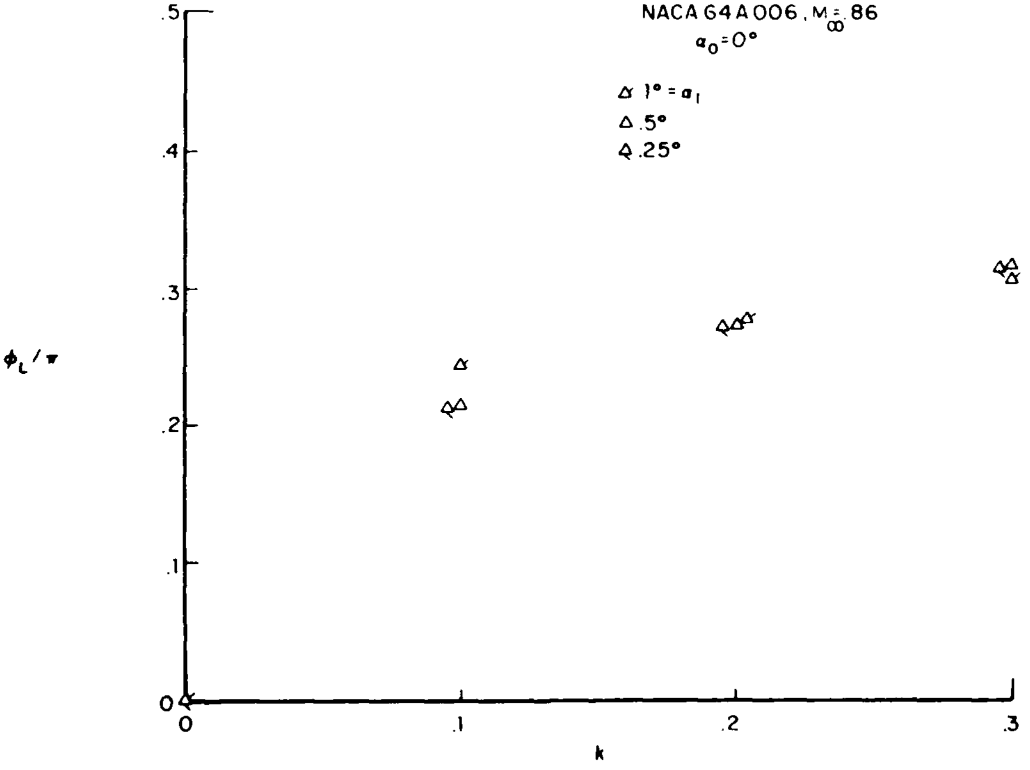

Fig.III-7(b) Effect of reduced frequency and dynamic amplitude on lift transfer function: Phase

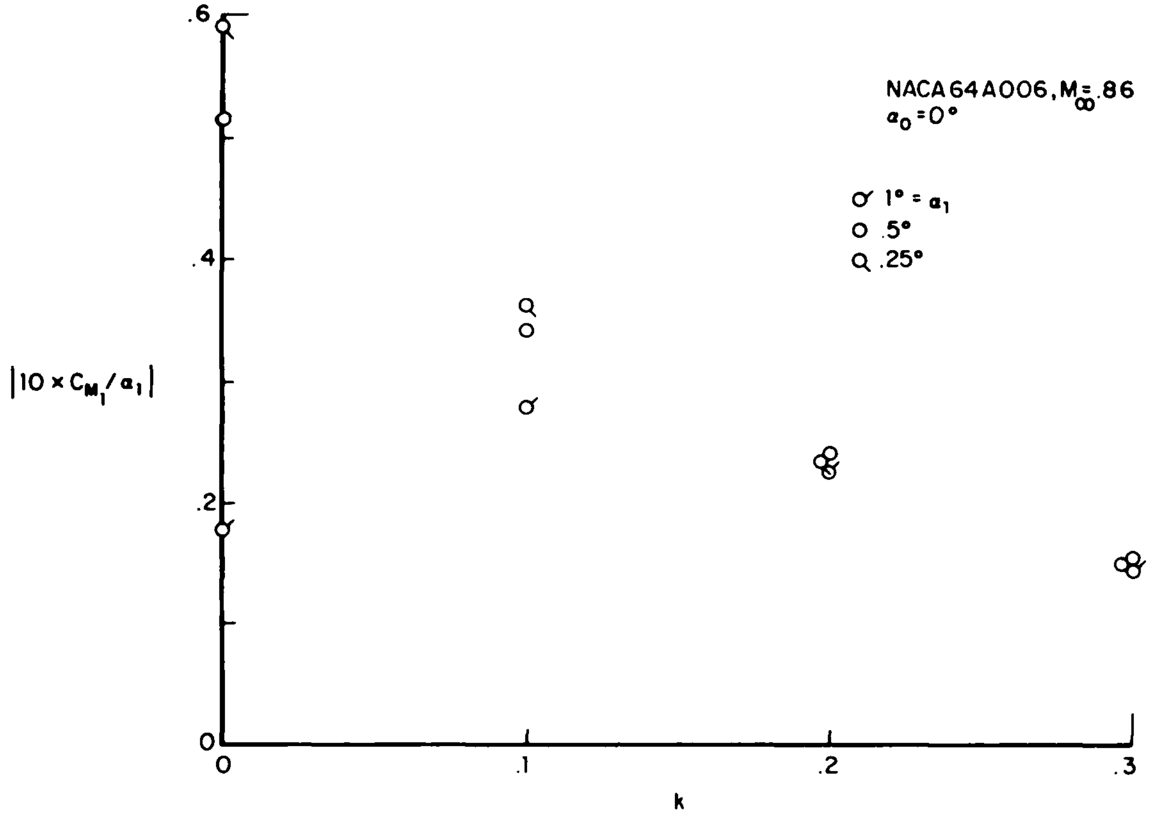

Fig.III-8(a) Effect of reduced frequency and dynamic amplitude on moment transfer function: Amplitudes

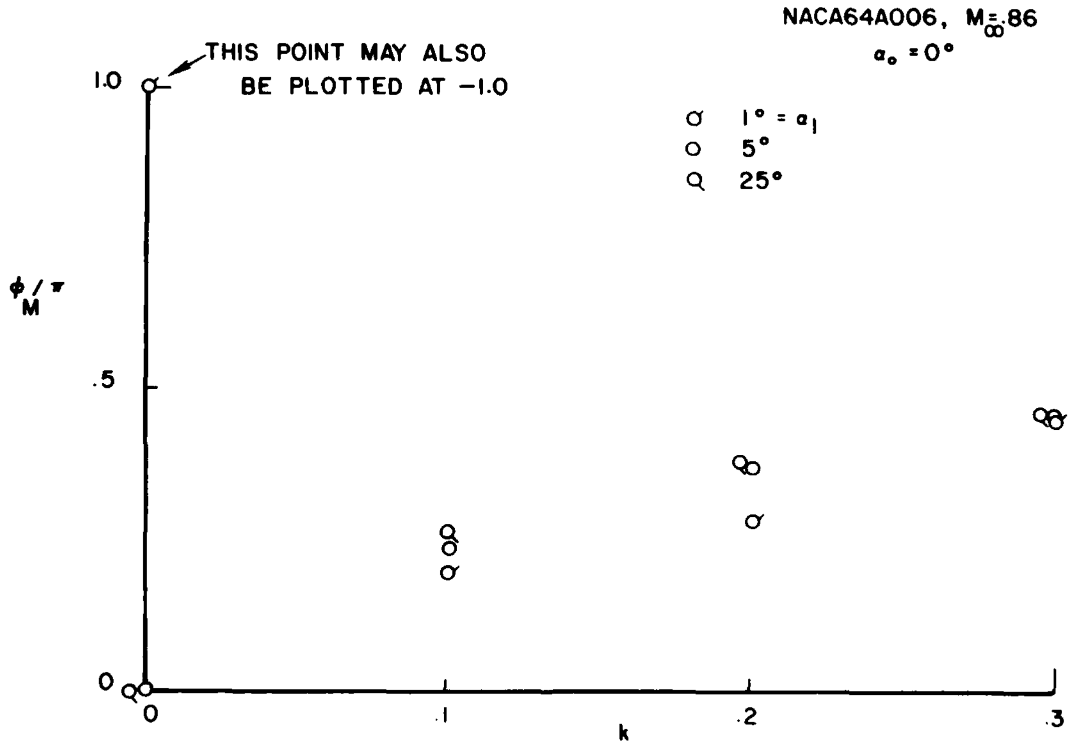

Fig.III-8(b) Effect of reduced frequency and dynamic amplitude on moment transfer function: Phase

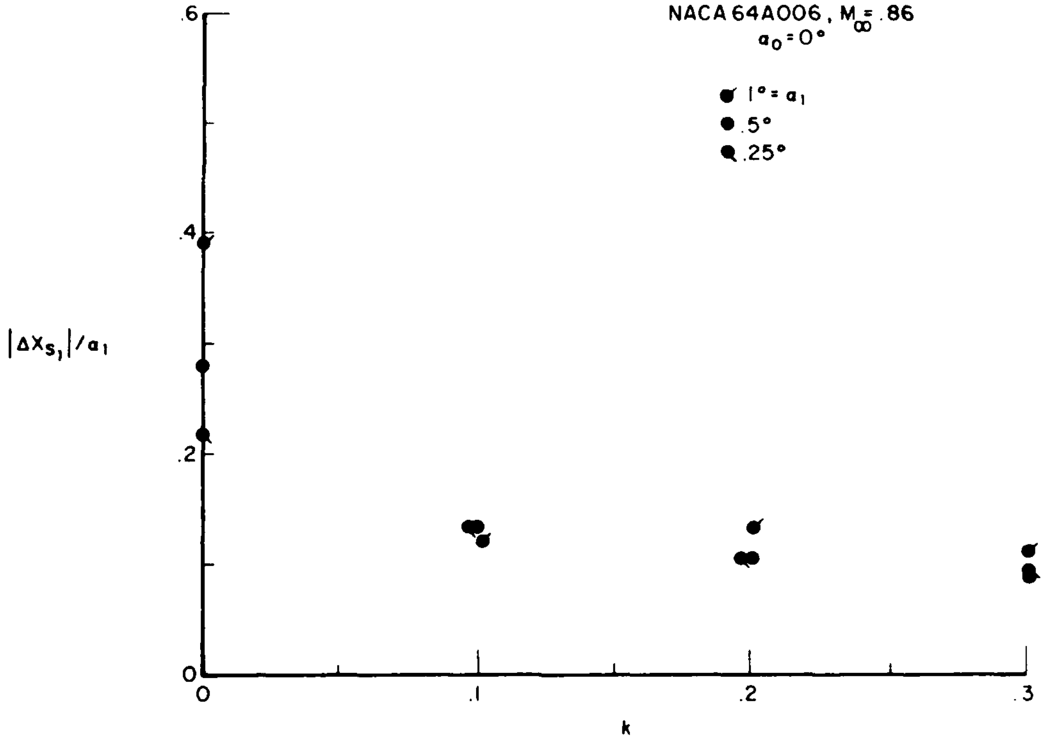

Fig.III-9 Effect of reduced frequency and dynamic amplitude on shock transfer function: Amplitudes

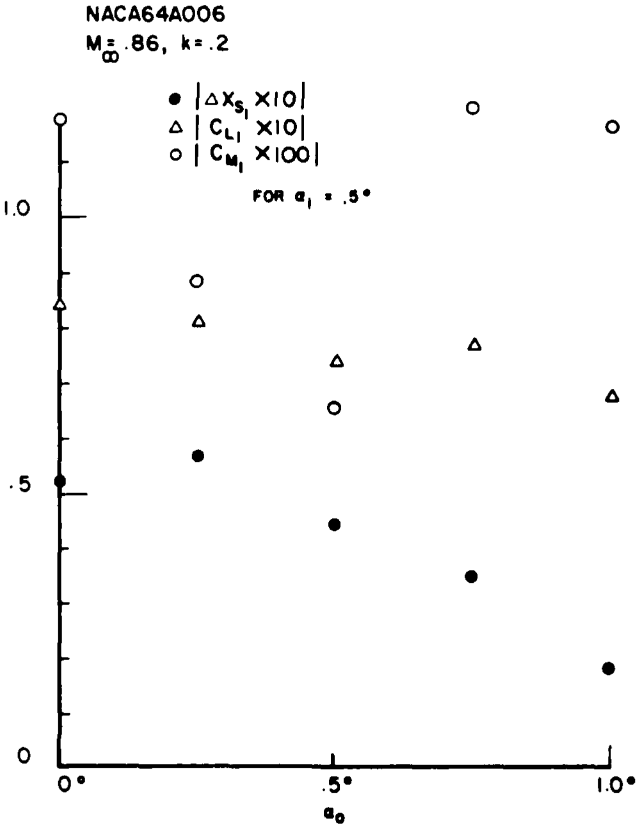

Fig.III-10(a) Effect of steady state angle of attack on dynamic forces and shock motion: Amplitudes

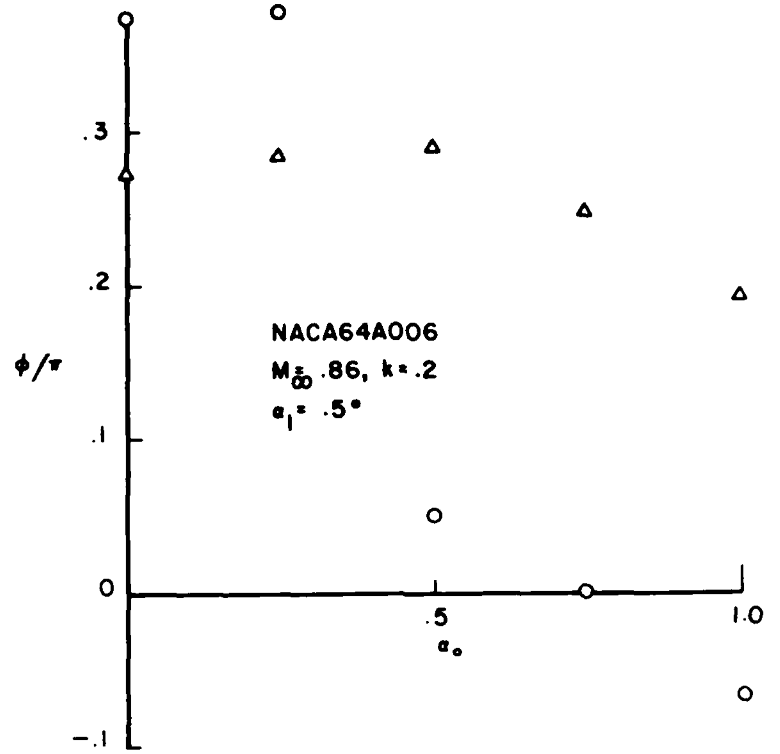

Fig.III-10(b) Effect of steady state angle of attack on dynamic forces: Phases

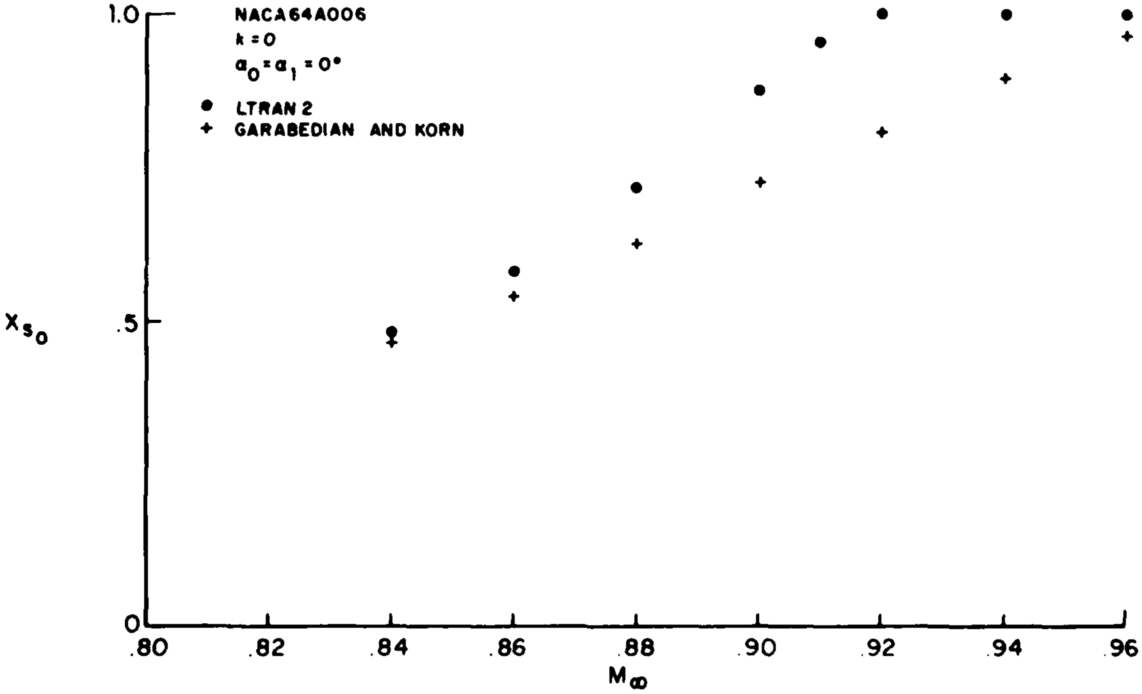

Fig.III-11(a) Shock position vs. freestream Mach number

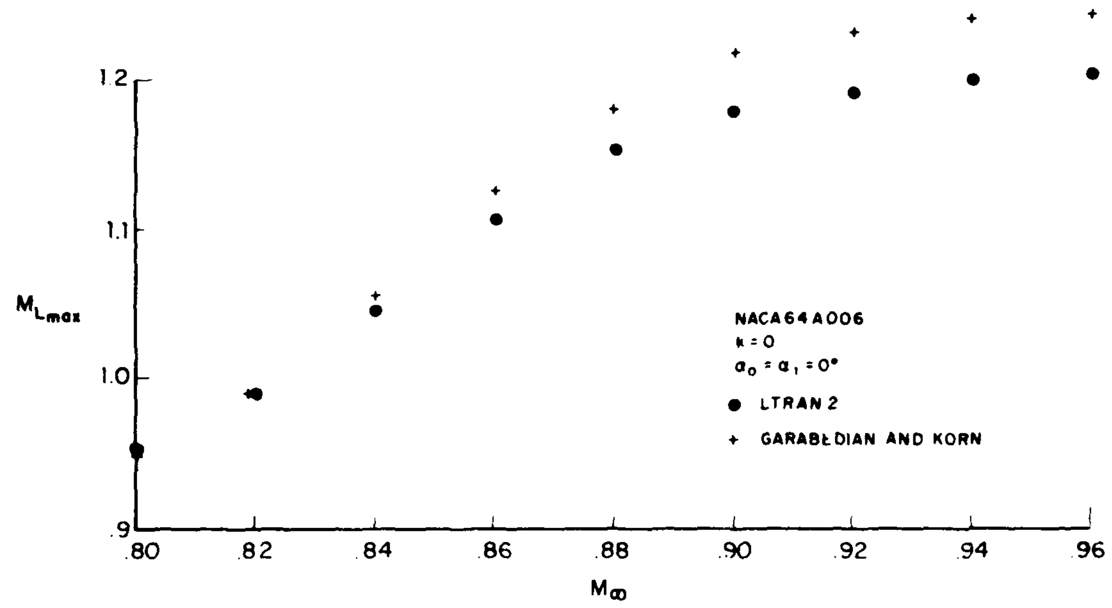

Fig.III-11(b) Maximum local Mach number

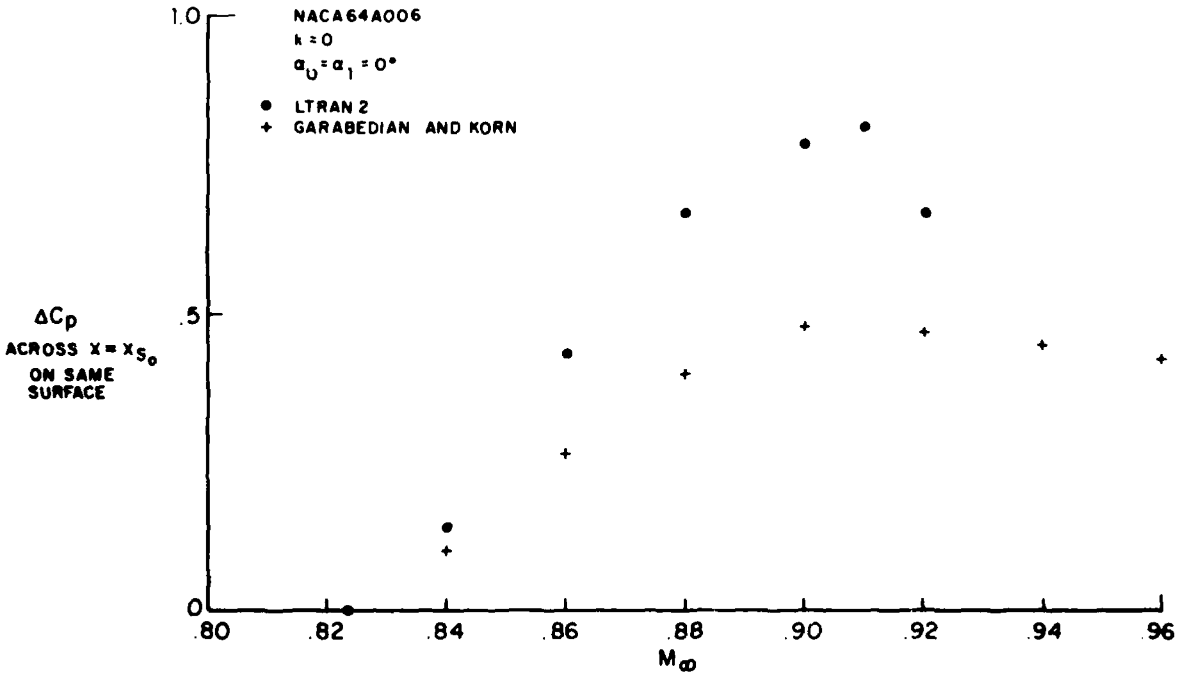

Fig.III-11(c) Pressure jump across shock

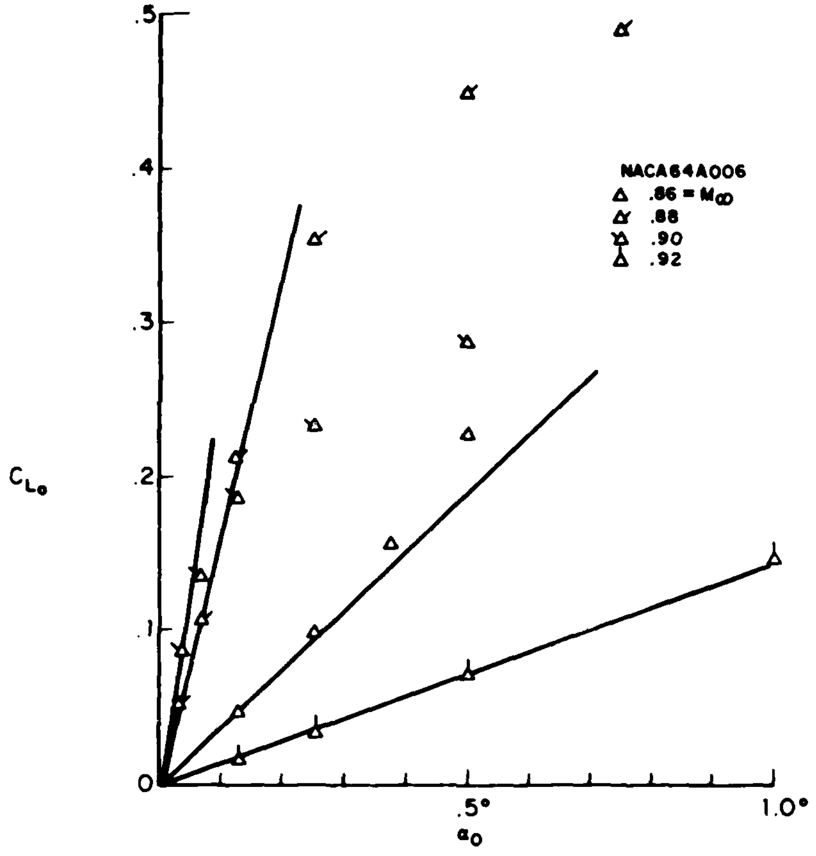

Fig.III-12(a) Lift vs. angle of attack

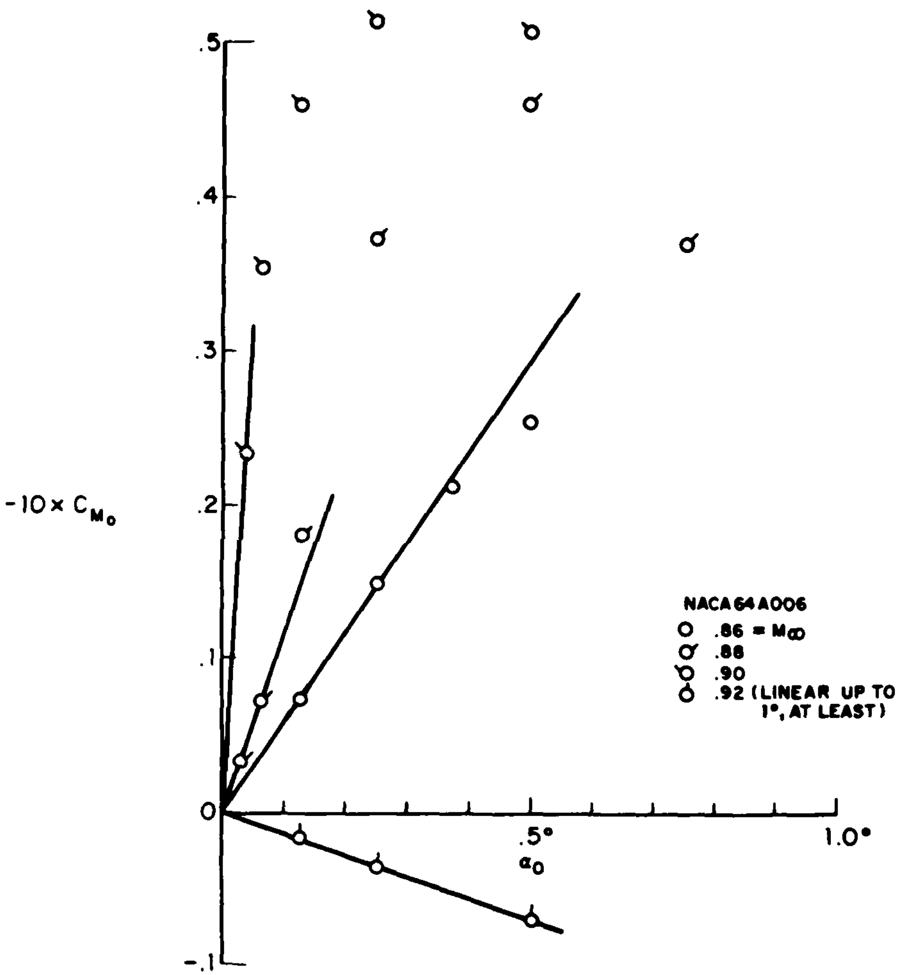

Fig.III-12(b) Moments vs. angle of attack

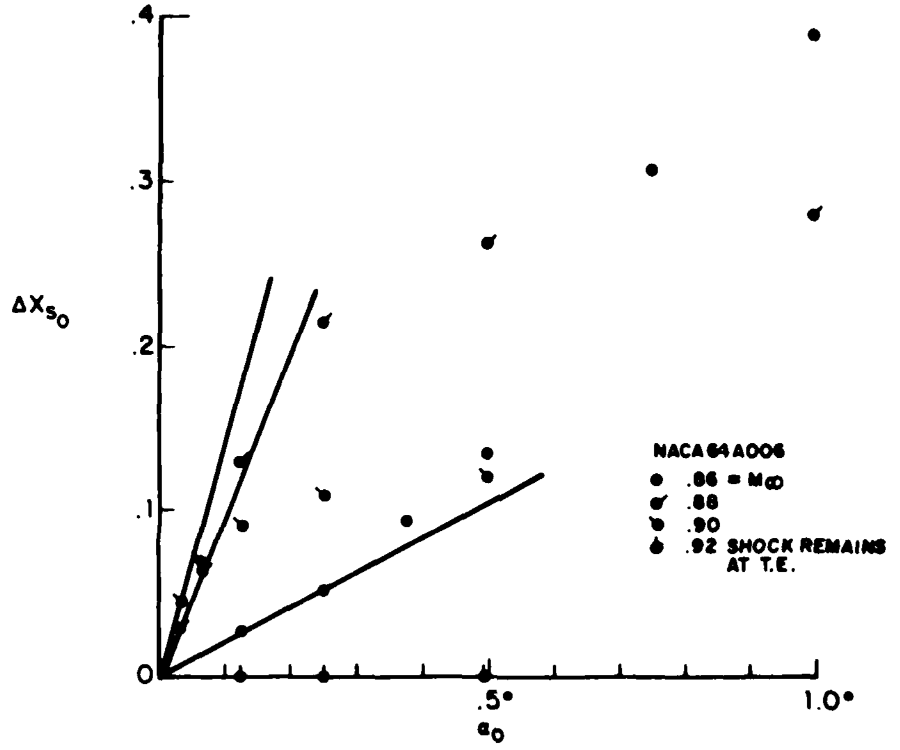

Fig.III-12(c) Shock displacement vs. angle of attack

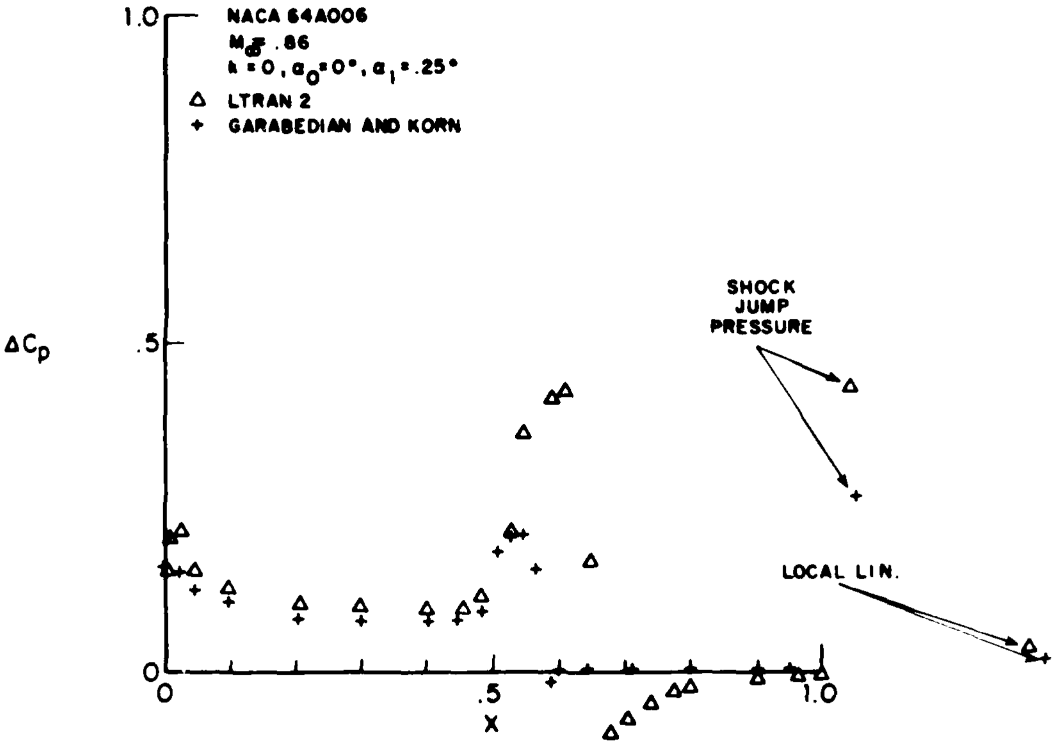

Fig.III-13(a) Differential pressure distribution

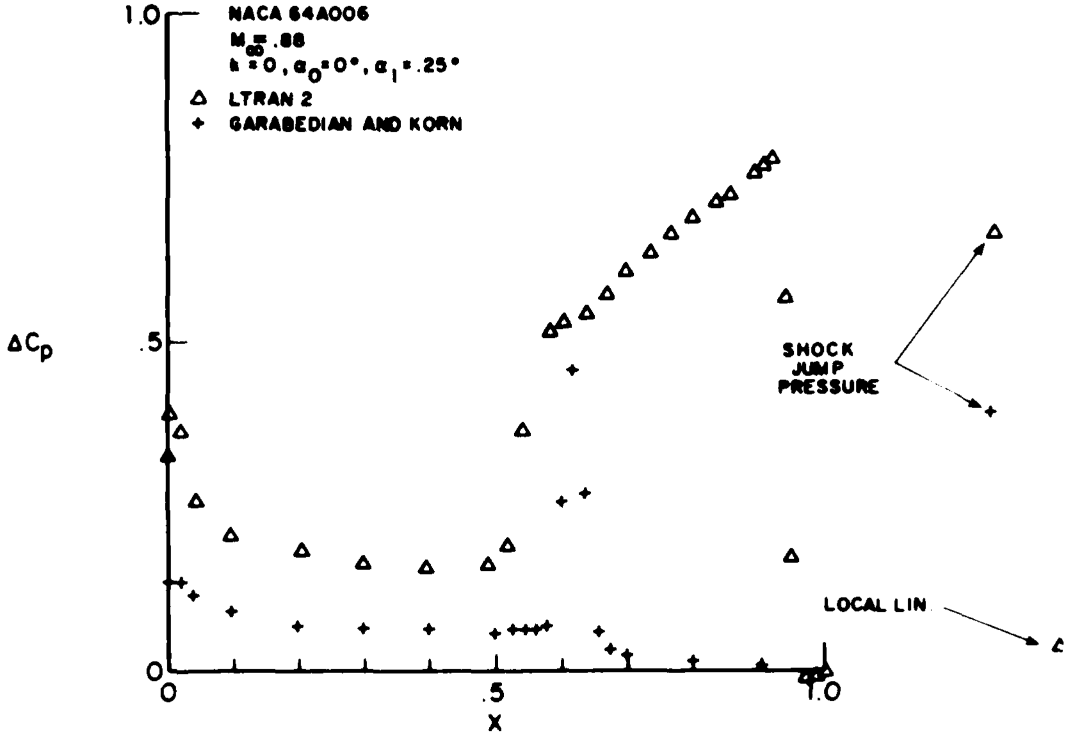

Fig.III-13(b) Differential pressure distribution

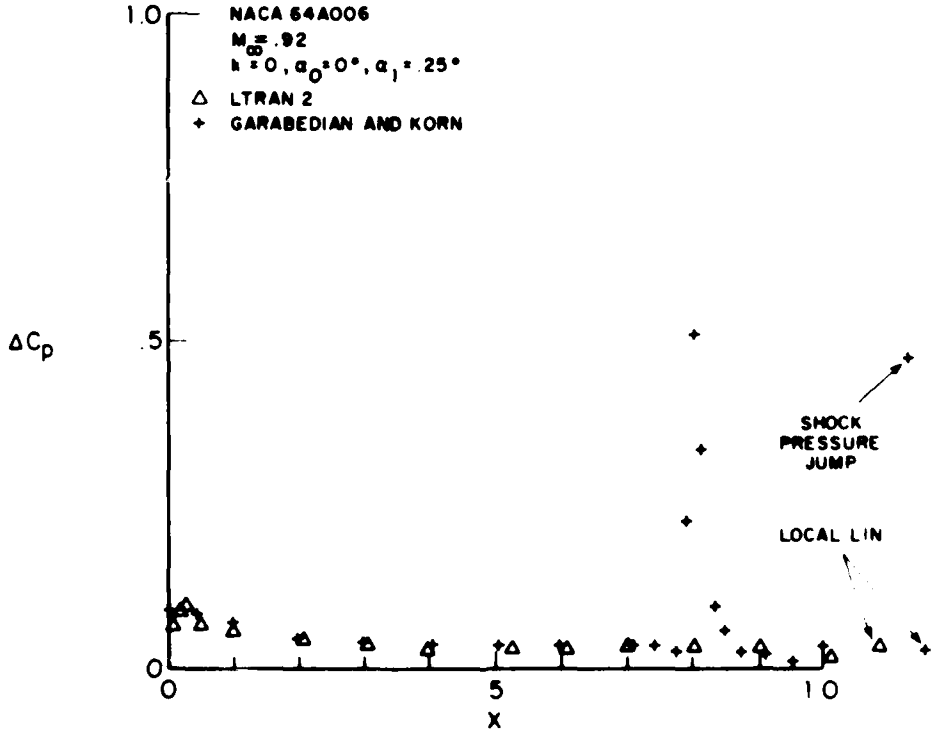

Fig.III-13(c) Differential pressure distribution

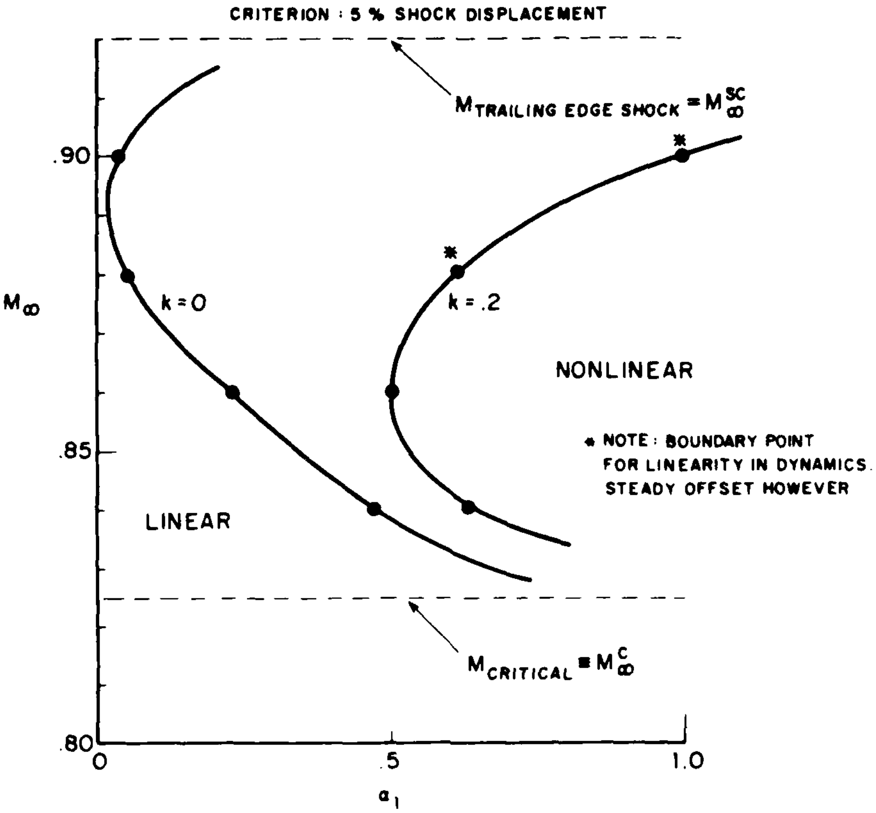

Fig.III-14 Linear/nonlinear boundary

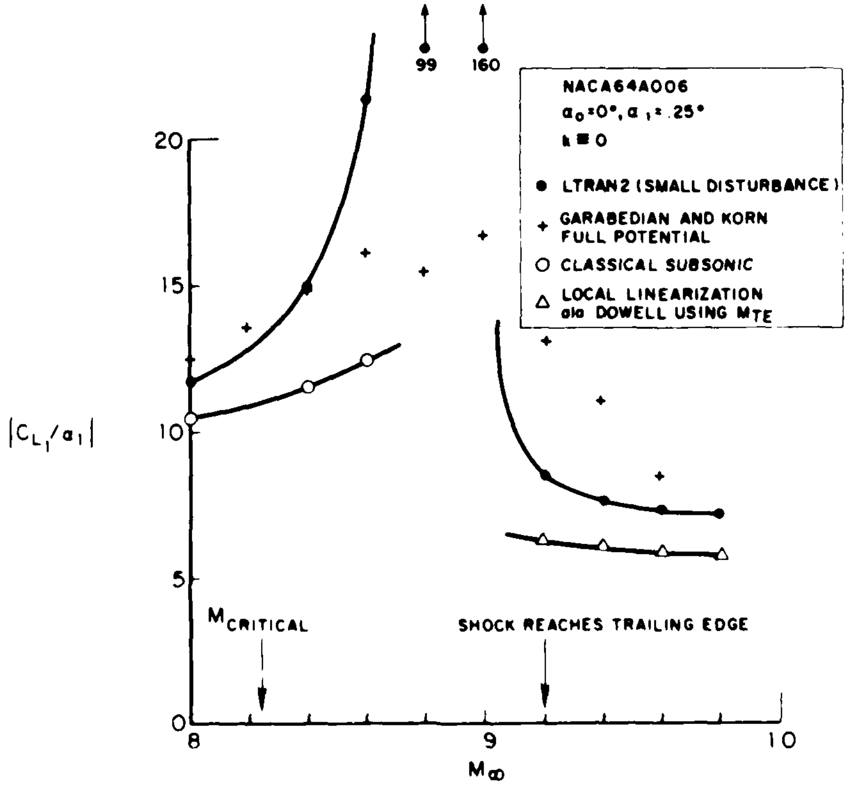

Fig.III-15(a) Lift curve slope vs. freestream Mach number

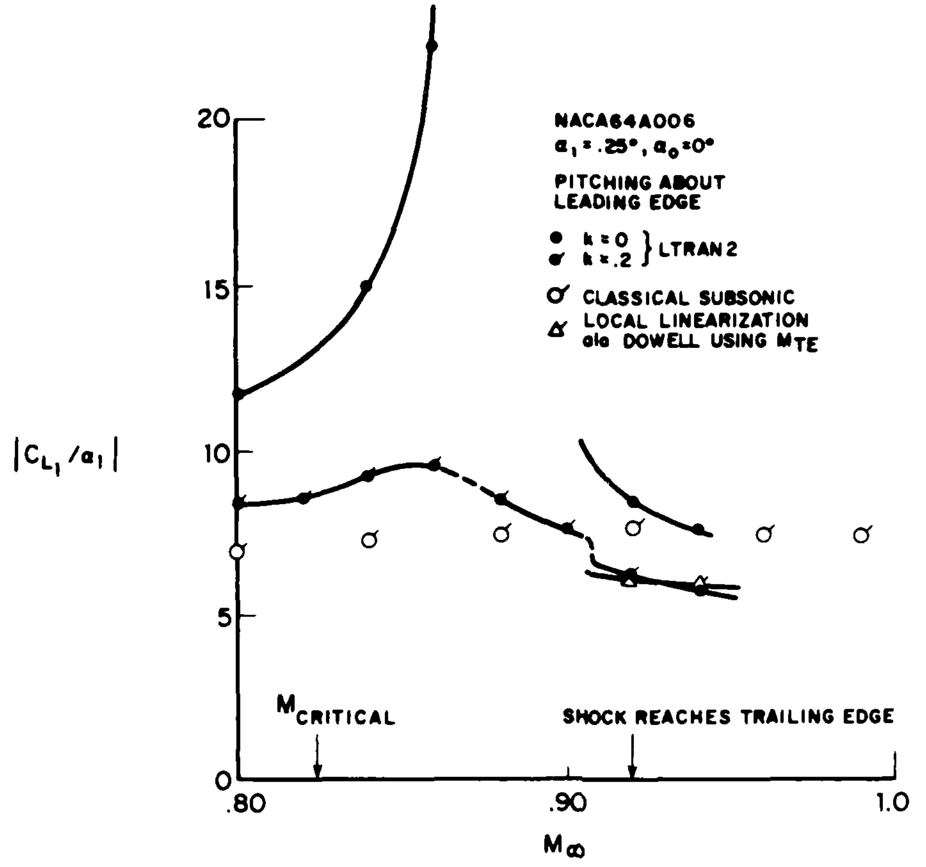

Fig.III-15(b) Lift curve slope vs. freestream Mach number

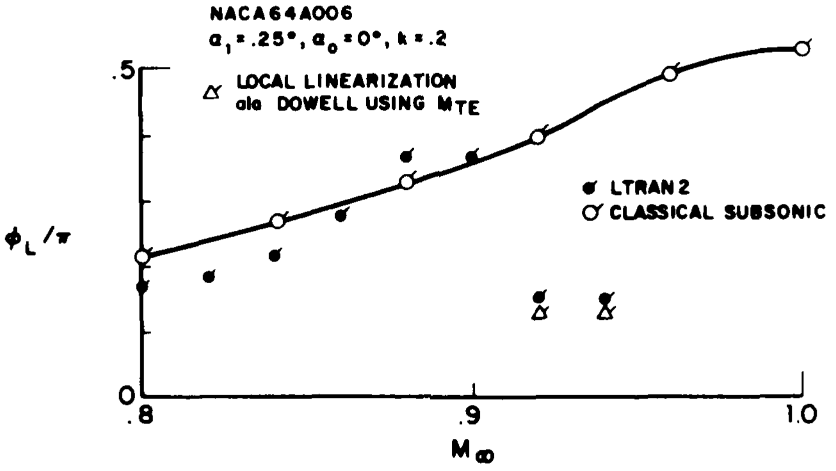

Fig.III-15(c) Phase of lift relative to pitch

OSCILLATING SUPERCRITICAL AIRFOILS IN THE TRANSONIC REGIME WITH VISCOUS INTERACTIONS

D. P. Rizzetta, Specialist Engineer, and
H. Yoshihara, Engineering Manager
Boeing Military Airplane Company
P. O. Box 3999 M/S 41-18
Seattle, Washington 98124

SUMMARY

A method is presented for computing the unsteady transonic flowfield about thick supercritical airfoils in the small disturbance limit. In order to compensate for the limitations of the small disturbance assumption and also to account for the aft decambering effect of viscous displacement, the airfoil geometry is modified such that the steady mean experimental pressure distribution is recovered. In addition, effects of the unsteady shock-boundary layer interaction are simulated by placing a moving wedge-nosed ramp at the base of the shock to produce quasi-statically the reduced shock pressure rise which is observed experimentally in the steady case. As a computational example, a solution for the pitching oscillation of an NLR 7301 airfoil (NASA Ames model) at M = 0.75 is computed. Comparison with experimental data indicates that even for relatively thick airfoils reasonable unsteady surface pressure distributions may be obtained using this procedure.

1. INTRODUCTION

Solutions of planar inviscid unsteady transonic flow fields about oscillating airfoils are commonly obtained by time integration of the differential equation governing the velocity potential function. This method is particularly attractive because it permits the treatment of nonlinear flow phenomena including irregular shock wave motion. Development of the LTRAN2 code by Ballhaus and Goorjian[1] has made available an efficient time-implicit finite difference algorithm for obtaining solutions to the *low-frequency* small disturbance transonic potential equation. This code is currently in extensive use for computing unsteady transonic flows over arbitrary thin airfoils and has evolved as a useful tool for performing aeroelastic calculations and flutter analysis.

Unlike more conventional sections, the flow field about a thick supercritical airfoil is not readily computed using an inviscid small perturbation analysis. In this case, not only are the small disturbance assumptions violated, but viscous effects tend to play a significant role in determining the resultant surface pressure distribution. While a more exact set of governing equations may be employed for the flow field solution, the computational effort involved is prohibitive for practical aeroelastic applications. If the primary purpose of a calculation is to establish with reasonable accuracy the unsteady surface pressure distribution, this may be obtained in an efficient manner using a purely inviscid small disturbance calculation technique which is suitably modified to account for the effects of thickness, viscous displacement, and unsteady shock-boundary layer interaction. It is the intent here to describe such a calculation and to provide a computational example for comparison with experiment.

2. GOVERNING EQUATION

If x and y are streamwise and normal Cartesian coordinates respectively normalized by the airfoil chord c, and t is the time nondimensionalized by the inverse of the circular oscillation frequency ω, then the small disturbance equation to be considered is:

$$kM^2\phi_{tt} + 2kM^2\phi_{xt} = \left[(1-M^2)\phi_x - \left(\frac{\gamma+1}{2}\right)M^2\phi_x^2\right]_x + \phi_{yy}\,. \tag{1}$$

Here ϕ is the perturbation velocity potential function normalized by cU where U is the freestream velocity, M the freestream Mach number, γ the specific heat ratio, and $k = \omega c/U$ is the reduced frequency. The corresponding local instantaneous pressure coefficient is then given by

$$C_p = -2(\phi_x + k\phi_t)\,. \tag{2}$$

For an airfoil surface defined by $y^{\pm} = f^{\pm}(x,t)$ the condition of flow tangency becomes

$$\phi_y^{\pm} = f_x^{\pm} + kf_t^{\pm}\,, \tag{3}$$

where Eq. (3) is evaluated on $y = 0$. Across the trailing vortex wake defined by $y = 0$ for $x > 1$, we impose the contact jump conditions

$$[\phi_y] = 0 \quad (\text{continuity of slope}) \tag{4}$$

$$[\phi_x + k\phi_t] = 0 \quad (\text{continuity of pressure}) \tag{5}$$

where the brackets denote the jump in the enclosed quantity from above to below the vortex sheet. At the outer boundaries the following are applied:

$$\phi = 0 \quad \text{far upstream,} \tag{6}$$

$$\phi_y = 0 \quad \text{far laterally,} \tag{7}$$

$$\phi_x + k\phi_t = 0 \quad \text{far downstream.} \tag{8}$$

Finally, description of the problem is completed by the initial conditions

$$\phi(x,y,0) = g(x,y), \quad \phi_t(x,y,0) = h(x,y) \tag{9}$$

where g and h are prescribed functions.

For the case of steady flow, a quasi-inverse problem is defined by replacing Eq. (3) with

$$\begin{aligned} \phi_y^+ &= f_x^+ \text{ for } 0 \le x \le x^+, \quad \phi_x^+ = -C_p^+/2 \text{ for } x^+ < x \le 1, \\ \phi_y^- &= f_x^- \text{ for } 0 \le x \le x^-, \quad \phi_x^- = -C_p^-/2 \text{ for } x^- < x \le 1. \end{aligned} \tag{10}$$

Equation (1) may then be integrated in time to achieve the steady state and the resulting airfoil slopes can be extracted. Since the design calculation is performed only downstream of the leading edge region, the question of uniqueness of the solution does not arise.

Equation (1) and its associated boundary conditions is similar to that considered by Ballhaus and Goorjian in the LTRAN2 code which was developed to treat only low frequency unsteady disturbances. The formulation adopted here includes higher order time derivatives of the velocity potential in the governing equation and unsteady airfoil surface and wake conditions. Solutions to this problem have been obtained with the code ExTRAN2 which results from a simple modification of the original LTRAN2. The ExTRAN2 code employs a first order accurate (in time) noniterative alternating direction implicit algorithm to advance the solution for ϕ from one time step to the next at each grid point in the computational flow field. Details of the algorithm may be found in Reference 3. A number of results generated by the ExTRAN2 code [2,3] have indicated that it is both stable and reliable. Furthermore, the additional terms in the potential equation and boundary conditions were found to be important for oscillations of moderate frequency[2,3].

3. VISCOUS MODELING

The significant consequences of the viscous displacement on a supercritical airfoil are two fold. The *primary effect is the shock-boundary layer interaction whereby a "wedging" displacement of the* boundary layer causes a reduced shock pressure rise and an upstream displacement of the shock, both relative to the inviscid case. For steady flows, a simple procedure has been developed for modeling shock-boundary layer interaction[4,5]. A wedge-nosed ramp is placed at the base of the shock in an inviscid calculation in order to produce the experimentally observed reduced shock pressure rise and hence a more acceptable shock location. More recently[2], this procedure has been implemented in an unsteady calculation to produce the reduced shock pressure rise in a quasi-static fashion, thus accounting for the unsteady shock-boundary layer interaction.

The second important viscous interaction is the aft decambering which arises due to the difference of the displacement thicknesses on the two sides of the airfoil. In a steady case the aft displacement ramps can be determined if suitable experimental pressure distributions are on hand. This is accomplished by prescribing in a finite difference inviscid calculation the measured pressures as boundary conditions aft of the leading edge region. Elsewhere the geometric slopes are prescribed. Such a calculation then yields the required aft ramps which in the present case of the thick supercritical airfoil would be composed, not only of the viscous displacement layers, but of the aft "compensation" ramps offsetting the consequences of the small disturbance approximation.

In the oscillating case, the aft pressures are closely invariant to the angle of attack. Thus in the present unsteady case, the above steady ramps evolved at the mean incidence are frozen onto the airfoil.

In addition, because small disturbance assumptions are violated near the leading edge of blunt airfoils, the upper and lower surface slopes in this region are adjusted to provide better agreement with experiment at the mean angle of attack.

The above procedure was applied to an NLR 7301 airfoil at $M = 0.75$ and $\alpha = 0.37$. The original airfoil geometry shown in Figure 1 corresponds to that of a NASA-Ames test model[6] which is approximately 16.8% thick. Figure 2 indicates a comparison between the initial and modified value of the airfoil surface slopes, where the original result was obtained by a cubic spline fit to the coordinates of the Ames test model.

A comparison of numerical results at the steady mean flow condition with the experiment of Davis[7] is presented in Figure 3. Here the unmodified solution includes slope alterations near the leading edge, but not those resulting from the design calculation. With the aft displacement ramps and the shock wedge, a reasonably good agreement is obtained for the steady mean flow.

Unsteady effects of the shock boundary-layer interaction as described above are simulated by placing a wedge-nosed ramp at the base of the moving shock in a quasi-steady fashion. This technique was previously implemented in steady calculations to produce the experimentally observed reduced post shock pressure rise[4,5]. A simple modification for extending this simulation to unsteady flows is found in Reference 2.

For the results presented here, we have adopted the following ramp geometry which is depicted schematically in Figure 4. The leading edge of the ramp is located ahead of the sonic point at a distance equal to 2% of the chord. This offset is commonly used in steady calculations in order to properly influence the numerical shock profile which typical has a width of three mesh intervals. Preceding the ramp leading edge is a 2% chord cusped-nose precursor in which the slope varies linear from zero to the ramp angle, θ . The function of the precursor is to moderate the impact of the sudden change in slope experienced by an isolated mesh point as the nose of the ramp moves across the computational mesh during corresponding unsteady shock motion. Following the precursor is the main ramp body with a length of 5% chord which varies the slope quadratically from θ at the nose to zero at the downstream end.

The value of θ is taken as that for maximum turning for an attached oblique shock and may be derived from the jump conditions of the low frequency (or steady) form of Eq. 1. In the course of the time integration of Eq. 1, θ and the location of the sonic point are obtained from the solution at time t . These two parameters completely define the ramp geometry which is then used to advance the solution to the next time step, $t + \Delta t$. Thus the angle and location of the ramp are free to adjust to unsteady shock wave motion in manner much like the physical boundary layer. It should be noted that the length of the ramp and amount of offset will vary in accordance with the nature of a particular solution, as well as with the computational mesh spacing.

4. RESULTS

Results presented in this section were generated on a 101 X 97 Cartesian grid defined by $-200 \le x \le 200$, $-397.8 \le y \le 397.8$, with 39 points lying on the airfoil surface. A smooth nonuniform computational mesh which is symmetric about y = 0 was employed. Minimum grid spacings were taken as $\Delta x_{min} = 0.02$ near the leading edge and $\Delta y_{min} = 0.01$ at y = 0. The initial profile is given by the steady state solution at the mean angle of attack, which is shown in Figure 3.

An unsteady solution was obtained for the angle of attack prescribed as $\alpha = 0.37^0 + 0.5^0 \sin t$ and $k = 0.6$, which duplicates the test conditions of Davis[7]. A time step was selected as $\Delta t = 0.01745$, corresponding to 1^0 of oscillation per time step at the reduced frequency. The choice of a very small time step was based solely upon accuracy considerations rather than for stability requirements. After three periods of oscillation, the solution was found to achieve a stationary state. This computation required approximately 5 minutes of central processing time on a CDC Cyber 175 computer.

In Figure 5 we first compare the calculated pressure distributions at quarter cycle intervals with the measured results of Davis[7], who obtained measurements only on the upper surface. The agreement seen here can be seen in more detail in Figures 6 and 7 where the amplitude and phase of the first harmonic of the pressure variations are plotted. It is to be noted here that the amplitude of the unsteady pressure variation of Figure 6 is small compared to the mean pressure values.

Finally, in Figure 8 we show the calculated lift and moment coefficients over the pitching cycle. The latter is referenced to the center of oscillation at X = 0.4.

5. CONCLUSIONS

A method has been presented for analyzing the unsteady flow over a thick supercritical airfoil oscillating in transonic flow. The method utilizes an efficient method for time integrating the small disturbance potential equation. Limitations of this simplifying assumption as well as viscous effects are then overcome by suitable geometric modifications of the airfoil following a design calculation. In addition, the unsteady shock-boundary layer interaction has been simulated using a simple computational artifice. The method is predicated on the use of steady experimental results to tailor the modelling of the displacement ramps to be used for subsequent unsteady analyses. A solution has been compared with experimental data and was shown to produce reasonable agreement which is acceptable for flutter analysis and aeroelastic applications.

REFERENCES

1. Ballhaus, W. F. and Goorjian, P. M., "Implicit Finite-Difference Computations of Unsteady Transonic Flows about Airfoils", AIAA Journal, Vol. 15, December 1977, pp 1728-1735.

2. Rizzetta, D. P. and Yoshihara, H., "Computations of the Pitching Oscillation of a NACA 64A010 Airfoil in the Small Disturbance Limit", AIAA Paper 80-0128, Pasadena, California, January 1980.

3. Rizzetta, D. P. and Chin, W. C., "Effect of Frequency in Unsteady Transonic Flow", AIAA Journal, Vol. 17, July 1979, pp 779-781.

4. Mason, W. H., Ballhaus, W. F., MacKenzie, C., Frick, J., and Stern, M., "An Automated Procedure for Computing the Three-Dimensional Transonic Flow Over Wing-Body Combinations, Including Viscous Effects", AFFDL-TR-77-122, Volume I, February 1977.

5. Yoshihara, H., "Fixes to the 3D Transonic Small Disturbance Theory", Convair Report CASD-ERR-75-012, 1975.

6. Olsen, J. J., "AGARD Standard Configurations for Aeroelastic Applications", AFFDL-TM-78-6-FBR, Part III Appendix, January 1978.

7. S.S. Davis, and Malcolm, G. N., "Unsteady Aerodynamics of Conventional and Supercritical Airfoils", AIAA Paper 80-0734, Seattle, Washington, May 1980; also private communication.

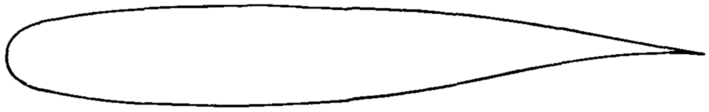

Figure 1. NLR 7301 Airfoil

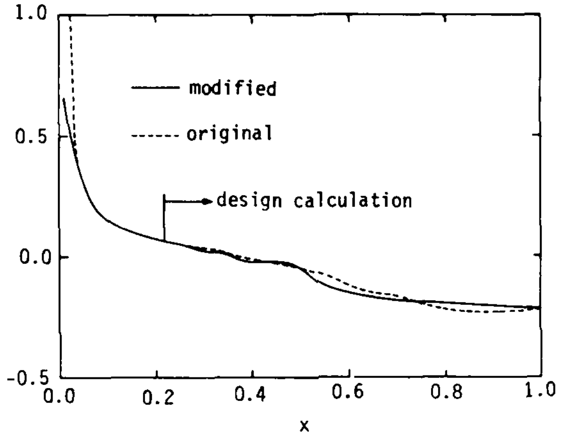

a) Upper Surface

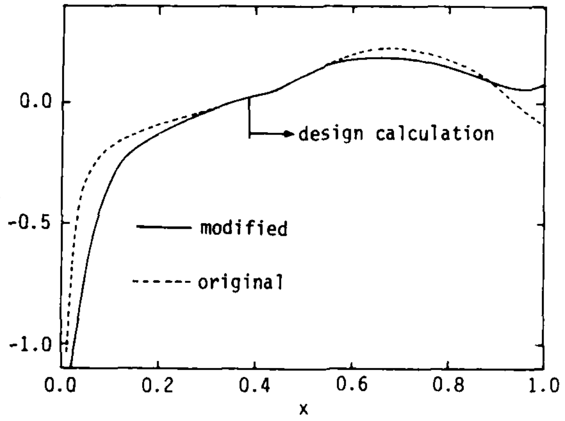

b) Lower Surface

Figure 2. Comparison of Original and Modified Airfoil Surface Slopes

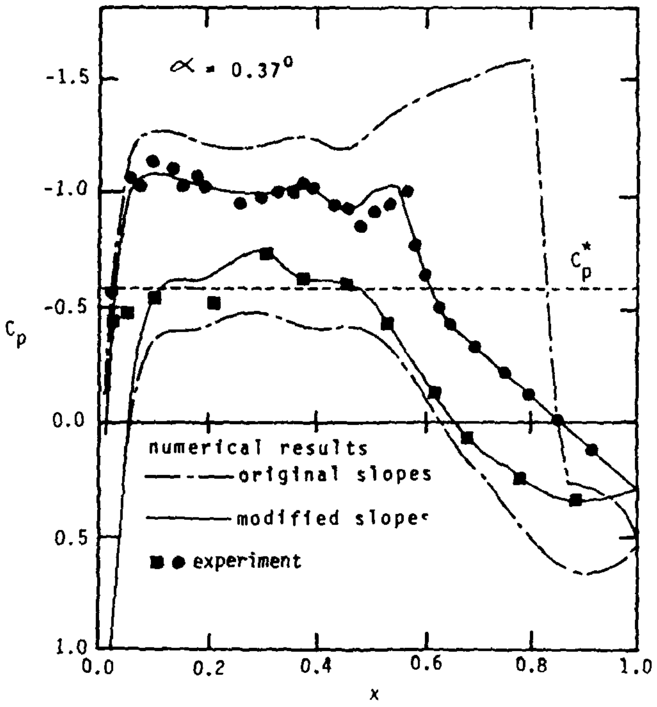

Figure 3. Comparison of Steady State Surface Pressure Distributions with Experiment

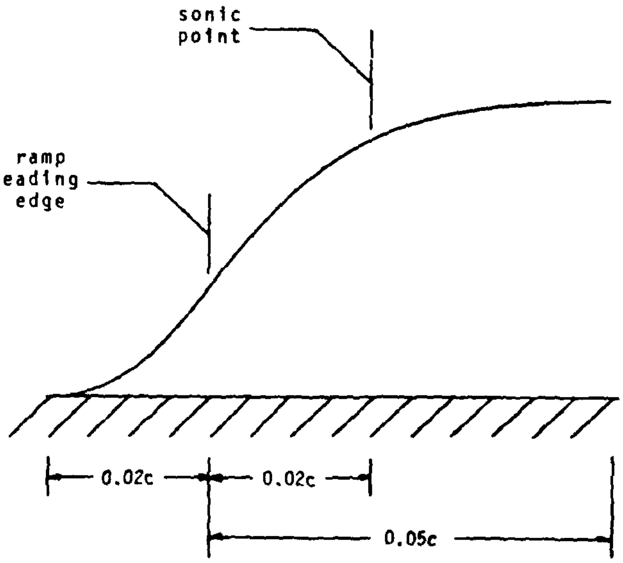
sonic point
ramp leading edge
0.02c
0.02c
0.05c

Figure 4. Ramp Geometry

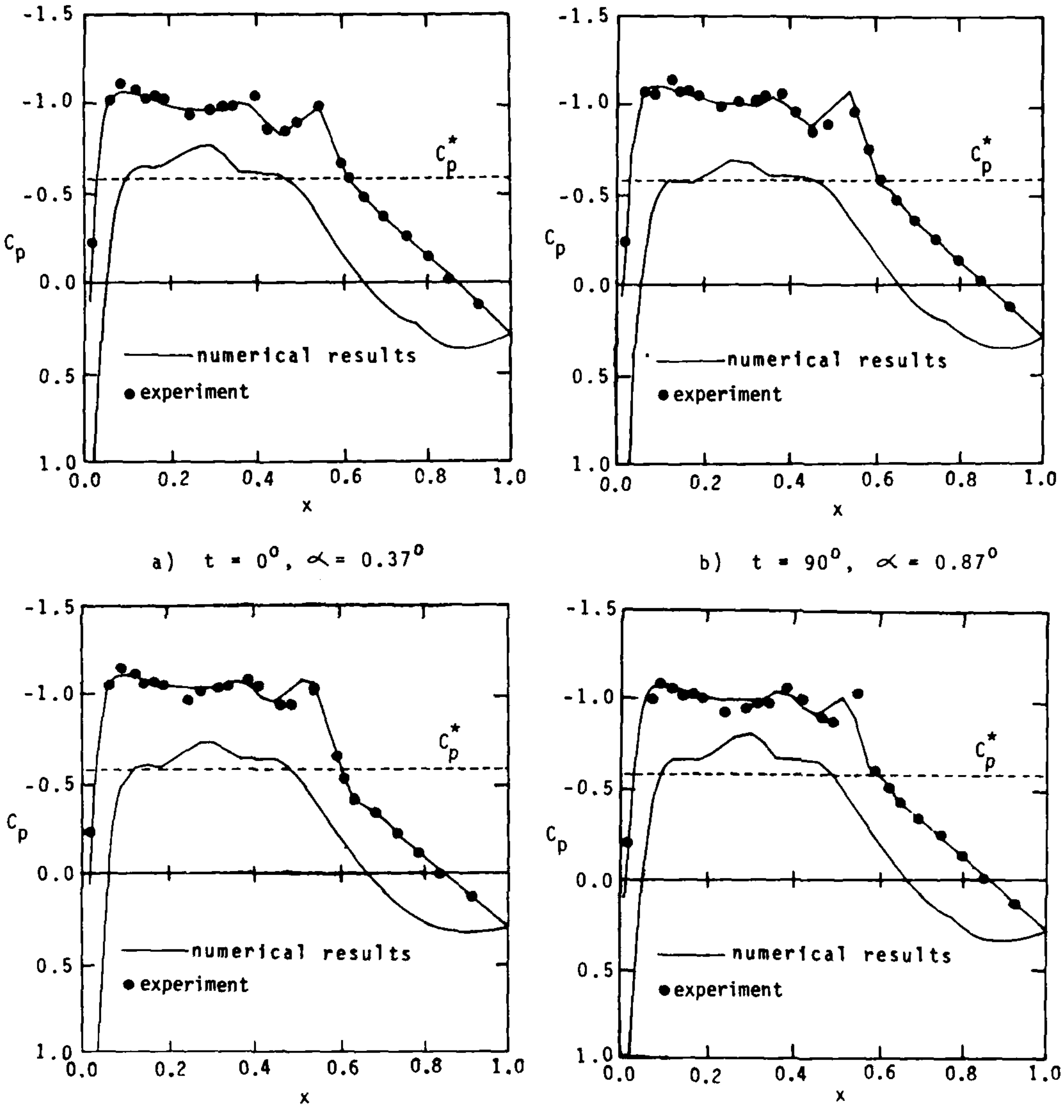

a) t = 0°, α = 0.37°

b) t = 90°, α = 0.87°

c) t = 180°, α = 0.37°

d) t = 270°, α = 0.13°

Figure 5. Comparison of Unsteady Surface Pressure Distribution with Experiment

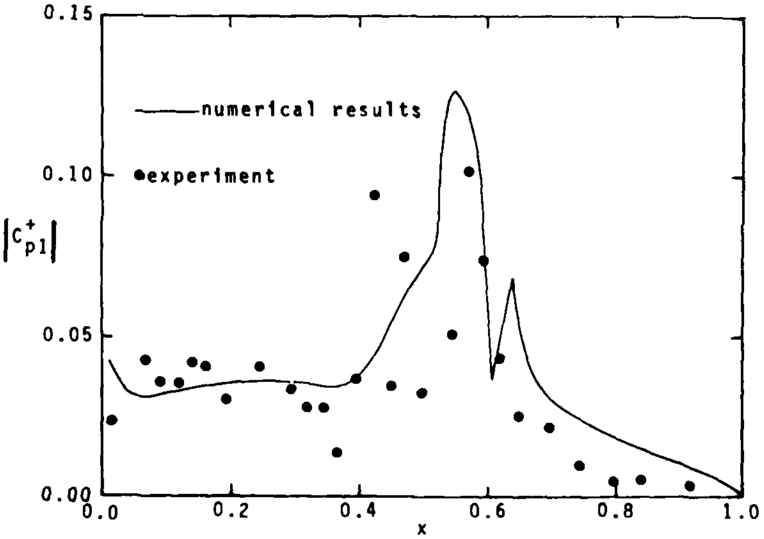

Figure 6. Comparison of Magnitude of First Harmonic of Unsteady Upper Surface Pressure Distribution with Experiment

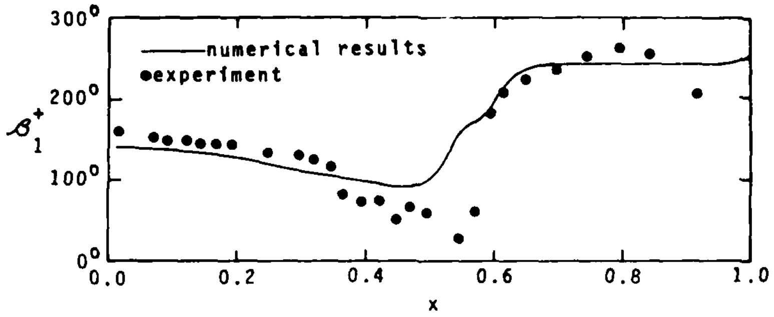

Figure 7. Comparison of Phase Angle of First Harmonic of Unsteady Upper Surface Pressure Distribution with Experiment

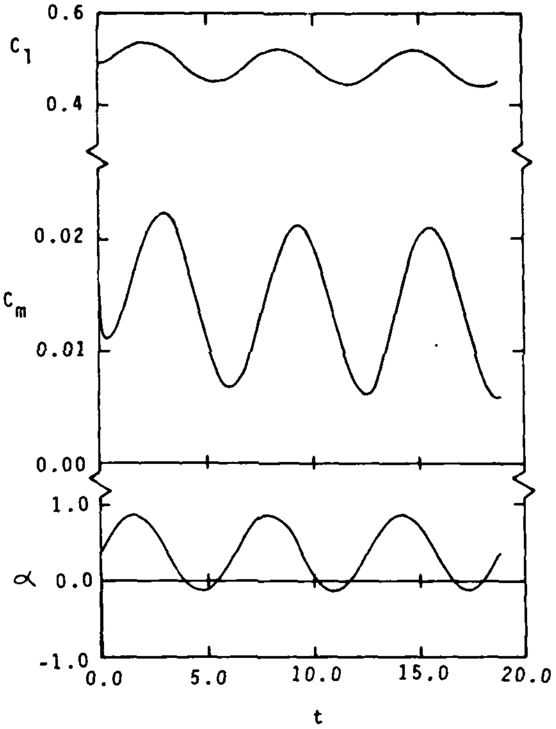

Figure 8. Unsteady Lift and Moment Coefficients

MÉTHODES DE CALCUL DES COUCHES LIMITES INSTATIONNAIRES

par

J.Cousteix, R.Houdeville, J.Javelle

ONERA/CERT
Département d'Aérothermodynamique
2 ave E.Belin
31055 Toulouse Cedex

RESUME

Plusieurs méthodes de calcul des couches limites turbulentes instationnaires ont été mises au point et étudiées en utilisant des niveaux de fermeture différents. Les plus complexes mettent en jeu un système d'équations de transport pour les composantes de l'énergie cinétique de turbulence, son taux de dissipation et la force de cisaillement turbulente. Les plus simples consistent à résoudre les équations globales de la couche limite. Pour certaines applications, une version linéarisée de cette dernière méthode a été développée. L'application de ces techniques et leurs limitations sont discutées à l'aide de comparaisons à des résultats expérimentaux.

Le problème de formation de singularités dans les calculs est abordé par l'analyse des propriétés des équations globales. Le recours aux méthodes inverses est également discuté.

SUMMARY

Several unsteady turbulent boundary layer prediction methods have been studied by using various levels of closure. The most complex methods are constituted by a set of transport equations for the components of the turbulence kinetic energy, its dissipation rate and the turbulent shear stress. The simplest methods consist in solving the global boundary layer equations. For certain applications, a linearized version of this latter method has been developed. The application of these techniques and their limitations are discussed through comparisons with experimental data.

The question of occurence of singularities in the calculations is tackled by analyzing the properties of the global equations. The recourse to inverse methods is also discussed.

NOTATIONS

x : Coordonnée longitudinale

y : Coordonnée perpendiculaire à la paroi

z : Coordonnée transversale

u, v, w : Composantes de la vitesse suivant x, y, z

u', v', w' : Fluctuations turbulentes de la vitesse

C_f : Coefficient de frottement $C_f/2 = \tau_p/\rho_e u_e^2$

τ_p : Frottement de paroi

ρ : Masse volumique

δ : Epaisseur conventionnelle de couche limite

δ_1 : Epaisseur de déplacement $\delta_1 = \int_0^\delta \left(1 - \frac{\rho u}{\rho_e u_e}\right) dy$

θ : Epaisseur de quantité de mouvement $\theta = \int_0^\delta \frac{\rho u}{\rho_e u_e}\left(1 - \frac{u}{u_e}\right) dy$

H : Paramètre de forme $H = \delta_1/\theta$

e : Indice relatif à l'écoulement extérieur

$\langle \; \rangle$: Dénote une moyenne d'ensemble

1. INTRODUCTION

Nous avons abordé le calcul des couches limites turbulentes, et plus spécifiquement ici en écoulement instationnaire, en adoptant deux points de vue aux exigences souvent très éloignées. Le premier consiste à essayer de prédire aussi finement que possible les caractéristiques de l'écoulement moyen et aussi quelques unes de la turbulence. Le second est beaucoup plus pratique puisqu'il vise à fournir des méthodes très rapides et commodes, capables cependant de rendre compte assez bien des effets les plus importants.

Nous avons ainsi été conduits à mettre en oeuvre deux classes de méthodes qui ne s'opposent pas mais qui sont plutôt complémentaires. Dans la première, on résout les équations locales de la couche limite à l'aide de modèles de turbulence s'appuyant sur des techniques modernes mettant en jeu des équations de transport pour certaines grandeurs caractéristiques de la couche limite. A l'aide de comparaisons à l'expérience, nous analyserons donc les qualités et défauts de ces méthodes en insistant notamment sur les problèmes soulevés par le caractère instationnaire de l'écoulement.

D'autre part, nous avons développé des méthodes qui reposent sur la résolution d'équations intégrales de couche limite. Il est clair que ces méthodes ne peuvent pas décrire aussi précisément que les précédentes les différents aspects de l'écoulement mais leurs performances très intéressantes nous ont amené à essayer de cerner leur domaine de validité en les comparant à l'expérience et aussi aux méthodes précédemment évoquées.

Enfin, nous aborderons le problème de la formation de singularités dans le calcul de couche limite instationnaire. Bien connue en stationnaire depuis les travaux de Goldstein, cette question n'a pas encore reçu de réponse aussi claire en instationnaire. Nous verrons comment on peut essayer d'apporter quelques éléments d'information en analysant les propriétés des équations globales de la couche limite.

2. METHODES DE CALCUL MISES EN OEUVRE

2.1. Résolution des équations locales - Modèles de turbulence

Nous abordons ici la description d'une méthode de champ destinée au traitement général des couches limites turbulentes bidimensionnelles instationnaires en écoulement incompressible. La méthode proposée conduit à la résolution de systèmes d'équations locales comportant, en plus des équations de continuité et de quantité de mouvement, les équations de transport de certaines grandeurs turbulentes. On trouvera dans les références /1/ et /3/ les éléments pour leur dérivation à partir des équations générales de Navier Stokes. Elles sont regroupées plus loin : paragraphe 2.1.5.. Toutes les variables y sont définies comme moyennes d'ensemble.

Diverses hypothèses permettant de fermer le problème en exprimant le frottement turbulent ont été analysées et leur validité contrôlée par une confrontation à l'expérience. Il est à souligner que malgré la complexité apparente de la modélisation et de certains schémas de turbulence proposés, nous disposons là d'un moyen de calcul rapide et précis, à large champ d'applications.

2.1.1. Schémas de turbulence

La résolution des équations locales nécessite l'introduction d'un schéma de turbulence permettant d'exprimer le frottement turbulent $-\rho\langle u'v'\rangle$. Les hypothèses les plus simples de fermeture constituent les modèles largement utilisés de longueur de mélange. Des schémas plus complexes introduisant les équations régissant l'évolution des composantes $\langle u'v'\rangle$, $\langle u'^2\rangle$, $\langle v'^2\rangle$ du tenseur de Reynolds, de l'énergie cinétique k de turbulence :

$$k = \frac{1}{2}\left(\langle u'^2\rangle + \langle v'^2\rangle + \langle w'^2\rangle\right)$$

et de son taux de dissipation :

$$\varepsilon = \nu \sum_{i,k} \left\langle \left(\frac{\partial u'_i}{\partial x_k}\right)^2 \right\rangle$$

ont été également confrontés entre eux et à l'expérience.

. Modèle de longueur de mélange :

La seule composante du tenseur de Reynolds exprimée est $-\langle u'v'\rangle$, sous la forme :

(F1) $$-\langle u'v'\rangle = \nu_t \frac{\partial U}{\partial y}$$

ν_t est une viscosité turbulente calculée à partir de la longueur de mélange par :

(F2) $$\nu_t = \ell^2 \frac{\partial U}{\partial y}$$

Près de la paroi, ℓ est proportionnelle à y : $\ell = \chi y$; $\chi = 0,41$

A l'extérieur, ℓ/δ est constante : $\ell = C\delta$; $C = 0,085$

Cette formulation peut être compliquée par l'adjonction de l'influence du gradient de pression moyen local, dans χ ou dans C.

Le système d'équations traité se réduit ici aux équations (E1), (E2) ; l'hypothèse de fermeture aux relations (F1) et (F2) accompagnées de la loi choisie pour la longueur de mélange.

. Modèle à deux équations de transport :

On joint dans ce modèle aux équations de continuité et de quantité de mouvement les équations de transport pour k et ε. Le frottement turbulent est encore exprimé par :

(F1) $$-\langle u'v'\rangle = \nu_t \frac{\partial U}{\partial y}$$

où la viscosité tourbillonnaire est déduite des grandeurs k et ε :

(F3) $$\nu_t = C_\mu \frac{k^2}{\varepsilon} \quad ; \quad C_\mu = \frac{C_{\tau 1}}{C_{\tau 2}} = 0{,}09$$

Le problème est alors entièrement défini par ces deux relations jointes aux équations (E1) à (E4).

. Modèle à trois équations de transport :

L'expression (F1) pour le frottement turbulent est abandonnée au profit d'un traitement par une équation supplémentaire pour $\langle u'v'\rangle$. La grandeur ν_t apparaissant dans les termes modélisés de diffusion reste définie par (F3). Le système local à résoudre est constitué des équations (E1) à (E5).

. Modèle à cinq équations de transport :

Les deux schémas précédents utilisent une hypothèse empirique pour l'évaluation des composantes $\langle u'^2\rangle$ et $\langle v'^2\rangle$, hypothèse de proportionnalité à k :

$$\langle u'^2\rangle = k \quad ; \quad \langle v'^2\rangle = 0{,}4\, k$$

Elle est remplacée dans ce modèle complet par un traitement des deux équations de transport supplémentaires pour ces grandeurs turbulentes.

On trouvera dans la référence /3/ une discussion complète des différents schémas utilisés dans les calculs de couches limites turbulentes.

2.1.2. Traitement près de la paroi

Tous ces schémas sont établis pour des valeurs élevées du nombre de Reynolds turbulent : $R_t = k^2/\nu\varepsilon$. Cette hypothèse est mise en défaut près de la paroi où un traitement particulier s'avère donc nécessaire. La solution qui a été retenue consiste à ne débuter le calcul par équations de transport qu'en un point où les effets de la viscosité deviennent négligeables. La région de paroi est traitée par un schéma de longueur de mélange, modifié pour tenir compte des faibles nombres de Reynolds de turbulence :

(F'2) $$\nu_t = F^2 \ell^2 \frac{\partial U}{\partial y}$$

F est une fonction correctrice de sous couche visqueuse : $F = 1 - \exp\left(-\frac{\ell}{26\chi\mu}(\tau\rho)^{1/2}\right)$
τ est le frottement total, visqueux et turbulent.

L'utilisation de cette fonction proposée par Van Driest, a été généralisée sous la forme indiquée par (MICHEL et al. (1969) /4/).

Il s'est avéré nécessaire d'introduire cependant dans certains termes des équations de transport des fonctions correctrices empiriques du nombre de Reynolds de turbulence : fonctions f_2, $f_{\tau 1}$, $f_{\tau 2}$ apparaissant dans (E4) et (E5), fonction f_μ appliquée à ν_t (Réf. /3/,/5/) :

(F'3) $$\nu_t = f_\mu C_\mu \frac{k^2}{\varepsilon}$$

2.1.3. Termes supplémentaires - Constantes ajustables

Les équations proposées diffèrent de celles déduites des hypothèses de couche limite classiques par l'adjonction de termes supplémentaires dont l'influence a été contrôlée dans le cadre d'une confrontation entre ces calculs et l'expérience. Il a déjà été montré en stationnaire /6/,/7/, que ces termes cessent d'être négligeables dans les régions à fort gradient de pression. On a observé ici leur importance y compris dans des configurations à faible gradient moyen. Le rôle prépondérant semble par ailleurs devoir être attribué au terme : $-(\langle u'^2\rangle - \langle v'^2\rangle)\frac{\partial U}{\partial x}$ pris en compte dans l'équation pour l'énergie cinétique de turbulence.

Ces termes sont reportés à la suite des équations locales complètes. Figurent également les valeurs attribuées aux constantes apparaissant dans ces équations. Dans l'étude des schémas à trois et cinq équations de transport et dans le cas d'une configuration expérimentale décrite plus loin, les constantes $C_{\tau 1} - C_{\tau 2} = 0.09. C_{\tau 1}$ – et σ_τ de l'équation pour la tension $\langle u'v'\rangle$ ont été modifiées pour obtenir un meilleur accord avec les données expérimentales. Les valeurs de $C_{\tau 1}$ et $C_{\tau 2}$ sont en effet dérivées de la valeur attribuée à la constante de modélisation du terme linéaire de la corrélation pression vitesse dans l'équation pour le tenseur de Reynolds. Cette valeur est à ajuster pour chaque type d'écoulement turbulent traité, de même que la constante σ_τ du terme de diffusion, grossièrement modélisé.

2.1.4. Méthode numérique

La discrétisation adoptée pour la résolution des équations locales est inspirée des travaux de PATANKAR et SPALDING sur les discrétisations de type volume fini /2/.

Ses qualités essentielles sont un large domaine de validité, la simplicité de mise en oeuvre et la rapidité, découlant du caractère non itératif du calcul. A cette fin et dans le cas de systèmes à plusieurs équations de transport, chaque équation est mise sous la forme générale (E) et résolue séparément.

(E) $$\frac{\partial \Phi}{\partial t} + U\frac{\partial \Phi}{\partial x} + V\frac{\partial \Phi}{\partial y} = S(\Phi,\Phi',\ldots) + \frac{\partial}{\partial y}\left(C(\Phi,\Phi',\ldots)\frac{\partial \Phi}{\partial y}\right)$$

Les différents termes apparaissant dans (E) sont alors évalués selon un schéma implicite, le calcul final de la quantité Φ le long de la normale à la paroi se réduisant cependant à la résolution simple d'un système tridiagonal.

Le calcul s'effectue en mode direct. Les données nécessaires englobent des conditions initiales sur tout le domaine géométrique, des conditions à chaque instant sur la frontière amont de ce domaine ainsi que l'évolution complète de la vitesse extérieure.

Les régions à écoulements de retour instationnaires sont inaccessibles par ce type de calcul. On présente au paragraphe 4 d'autres méthodes susceptibles d'aborder ces problèmes.

2.1.5. Equations locales

EQUATIONS LOCALES

Continuité :

$$\frac{\partial u}{\partial x} + \frac{\partial v}{\partial y} = 0 \qquad (E1)$$

Quantité de mouvement :

$$\frac{Du}{Dt} = -\frac{1}{\rho}\frac{\partial p_e}{\partial x} - \frac{\partial}{\partial x}(\langle u'^2\rangle - \langle v'^2\rangle) + \frac{\partial}{\partial y}\left(\nu\frac{\partial u}{\partial y} - \langle u'v'\rangle\right) \qquad (E2)$$

Transports de :

$$\frac{Dk}{Dt} = -\langle u'v'\rangle\frac{\partial u}{\partial y} - \varepsilon - (\langle u'^2\rangle - \langle v'^2\rangle)\frac{\partial u}{\partial x} + \mathcal{D}\{k\} \qquad (E3)$$

$$\frac{D\varepsilon}{Dt} = -C_{\varepsilon_1}\langle u'v'\rangle\frac{\varepsilon}{k}\frac{\partial u}{\partial y} - f_2 C_{\varepsilon_2}\frac{\varepsilon^2}{k} + \mathcal{D}\{\varepsilon\} \qquad (E4)$$

$$\frac{D\langle u'v'\rangle}{Dt} = -f_{\tau_1}C_{\tau_1}k\frac{\partial u}{\partial y} - (C_{\tau_2} + f_{\tau_2})\frac{\varepsilon}{k}\langle u'v'\rangle + \mathcal{D}\{\langle u'v'\rangle\} \qquad (E5)$$

$$\frac{D\langle u'^2\rangle}{Dt} = A\langle u'v'\rangle\frac{\partial u}{\partial y} + (2\beta k - B\langle v'^2\rangle)\frac{\partial u}{\partial x} + \left(D\frac{\partial u}{\partial x} - C_{\tau_2}\frac{\varepsilon}{k}\right)\langle u'^2\rangle + E\varepsilon + \mathcal{D}\{\langle v'^2\rangle\} \qquad (E6)$$

$$\frac{D\langle v'^2\rangle}{Dt} = A'\langle u'v'\rangle\frac{\partial u}{\partial y} + (B\langle u'^2\rangle - 2\beta k)\frac{\partial u}{\partial x} + \left(-D\frac{\partial u}{\partial x} - C_{\tau_2}\frac{\varepsilon}{k}\right)\langle v'^2\rangle + E\varepsilon + \mathcal{D}\{\langle v'^2\rangle\} \qquad (E7)$$

$$\mathcal{D}\{\Phi\} = \frac{\partial}{\partial y}\left(\left(\nu + \frac{\nu_t}{\sigma_\Phi}\right)\frac{\partial \Phi}{\partial y}\right)$$

Constantes

$\sigma_k = 1.$ $\sigma_\varepsilon = 1.3$ $C_{\varepsilon 1} = 1.57$ $C_{\varepsilon 2} = 2.$

$\sigma_\tau = 0.9$ $\sigma_{\langle u'^2\rangle} = \sigma_{\langle v'^2\rangle} = 1.$ $C_{\tau 1}$ et σ_τ $C_{\tau 1} = 0.135$ $C_{\tau_2} = 1.5$

ajustees dans
chaque configuration

Termes supplémentaires

Quantité de mouvement : $-\frac{\partial}{\partial x}(\langle u'^2\rangle - \langle v'^2\rangle)$

Transport de k : $-(\langle u'^2\rangle - \langle v'^2\rangle)\frac{\partial u}{\partial x}$

Transport de $\langle u'^2\rangle$: $(2\beta k - B\langle v'^2\rangle + D\langle u'^2\rangle)\frac{\partial u}{\partial x}$

Transport de $\langle v'^2\rangle$: $(B\langle u'^2\rangle - D\langle v'^2\rangle - 2\beta k)\frac{\partial u}{\partial x}$

2.2. Méthode intégrale

2.2.1. Principe

La méthode intégrale proposée repose sur la résolution d'un système d'équations globales de la couche limite. Les équations de base sont les équations de quantité de mouvement et de continuité intégrées entre $y = 0$ et $y = \delta$:

$$\frac{C_f}{2} = \frac{\partial\theta}{\partial x} + \theta\frac{H+2}{U_e}\cdot\frac{\partial U_e}{\partial x} + \frac{1}{U_e^2}\cdot\frac{\partial}{\partial t}(U_e\delta_1)$$

$$\frac{\partial\delta}{\partial x} - \frac{V_e}{U_e} = \frac{1}{U_e}\cdot\frac{\partial}{\partial x}\,U_e(\delta - \delta_1)$$

Le calcul de la couche limite, en mode direct, consiste à déterminer l'évolution suivant x et t des grandeurs caractéristiques de la couche limite à partir de conditions initiales et aux limites en supposant connue la distribution $U_e(x,t)$. Cinq inconnues apparaissent donc dans le système précedent : C_f, θ, $\delta_1(H = \delta_1/\theta)$, δ et $C_E = \partial\delta/\partial x - V_e/U_e$ Il est donc nécessaire d'ajouter des hypothèses supplementaires dites de fermeture qui sont des relations entre les caractéristiques de la couche limite. Ces relations de fermeture sont obtenues après établissement et analyse de solutions de similitude (analogues dans leur esprit aux solutions stationnaires de Falkner et Skan du laminaire). On suppose que les vitesses déficitaires obéissent à une loi de similitude de la forme $(U_e - U)/U_\tau = F'(\eta)$ avec $\eta = y/\delta(x,t)$. De cette façon les équations locales de couche limite qui sont des équations aux dérivées partielles en x, y, t se transforment en une équation différentielle ordinaire pour la fonction $F'(\eta)$. Cette équation dite de similitude peut alors être résolue en exprimant le frottement turbulent à l'aide d'un schéma de turbulence : nous avons choisi un modèle de longueur de mélange. La solution de cette équation de similitude est une famille de profils $F'(\eta)$ dépendant d'un paramètre. Ce paramètre, utilisé pour caractériser la forme de chaque profil $F'(\eta)$, est le facteur de Clauser $G = \int_0^1 F'^2 d\eta \,/\, \int_0^1 F' d\eta$. L'analyse des propriétés de cette famille de profils conduit alors au jeu des relations de fermeture nécessaire à la résolution des équations globales de la couche limite. Ces relations sont :

- une loi pour le rapport δ_1/δ :

$$\frac{\delta_1}{\delta} = \gamma F_1(G) \qquad\qquad \gamma = \left(\frac{C_f}{2}\right)^{1/2}$$

- une loi pour le frottement de paroi :

$$\frac{1}{\gamma} = \frac{1}{\chi} \ln R_{\delta_1} + D^*(G) \qquad\qquad \chi = 0{,}41$$

- une loi pour le coefficient d'entrainement :

$$C_E = \gamma P(G) - 1/U_e \; \partial\delta/\partial t$$

où F_1, D^*, P sont des fonctions du paramètre G obtenues d'après l'examen des propriétés des solutions de similitude. Ces fonctions ont été déterminées point par point pour plusieurs valeurs de G et ont été représentées analytiquement par les formules :

$$F_1 = 0{,}613\,G - (3{,}6 + 26{,}86\,(1/G - 0{,}154)^2)\,/\,G$$
$$D^* = 2\,G - 4{,}25\,G^{1/2} + 2{,}12$$
$$P = 0{,}074\,G - 1{,}0957\,/\,G$$

Remarquons que, par rapport au cas stationnaire, la méthode diffère par la présence des termes instationnaires dans l'équation globale de quantité de mouvement et dans l'expression du coefficient d'entrainement.

2.2.2. Extensions

La méthode dont le principe vient d'être exposé pour un écoulement bidimensionnel incompressible a été étendue au cas d'un écoulement faiblement compressible $(M < 1)$ sur paroi athermane. Elle a également été étendue au cas d'un écoulement tridimensionnel en vue notamment d'applications au calcul de la couche limite sur des pales d'hélicoptères.

Signalons aussi qu'une version linéarisée de la méthode a été mise au point pour le calcul d'écoulements périodiques. Elle consiste à développer les équations et les relations de fermeture en séries harmoniques. En supposant que les harmoniques supérieurs sont faibles, on aboutit d'une part à un jeu d'équations pour les composantes moyennes et d'autre part à un jeu d'équations pour les amplitudes et les phases.

Finalement, nous rappelons que les relations de fermeture présentées ici sont valables tant qu'il n'existe pas d'écoulement de retour. Pour ces derniers cas un autre jeu de relation est utilisé (RÉF. 8).

3. APPLICATIONS - COMPARAISONS A L'EXPERIENCE

3.1. Couche limite turbulente en écoulement pulsé avec gradient de pression moyen défavorable (RÉF. 13)

Une couche limite turbulente soumise à un écoulement extérieur pulsé se développe sur le plancher d'une veine d'essais de section rectangulaire. La transition est déclenchée artificiellement dans le collecteur. En aval de la région d'étude, la rotation d'une vanne crée la pulsation de l'écoulement par variation de la perte de charge totale du circuit.

Un corps profilé induit sur le plancher de la veine un gradient moyen longitudinal de pression ajustable. Il s'est avéré nécessaire d'aspirer une partie du débit supérieur pour éviter un phénomène de blocage au bord de fuite du corps central. Une seconde aspiration latérale prévient le décollement des couches limites latérales et recule les effets tridimensionnels : la figure 3 reproduit de manière simplifiée ce dispositif expérimental.

Les mesures de vitesse instantanée ont été effectuées soit par anémométrie à fil chaud, soit par anémométrie laser dans les régions aval où apparaissent périodiquement des écoulements de retour. Une analyse statistique de ces données permet de séparer les composantes moyennes -au sens de moyennes d'ensemble- des parties turbulentes. Des comparaisonsentre les résultats de calculs appliqués à cette configuration expérimentale et ces données très complètes ont pu être réalisées.

Les figures 1 et 2 présentent les évolutions longitudinales, expérimentales et calculées, des valeurs moyennes, des amplitudes et des déphasages par rapport à la vitesse extérieure [illegible] de l'épaisseur de déplacement δ_1 et du paramètre de forme H. Trois des méthodes décrites plus haut ont été exploitées : une version linéarisée de la méthode intégrale, la méthode intégrale ainsi qu'un modèle local à cinq équations de transport. Cette dernière conduit à une prévision très correcte des caractéristiques de l'harmonique de δ_1. L'accord concernant le paramètre de forme, entre l'expérience et un calcul par la méthode intégrale reflète mal en conséquence l'imprécision de celle-ci dans la prédiction du comportement de δ_1 et θ. Mais les tendances de ces trois méthodes jusqu'aux régions à écoulements de retour sont acceptables néanmoins.

La figure 3 présente à une station avec gradient de pression moyen modéré les résultats comparés de la méthode de champ, pour trois schémas de turbulence, concernant l'évolution dans la période des épaisseurs δ_1 et θ. L'apport de modèles à équations de transport complets y apparaît très sensible. A la même station nous présentons figure 4 les courbes d'amplitude et de déphasage par rapport à la vitesse extérieure du premier harmonique de la vitesse au sein de la couche limite, pour ces mêmes calculs. Des caractéristiques fondamentales en écoulement instationnaire telles que l'"overshoot" du profil d'amplitude, le comportement du déphasage de la vitesse près de la paroi, sont correctement prédites par un modèle de fermeture élaboré.

On trouvera enfin sur la figure 5 un exemple des évolutions dans une période du profil de frottement turbulent réduit pour trois modèles de turbulence :

1) - 3 équations de transport,
2) - 3 équations de transport avec termes supplémentaires,
3) - 5 équations de transport.

Les tendances du calcul sont conformes aux déformations observées du profil expérimental.

3.2. Exemple d'application de la méthode intégrale en tridimensionnel

Pour illustrer cette méthode, des calculs ont été effectués dans lesquels la couche limite se développe sur une pale hypothétique d'un hélicoptère se déplaçant à vitesse constante perpendiculairement à l'axe de rotation du rotor.

Deux cas de vitesse extérieure ont été étudiés, en utilisant un résultat proposé par Mc CROSKEY-YAGGY /REF. 14/ :

. Cas I :

$$\frac{u_1}{U_\infty} = \frac{\Omega c}{U_\infty} \cdot \frac{Z}{c} + \sin\psi$$

$$\frac{w_1}{U_\infty} = -\frac{\Omega c}{U_\infty} \cdot \frac{X}{c} + \cos\psi$$

c : corde de la pale

$\psi = \psi_0 + \Omega t$

. Cas II :

$$\frac{u_1}{U_\infty} = \left(\frac{\Omega c}{U_\infty} \cdot \frac{Z}{c} + \sin\psi\right)\left(1 - \frac{X}{3c}\right)$$

$$\frac{w_1}{U_\infty} = \frac{\Omega c}{U_\infty}\left(-\frac{X}{c} - \frac{X^2}{6c^2}\right) + \cos\psi$$

Le profil est mince et placé à faible incidence. Les coordonnées x et X sont confondues.

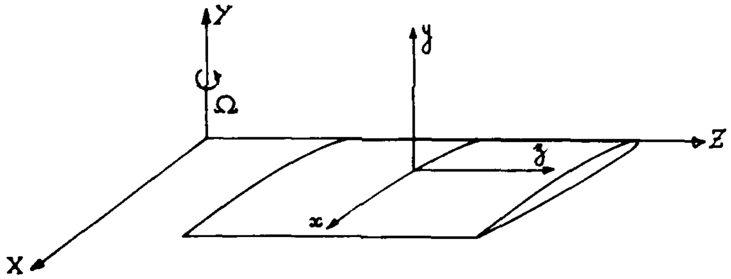

Un calcul quasi-stationnaire est comparé à la méthode intégrale instationnaire pour ces deux cas de répartition de vitesse extérieure et deux sections en Z : une section située près du rotor: $(Z/c = 10)$ et une station située en extrémité de pale : $(Z/c = 23{,}3)$. Les résultats sont présentés pour le point appartenant au bord de fuite.

Sur les figures 8 et 9 sont tracées les évolutions en fonction du temps du paramètre de forme $H = \delta_1/\theta_{11}$. Le niveau moyen de H est plus faible dans le cas I que dans le cas II. Le facteur essentiel dans cette différence de comportement est la valeur du gradient de vitesse extérieure ; les effets instationnaires sont d'autant plus sensibles près de l'axe du rotor, qu'ils sont associés à des gradients importants. La valeur du nombre de Reynolds joue également : dans la configuration II, on note que H est plus élevé dans la zone voisine de $\psi = 270°$, près de l'axe du rotor, lorsque la vitesse devient très faible et donc aussi le nombre de Reynolds.

Les effets tridimensionnels dûs à la couche limite sont abordés par l'intermédiaire de l'angle β_0 entre la vitesse extérieure relative et la ligne de courant relative à la paroi. En bout de pale et dans le cas I, cet angle demeure très voisin de zéro ; ses évolutions n'ont pas été tracées. Elles restent faibles même près du rotor. Il n'en est pas de même dans le cas II, surtout au voisinage de l'axe du rotor (Figures 6 et 7).

On notera que dans la configuration I, les calculs instationnaires et quasi-stationnaires donnent des résultats très voisins. Dans le second cas, le calcul quasi-stationnaire prevoirait un décollement de la couche limite pour ψ voisin de 30° contrairement au calcul instationnaire ; ceci peut s'expliquer par l'effet favorable du gradient $\frac{\partial U_e}{\partial t}$ qui se rajoute au gradient spatial et évite le décollement.

3.3. Plaque plane soumise à un écoulement sinusoïdal

La configuration la plus complètement étudiée est celle d'une couche limite de plaque plane soumise à un écoulement extérieur sinusoïdal. Nous comparons sur les figures 10 et 11 les résultats obtenus à l'aide d'une méthode intégrale et d'une méthode linéarisée aux quelques données expérimentales disponibles. La comparaison porte sur l'évolution en fonction du nombre de Strouhal de l'amplitude et du déphasage par rapport à la vitesse extérieure du premier harmonique de l'épaisseur δ_1. Notons que le nombre de Strouhal n'est pas le paramètre unique de la solution : le nombre de Reynolds et l'amplitude de la fluctuation de vitesse jouent également un rôle. Les calculs ont été réalisés pour une fréquence de 4 Hz, une vitesse moyenne U_0 de 50 m/s et une amplitude de 0,125 U_0.

Il semble que pour des nombres de Strouhal intermédiaires allant de 1 à 5 les divers calculs se comparent de façon satisfaisante à l'expérience. Une dispersion apparaît par contre pour des valeurs supérieures. La difficulté majeure du calcul réside alors dans la modélisation de la turbulence dans la sous-couche visqueuse où se trouvent confinés les effets instationnaires aux grands nombres de Strouhal. A ce problème se rajoute aussi celui de l'interaction entre la pulsation forcée et la turbulence, la fréquence imposée pouvant se trouver dans la gamme des fréquences caractéristiques de la turbulence.

3.4. Plaque plane soumise à une perturbation sinusoïdale (propagation à célérité finie)

Les figures 12 et 13 montrent une comparaison aux expériences de M.H. PATEL /15/. Ces expériences ont été réalisées sur une plaque plane semi-infinie avec transition déclenchée à 0,275 m du bord d'attaque. Les données expérimentales résultent de mesures par anémométrie à fil chaud ainsi que de mesures par prises de pression statique placées à la paroi.

La pulsation de vitesse extérieure se propage dans ces expériences avec une célérité finie ; l'amplitude de fluctuation croît de plus suivant x. La vitesse extérieure se met sous la forme :

$$u_e = u_{es} + u_{e1}(x) \cdot \sin\left(\omega\left(t - x/Q\right)\right)$$

Patel donne :

$$u_{es} = 19{,}8 \text{ m/s}$$
$$Q = 0{,}77 \cdot u_{es}$$
$$u_{e1} = 0{,}762 \cdot \left(x - 0{,}275\right)$$

Des fréquences allant de 4 à 12 Hz ont été utilisées. La plage de mesures explorée en x conduit à des résultats qui couvrent une gamme de nombres de Strouhal de 1,65 à 6,65.

Différents calculs ont été réalisés au moyen d'une méthode intégrale, ou à l'aide de sa version linéarisée. Jusqu'au nombre de Strouhal le plus élevé (6,65), un bon accord avec l'expérience est obtenu, sauf en ce qui concerne les déphasages des épaisseurs δ_1 et θ par rapport à la vitesse extérieure. Ces écarts peuvent en partie s'expliquer par la difficulté de déterminer de tels déphasages avec précision par l'expérience. Une dispersion est à noter cependant dans les résultats théoriques aux grandes valeurs du nombre de Strouhal.

Il faut enfin remarquer qu'il se pose dans cette configuration les problèmes d'origine de la couche limite turbulente pour définir le nombre de Strouhal et de conditions initiales pour commencer le calcul aux faibles fréquences réduites.

4. SINGULARITES EN MODE DIRECT - METHODE INVERSE

4.1. Rappel des résultats en écoulement stationnaire

En écoulement bidimensionnel stationnaire, il a été montré que le système des équations globales devient singulier au voisinage du point d'annulation du coefficient de frottement pariétal. Cette singularité, *analogue à celle de Goldstein* pour les équations locales, se traduit en particulier par le fait que la dérivée $d\delta_1/dx$ devient infinie. Cette singularité peut être illustrée à l'aide de l'équation modèle suivante :

$$a(y)\frac{dy}{dx} = \frac{df}{dx} - b(f,y) \qquad \text{(F8)}$$

où y est l'inconnue ; $f(x)$, $b(f,y)$ et $a(y)$ sont des fonctions connues et $a(y)$ a la particularité de s'annuler en un point $y = y_0$. En général, la solution de cette équation est singulière au point $y = y_0$ pour lequel la dérivée dy/dx est infinie. Pour éviter cette singularité une condition nécessaire est d'avoir $df/dx = b(f,y)$ qui n'est pas réalisée en général car $f(x)$ est imposé.

Pour échapper à cette difficulté certains auteurs ont imaginé des méthodes dites inverses /9/. Elles consistent à imposer l'évolution d'une grandeur autre que la pression, par exemple l'épaisseur de déplacement, et la pression devient alors une inconnue. Ce changement d'inconnues est illustré sur l'équation modèle (F8) en permutant le rôle de y et f. En considérant f comme inconnue, il est clair que la solution sera exempte de toute singularité pour toute distribution régulière $y(x)$ imposée.

Naturellement, ce mode inverse ne constitue pas un calcul de couche limite au sens où on l'entend habituellement. Il est cependant indispensable si on désire étudier les écoulements au voisinage du point $C_f = 0$. De plus la validité des équations de couche limite n'est pas remise en cause par la singularité du mode direct qui est en fait un problème inhérent à ce mode. Sur cette base des méthodes de couplage fondées sur des équations de fluide parfait et des équations de type couche limite, résolues en forte interaction ont pu être développées même en présence de zones avec écoulements de retour /10/. Les méthodes inverses trouvent aussi leur application dans les méthodes de "design" : on impose une caractéristique de la couche limite et on déduit la distribution de pression qui permet de calculer la forme de la paroi à l'aide d'un calcul inverse de fluide parfait. Le mode inverse est encore indispensable si on cherche à contrôler par comparaison à l'expérience la validité de relations de fermeture pour une couche limite avec écoulement de retour.

4.2. Ecoulement instationnaire

L'analyse des propriétés des équations globales instationnaires apporte un éclairage nouveau au problème de la formation de singularités dans les calculs de couche limite en mode direct. On a montré /11/, /12/ que le système des équations instationnaires possède deux directions caractéristiques qui, avec une hypothèse simplificatrice assez mineure, s'expriment par :

$$\lambda_1 = \left(1 + 0,623(H-1)\right)/H$$
$$\lambda_2 = \left(1 - 0,623(H-1)\right)/H$$

où λ est la direction caractéristique réduite $\lambda = dx/u_e dt$

Pour le domaine $H > 1$, on tire donc les conclusions suivantes :

- . Puisqu'il existe toujours deux directions caractéristiques réelles distinctes, le système est hyperbolique.
- . La première valeur caractéristique est toujours positive. Elle reste même assez voisine de 1 : elle est comprise entre 0,62 et 1.
- . La deuxième valeur caractéristique est positive pour $H < H_c$; elle est négative pour $H > H_c$ ($H_c \simeq 2.6$).

Or, en stationnaire, l'analyse des équations montre que la valeur critique $H = H_c$ définit la singularité. A un très léger ajustement près des relations de fermeture, ce point correspond d'ailleurs à l'annulation du coefficient de frottement (en stationnaire comme en instationnaire).

Contrairement au cas stationnaire, il apparaît donc que le point $H = H_c$ n'est généralement pas singulier en instationnaire. Le changement de signe de la deuxième valeur caractéristique à la traversée de ce point se signale seulement par une influence de l'aval sur l'amont quand H devient supérieur à H_c (Fig. 14). Cette influence est tout à fait claire car elle est liée à la présence d'écoulements de retour.

En instationnaire, la présence éventuelle d'une singularité de la solution n'est donc pas liée au point $H = H_c$. Le système possède des solutions faibles avec discontinuité qu'on peut étudier analytiquement après avoir remarqué que les équations se mettent sous forme quasi-conservative, condition nécessaire d'existence de solutions faibles. Cette forme est :

$$\frac{\partial}{\partial x}\left[u_e(\delta-\delta_1)\right] + \frac{\partial \delta}{\partial t} = \gamma\, P(G)\, u_e$$
$$\frac{\partial}{\partial x}\left[u_e^2\theta\right] + \frac{\partial}{\partial t}\left[u_e\delta_1\right] = u_e^2\frac{C_f}{2} - \delta_1 u_e\frac{\partial u_e}{\partial x}$$

Plus précisement ce sont les lignes caractéristiques définies par λ_2 qui peuvent donner naissance à des lignes de discontinuite après avoir focalisé.

A l'aide d'exemples numériques, en résolvant les équations globales soit par une méthode aux différences finies, soit par une méthode de caractéristiques, nous avons pu mettre en évidence des cas où les lignes caractéristiques λ_2 focalisent pour former une ligne à la traversée de laquelle l'épaisseur de déplacement est discontinue. Un tel exemple est donné sur la figure 15 . Pour $t = 0$ des conditions de couche limite de plaque plane sont imposées et ensuite la vitesse évolue linéairement en x et t, comme indiqué schématiquement sur la figure 15 . Les points où la tangente à la ligne caractéristique λ_2 est parallele à l'axe des temps correspondent à $H = H_c$: on ne note aucun signe de singularité.

En revanche, on constate pour $t > 0,03$ une focalisation des lignes λ_2 et la formation d'une ligne de discontinuité. Remarquons aussi la forme en éventail du tracé au voisinage du point $x/C = 1$, qui correspond au point où la vitesse devient croissante en fonction de x .

Evidemment, il ne faut pas chercher de signification physique à la formation d'une ligne de discontinuité pas plus qu'il ne fallait en chercher aux solutions singulières en stationnaire. En aucun cas, il ne faut considérer qu'il s'agit d'un critère de décollement. Il s'agit seulement d'un problème inhérent au mode direct et imputable à l'approche classique de couche limite associée à une théorie où le couplage avec l'écoulement extérieur est un couplage faible. Nous pensons qu'on doit alors recourir à la théorie du couplage fort, sans pour cela renoncer à l'utilisation des équations de couche limite.

Nous avons pu nous assurer de cette hypothèse sur un modèle de couplage schématique dans lequel l'écoulement de fluide parfait était supposé réduit à un écoulement monodimensionnel /12/ . Cependant, le problème complet du couplage instationnaire en régime de forte interaction visqueuse n'est pas encore résolu. On peut quand même penser que, de la même façon qu'en stationnaire, les méthodes inverses seront d'un précieux secours.

Nous avons d'ailleurs montré que l'élimination des singularités évoquées plus haut peut être obtenue en procédant suivant le mode de résolution inverse. Parmi la variété de méthodes inverses qu'on peut imaginer suivant le choix des données, deux solutions ont été étudiées. Dans les deux cas, la grandeur dont l'évolution est imposée est la direction de l'écoulement du fluide parfait le long d'une frontière située à l'altitude y . Soit α_y cette direction. On montre /10/ que si cette frontière est confondue avec l'épaisseur de déplacement $(y = \delta_1)$, on a une condition de tangence le long de cette frontière c'est-à-dire que la direction $\alpha(y=\delta_1)$ est donnée par :

$$\alpha(y=\delta_1) = \frac{\partial \delta_1}{\partial x} \tag{E9}$$

Si la frontière est confondue avec la paroi $(y=0)$, on montre /10/ qu'on obtient une condition de soufflage telle que :

$$\alpha(y=0) = \frac{\partial \delta_1}{\partial x} + \frac{\delta_1}{u_e} \frac{\partial u_e}{\partial x} \tag{E10}$$

Les deux méthodes inverses analysées consistent donc à supposer soit que $\alpha(y=\delta_1)$ est connue en fonction de x et t , soit que $\alpha(y=0)$ est connue en fonction de x et t .

Ainsi, on ajoute une équation (équation (E9) ou équation (E10)) au système des équations de couche limite mais on considère que $u_e(x)$ est une inconnue.

Dans chacun des cas, l'analyse des propriétés du système d'équations montre qu'il s'agit d'un problème totalement hyperbolique et que les directions caractéristiques sont toujours positives. On en conclut donc que pour la couche limite résolue isolément en mode inverse, des conditions aux limites sont seulement nécessaires à l'amont et l'intégration peut être effectuée d'amont en aval. D'autre part, on a montré que suivant la deuxième méthode (α_y 0) imposé) l'existence des lignes de discontinuité est à exclure. Suivant la première méthode, le calcul montre que les pentes des directions caractéristiques varient peu suivant les valeurs du facteur de forme H ce qui devrait limiter le risque de lignes de discontinuité.

4.3. - Application d'une méthode inverse - Comparaison à l'expérience

L'un des premiers objectifs d'application de ces méthodes inverses a été notamment de contrôler les relations de fermeture en instationnaire avec écoulement de retour en s'appuyant sur des comparaisons à l'expérience.

Les résultats expérimentaux /13/, déjà évoqués au paragraphe 3.1., sont constitués de sondages détaillés de la couche limite à différentes stations et ont comporté notamment la détermination des moyennes de phase de la vitesse. Ainsi, on connaît de façon précise l'évolution de la couche limite en fonction du temps et en particulier, la distribution $\delta_1(x,t)$.

Pour atteindre le but recherché, il apparaît donc un peu plus simple de mettre en oeuvre la première méthode inverse (celle où on impose $\alpha(y=\delta_1)=\partial\delta_1/\partial x$) qui revient en fait à prescrire l'évolution de l'épaisseur de déplacement $\delta_1(x,t)$. Les calculs ont été effectués en considérant la distribution mesurée de $\delta_1(x,t)$ comme une donnée du problème. Cette distribution a été représentée par un développement harmonique des valeurs mesurées ; seul le fondamental a été retenu. Ces données, représentées sur la figure 16 ont été introduites point par point.

Sur les figures 17 et 18 , on compare les résultats du calcul et de l'expérience concernant les distributions du facteur de forme et de la vitesse représentées à l'aide d'une analyse harmonique. Un bon accord général est obtenu, y compris dans la région située en aval de x = 435 mm où apparaissent périodiquement des courants de retour. Bien que l'une des caractéristiques de la couche limite soit introduite comme donnée, la comparaison de l'évolution du facteur de forme n'est pas triviale car les relations de fermeture utilisées laissent arbitraires les valeurs de deux caractéristiques de la couche limite.

Précisons encore que les résultats des calculs effectués suivant le mode direct (avec la méthode complète ou linéarisée) montrent un bon accord jusqu'à la station x = 435 mm. Mais insistons sur le fait qu'une tentative de calcul en mode direct au-delà du point x = 435 mm, sans tenir compte de condition aval. avait échoué très rapidement par suite d'apparition de fortes instabilités numériques.

CONCLUSIONS

On dispose d'un ensemble de méthodes de calcul permettant, soit une description globale de l'écoulement par résolution des équations intégrales, soit une description fine du champ de vitesses et même de certaines grandeurs caractéristiques de la turbulence par résolution d'un jeu d'équations de transport.

A l'aide de comparaisons détaillées à l'expérience, il a été montré que pour atteindre une amélioration sensible par rapport aux méthodes les plus simples, il faut faire appel à un système d'équations de transport dont le niveau de complexité est élevé. Si on se limite aux modèles plus simples, la prévision des épaisseurs de couche limite, sans être mauvaise, n'est pas améliorée par rapport à ce qu'on obtient par la méthode intégrale. De ce point de vue, la méthode intégrale donne des résultats tout à fait acceptables compte tenu en plus du gain de temps de calcul. De plus, avec les modèles d'équations de transport les plus simples, la description des profils de vitesses présente des défauts, notamment sur le dépassement que présentent les profils d'amplitude.

Pour les grandes valeurs du nombre de Strouhal, (supérieures à 5) les quelques résultats expérimentaux existants semblent montrer que les modèles à préciser avec équations de transport indiquent des tendances correctes si on en juge d'après la phase de l'épaisseur de déplacement. Cependant, les expériences ne sont pas suffisamment systématiques pour apporter des conclusions définitives. Une remarque analogue peut êt aite pour les nombres de Strouhal faibles (inférieurs à 1) pour lesquels on manque aussi de données périmentales.

Sign encore qu'il serait très instructif de disposer d'informations expérimentales sur l'évolution du co ent de frottement pariétal. Les seules indications dont on dispose actuellement peuvent être obtenue par la mesure des profils de vitesse et l'hypothèse que la loi de paroi établie en stationnaire reste able en instationnaire.

Grâce à l'analyse des propriétés des équations globales de la couche limite, nous avons pu mettre en évidence les conditions dans lesquelles des singularités peuvent apparaître dans les calculs de couche limite en mode direct. On a pu ainsi apporter un éclairage nouveau à cette question en montrant que le problème bidimensionnel n'était qu'un cas très particulier d'un problème plus général. Bien que l'analyse ne soit pas identifiable à celle des équations locales de la couche limite, on peut raisonnablement penser que des difficultés analogues peuvent exister quand on résout ces équations. En fait, l'existence de deux directions caractéristiques dans le système des équations globales est le reflet, après intégration, de l'existence d'une infinité de directions caractéristiques (qui sont les lignes d'émission) dans le système des équations locales.

La mise en oeuvre du mode inverse de résolution des équations de couche limite permet d'échapper aux singularités du mode direct. On montre donc que ces singularités ne remettent pas en cause l'utilisation des équations de couche limite.

Enfin, on a pu contrôler par comparaison à l'expérience que des zones avec écoulement de retour au moins de faible étendue peuvent être correctement calculées à l'aide de la méthode intégrale.

REFERENCES

/ 1 / LAUNDER B.E.

Progress in the modelling of turbulent transport.

. VKI Lecture Series 76, March 3-7, 1975.

/ 2 / PATANKAR S.V., SPALDING D.B.

Heat and Mass Transfer in Boundary Layers, 2nd Edition, Intertext Books, London 1970.

/ 3 / COUSTEIX J.

Progrès dans les méthodes de calcul des couches limites turbulentes bi- et tridimensionnelles.

. Note Technique ONERA, 1976-15.

/ 4 / MICHEL R., QUEMARD C., DURANT R.

Application d'un schéma de longueur de mélange à l'étude des couches limites turbulentes d'équilibre.

. Note Technique ONERA, 1969-154.

/ 5 / DESOPPER A.

Etude expérimentale des couches limites turbulentes et transitionnelles en écoulement pulsé, essais de prévision théorique.

. Thèse de Docteur Ingénieur - ONERA CERT, 1977.

/ 6 / SIMPSON R.L., COLLINS M.A.

Prediction of turbulent boundary layers in the vicinity of separation.

. Synoptic in AIAA Journal, April 1978.

/ 7 / SIMPSON R.L., STRICKLAND J.H., BARR P.W.

Features of a separating turbulent boundary layer in the vicinity of separation.

. Journal of Fluid Mechanics - 1977, Vol. 79, Part 3.

/ 8 / COUSTEIX J., LE BALLEUR J.C., HOUDEVILLE R.

Calcul des couches limites turbulentes instationnaires en mode direct ou inverse, écoulements de retour inclus. Analyse des singularités.

. La Recherche Aérospatiale n° 1980-3.

/ 9 / CARTER J.E

Inverse solutions for laminar boundary layer flows with separation and reattachment.

. NASA TR-R-447, 1975.

/ 10 / LE BALLEUR J.C.

Calculs couplés visqueux-non visqueux incluant décollements et ondes de choc en écoulement bidimensionnel.

. VKI/AGARD, LS-94 on three-dimensional and unsteady separation at high Reynolds numbers (Feb. 1978).
T.P. ONERA, n° 1978-5.

/ 11 / COUSTEIX J., HOUDEVILLE R., DESOPPER A.

Résultats expérimentaux et méthodes de calcul relatifs aux couches limites turbulentes en écoulement instationnaire.

. AGARD-CP-227, 1977.

/ 12 / COUSTEIX J., HOUDEVILLE R.

Turbulent boundary layer calculations in unsteady flow. Numerical methods in Applied Fluid Dynamics. University of Reading, 4-6 Jan. 1978.

. T.P. ONERA, n° 1978-2.

/ 13 / HOUDEVILLE R., COUSTEIX J.

Couches limites turbulentes en écoulement pulsé avec gradient de pression moyen défavorable.

. La Recherche Aérospatiale, n° 1979-1.

/ 14 / Mc CROSKEY-YAGGY

Laminar Boundary Layers on helicopter rotors in forward flight.

. AIAA Journal, Vol. 6, n° 10, Oct. 1968.

/ 15 / PATEL M.H.

Two simplified integral approaches to the oscillating turbulent boundary layer.

. Communication présentée à la Réunion d'un Groupe de Travail EUROVISC, Orléans, Février 1978.

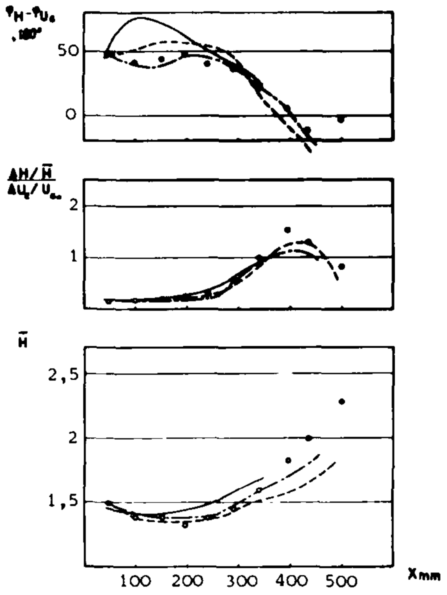

$$u_e = u_{e_0} + \Delta u_e . \sin(\omega t + \varphi_{u_e}) + \ldots$$

$$H = \bar{H} + \Delta H . \sin(\omega t + \varphi_H) + \ldots$$

—— Equations de transport
— —Méthode intégrale
----Equations linéarisées

Fig.1 - Couche limite turbulente bidimensionnelle avec gradient de pression moyen positif - analyse harmonique du facteur de forme - calculs - expérience.

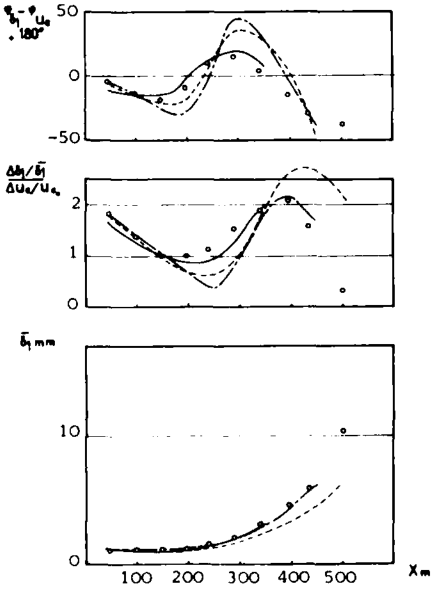

$$u_e = u_{e_0} + \Delta u_e . \sin(\omega t + \varphi_{u_e}) + \ldots$$

$$\delta_1 = \bar{\delta}_1 + \Delta\delta_1 . \sin(\omega t + \varphi_{\delta_1}) + \ldots$$

—— Equations de transport
— —Méthode intégrale
----Equations linéarisées

Fig. 2 - Analyse harmonique de l'épaisseur de déplacement - calculs - expérience.

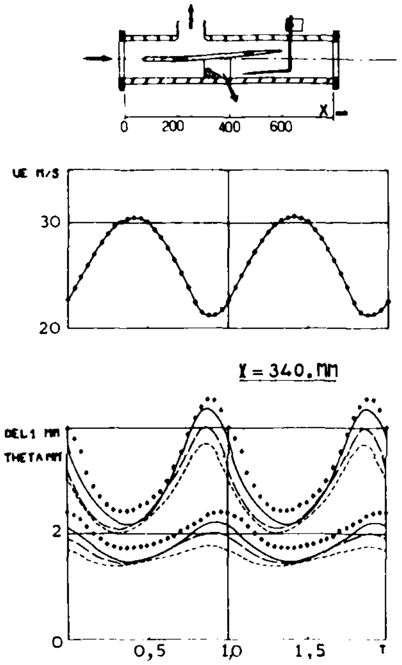

———— 5 EQUATIONS
– – – – 2 EQUATIONS
------ LONG. MEL.

Fig.3 - Evolution des épaisseurs de déplacement et de quantité de mouvement au cours d'une période expérience - calculs par une méthode de champ avec différents schémas de turbulence.

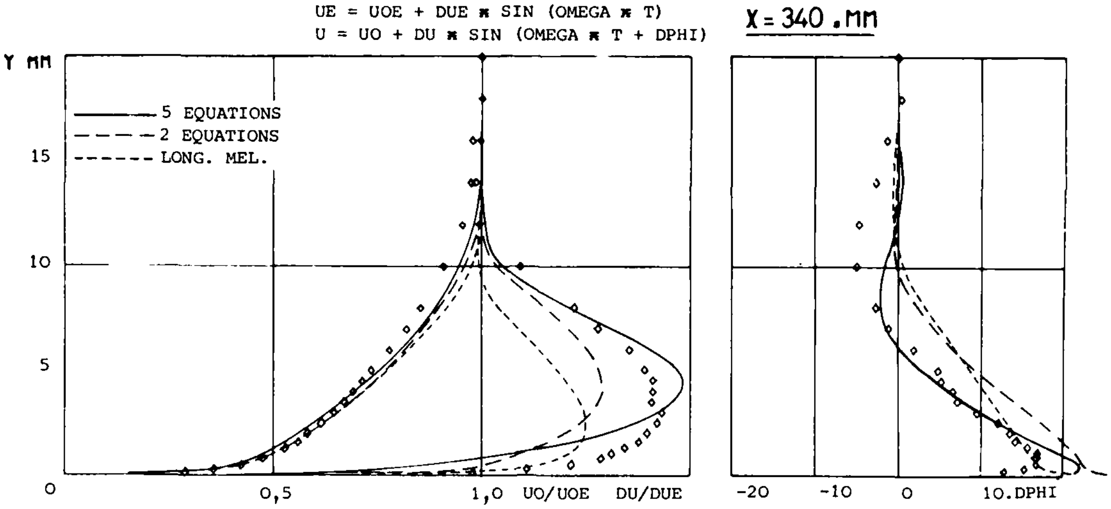

Fig. 4 - Analyse harmonique de la vitesse dans la couche limite - expérience - calculs avec différents schémas de turbulence.

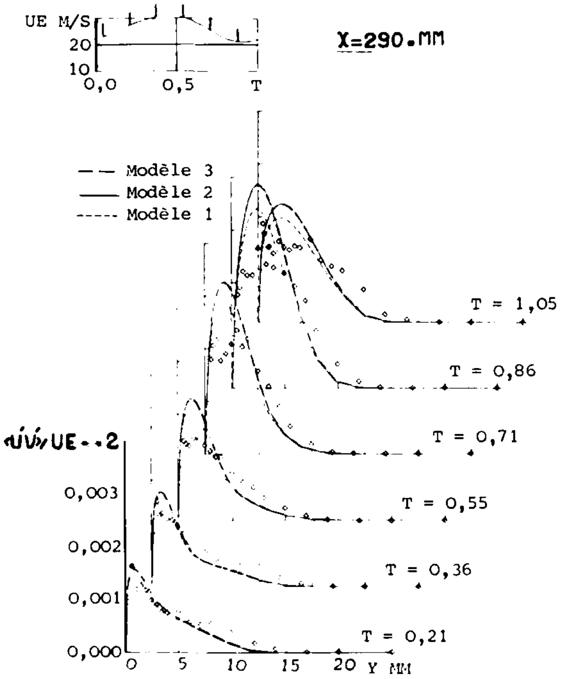

Fig. 5 - Evolution des profils de frottement turbulent au cours d'une période - expérience - calculs avec différents schémas de turbulence.

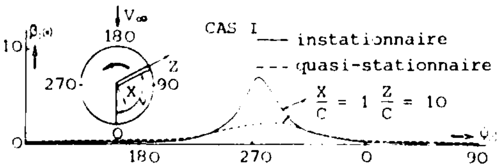

Fig. 6 : Couche limite turbulente tridimensionnelle instationnaire. Angle limite β_o .

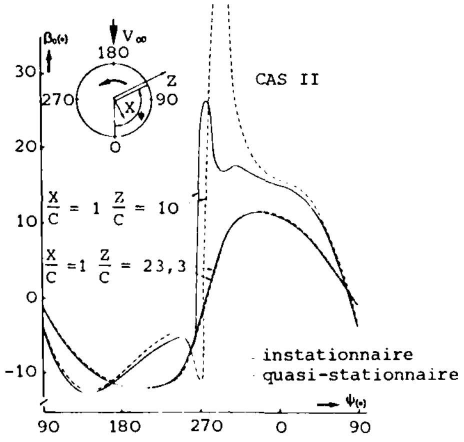

Fig. 7 - Couche limite turbulente tridimensionnelle instationnaire. Angle limite β_o .

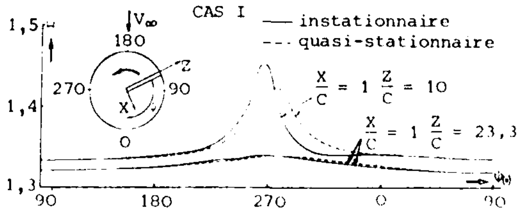

Fig. 8 - Couche limite turbulente tridimensionnelle instationnaire. Facteur de forme.

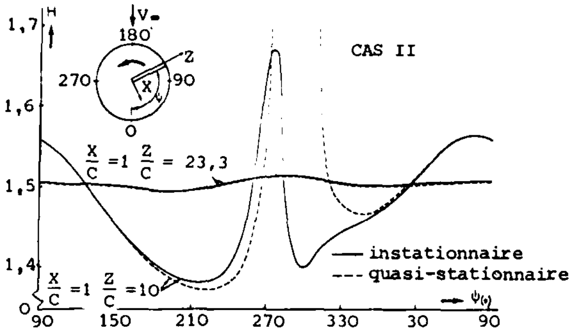

Fig. 9 - Couche limite turbulente tridimensionnelle instationnaire. Facteur de forme.

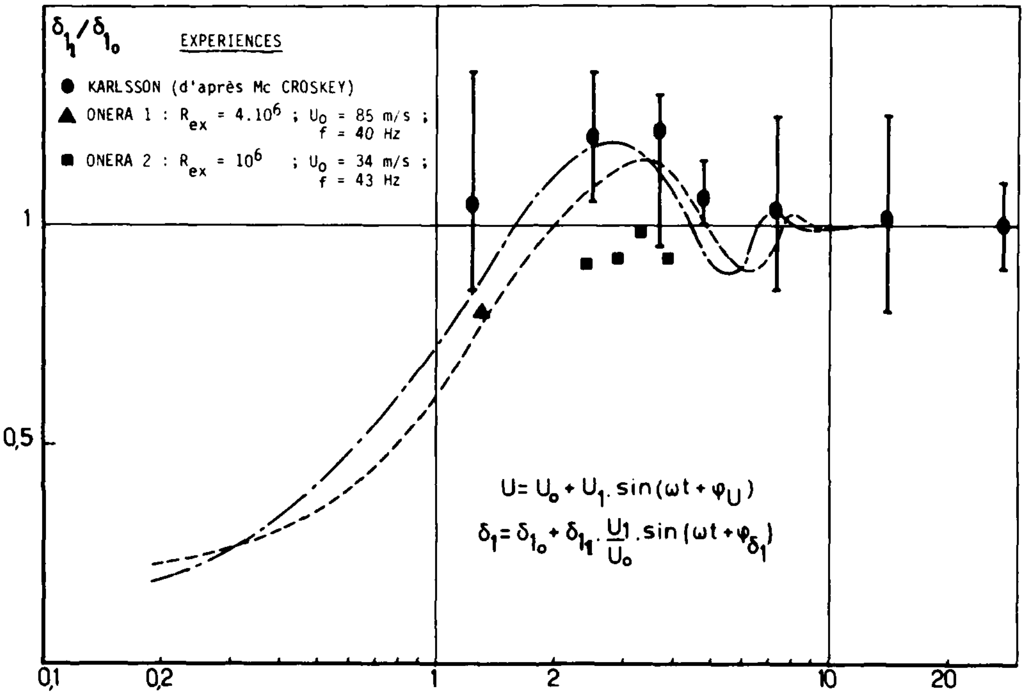

FIG. 10 : Couche limite turbulente bidimensionnelle en écoulement oscillatoire - Amplitude réduite de l'épaisseur de déplacement - Calculs - Expériences.

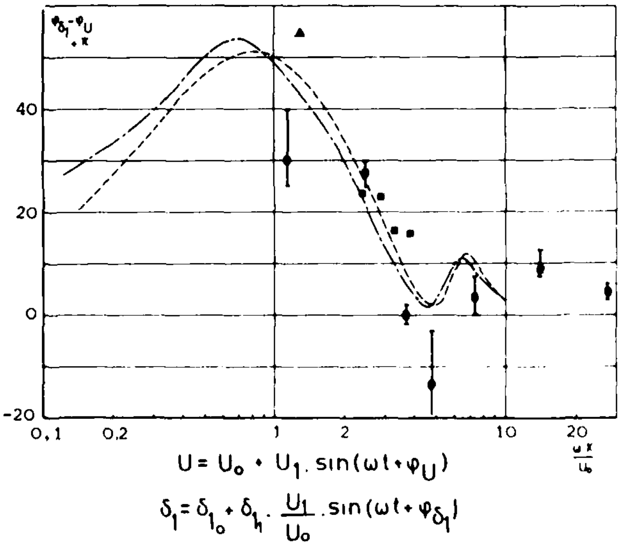

Fig. 11 - Couche limite turbulente bidimensionnelle en écoulement oscillatoire - phase de l'épaisseur de déplacement - calculs - expériences.

Expériences

● Karlsson (d'après Mc Croskey)

▲ ONERA 1 : $R_{ex} = 4.10^6$; U_o = 85 m/s ; f = 40 Hz

■ ONERA 2 : $R_{ex} = 10^6$; U_o = 34 m/s f = 43 Hz

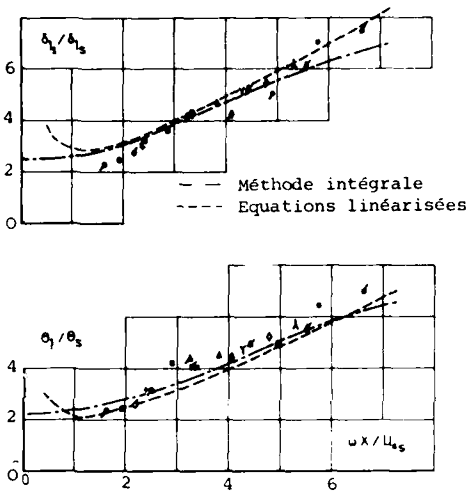

$$U_e = U_{e_s} + U_{e_1}\,.\sin(\omega[t - X/Q])$$

$$\delta_1 = \delta_{1s} + \delta_{11}\frac{U_{e1}}{U_{e_s}}\,.\sin(\omega[t - X/Q] + \pi + \varphi_{\delta_1})$$

$$\theta = \theta_s + \theta_1\frac{U_e}{U_{e_s}}\,.\sin(\omega[t - X/Q] + \pi + \varphi_\theta)$$

Fig. 12 - Expériences de M.H. Patel - Amplitudes réduites des épaisseurs de déplacement et de quantité de mouvement - calculs - expériences.

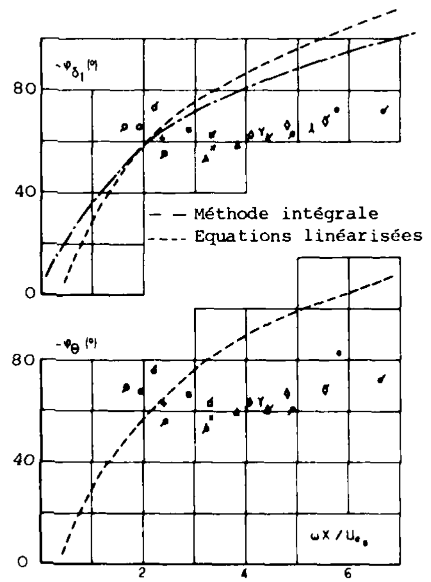

$$U_e = U_{e_s} + U_{e_1}\,.\sin(\omega[t - X/Q])$$

$$\delta_1 = \delta_{1s} + \delta_{11}\frac{U_{e1}}{U_{e_s}}\,.\sin(\omega[t - X/Q] + \pi + \varphi_{\delta_1})$$

$$\theta = \theta_s + \theta_1\frac{U_e}{U_{e_s}}\,.\sin(\omega[t - X/Q] + \pi + \varphi_\theta)$$

Fig. 13 - Expériences de M.H. Patel - Phases des épaisseurs de déplacement et de quantité de mouvement - calculs - expériences.

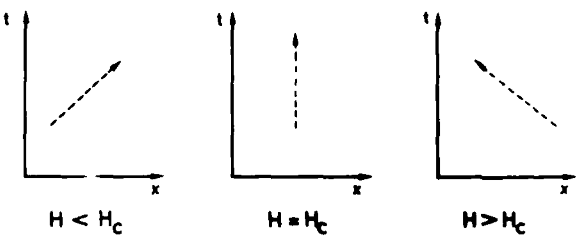

Fig. 14 - Variation de la pente de la caractéristique λ_2 en fonction du facteur de forme H.

$\frac{C}{U_o\, t_s} \times \frac{C}{x_o} = 0{,}175 \qquad \frac{U_o C}{\nu} = 10^7 \qquad C = 1\,m$

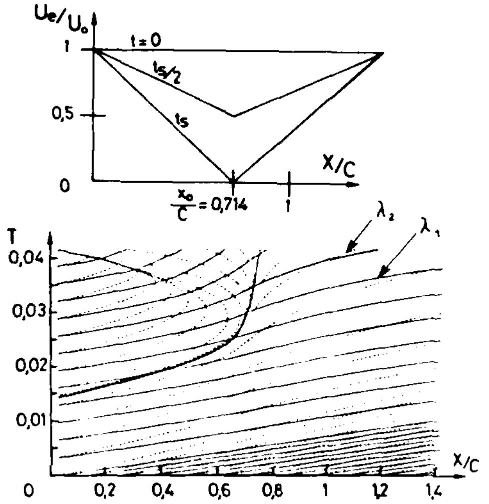

Fig. 15 - Exemple de calcul en mode direct avec singularité - couche limite bidimensionnelle instationnaire - trace des lignes caractéristiques.

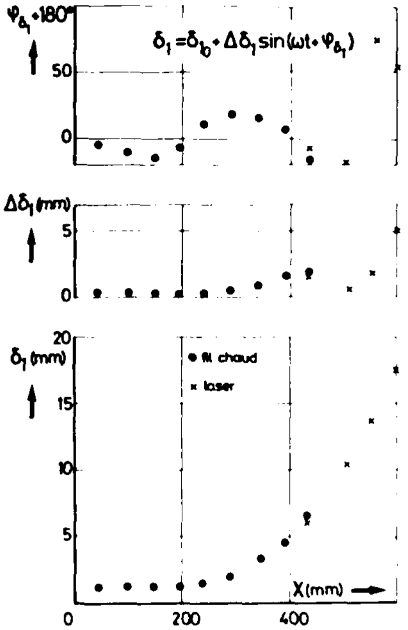

Fig. 16 - Application de la méthode intégrale en mode inverse - données du calcul : évolution de δ_1.

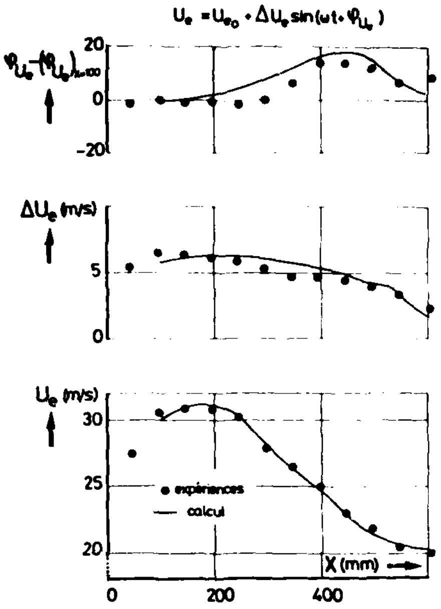

Fig. 17 - Application de la méthode intégrale en mode inverse - comparaison à l'expérience : vitesse extérieure.

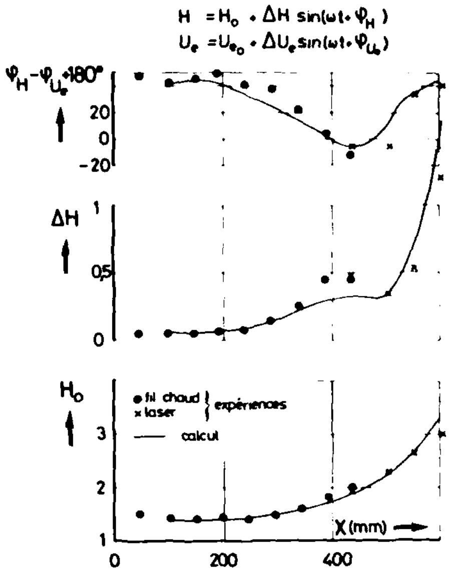

Fig.18 - Application de la méthode intégrale en mode inverse - comparaison à l'expérience : facteur de forme.

VISCOUS EFFECTS ON UNSTEADY AIRLOADS OF OSCILLATING CONFIGURATIONS

by
W. Geissler
DFVLR - AVA Göttingen
Institut für Aeroelastik
Bunsenstr. 10, 3400 Göttingen, Germany

Summary

Viscous effects on small amplitude oscillating wings and bodies can be considerably influential on unsteady airloads needed for aeroelastic investigations.

The steady and unsteady Kutta-Joukowsky condition, boundary layer displacement effects, gap flows on wings with oscillating controls and vortex formations on rotor blade tips, on wings with highly swept leading edges and on bodies at *incidence* severely influence the unsteady pressure distributions and overall forces.

Numerical calculations of unsteady airloads based on a sophisticated potential theory have been compared with carefully measured experimental data to obtain detailed information of the viscous effects involved.

Contents

	Page
List of symbols	1
1. *Introduction*	2
2. Potential theoretical method and the Kutta-Joukowsky condition	2
3. Boundary layer displacement effects	2
4. Vortex flows	2
4.1 Tip vortex	3
4.2 Swept-wing vortex interaction	3
4.3 Body-vortex interaction	4
5. Rearward body separation	4
6. Conclusion	5
7. References	5

List of symbols

x, y, z	cartesian coordinates
x, r, φ	cylindrical coordinates
L, ℓ	reference length
ℓ_{ϑ}	local chord
U_{∞}	main flow velocity
a_{∞}	velocity of sound
Ma_{∞}	Mach number, $Ma_{\infty} = U_{\infty} / a_{\infty}$
p	static pressure
ρ	density
q_{∞}	dynamic pressure of undisturbed flow, $q_{\infty} = 1/2 \, \rho \, U_{\infty}^2$
c_p	steady pressure coefficient, $c_p = (p - p_{\infty}) / q_{\infty}$
$\bar{c}_p$	complex unsteady pressure coefficient, $c_p = c_p' + i c_p'' = p / (q_{\infty} \alpha')$
α	angle of incidence
δ	angle of flap deflection
α'	amplitude of oscillation
t	time
f	frequency
ω^*	reduced frequency, $\omega^* = \omega \cdot \ell / U_{\infty}$

1. Introduction

Recent developments of prediction methods for unsteady airloads on three-dimensional oscillating wings [1] and bodies [2] take into account the exact boundary condition of the real surface of the configuration as well as the exact Bernoulli Equation within a body-fixed, oscillating frame of reference. In addition to a lifting surface theory several additional parameters such as thickness and camber of the airfoil section, mean steady incidence, mean flap deflection and gap geometry can now be considered. Comparisons with detailed experimental results enables a decision to be made about the quality and quantity of the viscous effects involved. A further step is the intoduction of a special flow model representing for instance boundary layer displacement thickness, separation of the free vortex layer type or even rear body separation.

In the following paper a discussion of different viscous flow phenomena is presented by drawing comparisons between theory and experiment. The problems are closely related to aeroelastic instability investigations and are therefore limited to small amplitude oscillations. Problems related to high amplitude oscillations of helicopter rotor blades, i.e. dynamic stall, are not examined here. The investigations are further limited to subsonic flows, although some of the viscous phenomena observed in subsonic flow have similar or even identical effects in transonic flow.

2. Potential theoretical method and the Kutta-Joukowsky condition

For the numerical solution of the potential theoretical problem a panel-type method is used, dividing the real surfaces of the 3-d wing or body into a corresponding large number of surface elements. The unknown singularity strengths are then obtained as the solution vectors of a large linear system of algebraic equations. In the wing case, a combination of sources and doublets is used. A source distribution alone would not give satisfactory results: the overall lift of the wing would then be zero with a flow around the trailing edge of the wing. It is well known from flow observations that in a real viscous flow the fluid particles leave the trailing edge smoothly and a singular behavior of the pressure at this station is therefore avoided. To model this viscous situation of smooth flow off the trailing edge, the Kutta-Joukowsky condition has to be taken into consideration. This condition is therefore a phenomenological one which accounts for the main effect of viscosity in a non-separated flow.

Different possibilites exist to fulfill the Kutta-Joukowsky condition numerically: in the present calculation scheme the pressures at the two control points adjacent to the trailing edge are made equal. This condition has to be fulfilled simultaneously for all "Kutta points". Fig.1 shows a landing configuration with a well-defined gap between wing and control. In this case, Kutta points exist not only on the oscillating control-trailing edge with a corresponding control-wake, but also on the wing trailing edge with a corresponding wing-wake. Difficulties occur in the numerical treatment of the Kutta-Joukowsky condition at the trailing edge of the wing due to the strong interference effects in this region. Experimental investigations [3] of this configuration with oscillating control and with open and closed gap have shown the severe influence of the gap flow on the steady and unsteady pressure distributions and overall lift for this configuration. These problems are significant for the treatment of active control problems.

3. Boundary layer displacement effects

If the flow is still attached, it is relatively simple to heed a higher order effect of viscosity due to the displacement effect of the boundary layer. This effect can be represented in different ways:

1) by adding the displacement thickness, i.e. by thickening the profile,
2) by modifying the boundary condition allowing non-zero normal velocities prescribed by the boundary layer displacement.

In the present method the first alternative is chosen. Fig.2 shows the effects of profile thickness and boundary layer displacement in a section of a swept, tapered wing with a NACA 0010 symmetrical airfoil. Included are pressure distributions obtained by lifting surface theory (dashed lines) and experimental results [4]. The results for the real parts show that the introduction of profile thickness and boundary layer displacement reveals good agreement with the experimental results whereas the representation of thickness alone over-predicts the pressure distributions of the real parts. Similar results have been presented in [5] for subsonic and transonic flows. Only small influences of boundary layer displacement can be found in the imaginary parts of the pressure distributions.

The calculation procedure for taking into account boundary layer displacement thickness is performed in three different steps:

1) calculation of the steady pressure distribution on the wing surface,
2) calculation of the boundary layer for each wing section with the steady pressures of step 1) by means of a two-dimensional boundary layer code [6],
3) addition of the boundary layer displacement thickness and calculation of steady and unsteady pressure distributions on the thickened wing.

In most cases it is sufficient to stop this calculation process after the first cycle. It is no problem however to repeat the calculation for additional cycles.

4. Vortex flows

Two different types of 3-d separation described already by Maskell [7] and others may occur on arbitrary 3-d configurations the free vortex-type separation and the bubble-type separation.

The free vortex type is already represented by the wake behind a wing. Free vortex layers located within a pressure field have the tendency to roll up forming concentrated vortices. These vortices can be observed within the flow about various configurations creating interference effects on the steady and unsteady pressure distributions at the body surfaces

Three configurations have recently been investigated experimentally (Fig.3):

1) the tip-vortex on a blade tip (rectangular wing with NACA 0012 airfoil section),
2) the leading edge vortex on a 3-d wing with highly swept leading edge (NORA-experiment),
3) the body-vortex on a blunt body of revolution at incidence (ellipsoid of axis ratio 3).

These three cases have also been investigated numerically by the potential theoretical method calculating steady as well as unsteady pressure distributions on the different oscillating body surfaces. The comparisons between theory and experiment will be discussed next.

4.1 Tip vortex

The sketch in Fig.4 shows the configuration which has been investigated experimentally in the low speed flow regime [8]. This blade tip has a NACA 0012 airfoil section and a rounded tip. Steady and unsteady pressure distributions have been measured in eight chordwise sections where four sections are concentrated in the very tip region ($0 < \eta < 0.1$). The blade was oscillating in pitch about the quarter chord axis. The cases discussed here were measured at a frequency of 8 Hz and $U_\infty = 50$ m/s ($\omega^* = 0.402$, based on chord).

Figs.4-6 show theoretical and experimental chordwise pressure distributions for three different incidence cases ($\alpha = 0^\circ / 4^\circ / 6^\circ$).

The plots on the left-hand side show steady and unsteady pressures at an inboard station with quasi 2-dimensional flow. The right-hand plots show the situation in the very tip region. In all cases the differences between theory and experiment are very small at the inboard section. Remarkable differences however occur in the tip region. Such differences appear in a steep negative increase of the steady and particularly the real parts of the unsteady pressures with increasing incidences. These effects are due to the tip vortex formation shown in Fig.3 affecting mainly the y-velocity component on the wing surface (outboard velocity on the suction side due to the tip vortex).

A simple quasi-steady correction based on the measured steady pressures can be made to modify the calculated unsteady pressures. From the steady pressure coefficient

$$c_p = 1 - \nu_{xs}^2 - \nu_{ys}^2 \tag{1}$$

with ν_{xs} and ν_{ys} as the steady velocity components relative to the surface (non-dimensionalized), one can calculate the experimental ν_{ys}-velocities under the assumption that the x-components remain unchanged by the influence of the tip vortex. The measured and the calculated ν_{xs}-components are therefore approximately equal.

Plotting ν_{ys} at various stations x/ℓ versus the angle of incidence and determining the slopes of the $\nu_{ys}(\alpha)$ curves, one obtains the quasi-steady velocities $\bar{\nu}_{yi}$ by introducing the Bernoulli formula for the calculation of unsteady pressures [1].

$$\begin{aligned} c_p{}' &= -2\left(-\omega^* \bar{\varphi}_i{}'' + \nu_{xs}\,\bar{\nu}_{xi}{}' + \underline{\nu_{ys}\,\bar{\nu}_{yi}{}'}\right) \\ c_p{}'' &= -2\left(\omega^* \bar{\varphi}_i{}' + \nu_{xs}\,\bar{\nu}_{xi}{}'' + \underline{\nu_{ys}}\,\bar{\nu}_{yi}{}''\right) + 2\,\omega^* \vec{U}\,\bar{V} \end{aligned} \tag{2}$$

The underlined terms in Eq.(2) are now modified by the measured data, whereas all other terms remain unchanged. One observes from Eq.(2) that the real parts $\bar{c}_p{}'$ are modified by the product $\nu_{ys} \cdot \bar{\nu}_{yi}{}'$ which is large where the influence of the tip vortex is large. The correction of the theoretical curve is represented by the dashed line in Figs.5 and 6 (suction side only). The correspondence with the measured data is satisfactory. The influence on the imaginary parts however is very small. The reason for this seems to be that the tip vortex is moved by the pitching oscillations approximately in a plane normal to the wing surface. This leads to negligible phase shifts in points on the surface.

Another interesting viscous effect on the unsteady pressures can be observed mainly at the inboard section (Figs.4-6). Starting with a laminar boundary layer calculation [6] from the stagnation point, the program signals transition at specific points on the suction and pressure side of the wing (points indicated by an asterisk in Figs.4-6). In the upstream proximity of these points a jump in the measured real and imaginary pressures can be observed which is large on the suction side. The influence on the steady pressures however is very small.

The effects of a boundary layer displacement correction is shown in Fig.5. The changes of the pressure distributions show the previously discussed tendencies. The effects are relatively small.

4.2 Swept-wing vortex interaction

Figs.7 and 8 show calculated and measured steady and unsteady chordwise pressure distributions on a 3-d wing with a highly swept leading edge undergoing pitching oscillations. The experimental results were obtained from the NORA experiments [9]. Only the subsonic case ($Ma_\infty = 0.6$) has been compared with the incompressible theory. The complicated profile of the NORA-model (droop-nose) has been taken into consideration. Again a good correspondence between theory and experiment can be observed in the zero-incidence case (Fig.7). With increasing incidence however severe deviations from the calculated pressures are observed in the steady and unsteady experimental data (Fig.8). In this case both the real and imaginary pressures are affected. These effects which have been found for all experimental results within the measured Mach number regime must be referred to a leading edge vortex shown qualitatively in Fig.3. Aside from the tip vortex effects, there are now remarkable phase shifts due to the fact that the leading edge vortex is moved by the pitching oscillations mainly parallel to the wing surface. The phase shift between the wing motion and the vortex motion is clearly represented in the imaginary pressures.

A correction of the unsteady calculated pressures using the measured steady pressures in the vortex region is now more difficult due to the missing information of the mentioned phase shift.

Fig.9 shows calculated and measured steady pressures at four chordwise positions at the leading edge plotted with respect to incidence. The slopes of the curves are obtained from the amplitudes of the unsteady experimental results. The theory shows the expected linear dependency of α . The experimental curves are linear only at very small incidences. The steep gradients of the experimental curves show the downstream shift of the leading edge vortex with increasing incidence.

It is important to note in Fig.9 that the absolute values of the measured pressure coefficients and the slopes of the $c_{ps}(\alpha)$ curves obtained from the measured unsteady pressure amplitudes fit together quite satisfactorily. This is again an indication of the quasi-steadiness of the vortex influence on the unsteady airloads of the oscillating wing.

4.3 Body-vortex interaction

Different types of viscous phenomena can be observed on blunt bodies of revolution at incidence. Aside from a bubble-type separation at the rear part of the body which occurs even at zero-incidence, body vortices are formed at small to moderate angles of attack. This latter type is a free vortex layer separation which has been investigated experimentally [10], [11] and numerically [12], [13] by several authors.

The three-dimensional laminar boundary layer calculation on ellipsoids at incidence by means of a finite difference method is described in [13]. Fig.10 shows the development of the calculated boundary layer thickness on the entire body surface along different equipotential lines. The boundary layer thickness shows a steep maximum at a certain position on the leeward side of the body. Further downstream from this position the numerical calculation becomes unstable. The line of instability points is interpreted as the separation line, i.e. the origin of the two counterrotating body vortices. Fig.10 shows a side- and top-view of the calculated separation lines on an ellipsoid of axis ratio 4 .

The panel-type method for oscillating blunt bodies at incidence ([2]) takes into account the exact boundary condition on the real body surface and uses a body-fixed frame of reference. With this concept it should be possible to obtain a good correspondence between theory and experiment even on bodies with considerable bluntness. Intensive experimental studies have been performed on an ellipsoid of axis ratio 3 at pitching oscillations in the low-speed flow regime [14]. The following comparisons between theory and experiment are made for the case: $f = 8$ Hz , $U_\infty = 40$ m/s ($\omega^* = 1.257$, based on total body length).

Figs.11 and 12 show steady and unsteady pressure distributions along the leeward line of symmetry of the body at zero-incidence (Fig.11) and at $\alpha = 30^\circ$ incidence (Fig.12). Two other theoretical methods are included in Fig.11 : the slender body theory with a singular behavior at the leading and trailing edges of the body and a method [15] based on the application of spheroid functions for the solution of the governing Helmholtz equation. The panel method, which uses a pure source distribution, yields a very good correspondence with the experimental results at the front part of the body.

Hardly any deviations can be observed in the steady pressure distribution at zero-incidence except at the very rear part ($x/L > 0.95$) of the body. Larger deviations however can be seen in the real and imaginary parts of the unsteady pressure distributions. In the high-incidence case (Fig.12) the correspondence between potential theory and experiment is again extremely good at the front part. The steady pressures show the expected deviations due to the blunt body separation at the rear. Some additional viscous effects can be observed further upstream showing a remarkable peak in the imaginary pressure which is shifted upstream with increasing incidence. Both real and imaginary pressures reveal deviations from potential theory downstream from this pressure peak. These viscous effects must be referred to the influence of the body vortices. In the case of a very thick ellipsoid of axis ratio 3 at moderate angles of attack, the strength of the body vortices and their effect on the surface pressure distribution is relatively small. It is interesting to note that these viscous effects can only be observed in the unsteady but not in the steady pressure distributions. Unsteady pressures due to small amplitude oscillations are a very sensitive indicator of viscous effects. The differences between experiment and a sophisticated potential theory very clearly show these effects of viscosity.

More details of the influence of the originating body vortices can be found in Figs.13 and 14 . Steady and unsteady pressures are plotted against the circumferential angle φ with the angle of incidence α as a parameter. Fig.13 shows the situation at $x/L = 0.088$. In all incidence cases the differences between theory and experiment are very small. Further downstream at $x/L = 0.196$ the differences are again small for the lower incidence cases. Remarkable deviations from potential theory are observed however for the $\alpha = 30^\circ$ case at the position $\varphi \approx 143^\circ$. Both real and imaginary pressure parts are affected. The position $x/L = 0.196$ approximately coincides with the location of the pressure peak within the imaginary part in Fig.12 . It must be pointed out again that the steady pressures in Fig.14 show only small differences compared to potential theory.

The reason both real and imaginary pressure parts are influenced by the body vortices can again be explained by the particular location of the body vortices with respect to the axis of rotation. Fig.3 shows the situation qualitatively. The pitching oscillation of the body about a pitching axis parallel to the y-axis causes an oscillatory motion of the body vortices along the body surface. A phase shift between body motion and vortex motion influences the unsteady pressures on the body surface accordingly.

5. Rearward body separation

On blunt bodies at incidence, two different viscous phenomena at the rear part of the body can be distinguished:

1) The alternating separation of the body vortices at very high incidence ($\alpha \geq 30^\circ$) . The frequency of this alternating separation is determined by a special Strouhal number.

2) Separation of the turbulent boundary layer forming a rearward separation region and a wake behind the body. This phenomenon occurs even in the zero-incidence case.

These two viscous phenomena occur also on non-oscillating bodies. As long as the forced oscillation frequencies of the body are small there is no influence on these two separation types. On the other hand there is a severe influence of the rear-body separation on the unsteady airloads. It is very difficult to make allowances for these influences. One possibility would be to perform a boundary layer calculation (at least in the two-dimensional, axisymmetric case) to determine the turbulent separation point. Downstream from this separation point the wake could be approximately replaced by a rigid body. Such a modelling of the separation region achieves the proper correction of the steady pressures. It should also correctly influence at least the amplitudes of the unsteady pressures. Further intensive studies of these complicated flow situations with respect to unsteady airloads are necessary in the future.

6. Conclusion

Potential theoretical calculations of steady and unsteady airloads on oscillating wings and bodies have been compared with corresponding experimental results. The deviations between theory and experiment yield direct information about the type and magnitude of the different viscous phenomena involved.

It has been mentioned that the Kutta-Joukowsky condition as a phenomenological condition includes the major viscous effect for lifting configurations without flow separation. A higher order effect of viscosity including the boundary layer displacement is taken into account.

Three-dimensional flow separation can be of the free vortex layer type or of the bubble type. Vortex systems have been investigated about the following configurations:

1) blade tip with tip vortex,
2) leading edge vortex on wing with highly swept leading edge,
3) body vortex on axisymmetric body at incidence.

In all three cases the effects of the vortex flows on the steady and unsteady airloads may be clearly localized. If the vortex location is known a priori as in the blade tip case, a quasi-steady correction of the unsteady airloads using the measured steady pressure distributions can be successfully used to represent the major effects of the vortex flow on the unsteady airloads.

Measured unsteady pressures are found to be a very sensitive indicator of viscous effects, while local deviations from potential theory signal boundary layer transition. The origin of the body vortices on blunt bodies at incidence can be localized clearly where influences on the steady pressures are still very small.

A simple model representing the rear body separation region should give a corresponding correction of the steady as well as unsteady pressures within these regions.

7. References

[1]	Geissler, W.	Nonlinear Unsteady Potential Flow Calculations for Three-Dimensional Oscillating Wings. AIAA-Journal, Vol.16, No.11, Nov. 1978, pp.1168-1174
[2]	Geissler, W.	Der harmonisch schwingende Rumpf in Unterschallströmung - Einfluß der Kompressibilität - DFVLR-FB 78-24, 1978
[3]	Kienappel, K. Round, D. Vasel, A.	Experimentelle Untersuchungen an einer harmonisch schwingenden Hinterkantenklappe mit Spalt. Deutsche Gesellschaft für Luft- und Raumfahrt Jahrestagung, 28-30 April 1980, Braunschweig
[4]	Triebstein, H.	Instationäre Druckverteilungsmessungen an Flügel-Außenlastkombinationen in inkompressibler Strömung. Deutsche Luft- und Raumfahrt Forschungsbericht, DLR-FB 77-12, 1977
[5]	Tijdeman, H.	Investigations of the Transonic Flow Around Oscillating Airfoils. NLR-TR 77090 U, 1977
[6]	Rotta, J. C.	FORTRAN IV-Rechenprogramm für Grenzschichten bei kompressiblen, ebenen, und rotationssymmetrischen Strömungen. Deutsche Luft- und Raumfahrt Forschungsbericht, DLR-FB 77-12, 1977
[7]	Maskell, E. C.	Flow Separation in Three Dimensions. RAE Rept. Aero. 2565, Nov. 1955, Royal Aircraft Establishment, Bedford, England
[8]	Kienappel, K.	Einfluß der Blattspitzengeometrie auf die instationäre Druckverteilung an einem Rotorblatt Teil I: Rechteckblattspitze. DFVLR-FB in preparation
[9]	Lambourne, N. Kienappel, K. Destuynder, R. Roos, R.	Comparative Measurements in Four European Wind Tunnels of the Unsteady Pressures on an Oscillating Model (The NORA Experiments). AGARD-R-673, Oct. 1979
[10]	Grosche, F.-R.	Windtunnel Investigation of the Vortex System Near an Inclined Body of Revolution with and without Wings. AGARD-CP-71, 1971, pp.2-1 to 2-13
[11]	Meier, H. U. Kreplin, H.-P.	Pressure Distributions and Flow Visualisations on an Ellipsoid 1:6 Designed for Three-Dimensional Boundary Layer Investigations. Proc. AFFDL-TR-78-111, 1978, pp.197-208

[12] Wang, K. C. Separation Patterns of Boundary Layer over an Inclined Body of Revolution.
AIAA-Journal, Vol.10, 1972, No.8, pp.1044-1050

[13] Geissler, W. Three-Dimensional Laminar Boundary Layer over a Body of Revolution at Incidence and with Separation.
AIAA-Journal, Vol.12, No.12, Dec. 1974, pp.1743-1745

[14] Kienappel, K.
Stange, H.
Wagner, W.
Instationäre Druckverteilungsmessung an einem Rotationsellipsoid.
DFVLR-Internal Report, IB 253 - 80 J 02, 1980

[15] Chao, K.-L. Analytische Lösung der verallgemeinerten Helmholtz-Wellengleichung für kompressible Unterschallströmung und Berechnung der instationären Druckverteilungen an harmonisch schwingenden rotationselliptischen Körpern.
Deutsche Luft- und Raumfahrt Forschungsbericht, DLR-FB 77-11, 1977

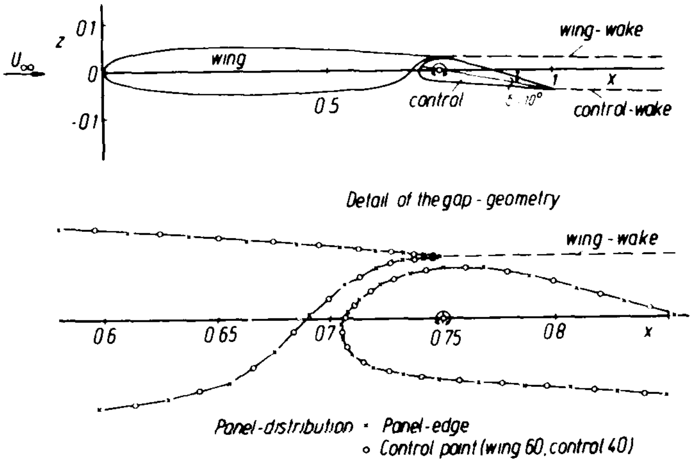

z
0.1
U_∞
0
-0.1
wing
0.5
control
δ = 10°
1
x
wing-wake
control-wake
Detail of the gap-geometry
wing-wake
0.6
0.65
0.7
0.75
0.8
x
Panel-distribution · Panel-edge
○ Control point (wing 60, control 40)

Figure 1: Wing with oscillating control, details of gap-geometry

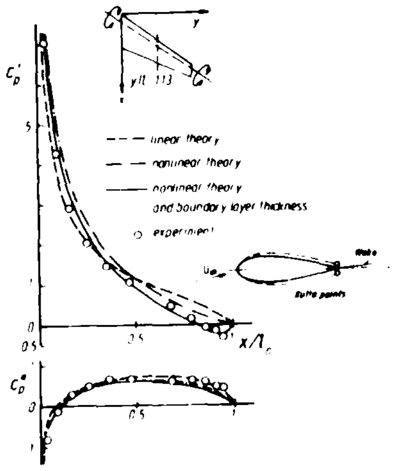

Figure 2: Influence of wing thickness and boundary layer displacement on unsteady airloads

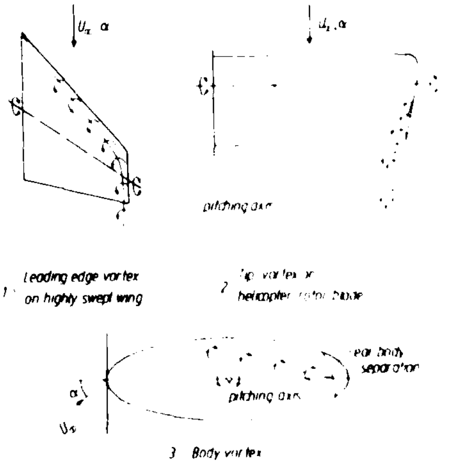

U_∞, α
U_∞, α
pitching axis
1 Leading edge vortex on highly swept wing
2 tip vortex on helicopter rotor blade
rear body separation
pitching axis
α
U_∞
3 Body vortex

Figure 3: Vortex formations on lifting configurations and bodies

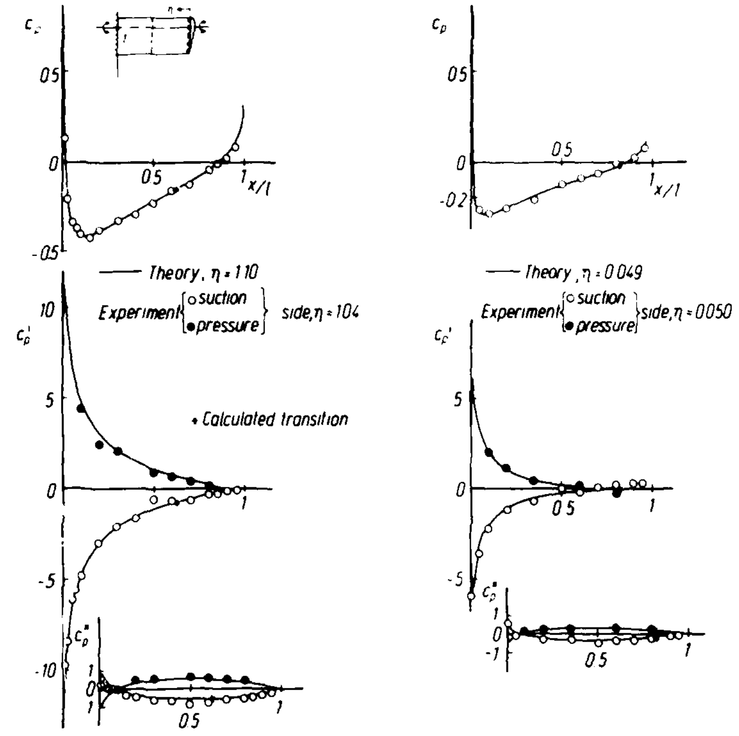

Figure 4: Steady and unsteady pressure distributions on an oscillating blade tip (α = 0°, ω^* = 0.402)

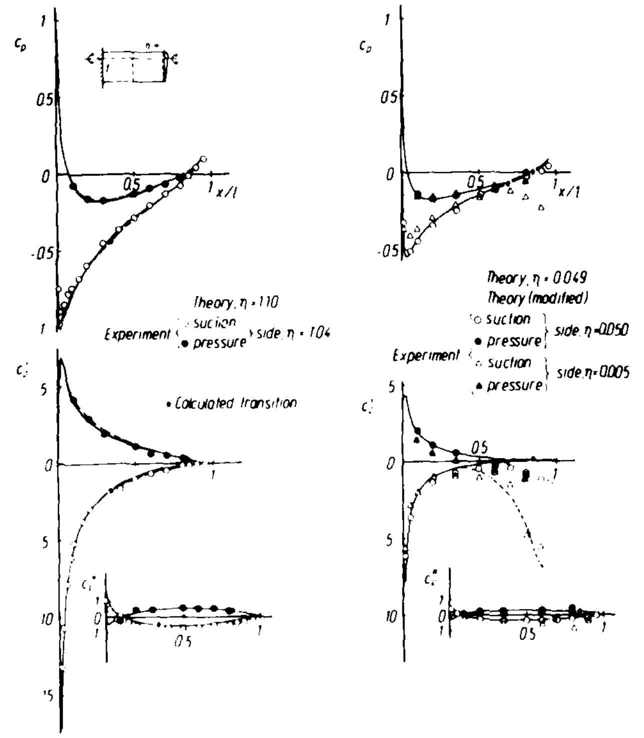

Figure 5: Steady and unsteady pressure distributions on an oscillating blade tip (α = 4°, ω^* = 0.402)

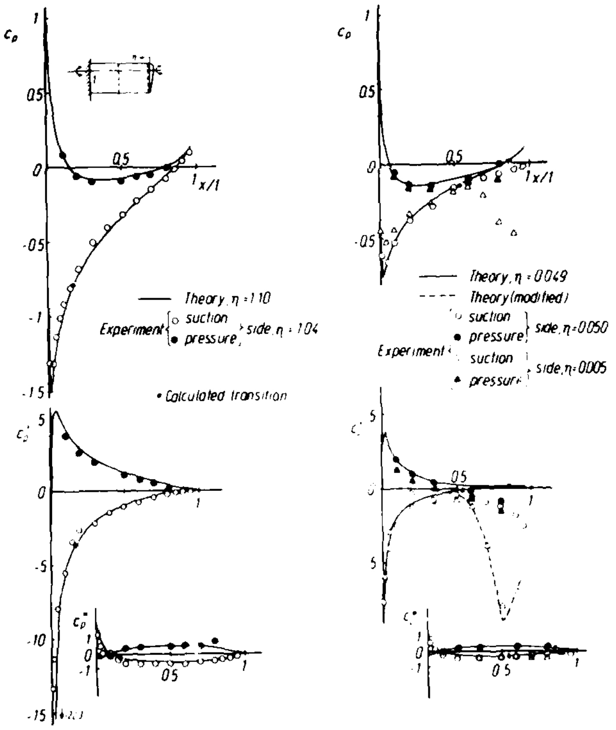

Figure 6: Steady and unsteady pressure distributions on an oscillating blade tip
(α = 6°, ω^* = 0.402)

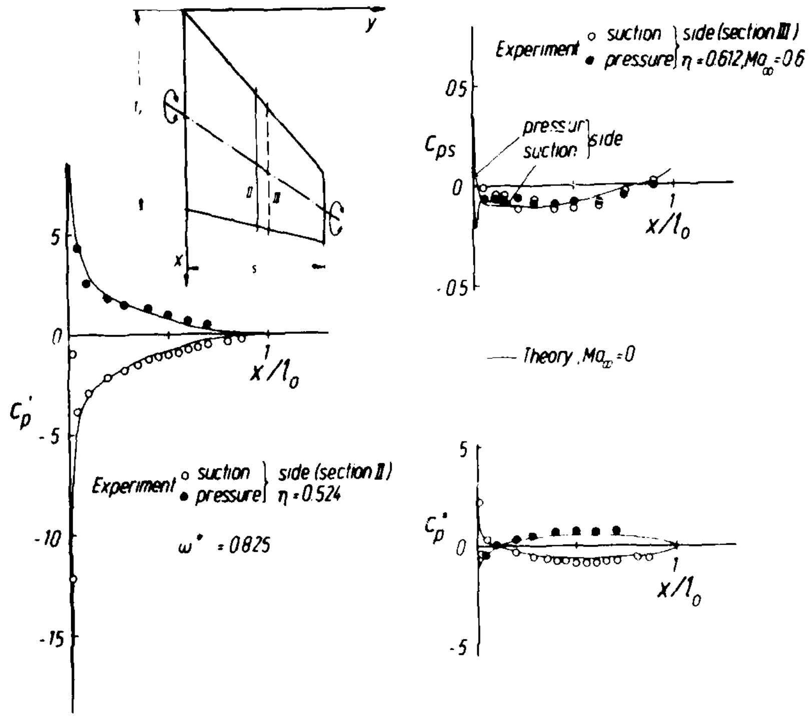

Figure 7: NORA-wing: Steady and unsteady chordwise pressure distributions
(α = 0°, ω^* = 0.825)

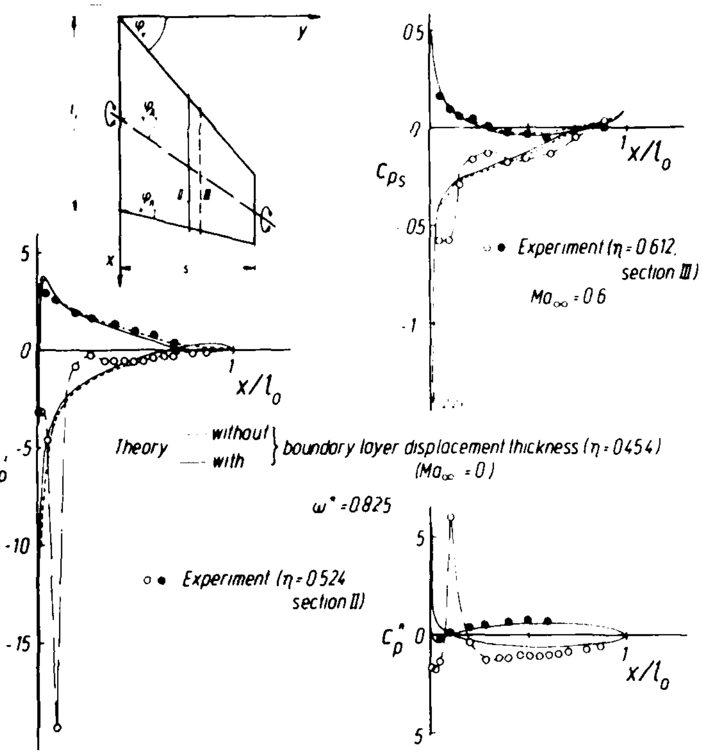

Figure 8: NORA-wing: Steady and unsteady chordwise pressure distributions (α = 4°, ω^* = 0.825)

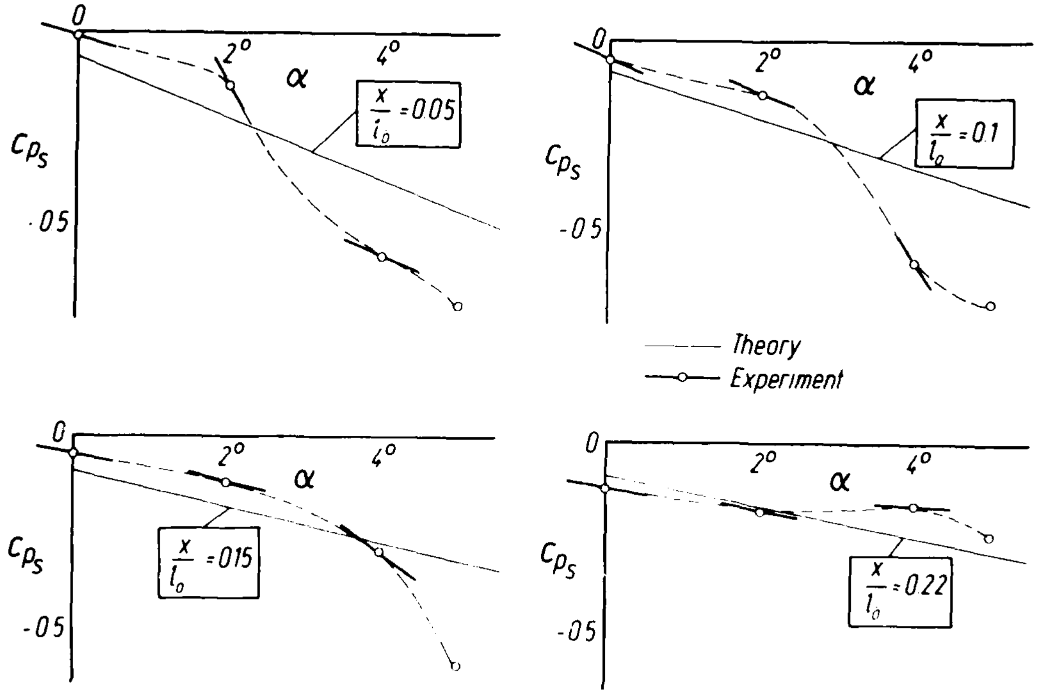

Figure 9: NORA-wing: Leading edge vortex formation

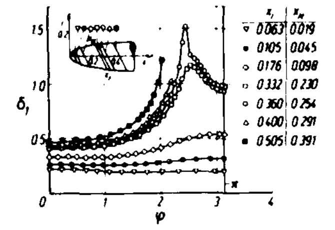

Boundary layer displacement thickness δ_1 on Ellipsoid, $a/b = 4$, $\alpha = 15°$

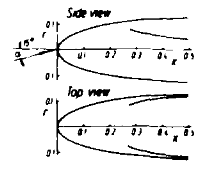

Separation lines on Ellipsoid, $a/b = 4$, $\alpha = 15°$

Figure 10: Ellipsoid of axis ratio $a/b = 4$ at $\alpha = 15°$ incidence.
Boundary layer displacement thicknesses δ_1 along different equipotential lines.
Lines of numerical instability interpreted as separation lines [13].

Figure 11: Ellipsoid of axis ratio $a/b = 3$ (no incidence case).
Steady and unsteady pressure distributions along the leeward symmetry line.
Comparison of three different theoretical approaches with experimental results [14]:

a) Slender body theory
b) Spheroid function approach [15]
c) Present panel method.

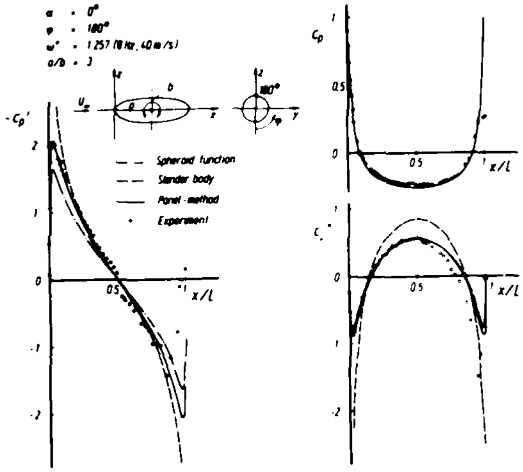

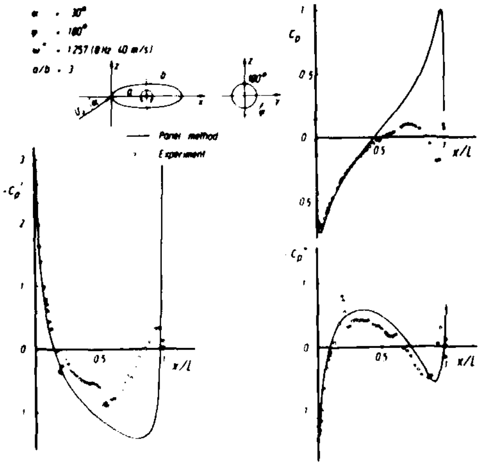

Figure 12: Ellipsoid of axis ratio $a/b = 3$ at $\alpha = 30°$ incidence.
Steady and unsteady pressure distributions calculated by the present panel method compared with experimental results [14].

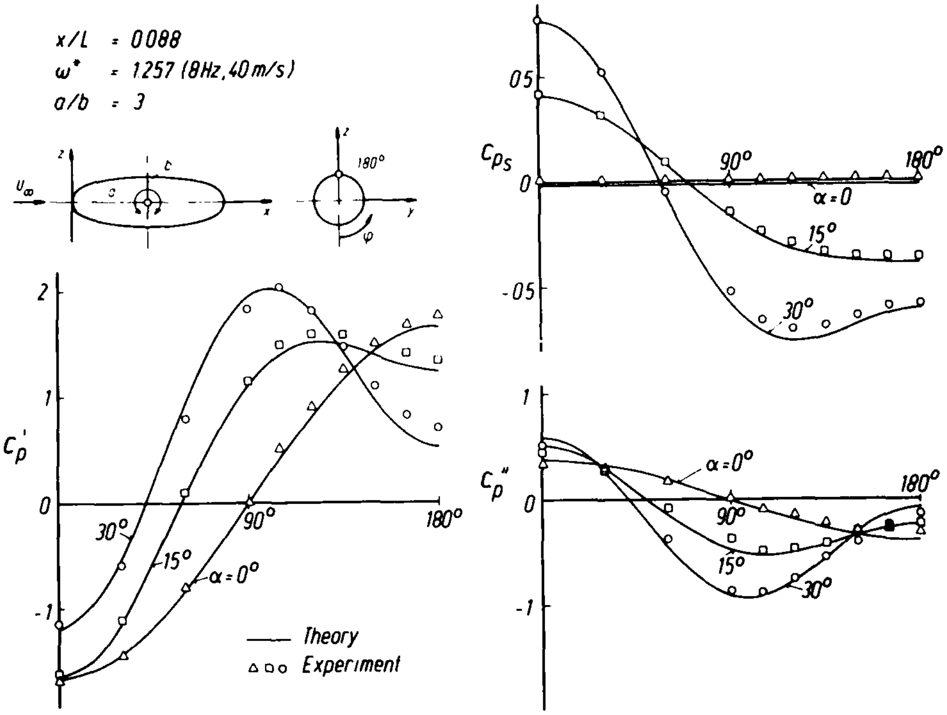

Figure 13: Circumferential pressure distributions on a prolate spheroid (x/L = 0.088)

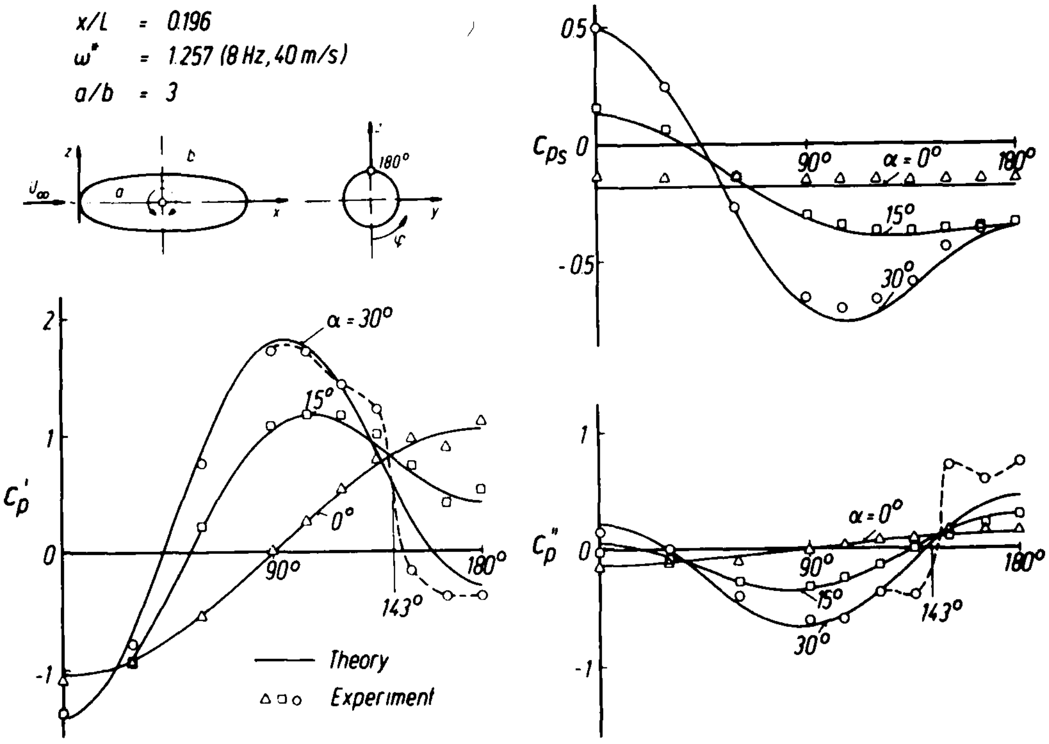

Figure 14: Circumferential pressure distributions on a prolate spheroid (x/L = 0.196)

SOME REMARKS ON BOUNDARY LAYER EFFECTS ON UNSTEADY AIRLOADS

by
R. Houwink
National Aerospace Laboratory NLR
Anthony Fokkerweg 2
1059 CM AMSTERDAM
The Netherlands

SUMMARY

These notes of an oral presentation discuss steady, quasi-steady and unsteady boundary layer effects on unsteady airloads on oscillating airfoils. The discussion is illustrated by experimental and theoretical data for wing sections with oscillating flap. The notes reflect results of current investigations at NLR to obtain insight in boundary layer effects, and to include these effects in prediction methods for unsteady airloads.

LIST OF SYMBOLS

c	chord length
c_ℓ	lift coefficient
c_n	hinge moment coefficient (positive tail up)
C_p	pressure coefficient
k	$= \frac{\omega c}{2U_\infty}$ reduced frequency
k_c	$= \frac{1}{\pi}\frac{c_{\ell_1}}{\delta_1}$ unsteady lift coefficient due to flap deflection
M_∞	free-stream Mach number
n_c	$= \frac{2}{\pi}\frac{c_{n_1}}{\delta_1}$ unsteady hinge moment coefficient due to flap deflection

R	ratio of boundary layer effect vector to inviscid lift vector (Figs 8,9)
Re	Reynolds number based on chord
U_∞	free-stream velocity
x_t	transition point location
α_o	mean angle of attack
δ_o	mean flap angle
δ_1	flap amplitude
δ^*	boundary layer displacement thickness
ΔC_p	$= \frac{C_{p_1}}{\delta_1}$ unsteady pressure coefficient
index	
1	first harmonic component of response to sinusoidal motion

1 INTRODUCTION

The background for the interest in boundary layer effects on unsteady airloads at NLR is the prediction of operational limits with respect to flutter, buffet and buzz. Typical flow regions of interest (subsonic and transonic attached flow, separated flow) encountered by an airplane within its C_L-M_∞ boundaries are shown in figure 1. The basic aerodynamic problem studied at these flow conditions, is the determination of unsteady airloads on wing sections and control surfaces in harmonic motion (e.g. Tijdeman[1]).

Various problems hamper the prediction of unsteady airloads for free-flight conditions:
- wind tunnel data are affected by wall interference and scale effects (in particular of Reynolds number),
- inviscid subsonic and transonic flow theories breakdown due to the neglect of viscous effects in separated flows, as well as in attached flows with strong pressure gradients (e.g. at transonic flow conditions, control surface deflections).

In the latter case, for instance, the applicability of linear theory breaks down because the errors due to the neglect of both thickness and boundary layer effects do not cancel each other, like in many low subsonic flow applications. For a better theoretical prediction of unsteady airloads, both effects should be taken into account.

In these notes first some general information on boundary layer effects is given. Next the effects of thickness and boundary layer on unsteady airloads on two airfoils (NACA64A006 and NLR 7301) with oscillating flap are illustrated by experimental and theoretical results. Besides quasi-steady results of coupled steady inviscid flow-boundary layer computations (using the BGKJ method[2]) also preliminary results are shown of a coupled unsteady inviscid transonic flow-steady boundary layer computation (using the LTRAN2 - NLR code[3] and Green's lag-entrainment method[4]).

2 BOUNDARY LAYER EFFECTS IN STEADY FLOW

Some important aspects of the boundary layer effect on airfoils in steady flow can be summarized as follows:
- The boundary layer affects the steady flow by interaction with the (approximately) inviscid outer flow and the airfoil. This results in: drag, decrease of lift and change of moment on the airfoil.
- The main effect is explained by the displacement thickness of the boundary layer, which changes the effective geometry of the airfoil.
- The flow can be predicted by interactive computation of inviscid outer flow and displacement thickness (e.g. BGKJ method[2]), together with special treatment of strong interaction regions (wake, separated flow, e.g. Le Balleur[5], Melnik[6]).

Figure 2 shows a sketch of the mean steady and unsteady transonic flow about an airfoil with flap, in which the various regions of interest are indicated.

3 UNSTEADY BOUNDARY LAYER EFFECTS

3.1 General remarks

The unsteady flow is characterized by the change of all flow quantities with time relative to the mean steady state (Fig. 2). The boundary layer affects the unsteady airloads both by its mean steady state and its unsteady change.

- The mean steady state of the boundary layer affects the mean steady state of the entire flow, depending on geometry, incidence α_0, Mach number M_∞, Reynolds number Re. The unsteady airloads depend on this mean steady state, in particular at transonic flow conditions.
- The unsteady change of the boundary layer (in particular of the displacement thickness) influences the effective motion of the airfoil. This effect depends on the mean steady state of the flow and (for harmonic motions) on the vibration mode, amplitude and reduced frequency of the motion.

Besides motion-dependent effects, the boundary layer may cause unsteady effects independent of motion (e.g. turbulence, unsteady shock-induced separation), which usually interfere with motion-generated effects. In *the following only motion-dependent effects are discussed.*

In the case of unsteady flow due to a harmonic motion, the boundary layer effect on the unsteady airloads will consist of:

- influence on magnitude and phase angle of the first harmonic components (both in separated and attached flow),
- non-linear effects as (influence on) higher harmonic components and dependence of airloads on amplitude (in particular in separated flows).

These effects are important for aeroelastic behaviour (e.g. for flutter boundaries, limit cycle motions etc.).

In the following, some of the boundary layer effects discussed are analysed by theoretical and experimental results for the NACA64A006 airfoil (in subsonic and transonic attached flow) and the NLR 7301 airfoil (in transonic separated flow) with oscillating flap. The analysis will be split into:

- quasi-steady analysis of steady flow data to determine the effect of the boundary layer for the given vibration mode and amplitude (1° flap deflection) at infinity slow motion,
- subsequently, analysis of unsteady airloads to determine the effect of reduced frequency on the boundary layer and thickness effects.

It should be noted that the experimental data are affected by wall interference effects. However, in view of the dominating effect of the boundary layer in quasi-steady cases considered in the next part, it is believed that such a comparison gives at least a qualitatively correct picture of the effect of the boundary layer.

3.2 *Discussion of examples for attached flow*

The present results for the NACA64A006 airfoil concern a subsonic case ($M_\infty = 0.8$) and a transonic case with shock wave ($M_\infty = 0.85$), both for zero mean incidence and flap angle ($\alpha_0 = \delta_0 = 0$). The data shown are:

- experimental data from Tijdeman[1] (Re = 2×10^6, transition fixed at 10 % chord)
- in the quasi-steady analysis, theoretical results from the BGKJ program (quasi-conservative full-potential theory) with and without boundary layer computation
- in the unsteady analysis, theoretical results from the LTRAN2 - NLR code (improved low-frequency transonic small perturbation theory)
- results of linear theory.

Steady and quasi-steady analysis

Figure 3a shows the effect of the boundary layer on the steady pressure distribution in the transonic case at one degree flap deflection. Figure 3b shows the quasi-steady pressure distribution $\left(\Delta C_p = \frac{\partial C_p}{\partial \delta}\right)$ derived from figure 3a. The boundary layer leads to a more upstream location of the shock wave (effect of its mean steady state) and to a lower ΔC_p level (effect of both its mean steady state and its quasi-steady change). Globally, the boundary layer reduces the effect of thickness, and dominates the wall-interference effects. This is also reflected in the overall lift and moment coefficients (AGARD notation) shown in table 1. Note the stronger effects of thickness and boundary layer in the transonic case.

Figure 4 shows the distributions of displacement thickness δ^* on upper and lower side at one degree flap deflection, for $M_\infty = 0.8$ and $M_\infty = 0.85$. The difference $\Delta\delta^*$, corresponding to the quasi-steady change at one degree amplitude, decambers the airfoil like a "viscous flap" opposite to the geometric flap motion. This effect is propably due to the strong quasi-steady pressure peaks at the flap leading edge and, in the transonic case, at the shock wave (Fig. 3).

Unsteady analysis

Figure 5 shows experimental and theoretical mean steady pressure distributions for the transonic case. The results of inviscid transonic theory (LTRAN2 - NLR) show a slightly stronger and more downstream shock wave, (partly) due to the neglect of the boundary layer.

Figures 6 and 7 show the effects of thickness (difference between linear and transonic theory) and boundary layer (main part of difference between transonic theory and experiment) on the unsteady lift and *hinge moment coefficients, both for the subsonic and the transonic case. In the lift coefficients,* (Fig. 6) the effect of the boundary layer is strong, it depends on frequency and Mach number and is opposite the thickness effect. The hinge moments in figure 7 show a different effect of the boundary layer: mainly reducing the magnitude, and only slightly dependent on M_∞ and k.

The different boundary layer effects on lift and hinge moment indicate:

- the effect on the hinge moment is dominated by an approximately quasi-steady "viscous flap" effect
- the effect on the lift is a combination of the above "viscous flap" effect and the unsteady effect of the interaction of the boundary layer with the unsteady pressures upstream of the flap (in particular at the shock wave in transonic flow, possibly a "viscous ramp" effect[7]). These pressures generally show large phase lags, depending on k, and so introduce phase lags and frequency dependence in the boundary layer effect on the overall unsteady airloads.

The boundary layer effect can be illustrated even more clearly by considering a vector plot of the unsteady airloads, for example in figure 8 for the lift in the transonic case. The difference vector of the experimental and theoretical results, which mainly represents the effect of the boundary layer, shows a strong decrease in magnitude and an increasing phase lag, with increasing value of k. In figure [illegible] this effect is shown both for the transonic and the subsonic case in a slightly different way, by the ratio of the difference vector to the inviscid lift vector (for the transonic case derived from figure [illegible]). The stronger boundary layer effect in the transonic case is largely due to the shock wave.

Prediction methods

Analogously to steady flow, a feasible prediction of the above boundary layer effects in unsteady flow can be expected from coupled unsteady inviscid flow-boundary layer computations (e.g. [illegible] and Grenon[8]). In applications of this procedure for transonic flows with shock waves, [illegible] "viscous ramp" effect at the shock wave (as modelled and applied successfully by Yoshihara[7]) and the "viscous flap" [illegible] can be accounted for properly.

At NLR, as a first step towards such a procedure the LTRAN2-NLR code has been [illegible] with the lag-entrainment method of Green for a steady turbulent boundary layer. Figure [illegible] shows [illegible] an unsteady pressure distribution for the NACA64A006 airfoil at transonic conditions (M_∞ = [illegible], α = [illegible]) with oscillating flap ($\delta_1 = 1^\circ$, k = 0.24). Accounting for the boundary layer displacement [illegible] leads to a considerably better agreement with the experimental data.

Remarks on further investigations

In order to support the development of prediction methods, further experimental and theoretical investigations are necessary on:

- modeling of local unsteady strong interaction regions and the unsteady wake
- non-linearity of the boundary layer effect
- unsteadiness of the boundary layer response to unsteady pressure distributions, to determine the limits of applicability of quasi-steady boundary layer prediction methods.

Besides the above investigations on boundary layer effects, also further study of wall-interference effects is necessary to facilitate the interpretation of theory-experiment comparisons.

The above remarks also apply to strongly separated flows, where the ingredients for similar prediction methods are hardly available. An example of unsteady airloads in separated transonic flow is discussed in the next chapter.

3.3 Discussion of example for separated transonic flow

The present results for the NLR 7301 airfoil concern a transonic case (M_∞ = [illegible], α = [illegible], δ = [illegible]) with a separated boundary layer downstream of a shock wave on the upper surface. The experimental data are related to Re = [illegible]x10^6 with transition fixed at 30 % chord. Figure 11 shows the mean steady pressure distribution. In figure 12, the quasi-steady pressure distribution on the upper side at one degree flap deflection shows the dominating effect of the flow separation, by the strong loading on the rear part of the airfoil and by the negative pressure peak at the shock wave (indicating an upstream motion of the shock at a downward flap deflection).

Figures 13 and 14 show the effects of thickness and boundary layer on the unsteady lift and hinge moment coefficients. The inviscid transonic theory results were computed for a comparable airfoil at a lower angle of attack, having the same shock wave location. In this way the effect of the mean steady flow field (the thickness effect) on the unsteady airloads is accounted for approximately in a correct way. The separated boundary layer appears to cause a strong variation of the unsteady airloads with frequency, both in magnitude and phase angle. The present behaviour of the lift is quite similar to that in the case of the NACA64A010 airfoil oscillating in pitch, reported by Davis[9].

The peaks in magnitude and strong variations of phase angle with frequency indicate a type of resonance in the viscous-inviscid interaction. This also shows up if the boundary layer effect on the lift coefficient is determined as the difference vector of the inviscid results and the experimental data, analogous to the attached flow example. Figure [illegible] shows the relative boundary layer effect, by the ratio of this difference vector to the inviscid lift vector (compare with Fig. 9). Contrary to the attached flow results, the present boundary layer effect shows a peak in magnitude near k = [illegible], and a [illegible] phase angle of more than [illegible].

The above effects of the boundary layer [illegible] play an important role [illegible] and wake [illegible] by Lambourne[10] and Ericsson[11]. [illegible] more empirical data will have to be derived from experimental investigations.

4 REFERENCES

1. Tijdeman, H.: Investigations of the transonic flow around oscillating airfoils. NLR TR 77090 U (1977).
2. Bauer, F., Garabedian, P., Korn, D., Jameson, A.: Supercritical wing sections II, Lecture notes in economics and mathematical systems, Vol. 108, Springer-Verlag, Berlin (1975).
3. Houwink, R., van der Vooren, J.: Some results of an improved version of LTRAN2 for unsteady transonic flow computations. AIAA paper 79-1553 (1979).
4. Green, J.E., Weeks, D.J., Broomen, J.W.F.: Prediction of turbulent boundary layers and wakes in compressible flow by a lag-entrainment method. RAE TR 72231 (1973).
5. le Balleur, J.C.: Calculs couplés visqueux-non visqueux incluant décollements et ondes de choc en écoulement bidimensionnel. AGARD LS 94, paper 4 (1978).
6. Melnik, R.E., Chow, R. Mead, H.R.: Theory of viscous transonic flow over airfoils at high Reynolds number. AIAA paper 77-860 (1977).
7. Magnus, R., Yoshihara, H.: The transonic oscillating flap. AIAA paper 76-327 (1976).
8. Desopper, A., Grenon, R.: Viscid-inviscid coupled calculations for two-dimensional transonic unsteady flow. Report of Eurovisc meeting on unsteady turbulent boundary layers and shear flow. University of Liverpool, 18-19 April 1979, p.p. 90-112.
9. Davis, S.S., Malcolm, G.N.: Experiments in unsteady transonic flow. AIAA paper 79-0769 (1979).
10. Lambourne, N.C.: Some instabilities arising from the interactions between shock waves and boundary layers. AGARD report 182 (1958).
11. Erickson, L.L.: Transonic single-mode flutter and buffet of a low aspect ratio wing having a subsonic airfoil shape. NASA TN-D-7346, (1974).

TABLE 1

Quasi-steady airloads on NACA64A006 airfoil with oscillating flap

	Thin-airfoil theory		Theory of Ref. 2				Experiment			
			Incl. thickness		Incl. thickness + bound. layer		Incl. tunnel-wall correction		Uncorrected	
M_∞	k_c	m_c	k_c	m_c	k_c	m_c	k_c	m_c	k_c	m_c
0.8	2.03	0.69	2.44	0.80	1.88	0.65	1.66	0.61	1.32	0.61
0.85	2.31	0.79	3.61	1.29	1.94	0.60	1.82	0.75	1.41	0.75

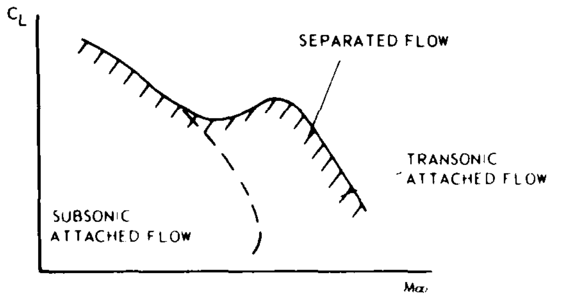

C_L
SEPARATED FLOW
TRANSONIC ATTACHED FLOW
SUBSONIC ATTACHED FLOW
M_∞

Fig. 1 Types of flow in C_L-M_∞ plane of airfoils

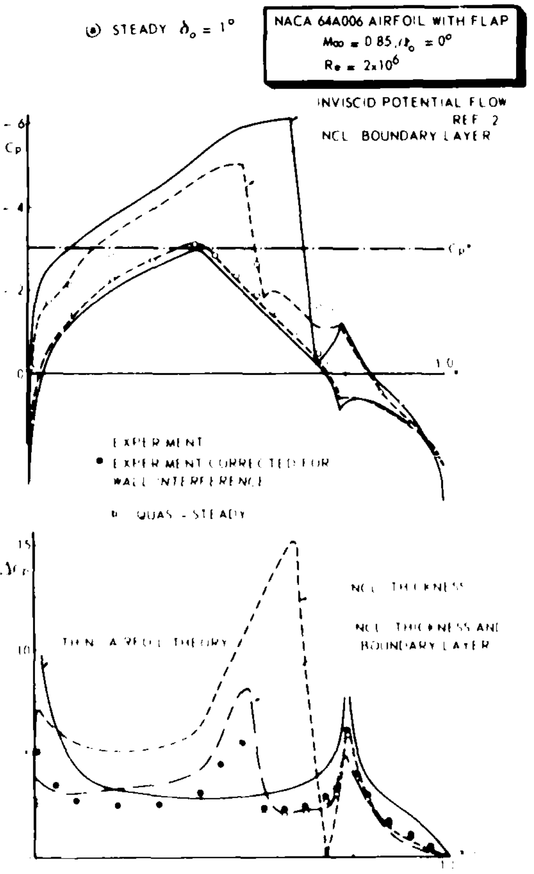

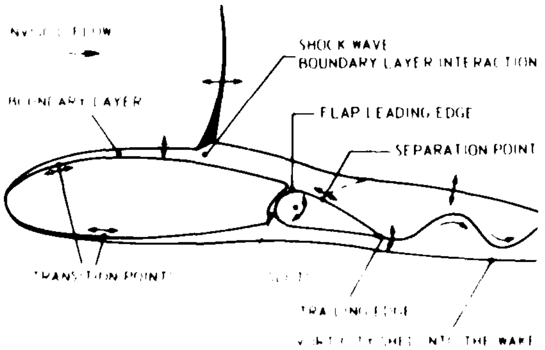

INVISCID FLOW
SHOCK WAVE BOUNDARY LAYER INTERACTION
BOUNDARY LAYER
FLAP LEADING EDGE
SEPARATION POINT
TRANSITION POINT
TRAILING EDGE
VORTEX PATCHES INTO THE WAKE

Fig. 2 [illegible]

Fig. 3 Effect of thickness and boundary layer on the steady and quasi-steady pressure distribution in transonic flow

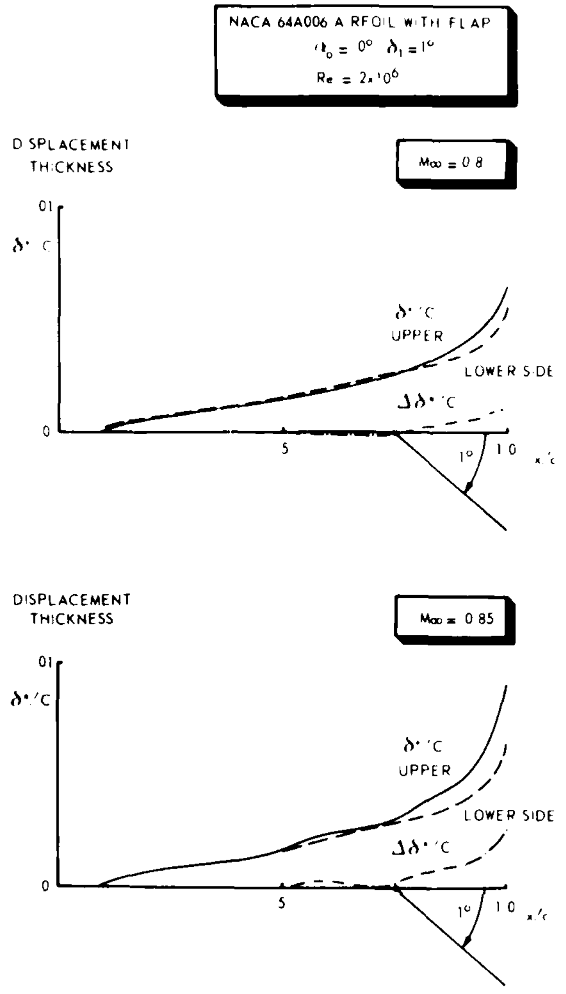

Fig. 4 Steady and quasi-steady boundary layer displacement thickness (rel. to airfoil chord)

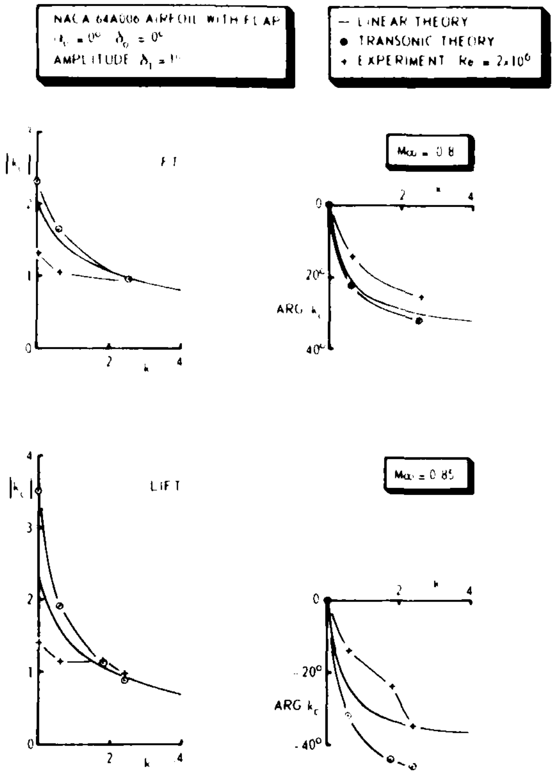

Fig. 6 Unsteady lift coefficients showing effect of thickness and boundary layer for subsonic and transonic flow

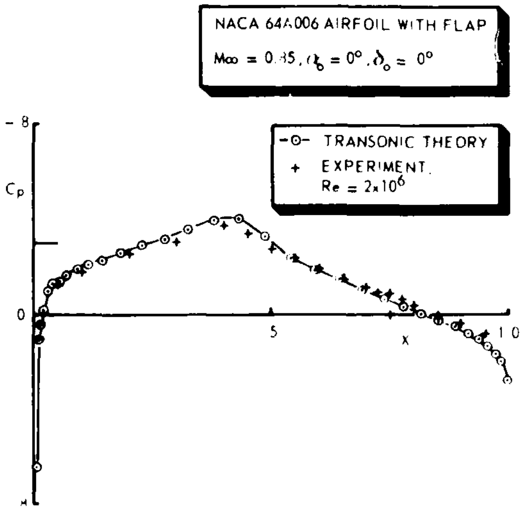

Fig. Mean steady pressure distribution

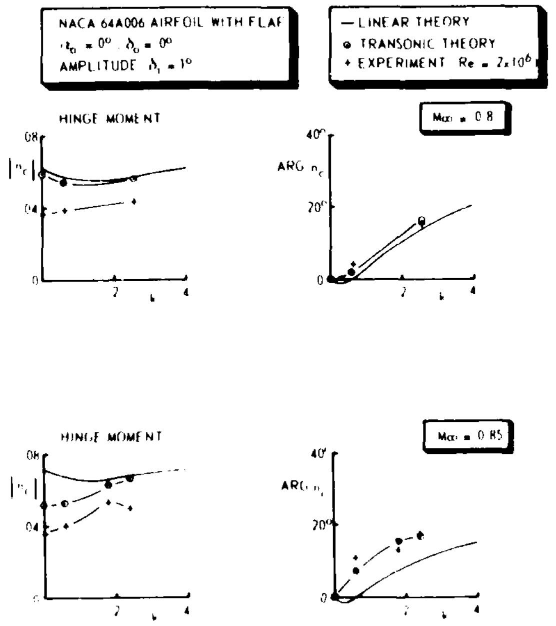

Fig. 7 Unsteady hinge moment coefficients showing effect of thickness and boundary layer for subsonic and transonic flow

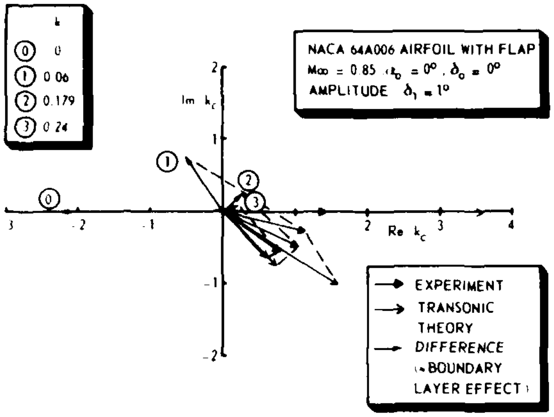

Fig. 8 Vector plot of lift showing effect of boundary layer

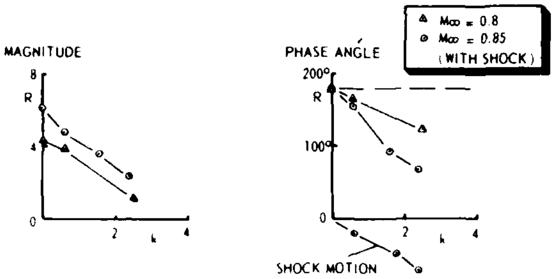

Fig. 9 Ratio R of boundary layer effect vector to inviscid lift vector, showing relative effect

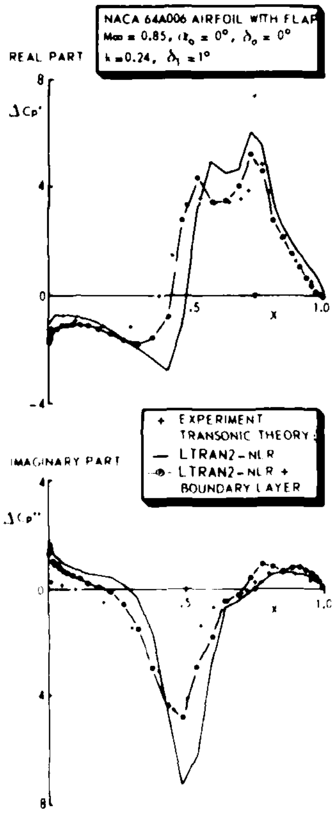

Fig. [illegible] Unsteady pressure distribution [illegible] showing effect of quasi-steady boundary layer

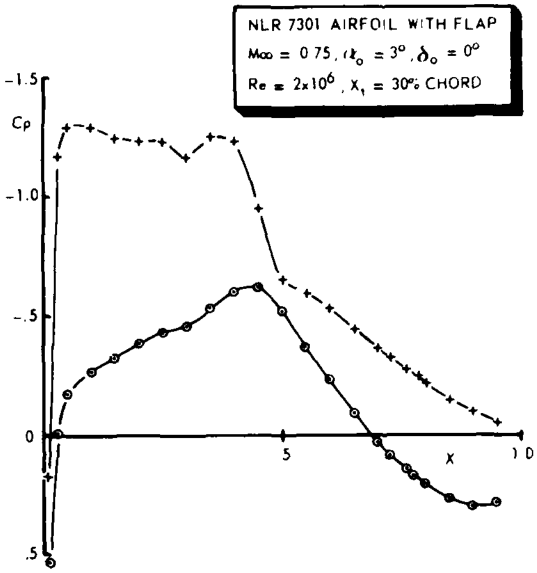

Fig. 11 Steady pressure distribution showing shock wave and flow separation on upper side

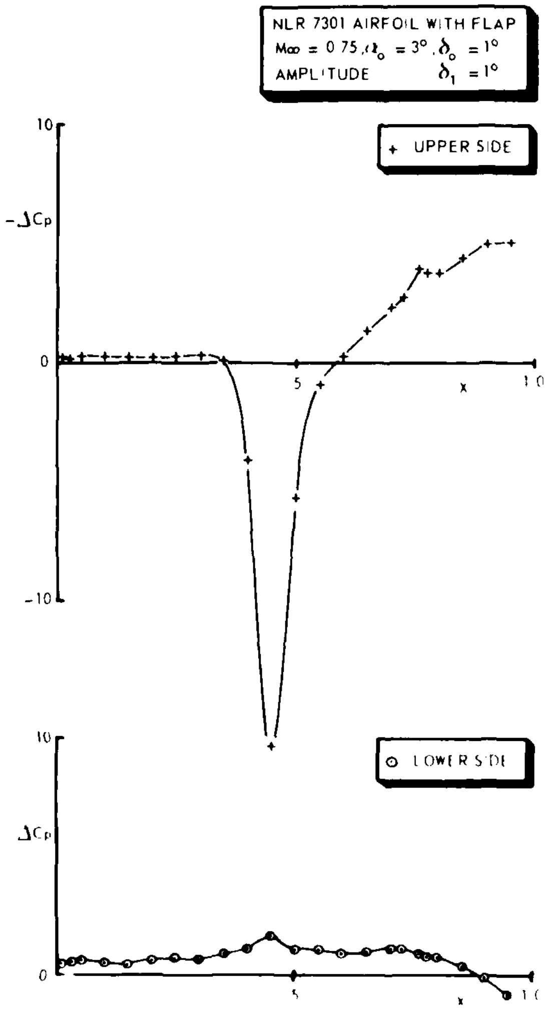

Fig. [illegible] Quasi-steady pressure distribution

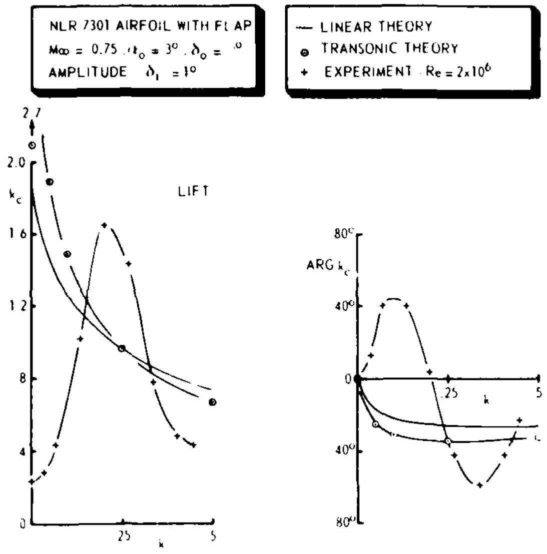

Fig. [illegible] Unsteady lift coefficients showing effect of thickness and boundary layer

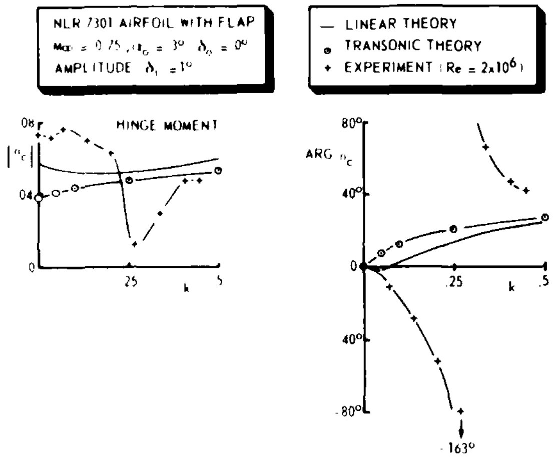

Fig. [illegible] Unsteady hinge moment coefficients showing effect of thickness and boundary layer

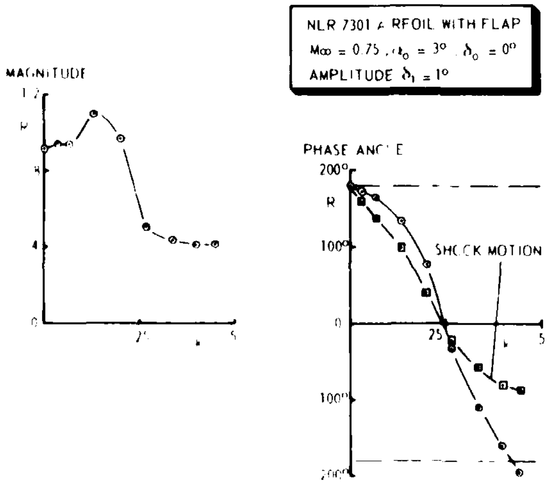

Fig. [illegible] [illegible] boundary layer effect vector [illegible] [illegible] showing [illegible] effect

PRISE EN COMPTE D'EFFETS DE COUCHE LIMITE INSTATIONNAIRE DANS UN CALCUL BIDIMENSIONNEL TRANSSONIQUE(*)

par

M.Couston, J.J.Angelini, J.C. le Balleur, P.Girodroux-Lavigne

Office National D'Etudes et Recherches Aerospatiales (ONERA)
29 Ave de la Division Leclerc
92320 Chatillon (France)

[illegible] fluide visqueux des écoulements instationnaires sur profils d'ailes est recher- [illegible] développées à l'ONERA, d'une part pour le fluide parfait en théorie des petites [illegible] d'autre part pour le calcul et le couplage des couches visqueuses en régime [illegible]

[illegible] solution non-visqueuse, calculé par une méthode intégrale, détermine la vitesse [illegible] sur les parois. Les deux problèmes, résolus par des méthodes implicites, sont [illegible] "fort", garantie de validité du modèle visqueux et de régularité des solutions [illegible], ce couplage n'a toutefois été traité numériquement que sur des configurations [illegible] notamment aux profils avec gouverne.

INTRODUCTION OF UNSTEADY BOUNDARY LAYER EFFECTS
IN TWO-DIMENSIONAL TRANSONIC CALCULATION

SUMMARY

A computation of viscous unsteady flows over wing profiles is researched using two methods elaborated at ONERA, on one hand for the inviscid flow, within a transonic small disturbance approach, on the other hand for the calculation and coupling of viscous layer, within a strong interaction analysis.

The difference between the viscous and inviscid solutions, calculated by an integral method, determines the inviscid normal velocity at the wall. The two problems, solved by implicit methods, are linked through a "strong" coupling, guarantee of validity for the viscous model and of regularity for separated flows solutions. For the time being, the coupling has been applied numerically only to non-separated flows configurations, namely for profiles with trailing edge flap.

(*) [illegible]

NOTATIONS

c	corde
h	géométrie du profil - $h\ (X,t)$
k	fréquence réduite - $k = \omega c / U$
t	temps
x, y	coordonnées du repère relatif
C_f	coefficient de frottement
C_l	coefficient de portance
C_m	coefficient de moment au quart avant
	(moment positif entraîne le bord de fuite vers le bas)
C_n	coefficient de *moment de charnière*
	(moment positif entraîne le bord de fuite vers le bas)
C_p	coefficient de pression instationnaire
K_p	coefficient de pression stationnaire
M_∞	nombre de Mach amont
R_e	nombre de Reynolds
X, Y	coordonnées du repère absolu
α	paramètre de forme
δ	épaisseur de couche limite
δ	braquage de la gouverne
	(positif si le bord de fuite est vers le bas)
δ^*	épaisseur de déplacement de couche limite
θ	*épaisseur de quantité de mouvement*
Θ	déflection induite par la couche limite : $\Theta\ (X,t)$
ρ	masse volumique
φ	phase ou potentiel de perturbation
ω	pulsation
Γ	circulation

INDICES

i	instationnaire ou incompressible
m	moyen ou stationnaire
n	*indice temporel*
δ	relatif au braquage de gouverne
1	relatif au premier harmonique
$*$	critique ou relatif à l'épaisseur de déplacement
$-$	relatif à l'écoulement visqueux
$\sim$	variable intermédiaire

I. INTRODUCTION

Les méthodes de calcul linéaires sont le support essentiel de la prédiction des écoulements instationnaires pour les aéroélasticiens. Toutefois, ces méthodes ne sont pas applicables dans le domaine transsonique où l'on observe d'importantes non-linéarités introduites par la présence d'ondes de choc. Ces dernières années, diverses méthodes ont été proposées pour calculer les écoulements tridimensionnels de fluide parfait en transsonique. Ces méthodes de résolution s'appuient, soit sur l'équation des petites perturbations transsoniques [1,2,3,4], soit sur les équations d'Euler [5,6]. Ces dernières nécessitent des temps de calcul importants ce qui limite fortement leurs possibilités d'application bien qu'en principe elles soient plus rigoureuses.

Au vu de confrontations avec l'expérience, on remarque que l'hypothèse qui consiste à négliger les effets de la viscosité pour ne considérer que le fluide parfait introduit, particulièrement en régime transsonique, des erreurs importantes. Ainsi la position de l'onde de choc et son intensité sont étroitement liées aux caractéristiques de la couche limite. Un calcul en fluide visqueux des écoulements instationnaires doit dès lors être recherché.

Une première approche consiste à adjoindre au calcul en fluide parfait un calcul de couche limite et à assurer entre eux un couplage partiel, qualifié de couplage faible, c'est-à-dire ne respectant pas totalement la réciprocité des influences visqueuses et non-visqueuses. Cette approche, cohérente avec la théorie de la couche limite classique et les régimes de faible interaction visqueuse, conduit à une simplification numérique majeure en raison du découplage partiel des deux calculs. En instationnaire, des améliorations notables ont déjà été apportées de cette façon [7] aux calculs en fluide parfait.

Néanmoins, en stationnaire ou en instationnaire, ce type d'approche contient en lui-même d'importantes limitations, qui ont été détaillées par ailleurs [8,9,10,11,12,13]. Rappelons ici seulement :

(i) la restitution imparfaite et parfois inconsistante des domaines d'influence du fluide visqueux inhérente au couplage faible, notamment pour les intéractions visqueuses en supersonique ou transsonique aux pieds des ondes de choc, ainsi que pour les problèmes de décollement ou de bord de fuite.

(ii) la présence possible de singularités irréalistes dans les solutions de couche limite, généralement en liaison avec l'apparition de courants de retour. Bien que de natures différentes en stationnaire et en instationnaire, ces singularités sont artificielles, n'indiquent pas une limite de validité des approximations de couche mince, même au niveau le plus restrictif des équations de Prandtl, mais traduisent avant tout la nécessité d'un calcul de forte intéraction visqueuse.
Ces singularités peuvent notamment être éliminées [9,12] par des méthodes de résolution inverses, ou encore par un couplage rigoureux au fluide parfait, qualifié de couplage fort.

Les limitation précédentes imposant le développement de calculs de forte interaction visqueuse, deux grandes voies d'analyse sont possibles [8]. La première consiste en une approche globale, résolvant un système d'équations unique valable dans tout le champ d'écoulement (équations de Navier-Stokes complètes ou tronquées). Nous nous intéressons ici à la seconde possibilité, l'approche par couplage fort, dans laquelle un calcul en fluide parfait peut être maintenu, grâce à la résolution séparée mais couplée d'un problème visqueux complémentaire, qui généralise le concept de couche limite, et qui détermine en pratique les conditions aux limites du fluide parfait.

Nous considérons en outre ici un couplage fort dans lequel des approximations de type couche mince, attachées ou décollées, peuvent être valablement invoquées pour le problème visqueux. A ce niveau d'approximation, Le Balleur a montré [8,9,11] qu'une formulation déficitaire pour recomposer la solution visqueuse réelle, à partir des deux calculs couplés visqueux et non-visqueux constitutifs, permet non seulement d'éviter les limitations des méthodes de couplage faible, mais encore celles des méthodes classiques de couplage fort, dans lesquelles sont mises en jeu des équations de Prandtl, ainsi qu'un couplage par raccordement sur une frontière externe ou encore par addition d'une épaisseur de déplacement. La formulation déficitaire du couplage adoptée ici suppose en pratique le recouvrement des domaines de calculs visqueux et non-visqueux, le rôle du calcul visqueux se bornant à évaluer, dans les régions de couches limites, l'écart qui existe entre la solution de fluide parfait calculée, et la solution visqueuse réelle. Cette analyse [8,11] apporte d'une part la commodité numérique d'un domaine de calcul du fluide parfait s'appuyant sur les parois, et surtout d'autre part la prise en compte, au moins approximative, des gradients de pression normaux internes aux couches visqueuses.

[illegible] parfait, le souci de limiter le coût des calculs a conduit à adopter une [illegible] visqueux. Dès lors, moyennant un choix approprié des équations de [illegible] déficitaire ne conduit pas à des équations intégrales visqueuses [illegible] couplage faible, mais exige par contre la réalisation numérique [illegible] parfait, ainsi que la définition d'une méthode intégrale calculant [illegible]

[illegible] [8,10,11] ont été réalisant ce couplage fort, avec un [illegible] calculs ont pu être proposés notamment dans le cas où le [illegible] de relaxation pour l'équation des petites perturbations trans-[illegible]

[illegible] du problème du couplage fort [illegible] les premiers résultats de calcul [illegible] d'écoulements instationnaires, [illegible] tant en temps le couplage fort. Ces calculs s'appuient d'une part sur la méthode implicite des directions alternées résolvant l'équation du potentiel des petites perturbations transsoniques et instationnaires, développée par COUSTON, ANGELINI, MULAK [1,2]. Ils s'appuient d'autre part sur une méthode intégrale implicite de calcul des couches limites et sillages turbulents, ainsi que sur des techniques de couplage, développées par LE BALLEUR et GIRODROUX-LAVIGNE [8,9,12,13]. Présentement, bien que le calcul visqueux instationnaire puisse être poursuivi dans les zones à courants de retour grâce à une résolution de type inverse [12], le couplage fort n'a été réalisé numériquement que sur des configurations non-décollées, ainsi qu'avec un traitement simplifié du sillage visqueux. Les exemples d'application sont relatifs à des écoulements transitoires, ainsi qu'à des profils avec gouvernes oscillantes, en régimes subcritiques ou supercritiques.

II. FLUIDE PARFAIT

Equation des petites perturbations transsoniques

Les équations d'Euler instationnaires qui régissent l'écoulement de fluide parfait se ramènent à l'équation complète du potentiel des vitesses si l'écoulement est isentropique et irrotationnel. L'hypothèse de petites perturbations transsoniques et instationnaires permet de simplifier encore le problème et fournit après normalisation l'équation (1) :

$$k^2 M_\infty^2 \frac{\partial^2 \varphi}{\partial t^2} + 2k M_\infty^2 \frac{\partial^2 \varphi}{\partial x \partial t} = \frac{\partial}{\partial x}\left[(1-M_\infty^2)\frac{\partial \varphi}{\partial x} - \frac{\lambda}{2}\left(\frac{\partial \varphi}{\partial x}\right)^2 \right] + \frac{\partial^2 \varphi}{\partial y^2} \qquad (1)$$

avec

$$\lambda = \left[(\gamma+1) M_\infty^2 + 3(1-M_\infty^2) \right] M_\infty^2$$

Cette équation représente la conservation de la masse approchée au sens des petites perturbations [1]. Son caractère non-linéaire autorise, au sens des solutions faibles, le calcul d'ondes de choc, ce qui est en contradiction avec l'hypothèse d'écoulement isentropique irrotationnel. On doit donc se limiter aux écoulements transsoniques avec chocs de faible intensité si l'on recherche une bonne approximation des équations d'Euler.

Conditions aux limites sur le profil

L'équation (1) est associée à des conditions aux limites. Sur le profil, la [illegible] nelle de la condition aux limites attachée aux hypothèses de petites perturbations s'écrit :

$$\left(\frac{\partial \varphi}{\partial y}\right)_{\text{profil}} \sim \frac{\partial h}{\partial x} + k\frac{\partial h}{\partial t}$$

où h (x, t) est la fonction décrivant la géométrie du profil. On soulignera qu'au voisinage du bord d'attaque des profils une condition plus complexe est utilisée afin d'améliorer le comportement de la solution [1].

C'est à ce niveau, comme nous le justifierons plus loin, qu'intervient le couplage fluide parfait-couche limite. Le fluide parfait est prolongé jusqu'à la paroi et la couche limite intervient comme un apport de masse au travers de celle-ci. Si l'on considère que l'équation (1) est l'équation de continuité approchée au sens des petites perturbations il est clair que $\partial\varphi/\partial y$ représente un débit de masse par unité de longueur. On doit donc ajouter à (2a) le débit d'injection de la couche limite, [illegible] traduit de manière angulaire par $\Theta(x,t)$ on aura :

$$\left(\frac{\partial \varphi}{\partial y}\right)_{\text{profil}} = \frac{\partial h}{\partial x} + \Theta(x,t) + k\frac{\partial h}{\partial t} \qquad (2b)$$

C'est au travers de cette condition aux limites (2b) que s'effectuera le couplage fort entre la couche limite et le fluide parfait.

Traitement du sillage

Dans toute solution du problème à potentiel des vitesses on doit définir le saut de potentiel Γ (ou circulation) au travers d'un sillage qui se développe à l'aval du bord de fuite. Le saut de potentiel doit traduire la continuité du coefficient de pression Cp. Dans le cadre des petites perturbations transsoniques [1] on a montré que :

$$\frac{C_p}{2} + \frac{\partial \varphi}{\partial x} + k\frac{\partial \varphi}{\partial t} \simeq 0 \qquad (3)$$

on a donc :

$$k\frac{\partial \Gamma}{\partial t} + \frac{\partial \Gamma}{\partial x} = 0 \qquad (4)$$

Cette équation hyperbolique traduit le transport de la circulation de l'amont vers l'aval le long du sillage, nous la considérerons comme valable dans le cadre des approximations visqueuses actuelles. Par contre on doit tenir compte du débit d'injection (ou de fuite) lié au sillage visqueux d'une manière similaire à ce qui est fait au niveau de la condition aux limites sur le profil. Nous présenterons par la suite des calculs avec et sans prise en compte de l'effet [illegible] du sillage visqueux pour faire ressortir son importance.

Schéma numérique

La resolution de l'équation (1) est obtenue par une extension de la méthode implicite des directions alternées (A.D.I.) décrite par Ballhaus [5]. Le schema numerique utilisé a été détaillé en [1], il permet de décrire l'évolution temporelle du phenomène d'un temps $n\Delta t$ a un temps $(n+1)\Delta t$ en travaillant simultanément sur deux variables : $\varphi(t)$, le potentiel de perturbation et $Z(t) = k\frac{\partial\varphi}{\partial t}$ la dérivée temporelle de ce potentiel.

Le domaine de calcul qui permet la discretisation spatiale est cartésien. Les conditions aux limites (pour le profil et le sillage) sont écrites sur une coupure parallèle à la vitesse à l'infini.

L'organigramme de calcul qui en résulte est représenté de manière condensée en figure 1. La partie en pointillée concerne la participation du couplage visqueux qui sera décrite ultérieurement. On notera (en faisant abstraction du couplage visqueux) que le fluide parfait se décompose schématiquement en trois "pas" principaux :

- une résolution implicite sur la variable $\tilde{\varphi}$ pour toutes les lignes de maillage $Y = Cste$. Ce pas incorpore le traitement conservatif du terme non-linéaire responsable des discontinuités de vitesse, à ce stade les conditions aux limites au niveau du profil sont connues (elles n'interviennent qu'au temps $n\Delta t$).

- une résolution implicite sur la variable φ^{n+1} en direction Y (pour toutes les lignes de maillage $X = Cste$ de l'amont vers l'aval). Ce pas qui se comporte comme un correcteur prend en compte la condition au limite $\left(\frac{\partial\varphi}{\partial Y}\right)^{n+1}_{profil}$ pour corriger la variable intermédiaire $\tilde{\varphi}$.

- une réactualisation de la variable $Z = k\frac{\partial\varphi}{\partial t}$ nécessaire au calcul de l'itération suivante. Le calcul se fait point par point et ne nécessite pas de résolution matricielle.

Considérons maintenant le problème de l'itération qui engendre le couplage fort entre les deux calculs. Comme on peut le voir (fig.1), il n'est pas nécessaire d'itérer sur l'ensemble du fluide parfait mais seulement sur la résolution implicite en direction Y. En effet, la variable de couplage est Θ^{n+1}, or, elle n'intervient qu'au niveau de la condition aux limites $\left(\frac{\partial\varphi}{\partial Y}\right)^{n+1}$ définie par l'équation (2a).

Lors du pas en X seul Θ^{n} va intervenir et c'est une donnée du pas de temps précédent. Cette remarque pour importante quelle soit, car elle réduit notablement les temps de calcul, n'a aucun caractère de généralité puisqu'elle découle seulement de l'utilisation de la technique des directions alternées (A.D.I.) pour le calcul du fluide parfait.

III. CALCUL VISQUEUX ET COUPLAGE

Nous désignerons ici, par un repère cartésien curviligne, tangent à la paroi ou bien à la ligne moyenne du sillage. Soit dans ce repère u,v les composantes de la vitesse p, ρ la pression et la masse volumique pour l'écoulement non visqueux. Soit $\bar{u}$, $\bar{v}$, $\bar{p}$, $\bar{\rho}$ leurs homologues pour la solution de fluide visqueux.

Les analyses de couplage fort supposent habituellement que les équations du fluide parfait sont résolues pour $y > \delta(x,t)$, δ étant l'épaisseur physique de la couche limite, et que les équations de Prandtl sont résolues pour $y < \delta(x,t)$, de sorte que l'approximation sur la pression s'y écrit $\bar{p}(x,y,t) = \bar{p}(x,t) = p(x,\delta,t)$. Cette formulation, qui ignore totalement les gradients de pression normaux internes aux couches visqueuses, conduit de surcroît, en dépit du couplage fort, à des insuffisances majeures dans la modélisation du fluide visqueux en supersonique ou transsonique, qualifiées de comportements supercritiques des couches limites.

Nous adoptons, ici, la formulation donnée par Le Balleur [8,9], qui met à profit le prolongement du calcul en fluide parfait à l'intérieur de la couche visqueuse pour éliminer les deux limitations précédentes, et notamment les solutions faibles discontinues associées aux couches supercritiques. Cette formulation élimine, en outre, les solutions faibles indésirables des méthodes intégrales inverses de couche limite instationnaire [12]. Elle élimine, enfin, toute importance majeure au choix, relativement arbitraire, de la frontière externe des couches visqueuses $y = \delta(x,t)$.

Equations intégrales

La différence entre les équations des solutions visqueuses et non-visqueuses est intégrée selon y, avec l'hypothèse d'un raccordement des solutions lorsque , $\longrightarrow \infty$. Les approximations de couche mince portent d'une part sur l'élimination des termes visqueux autres que celui des équations de Prandtl, et d'autre part sur l'hypothèse que le champ de pression visqueux $\bar{p}(x\ y\ t)$, bidimensionnel en espace, s'identifie en première approximation au champ de pression non visqueux $p(x\ y\ t)$. On obtient alors [8, 11, 13] :

Continuité :

$$\frac{1}{u}\left[\frac{\partial\hat{\delta}}{\partial t}+\frac{\hat{\delta}}{\rho}\frac{\partial\rho}{\partial t}\right]+\left[\frac{\partial\delta^{*}}{\partial x}+\frac{\delta^{*}}{\rho u}\frac{\partial\rho u}{\partial x}\right]=\frac{\rho v}{\rho u}=\Theta(x,0,t)$$

Quantité de mouvement selon x :

$$\frac{1}{u}\left[\frac{\partial(\delta^{*}-\hat{\delta})}{\partial t}-\frac{\hat{\delta}}{\rho}\frac{\partial\rho}{\partial t}+\frac{\delta^{*}}{\rho_u}\frac{\partial\rho u}{\partial t}\right]+\left[\frac{\partial\theta}{\partial x}+\frac{\delta^{*}+2\theta}{u}\frac{\partial u}{\partial x}+\frac{\theta}{\rho}\frac{\partial\rho}{\partial x}\right]=\frac{\overline{C_f}}{2}+\frac{\hat{\delta}}{u^{2}}\gamma_e$$

Entraînement :

$$\frac{1}{u}\left[\frac{\partial(\delta-\hat{\delta})}{\partial t}+\frac{\delta-\hat{\delta}}{\rho}\frac{\partial\rho}{\partial t}\right]+\left[\frac{\partial(\delta-\delta^{*})}{\partial x}+\frac{\delta-\delta^{*}}{\rho u}\frac{\partial\rho u}{\partial x}\right]=E$$

avec :

$$\delta^{*}(x,t)\left[\rho u\right]_{(x,0,t)}=\int_0^{\infty}\left[\rho u-\bar{\rho}\bar{u}\right]_{(x,y,t)}dy$$

$$\left[\delta^{*}(x,t)+\theta(x,t)\right]\left[\rho u^{2}\right]_{(x,0,t)}=\int_0^{\infty}\left[\rho u^{2}-\bar{\rho}\bar{u}^{2}\right]_{(x,y,t)}dy$$

$$\delta_i^{*}(x,t)\cdot u(x,0,t)=\int_0^{\infty}\left[u-\bar{u}\right]_{(x,y,t)}dy$$

$$\theta_i(x,t)\cdot u^{2}(x,0,t)=\int_0^{\infty}\left[u^{2}-\bar{u}^{2}\right]_{(x,y,t)}dy$$

$$\hat{\delta}(x,t)\ \rho(x,0,t)=\int_0^{\infty}\left[\rho-\bar{\rho}\right]_{(x,y,t)}dy$$

$$E(x,t)=\frac{1}{\rho u}\left[\frac{\partial\tau/\partial y}{\partial(u-\bar{u})/\partial y}\right](x,\delta,t)$$

$$H_i(x,t)=\frac{\delta_i^{*}}{\theta_i}$$

$$\overline{C_f}(x,t)=\left[\frac{2\tau}{\rho u^{2}}\right](x,0,t)$$

$$C_f(x,t)=\frac{2}{\rho_\infty u_\infty^{2}}\cdot\tau(x,0,t)$$

Dans ces équations intégrales, les grandeurs non-visqueuses ρ, u, v et leurs dérivées partielles sont relevées en $(x, 0, t)$. Par ailleurs apparaissent des termes liés à l'accélération d'entraînement γ_e, en raison du fait que les équations sont écrites dans le repère xOy, mobile par rapport au repère XOY du fluide parfait.

La formulation déficitaire [8,11] des équations visqueuses apparaît dans la définition des épaisseurs intégrales, qui prend en compte les variations selon y de $\rho(x.y.t)$ et $u(x.y.t)$ dans la solution de fluide parfait, et par voie de conséquence de $p(x.y.t)$. Les approximations du calcul autres que $\bar{p}(x.y.t) \simeq p(x.y.t)$ sont ainsi éliminées des équations de continuité et de mouvement. Ces approximations consistent en une modélisation de relations de fermeture liant les épaisseurs autres que δ^{*} et θ, ainsi que les termes visqueux C_f et E, modélisation issue d'une famille de profils de vitesses $\bar{u}/u$ représentative des couches limites attachées ou décollées, en stationnaire comme en instationnaire [9,12]. Dans cette modélisation, les profils $\bar{\rho}/\rho$ sont déduits de $\bar{u}/u$ moyennant l'hypothèse, admissible en écoulement turbulent adiabatique, d'une identité des enthalpies totales visqueuse et non-visqueuse.

Si on suppose par exemple que $\rho(x.0.t)$ et $u(x.0.t)$ sont donnés par le calcul de fluide parfait potentiel, la condition aux limites $v(x.0.t)$, ainsi que deux épaisseurs visqueuses indépendantes $\delta^{*}(x.t)$ et $\theta(x.t)$, sont calculées au moyen des équations intégrales de continuité, de mouvement et d'une équation de moment (entraînement ou énergie cinétique). Le choix de l'équation de moment, ici de l'équation d'entraînement est relativement indifférent dans l'hypothèse de Prandtl $\frac{\partial\bar{p}}{\partial y}=0$. Il devient par contre important [8,11,13] en cas de gradient normal $\frac{\partial\bar{p}}{\partial y}$ intense.

Pour un écoulement de fluide parfait potentiel stationnaire, la continuité de la pression $p(x\ 0)$ sur la ligne de sillage entraîne la continuité de la vitesse $u(x.0)$ et de la masse volumique $\rho(x\ 0)$. Dans ces conditions, on peut montrer que les équations intégrales du sillage sont formellement identiques aux équations de couche limite, à condition de remplacer $v(x.0)$ par $\langle v(x\ 0)\rangle$, la discontinuité de vitesse normale qui traduit dans le fluide parfait l'effet de déplacement visqueux.

Les épaisseurs visqueuses mises en jeu sont alors celles définies pour un sillage, par intégration selon y entre $-\infty$ et $+\infty$. Le terme de frottement C_f disparaît. Les relations de fermeture doivent être issues de profils $\frac{\overline{u}}{u}$ de sillage, mais elles sont identiques pour un sillage symétrique ou dissymétrique.

En première approximation, ces équations ont aussi été présentement retenues en instationnaire moyennant l'hypothèse, convenant aux basses fréquences, que la continuité de la pression $p(x.0.t)$ qui implique toujours la continuité de $\rho(x.0.t)$, conduit à une discontinuité de vitesse $<u(x.0.t)>$ relativement négligeable.

Dans le mode de résolution direct, à $\rho(x.0.t)$ et $u(x.0.t)$ donnés, les équations visqueuses, découplées du fluide parfait, forment un système hyperbolique, calculable d'amont en aval en l'absence de courants de retour, constituant un problème aux limites en x en présence de courants de retour [9].
Dans le mode de résolution inverse à $v/u(x.0.t)$ donné, le système hyperbolique des équations visqueuses découplées peut par contre être résolu d'amont en aval dans tous les cas [12].

Discrétisation numérique du système d'équations visqueuses

D'un point de vue pratique, les équations de couche limite sont écrites en choisissant comme variables de calcul :
- l'épaisseur de couche limite δ
- le paramètre de forme $\alpha = \delta_i^*/\delta$
- l'angle d'inclinaison du vecteur vitesse par rapport à la paroi Θ

Dans ces conditions le système visqueux peut s'écrire sous la forme :

$$\frac{1}{u} C_{ij} \begin{bmatrix} \frac{\partial \delta}{\partial t} \\ \delta \frac{\partial \alpha}{\partial t} \\ \Theta \end{bmatrix} + A_{ij} \begin{bmatrix} \frac{\partial \delta}{\partial x} \\ \delta \frac{\partial \alpha}{\partial x} \\ \Theta \end{bmatrix} = B_i + \frac{1}{u} D_{im} \begin{bmatrix} \frac{\partial \rho}{\partial t} \\ \frac{\partial u}{\partial t} \end{bmatrix} + E_{im} \begin{bmatrix} \frac{\partial \rho}{\partial x} \\ \frac{\partial u}{\partial x} \end{bmatrix}$$

$$i = 1.2.3 \qquad j = 1.2.3 \qquad m = 1.2$$

où les termes C_{ij}, A_{ij}, B_i, D_{im} et E_{im} sont calculés à partir des grandeurs du fluide parfait et des relations intégrales de fermeture du système de couche limite.

La discrétisation s'effectue dans le plan $(t.x)$ en utilisant un schéma implicite en $(n+1.i)$ du 1er ou du 2ème ordre en x, et du 1er ordre en temps. Dans le cas du schéma du 1er ordre, on écrit par exemple pour δ :

$$\delta_i^{n+1} = \delta_{i-1}^{n+1} + \Delta x \left(\frac{\partial \delta}{\partial x}\right)_i^{n+1} = \delta_i^n + \Delta t \left(\frac{\partial \delta}{\partial t}\right)_i^{n+1}$$

d'où :

$$\left(\frac{\partial \delta}{\partial t}\right)_i^{n+1} = \frac{\Delta x}{\Delta t} \left(\frac{\partial \delta}{\partial x}\right)_i^{n+1} + \frac{\delta_{i-1}^{n+1} - \delta_i^n}{\Delta t}$$

Pour le schéma du 2ème ordre, nous avons :

$$\delta_i^{n+1} = \delta_{i-1}^{n+1} + \frac{\Delta x}{2} \left[\left(\frac{\partial \delta}{\partial x}\right)_{i-1}^{n+1} + \left(\frac{\partial \delta}{\partial x}\right)_i^{n+1} \right] = \delta_i^n + \Delta t \left(\frac{\partial \delta}{\partial t}\right)_i^{n+1}$$

d'où :

$$\left(\frac{\partial \delta}{\partial t}\right)_i^{n+1} = \frac{\Delta x}{2\Delta t} \left(\frac{\partial \delta}{\partial x}\right)_i^{n+1} + \frac{\delta_{i-1}^{n+1} - \delta_i^n}{\Delta t} + \frac{\Delta x}{2\Delta t} \left(\frac{\partial \delta}{\partial x}\right)_{i-1}^{n+1}$$

On obtient des formules identiques pour $\partial\alpha / \partial t$. Le schéma du 1er ordre en x est préféré dans les zones à maillage grossier, pour sa plus grande stabilité. Si nous rejetons alors au 2ème membre tous les termes connus aux noeuds $(n+1, i-1)$ et (n, i) , le système local s'écrit au noeud $(n+1, i)$ sous la forme condensée :

$$A^*_{ij} \begin{bmatrix} \dfrac{\partial\delta}{\partial x} \\ \delta \dfrac{\partial\alpha}{\partial x} \\ \Theta \end{bmatrix} = B^*_i$$

La résolution, en chaque noeud du maillage de ce système permet, après intégration locale des dérivées $\frac{\partial\delta}{\partial x}$ et $\frac{\partial\alpha}{\partial x}$, de connaître les distributions $\delta(x), \alpha(x)$ à l'instant t^{n+1} ainsi que l'évaluation visqueuse $\tilde{\Theta}(x)$ à l'instant t^{n+1} . Une itération par une méthode de Newton résout de façon implicite les termes non-linéaires contenus dans A^*_{ij} et B^*_i

Méthode numérique en couplage (forte interaction)

Le couplage s'effectue, à un pas de temps fixé, de façon itérative. Un calcul de fluide parfait fournit à l'instant t^n la distribution $u(x, t^n)$ et $\rho(x, t^n)$ à la paroi, le calcul itératif s'effectuant sur la déflection $\Theta(x, t^n)$ selon le schéma de la figure 2

Il faut cependant noter qu'il ne suffit pas en général d'itérer pour atteindre la convergence, l'erreur $\tilde{\Theta} - \Theta$ en chaque point x pouvant très bien osciller sans jamais converger, et même tendre vers l'infini. Le comportement du calcul itératif couplé dépend à la fois des caractéristiques de l'écoulement calculé, ainsi que des pas de temps et d'espace Δt et Δx utilisés dans la méthode numérique. La figure 3 nous montre que, même pour une plaque plane sans incidence, un calcul convergent peut diverger si on augmente le pas de temps ou si l'on diminue le pas d'espace. La résolution du couplage fort par une simple itération de point fixe nécessite donc pour le moins d'introduire une sous relaxation afin d'assurer la stabilité du schéma itératif.

Cette constatation est en tout point analogue au problème du couplage itératif en stationnaire. Pour l'instant, il n'a pas encore été possible de définir une sous relaxation optimale, automatique, comme en stationnaire, et le coefficient de sous relaxation est estimé par tâtonnements.

IV . RESULTATS NUMERIQUES

Cas stationnaires

NACA 64A006 - $M_\infty = 0.50$ $\delta_m = 2°$

La figure 4 présente pour un cas stationnaire et subcritique le saut de pression normalisé pour un braquage moyen de la gouverne $\delta_m = 2°$. On compare ici les résultats obtenus avec et sans couplage visqueux à un calcul de plaque plane. A l'amont de la charnière les effets liés à l'épaisseur du profil se traduisent par un accroissement de la portance, ces effets sont partiellement compensés par les effets visqueux. Par contre sur la gouverne les effets d'épaisseur sont faibles alors que les effets visqueux introduisent une sensible diminution de la portance. On retrouve cet abattement en considérant le moment de charnière qui diminue d'environ 20 % par effet visqueux. Cette dernière remarque ainsi que le comportement du ΔK_p au bord de fuite correspond qualitativement aux résultats expérimentaux obtenus par Tijdeman [14,15]. Toutefois une comparaison directe à ces essais ne nous semble pas significative car les effets de parois sont importants (la hauteur de veine dans la soufflerie n'est que d'environ [illegible]).

Il faut souligner que ce calcul ne tient pas compte de l'évolution visqueuse dans le sillage et que ces résultats ont été obtenus avec un maillage de 4000 points dont 110 sur le profil. Le temps de calcul nécessaire pour générer à partir du transitoire le champ de pression stationnaire équivaut dans ce cas à [illegible] 7600 pour le calcul couplé. Le même champ stationnaire en fluide parfait ne demande qu'environ [illegible] de CDC 7600. Une sensible amélioration des temps de calcul est concevable en recherchant une optimisation au niveau du couplage par une approche similaire à celle présentée en réf [10]. A l'heure actuelle aucune tentative d'optimisation n'a été faite pour diminuer les temps de calcul, l'intérêt premier de cette étude étant de démontrer ce que l'on peut attendre d'un calcul avec couplage fort.

NACA 64A006 - $M_\infty = 0.875$ $\alpha_m = 0°$ $\delta_m = 0°$

Les figures 5 et 6 permettent de comparer les calculs visqueux et non-visqueux, ainsi que les essais effectués par TIJDEMAN [15]. La prise en compte de la couche limite entraîne un meilleur positionnement du choc, ainsi qu'une diminution de son intensité due, à la fois à une baisse du niveau de K_p en amont [illegible] et à une remontée du niveau aval.

Les deux figures ne se distinguent que par le maillage utilisé sur le profil, 60 points pour la figure 5, 110 points pour la figure 6. Un raffinement du maillage n'introduit pas de changements notables sur les résultats : cette conclusion ne saurait cependant être généralisée sans expériences numériques complémentaires dans la mesure où les paramètres de forme de couche limite sont ici modérés et que les non-linéarités visqueuses apparaissant aux voisinages des décollements ne sont donc pas pleinement mises en jeu. On peut cependant noter, pour le calcul visqueux, un bon comportement au niveau du choc, celui-ci se rapprochant des points expérimentaux ; par contre, on observe des valeurs de K_p légèrement supérieures juste en amont du choc, aussi bien pour le calcul couplé que pour le calcul fluide parfait.

L'influence de la prise en compte du sillage dans le calcul couplé est mise en évidence sur la figure 7, et se caractérise principalement par un recul de la position du choc, les K_p après choc au voisinage du bord de fuite remontant au niveau des points expérimentaux.

Il ne faut pas ici accorder une trop grande importance à la comparaison des calculs, effectués en atmosphère illimitée, avec les résultats expérimentaux obtenus en soufflerie, avec des parois poreuses situées à 3 cordes du profil. Les effets de parois qui sont ici négligés dans les calculs, expliquent probablement le positionnement trop arrière du choc.

Les distributions sur le profil du frottement C_f , de l'épaisseur de déplacement δ^* et de l'épaisseur de quantité de mouvement θ (figure 8) nous montrent, d'une part une variation rapide de ces paramètres au niveau du choc, et d'autre part que ces distributions dépendent peu du maillage utilisé. Avant de généraliser cette remarque il serait toutefois souhaitable de faire des calculs couplés sur des couches limites plus fortement déstabilisées.

Cas instationnaires

NACA 64A006 $M_\infty = .854$ - $k = .358$ - $\delta_i = 1°$

Les figures 9 à 12 présentent les pressions instationnaires mesurées et calculées pour un cas avec zone supersonique et onde de choc. Les calculs sont comparés aux essais de Tijdeman [14,15] aux figures 9 et 10 sous la forme du premier harmonique du coefficient de pression normalisé par l'amplitude du débattement de la gouverne (ici $\delta_i = 1°$). Ici encore la comparaison aux essais est difficile car les effets de parois sont non-négligeables comme l'ont montré à partir de corrections semi-expérimentales les calculs de Magnus [16].

On remarquera toutefois que le calcul en fluide parfait, figure 9, diffère des essais par l'intensité des C_p instationnaires dans la région traversée par le choc. La prise en compte des phénomènes visqueux sur le profil diminue sensiblement l'intensité du pic et de plus le déplace vers l'amont, figure 10. Ceci s'explique facilement à partir des pressions instantanées présentées en figure 11. En effet, tout comme en stationnaire, la présence de la couche limite déplace sensiblement l'onde de choc et diminue son saut de pression. Toutefois les pressions instationnaires restent trop importantes au droit du choc, ce qui implique que l'onde de choc est de trop forte intensité. Afin de vérifier si cette différence ne provient pas du sillage visqueux, celui-ci a été introduit dans le code de calcul avec les hypothèses simplificatrices indiquées plus haut probablement peu restrictives, au moins pour les faibles fréquences réduites. La figure 12 présente la comparaison des calculs visqueux avec et sans prise en compte du sillage. On remarque que la prise en compte du sillage n'apporte pas une modification importante des pressions instationnaires aussi bien en module qu'en phase. Tout au plus on note que le choc se déplace vers l'aval : la zone supersonique est donc plus importante ce qui modifie les phases sur la partie amont du profil et entraîne une légère augmentation des modules au niveau du choc. Ces différences sont attribuables à la modification du champ stationnaire moyen et ne sont probablement pas une conséquence de l'évolution instationnaire du sillage.

Le comportement de la phase à proximité du bord de fuite est plus régulier si l'on tient compte du sillage visqueux comme on le présente figure 12. Toutefois cette différence ne peut pas entraîner une modification importante des coefficients de portance et de moments car les modules des pressions instationnaires sont faibles à proximité du bord de fuite. Les différences qui subsistent entre les essais de Tijdeman [14,15] et le calcul (Fig.10) sont donc probablement imputables aux effets de parois. Un bon accord théorie-expérience passerait donc ici par la prise en compte simultanée des parois (avec leur perforation) et des effets visqueux. Malheureusement s'il est possible, comme le montre Magnus [16], de simuler des parois à fentes, on doit s'appuyer sur des coefficients expérimentaux , coefficients que l'on est loin de maîtriser en instationnaire.

La comparaison des coefficients globaux de portance et de moments entre le fluide parfait et le fluide visqueux permet de faire ressortir l'importance de la viscosité :

NACA 64 A006 $M_\infty = .854$ $k = .358$ $\delta_i = 1°$	$C_{l\delta}$		$C_{m\delta}$		$C_{n\delta}$	
	Module	Phase	Module	Phase	Module	Phase
Fluide Parfait	3.57	- 42°	1.73	164°	.0815	- 157°
Fluide visqueux sans sillage $Re = 2.49\ 10^6$	3.16	- 40°	1.40	168°	.0489	- 156°
Fluide visqueux avec sillage $Re = 2.49\ 10^6$	3.23	- 40°	1.45	165°	.0570	- 158°

Ce tableau montre clairement (ce qui recoupe des observations précédentes, ref.1) que si la phase des coefficients globaux est peu affectée par les effets visqueux les modules sont sensiblement différents. Par exemple on observe de 30 à 40 % de réduction sur le module du moment de charnière $C_{n\delta}$, correction non négligeable si l'on envisage une application au contrôle actif généralisé (C.A.G. ou C.C.V.). On peut également indiquer que l'on se trouve ici en présence d'une couche limite relativement peut chargée. En effet, les paramètres de forme que l'on présentera plus loin sont encore assez différents de ceux d'une couche limite fortement destabilisée. Dans le cas de profils plus chargés, comme les profils supercritiques, on doit donc s'attendre à des effets visqueux sensiblement plus importants. Il n'est pas exclu d'ailleurs que dans des cas plus sévères (en présence de décollements) les phases soient également très affectées par les effets visqueux. De plus, si le décollement s'étend au delà du bord de fuite on ne pourra pas ignorer les effets visqueux dans le sillage. En effet, le comportement de la zone décollée à l'aval du profil doit alors jouer un rôle très important dans la détermination du champ des pressions aussi bien stationnaires qu'instationnaires.

Considérons maintenant plus particulièrement, l'évolution des paramètres de couche limite. Dans les régions où les effets non-linéaires sont faibles, on constate que les grandeurs de couche limite varient, en une abscisse donnée, de façon sinusoïdale en fonction du temps, mais avec, d'une part, un déphasage, fonction de l'abscisse, par rapport au mouvement de gouverne et d'autre part, un déphasage entre les grandeurs visqueuses elles-mêmes. Ceci est illustré par la figure 13, où nous avons tracé l'évolution sur une période du paramètre de forme H_i et de l'épaisseur de déplacement δ^*, au bord de fuite. Par contre, cette même figure nous fait constater que l'évolution de H_i et δ^*, dans la région où se déplace le choc, n'est plus sinusoïdale. Ceci est probablement une conséquence des phénomènes non-linéaires dans cette région comportant notamment l'apparition et la disparition du choc à l'abscisse considérée. La comparaison des figures 11 et 13 montre que H_i et δ^* augmentent au fur et à mesure que le choc se déplace vers l'amont, en se rapprochant du point considéré, passent par un maximum quand le choc atteint ce point, puis décroissent au fur et à mesure que le choc s'eloigne vers l'amont et disparaît.

Les distributions $H_i(x)$ à différents instants sont représentées sur la figure 14. Une comparaison avec les C_p instantanés (figure 11) met en évidence la variation rapide de H_i au droit du choc (d'autant plus rapide que l'intensité du choc est élevée) et une variation beaucoup plus lente et regulière en l'absence de choc ($\omega t = 180°$). On retrouve également sur ces courbes le déphasage dépendant de l'abscisse dans l'évolution de H_i sur une période du mouvement de gouverne.

CONCLUSIONS

L'objectif de cette étude était d'étudier les possibilités offertes en fluide visqueux instationnaire par une méthode de couplage fort dans laquelle le calcul visqueux est realisé par une méthode intégrale implicite, et le calcul du fluide parfait par une méthode implicite (de directions alternées) pour la résolution de l'equation des petites perturbations transsoniques et instationnaires.

Les conclusions peuvent être présentées sous la forme des remarques suivantes :

- le problème numérique lié au respect du couplage fort a pu être resolu par itérations sur les calculs visqueux et non-visqueux, à chaque pas de temps, à condition d'introduire une sous-relaxation stabilisatrice, fonction notamment du pas de temps et du pas d'espace. Pour l'instant aucune optimisation de cette relaxation n'a été entreprise, ce qui penalise les temps de calcul, penalité qui ne pourra être reduite que par une analyse théorique du couplage au niveau local.

- Le calcul couplé a permis de générer les champs des pressions stationnaires (comme limite d'un transitoire) et instationnaires sur un profil NACA 64A006 équipé d'une gouverne oscillante en subsonique et transsonique.

- La comparaison de ces calculs avec le *fluide parfait a permis* de mettre en évidence l'importance des effets visqueux sur le profil et dans le sillage. En régime transsonique la position de l'onde de choc et son intensité semblent très sensibles à la prise en compte des effets visqueux.

- La prise en compte des effets visqueux va bien dans le sens d'un meilleur accord avec les essais. Cette amélioration toute qualitative souligne le besoin d'essais exempts d'effet de parois ou pour le moins d'essais entre parois pleines qu'il serait donc possible de traiter de manière rigoureuse dans le calcul.

- La prise en compte des effets visqueux réduit notablement les modules des pressions instationnaires dans la région balayée par le choc, ce qui est en bon accord avec les observations expérimentales.

- La prise en compte des effets visqueux est tout particulièrement sensible sur le module du coefficient de charnière bien que celui-ci dans le cas considéré ne soit pas sous l'action directe du choc.

- Dans les cas considérés on a pu montrer que le calcul couplé semble peu sensible au maillage. Des calculs complémentaires sont toutefois souhaitables pour vérifier si cette conclusion reste valable à l'approche du décollement ou pour des intéractions onde de choc-couche limite plus sévères.

- Les possibilités d'étendre le couplage fort par utilisation d'une méthode inverse ou semi-inverse doivent être étudiées afin de pouvoir traiter des écoulements avec décollements.

REFERENCES

[1] - COUSTON M., ANGELINI J.J. et MULAK P, Application de l'équation des petites perturbations transsoniques aux calculs d'écoulements bidimensionnels instationnaires. Rech. Aérosp.No 1979-5 (1979), p. 325-340.

[2] - COUSTON M. and ANGELINI J.J. - Solution of nonsteady two-dimensional transonic small disturbances potential flow equation. Communication au Symposium sur la dynamique des fluides instationnaires, ASME-San Francisco 10-15 Décembre 1978 et ASME Journal of fluids engineering Vol. 101, N°3, 1979, pp. 341-347.

[3] - BALLHAUS W.F. and GOORJIAN P.M. - Implicit finite-difference computations of unsteady transonic flows about airfoils. - AIAA Journal, 15, 12, (1977) or AIAA Paper 77-205, (January 1977).

[4] - CARADONNA F.X. and ISOM M.P. - Numerical calculation of unsteady transonic potential flow over helicopter rotor blades. AIAA Journal, 14, 4, (1975).

[5] - MAGNUS R. and YOSHIHARA H. - Calculations of transonic flow over an oscillating airfoil. AIAA Paper 79-98, (January 1975).

[6] - LERAT A. et SIDES J. - Calcul numérique d'écoulements transsoniques instationnaires. - AGARD - CP-226, (Avril 1977).

[7] - GRENON R., DESOPPER A. et SIDES J. - Effets instationnaires d'une gouverne en écoulement bidimensionnel subsonique et transsonique. AGARD CP-262, (Mai 1979).

[8] - LE BALLEUR J.C., PEYRET R , VIVIAND H. - *Numerical studies in high Reynolds number aerodynamics* - Computers and fluids, Vol. 8, N° 1, pp. 1-30 (March 1980).

[9] - LE BALLEUR J.C. - Couplage visqueux-non visqueux : Analyse du problème incluant décollements et ondes de choc. - Rech. Aéros p. N° 1977 - 6, p 349.358

[10] - LE BALLEUR J.C. - Couplage visqueux-non visqueux : Méthode numérique et applications aux écoulements bidimensionnels transsoniques et supersoniques, Rech. Aerosp. N° 1978-2, p. 65-76.

[11] - LE BALLEUR J.C. et VIVIAND.H. - Methode de calcul des ecoulements decolles bidimensionnels aux grands nombres de Reynolds. Communication présentée au XVI ème colloque d'Aerodynamique appliquée (AAAF), Lille, 13-15 Novembre 1979 TP.ONERA 1979 - 145.

[12] - COUSTEIX J, LE BALLEUR J.C et HOUDEVILLE R. - Calcul des couches limites turbulentes instationnaires en mode direct ou inverse , ecoulements de retour inclus - analyse des singularités. La Recherche Aérospatiale, année 1980, N°3 (Mai-Juin) , p. 147-157.

[13] - LE BALLEUR J.C -Interaction et couplage entre ecoulement de fluide parfait et ecoulement visqueux Document interieurs ONERA (1978).

[14] - TIJDEMAN H. - Investigation of the transonic flow around oscillating airfoils NLR Thesis, [illegible] 1977.

[15] - TIJDEMAN H. and SCHIPPERS P. - [illegible] pressure measurements on an airfoil with oscillating flap in two-dimensional high subsonic and transonic flow, Report NLR-TR [illegible]

[16] - MAGNUS R. - Calculations [illegible] unsteady transonic flows about the NACA [illegible] airfoils, Report AFFDL-TR-[illegible], (July [illegible]).

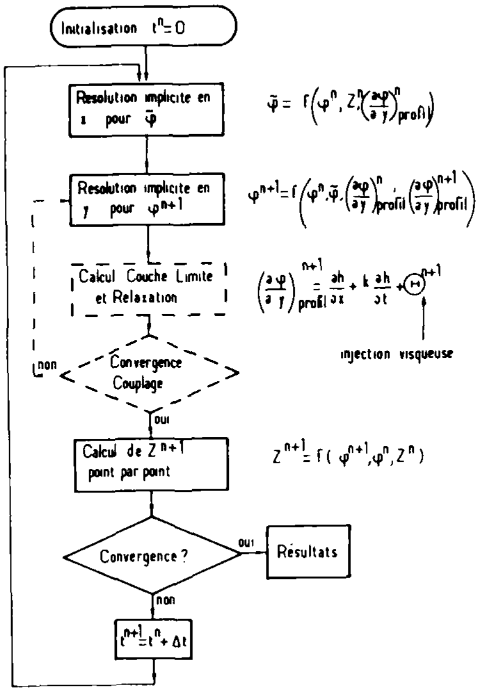
Initialisation $t^n=0$
Resolution implicite en x pour $\tilde{\varphi}$
$\tilde{\varphi}=f\left(\varphi^n, Z^n\left(\frac{\partial\varphi}{\partial y}\right)^n_{profil}\right)$
Resolution implicite en y pour φ^{n+1}
$\varphi^{n+1}=f\left(\varphi^n,\tilde{\varphi},\left(\frac{\partial\varphi}{\partial y}\right)^n_{profil},\left(\frac{\partial\varphi}{\partial y}\right)^{n+1}_{profil}\right)$
Calcul Couche Limite et Relaxation
$\left(\frac{\partial\varphi}{\partial y}\right)^{n+1}_{profil}=\frac{\partial h}{\partial x}+k\frac{\partial h}{\partial t}+Ⓗ^{n+1}$
injection visqueuse
Convergence Couplage
non
oui
Calcul de Z^{n+1} point par point
$Z^{n+1}=f(\varphi^{n+1},\varphi^n,Z^n)$
Convergence ?
oui
Résultats
non
$t^{n+1}=t^n+\Delta t$

Fig. 1 : Organigramme de résolution

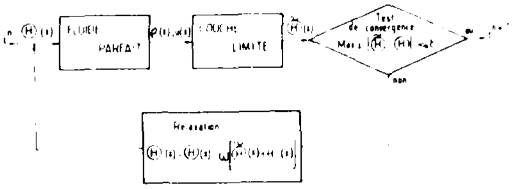
t^n
Ⓗ(x)
FLUIDE PARFAIT
$\varphi(x),w(x)$
COUCHE LIMITE
$\tilde{Ⓗ}(x)$
Test de convergence
Max $|\tilde{Ⓗ}-Ⓗ|<\varepsilon$
oui
t^{n+1}
non
Relaxation
$Ⓗ(x)=Ⓗ(x)+\omega[\tilde{Ⓗ}(x)-Ⓗ(x)]$

Fig. 2 : Organigramme de résolution au couplage

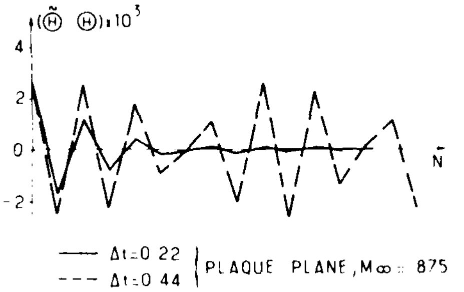

a) INFLUENCE DU PAS DE TEMPS SUR LA STABILITE

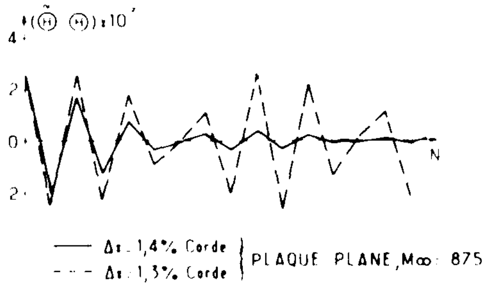

b) INFLUENCE DU PAS D'ESPACE SUR LA STABILITE

Fig. 3 : Erreur de couplage au bord de fuite en fonction des itérations de couplage N, à t fixé.

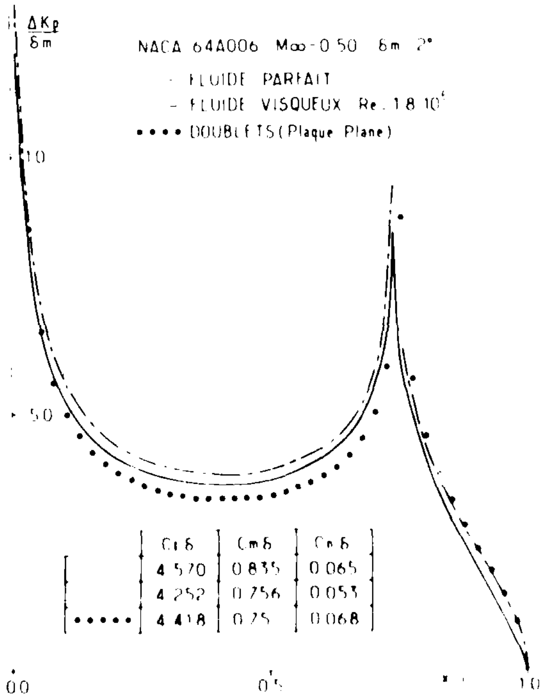

	Cl δ	Cm δ	Cn δ
	4.570	0.835	0.065
	4.252	0.756	0.053
•••••	4.418	0.75	0.068

Fig. 4 : Champs de pressions stationnaires normalisés.

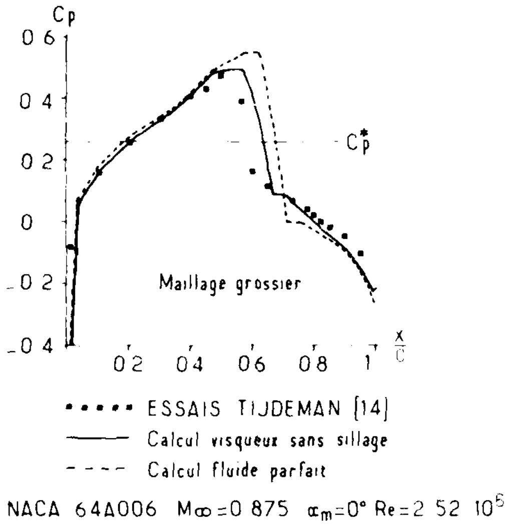

Fig. 5 : Comparaison des pressions stationnaires calculées avec un maillage grossier aux mesures.

Fig. 6 : Comparaison des pressions stationnaires calculées avec un maillage fin aux mesures.

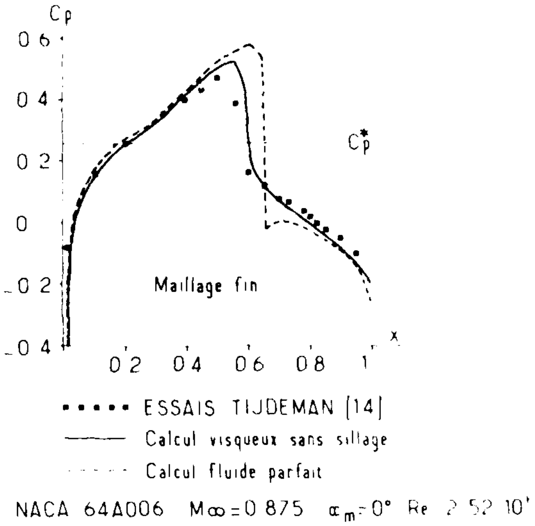

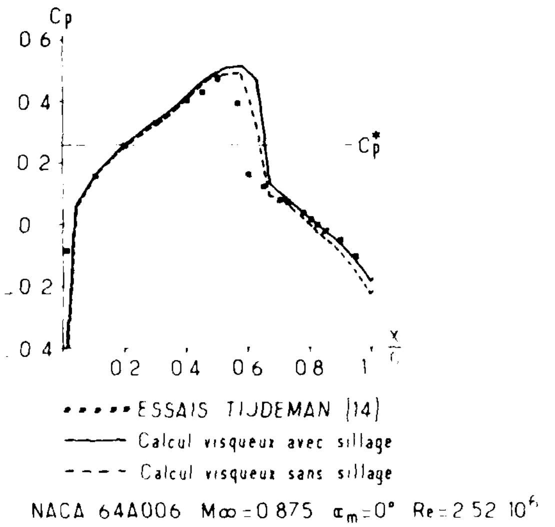

Fig. 7 : Influence du sillage sur le champ de pression stationnaire.

Fig. 8 : Evolution des grandeurs caractéristiques de couche limite.

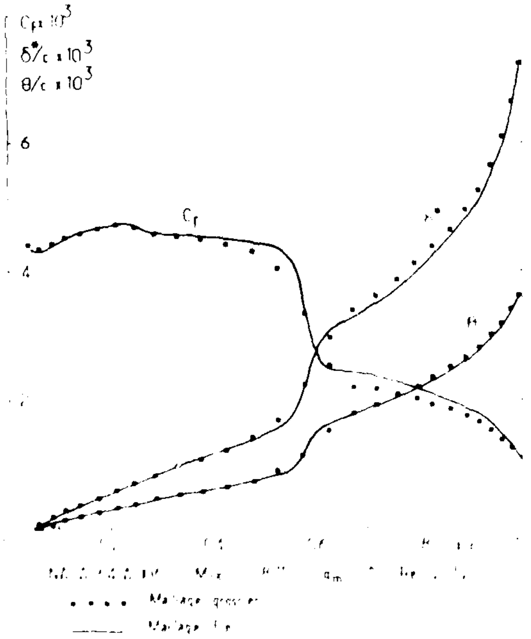

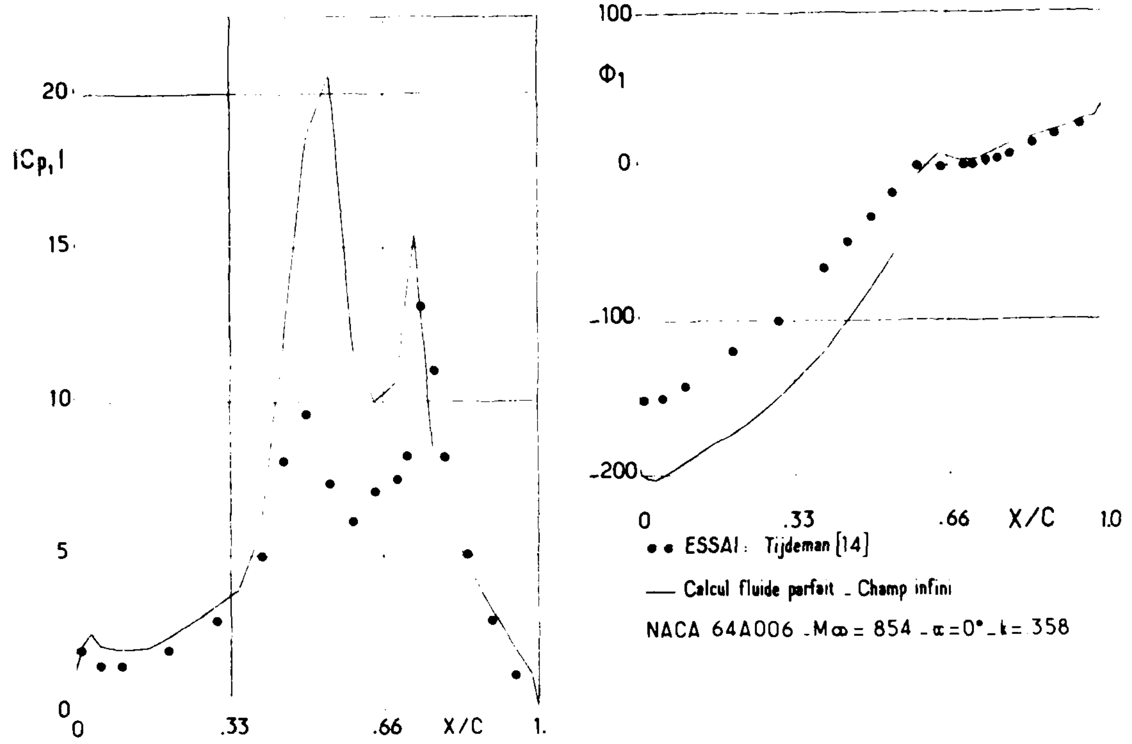

Fig. 9 : Champs des pressions instationnaires normalisées. Oscillation de gouverne 1°.

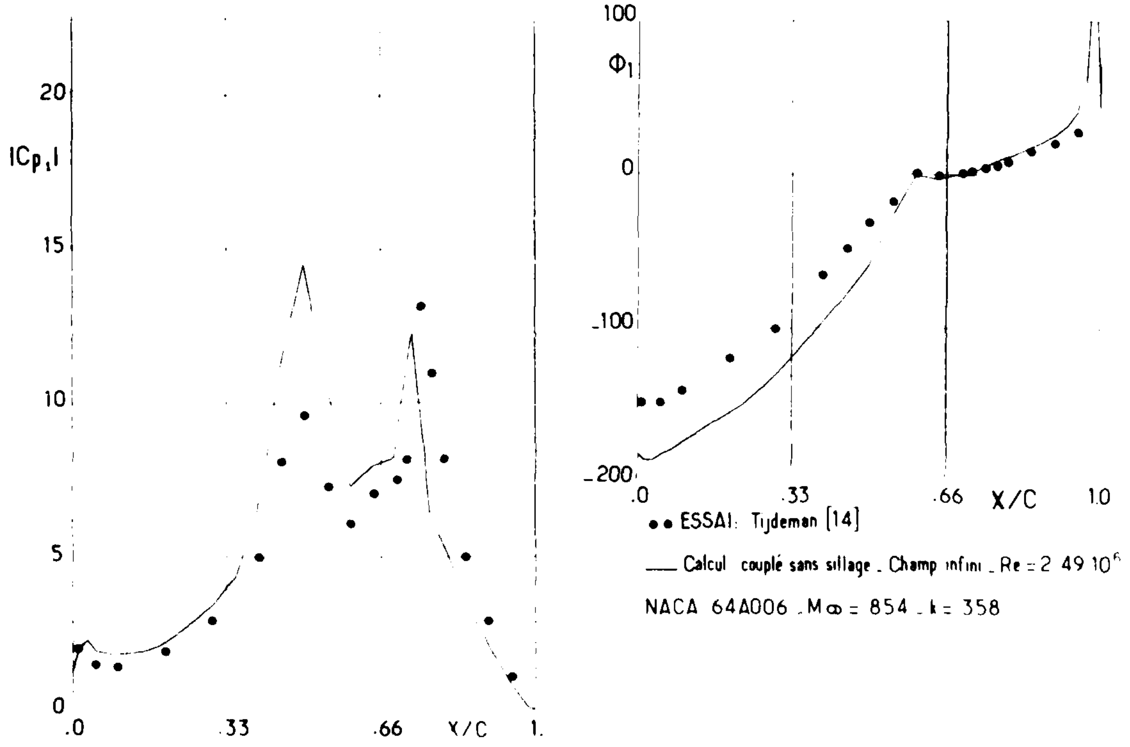

Fig. 10 : Champs des pressions instationnaires normalisées. Oscillation de gouverne 1°

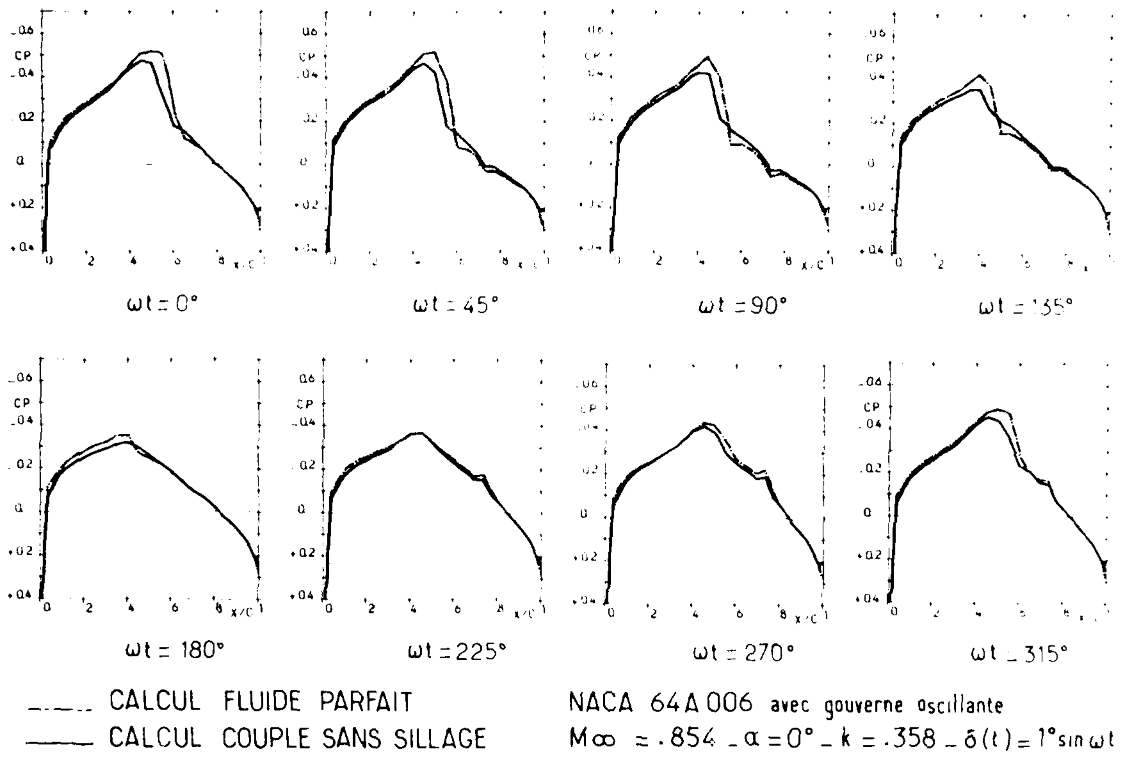

Fig. 11 : Distribution de pression instantanée.

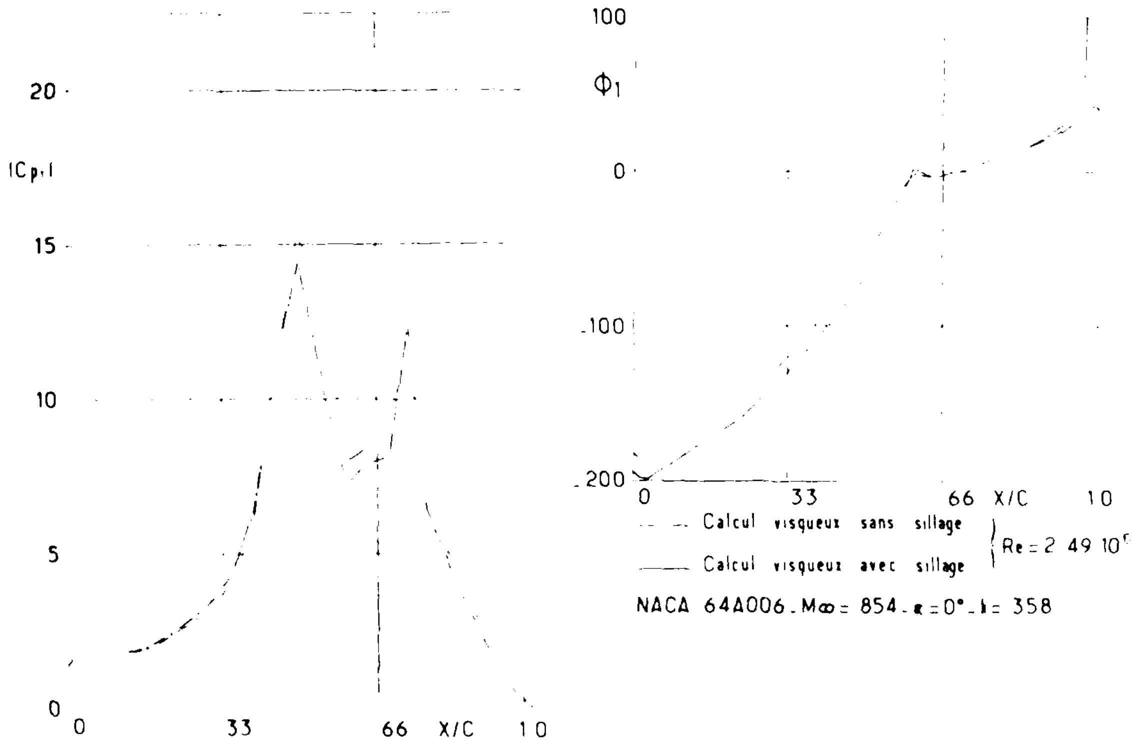

Fig. 12 : Champs des pressions instationnaires calculées avec et sans prise en compte du sillage visqueux.

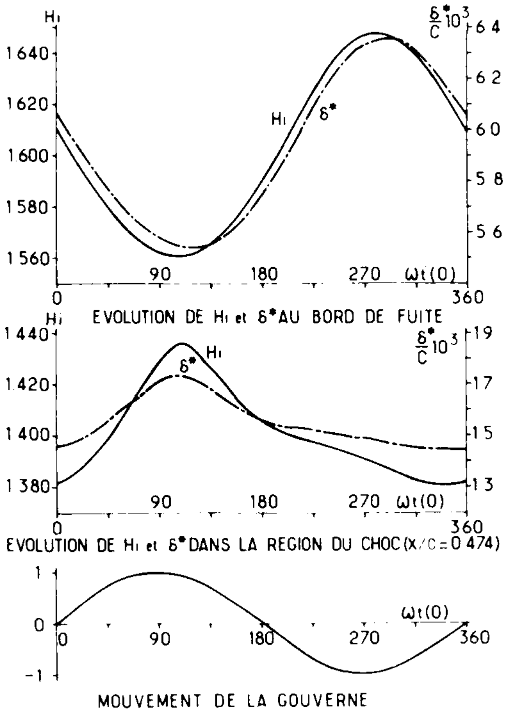

Fig. 13 : NACA 64 A 006 avec gouverne oscillante
= 0,854 ; K = 0,358 ;
= 0° ; Ji = 1° ;
Re = 2.49.10^6.

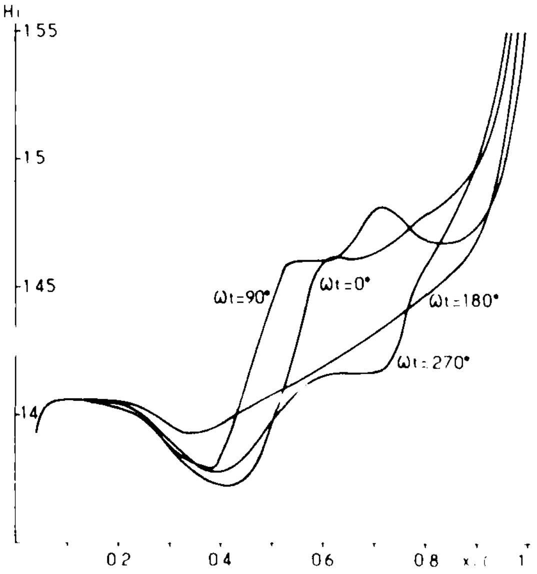

NACA 64A006 M∞= 854 α= 0° Re= 2 49 10^6
k= 0 358 δi(t) = 1° sin ωt

Fig. 14 : Evolution de Hi (x) au cours du cycle.

EXPERIMENTAL FLUTTER AT HIGH SUBSONIC SPEEDS AND ITS THEORETICAL PREDICTION, TAKING INTO ACCOUNT WING THICKNESS AND REYNOLDS NUMBER

H. C. Garner
Royal Aircraft Establishment, Structures Department
Farnborough, Hampshire, GU14 6TD, England

and
B. W. Payne
British Aerospace, Aircraft Group
Weybridge/Bristol Division, Weybridge, England

with
Appendix by J. C. A. Baldock
Royal Aircraft Establishment, Structures Department
"The Reason for the Large Increase in
Critical Flutter Speed with Mach Number"

SUMMARY

Half-model flutter tests of a symmetrical high-aspect-ratio wing at stream Mach numbers M_∞ between 0.75 and 0.90 are described. Equivalent air speeds at flutter, calculated with aerodynamics from subsonic lifting-surface theory, are in fairly good agreement with the measured values up to $M_\infty = 0.86$. In the range $0.86 < M_\infty < 0.90$ the measured flutter speed increases rapidly until the flow is stable, contrary to the predictions with the linear theoretical aerodynamics. However, the use of approximate theories compatible with steady and quasi-steady aerodynamics from transonic small perturbation (TSP) theory leads to the correct qualitative behaviour of flutter speed. With inviscid TSP aerodynamics the rapid rise in flutter speed is anticipated by about 0.02 in M_∞, but allowance for the boundary layers is shown to halve this discrepancy. The most crucial aerodynamic force coefficient is identified and its behaviour and influence are analysed. Further calculations illustrate the effects of mean incidence and Reynolds number on flutter speed. Typical changes in the oscillatory aerodynamic load distribution are discussed.

LIST OF SYMBOLS

$\mathbf{A}$	structural inertia matrix
b	determinant of scaled matrix $\mathbf{B}$ (see Appendix)
$\mathbf{B}$, $\mathbf{C}$	aerodynamic damping matrix, aerodynamic stiffness matrix
$c(\eta)$	local chord of wing
$\bar{c}$	geometric wing chord
c_{11}, c_{22}	scaled elements of matrix $\mathbf{C}$ (see Appendix)
C_L	steady lift/$(\frac{1}{2}\rho_\infty U_\infty^2 S)$
$C_p(\alpha)$	steady pressure coefficient $(p - p_\infty)/(\frac{1}{2}\rho_\infty U_\infty^2)$
$\bar{C}_p$	$C_p' + iC_p''$; oscillatory pressure coefficient in Eq. (1)
C_{p0}	mean pressure coefficient $C_p(\alpha_0)$
$\mathbf{E}$	structural stiffness matrix
f	frequency of oscillation (Hz)
F	ratio in Eq. (3)
G	local mean flow parameter in Eq. (6)
$\bar{K}$	complex quantity in Eq. (4) from linear theory
M_∞	stream Mach number
p	air pressure
q	column matrix of complex displacements
$\mathbf{Q}$	complex aerodynamic force matrix in Eq. (14)
$\mathbf{Q}_1$, $\mathbf{Q}_2$	force matrices in Eq. (12)
Q_{ij}	$Q_{ij}' + i\bar{\nu}Q_{ij}''$; generalized force coefficient in Eq. (10)
R	Reynolds number $U_\infty\bar{c}/\nu$
$\mathcal{R}$	real part of
s	semi-span of wing
S	area of wing planform
t	time
$\mathbf{T}$, $\mathbf{T}'$	transformation matrix and its transpose
T_0	stagnation temperature (K)
U	air speed
V	equivalent air speed in Eq. (16)

LIST OF SYMBOLS (concluded)

x	ordinate in streamwise direction
x_{ac}	position of aerodynamic centre
$x_L(\eta)$	local ordinate of leading edge
y	spanwise distance from centre line; see also the Appendix
z	downward vertical displacement
α	incidence of wing (radians, unless otherwise stated)
α_0	mean value of α
α_1	amplitude of pitching oscillation (radians)
γ	ratio of specific heats of air (= 1.4)
Γ_q, $\bar{\Gamma}_q$	loading functions (see Ref 7)
ΔC_p	$C_{p\ell} - C_{pu}$; steady loading coefficient
$\Delta \bar{C}_p$	$\Delta C'_p + i\Delta C''_p$; oscillatory loading coefficient in Eq. (1)
ζ	critical damping ratio (%)
η	non-dimensional spanwise distance y/s
$\theta(\eta)$	local displacement in nose-up pitch about flexural axis (radians)
ν	kinematic viscosity of air
$\bar{\nu}$	frequency parameter $\omega\bar{c}/U_\infty$
ξ	non-dimensional chordwise distance in Eq. (8)
$\xi_{ac}(\eta)$	position of local aerodynamic centre
ρ	air density
ρ_0	standard air density at sea level
σ	density ratio ρ_∞/ρ_0
$\bar{\Phi}$	complex oscillatory velocity potential on wing surface
ω	circular frequency of oscillation $2\pi f$; proportional quantity in the Appendix
0	subscript denoting mean flow at $\alpha = \alpha_0$
∞	subscript denoting undisturbed stream
c	subscript denoting unmatched calculation
f	subscript denoting matched flutter condition
i	subscript denoting force mode
j	subscript denoting mode of oscillation
ℓ	subscript denoting lower surface
u	subscript denoting upper surface
lin	subscript denoting linearized theory

1 INTRODUCTION

The prediction of flutter boundaries in the transonic speed range suffers from inadequacy of aerodynamic data in several respects. In the first place, the completely linearized data from subsonic oscillatory lifting-surface or doublet-lattice theory become increasingly suspect as the onset of supercritical flow is approached. Their defects are apparent from the evidence of two-dimensional transonic theory. A second consideration, which can only be transitory, is the non-availability of a general method of solving the three-dimensional equations of unsteady transonic flow. The present paper explores the results of flutter predictions based on approximate three-dimensional methods. A third important factor is the influence of the boundary layer. As many workers have pointed out, to include the effects of wing thickness without those of the boundary layer may improve the qualitative picture of the pressure distribution while the aerodynamic force coefficients may become less representative of the real flow. The approximate theoretical methods can incorporate boundary-layer effects on a quasi-steady basis, so that some account of Reynolds number will be taken. A fourth consideration is the influence of the mean flow on the aerodynamic force matrix for a given Mach number and frequency parameter, while the perturbations about the mean flow remain linear. This characteristic will be illustrated in the prediction of flutter speed as a function of mean incidence.

The focal point of the present study is the wind-tunnel investigation carried out on a high-aspect-ratio flutter model in the RAE 8 ft × 8 ft tunnel over the range of Mach numbers from 0.75 to 0.90. An account of this investigation is given in Section 2. The theoretical background is described in Section 3, and the flutter calculations are discussed in Section 4. The Appendix explains how a physical understanding of the flutter characteristics of the model is gained from a binary condensation of the problem and graphical display.

AD-A098 057 ADVISORY GROUP FOR AEROSPACE RESEARCH AND DEVELOPMENT--ETC F/G 20/4
BOUNDARY LAYER EFFECTS ON UNSTEADY AIRLOADS.(U)
FEB 81
UNCLASSIFIED AGARD-CP-296 NL

2 OF 2
AD A
098057

END
5-81

It should not be assumed that the present results are typical of modern wings designed for supercritical [illegible]. The essence of the experiment is its simplicity. The planform is uncranked, the aerofoil section is symmetrical and uniform, and the model was tested at zero lift. While the experiment was designed to produce flutter and to provide a straightforward test of the theoretical methods, the flutter actually disappears at the top end of the Mach number range. Therefore, special interest attaches to the ability to predict this disappearance by the available theoretical means.

2 WIND-TUNNEL FLUTTER TEST

The experimental programme stemmed from a proposal to design, build and test a wing model to help to assess the accuracy of flutter predictive methods at high subsonic speed. The model was designed for testing in the RAE 8 ft × 8 ft Tunnel at Bedford, and as this was to be the first test in this tunnel of a flutter model, particular care was taken to reduce the possibility of model failure which could damage the tunnel compressor blades. Static and fatigue loads were given careful consideration and the decision taken to use mainly fast-frequency-sweep testing, to reduce test time, instead of the discrete-frequency method customary at that time. Ref 1 discusses the model design and testing and Ref 2 the theoretical studies and analysis of the wind-tunnel results.

2.1 Design of Model

The model was designed, in the first place, as a simple representation of the port half of a high-aspect-ratio clean wing, designed for a BAe rear-engined project. The simplifications included the use of straight leading and trailing edges, no camber and a constant streamwise NACA 64A010 section (see Fig 1). Stiffnesses were scaled so that a flutter speed could be found within the tunnel operating limits and within the Mach number range 0.75 to 0.90.

The design finally used was based on a single box spar centred at 40% chord which provided the majority of the bending and torsional stiffness of the model. The external shape of the wing was achieved by shaping balsa wood glued to the spar with fibreglass strengthening. The spar root terminated in a solid block which was mounted on a two-flexure support system which allowed the wing to pitch. Excitation was applied to the root block through an electro-magnetic vibrator. The wing projected through a fixed non-representative body provided to contain the support and excitation system and to achieve suitable flow in the tunnel test.

The tests described were all carried out at zero mean incidence, but there remains the possibility of further tests at small incidence.

2.2 Bench Tests

Throughout the manufacture period, bench tests were carried out in order to test the structural data to be incorporated in the mathematical model to be used for the flutter predictions.

The spar was bench tested before the addition of fibreglass and balsa cladding. Both bending and torsional stiffness tests were carried out, followed by resonance tests, and small adjustments made to the data calculated from the drawings. On completion of the model, further stiffness and resonance tests were carried out. Structural influence coefficients were measured over a grid of 45 points (9 × 5) used for both load application and deflection measurement. Resonance tests were conducted with the model mounted in the support rig, which was itself attached to a massive bench structure, and the first five normal modes of the model were measured together with the pitch mode on the root mounting block. Final adjustments were then made to the structural mathematical model.

The overall changes made from both the spar tests and the complete model tests were as follows:

All mass data factored by	1.20
Bending stiffness factored by	0.90
Torsional stiffness factored by	1.20 .

Measured modes are shown in Fig 2 and the calculated modes obtained by using the empirical factors are shown in Fig 3. Modal frequencies are listed in Table 1.

2.3 Wind-Tunnel Test Procedures

The wind-tunnel tests took place at Bedford in May 1976, and covered the Mach number range 0.75 to 0.90. Model response was measured by flexure strain gauges mounted on the model at the root and at 60% span. At first results were obtained from automated analysis of fast frequency sweeps with the aid of fast Fourier transform techniques, although some spot checks were made by using response at discrete frequencies together with vector-plot techniques. It was found, however, that the lowly-damped root-mounting-block pitch mode, excited by tunnel turbulence, dominated the response throughout the sweep, thereby reducing considerably the levels at which the model mode responses could be recorded. The response of the model to tunnel noise alone was also recorded at each stagnation pressure, and it was found that, although the root-mounting-block response again dominated the signal, those signals contained adequate definition to permit analysis. This change in excitation allowed some additional tests with the mounting block rigidly locked.

2.4 Wind-Tunnel Test Results

A list of the Mach numbers at which tests were carried out together with the inferred flutter speeds and frequencies is given in Table 2. Typical plots of experimental modal critical damping ratio, ζ , and frequency, f , *versus* airspeed are shown in Fig 4 for a Mach number of 0.803. Two roots are traced over the speed range tested, and root 1 is seen to be approaching flutter at an extrapolated speed of 278 m/s.

Tests showed clearly that the effect of the mounting-block freedom was negligible and results for both conditions of mounting block, free and locked, are plotted together in Fig 5, in which the variations of flutter speed and frequency with Mach number are shown. The sudden upturn in both critical speed and frequency is seen in the Mach number range between 0.87 and 0.89.

3 THEORETICAL AERODYNAMICS

In past decades flutter prediction has relied increasingly on the completely linearized aerodynamics of the lifting-surface or doublet-lattice methods. In the present investigation the lifting-surface theory of Davies[3] has been used. In industrial applications it has been common practice to make allowance for aerofoil section, boundary layers and other effects not represented in the theory, by applying empirical factors, based on wind-tunnel or flight experience, to the force coefficients. Empirical corrections of this kind stand a reasonable chance of success when the qualitative changes between the calculated and the real load distributions are minor ones. At high speeds, however, this is no longer the case.

From two-dimensional considerations it is apparent that, with the development of local supersonic regions and eventually shock waves, transonic flow introduces major changes in the character of the steady aerodynamic loading. The consequences for the oscillatory aerodynamic loading are even greater. The topic has been reviewed by Tijdeman[4], and Fig 10.7 of Ref 4 illustrates the large effects on the incremental pressure distribution due to a change of incidence mainly on account of the displacement of a well-developed shock wave. An example of the measured frequency effect on the oscillatory pressure distribution is given in Fig 10.11 of Ref 4, and this is a further illustration of the deficiencies of linear flat-plate theory. Theoretical progress in unsteady two-dimensional transonic flow is reviewed in Part IV of Ref 4, where Fig 13.5 makes the point that inviscid transonic theory can introduce qualitative improvement at the expense of large quantitative inaccuracy. By theoretical allowance for the boundary layer and by correction of the experimental results for wall interference the agreement between them is improved considerably. Viscous effects can be expected to grow rapidly as transonic conditions develop and to influence the location of shock waves. Empirical factors to the force coefficients are unlikely to succeed in this flow regime.

It cannot even be said that there is an available method for solving the equations of inviscid three-dimensional unsteady transonic flow. There is a pilot program by Weatherill *et al*[5], which has been run for a rectangular wing in pitching oscillation, and it can only be a matter of time and costly effort before there will emerge a general method for solving a finite-difference approximation to the transonic-small-perturbation equations for oscillatory flows past finite wings. In the interim there is a place for approximate methods, two of which are used in the present investigation. One is an adaptation of strip theory to be considered in Section 4.3. The other, to be discussed in Sections 3.1 and 3.2, has been described in Refs 6 and 7.

3.1 Description of Theory

The basic equations of the approximate method are derived in Ref 6. The underlying principles and the key equations are summarized in Section 3 of Ref 7. The local pressure coefficient is expressed as

$$C_p = (p - p_\infty)/(\tfrac{1}{2}\rho_\infty U_\infty^2) = C_{p0} + \mathcal{R}\left\{\bar{C}_p e^{i\omega t}\right\} , \qquad (1)$$

where p_∞, ρ_∞ and U_∞ are the pressure, density and velocity of the undisturbed stream, C_{p0} corresponds to the mean flow and ω is the circular frequency of oscillation. It is sufficient here to say:

(i) that a one-dimensional form of Bernoulli's equation is used to relate the local values of the oscillatory pressure coefficient $\bar{C}_p$, the mean value C_{p0} , the complex oscillatory velocity potential $\bar{\Phi}(x,y)$ and its derivative $\partial\bar{\Phi}/\partial x$;

(ii) that the ratio of $\partial\bar{\Phi}/\partial x$ to its value as frequency tends to zero is set equal to the corresponding ratio from linear theory[3];

(iii) that the ratio of the quasi-steady rate of change of surface pressure to the corresponding quantity from linear theory is assumed to be the same for each mode of deformation, so as to equal the ratio for the mode of rigid pitching calculated with the aid of steady pressure distributions over a range of incidence covering the mean flow condition.

The final expression for the oscillatory part of the pressure coefficient at a given section of $y = \eta s$ is

$$\bar{C}_p(\xi) = F(\xi)\bar{K}(\xi) + \frac{i\bar{\nu}c(\eta)G(\xi)}{\bar{c}} \int_0^{\xi} \frac{F(\xi')\bar{K}(\xi')U_\infty}{G(\xi')U_0(\xi')}\,d\xi' \,, \tag{2}$$

where

$$F(\xi) = \frac{(\partial C_p/\partial\alpha)_{\alpha=\alpha_0} \text{ (from steady data)}}{\partial(\Delta C_p)/\partial\alpha \quad \text{(from linear theory)}} \,, \tag{3}$$

$$\bar{K}(\xi) = \frac{4}{U_\infty}\frac{\partial\bar{\Phi}_{lin}}{\partial x} \text{ for the upper surface ,} \tag{4}$$

$$\bar{\nu} = \omega\bar{c}/U_\infty \text{ is the frequency parameter ,} \tag{5}$$

$$G(\xi) = \left[1 + \tfrac{1}{2}\gamma M_\infty^2 C_{p0}(\xi)\right]^{1/\gamma} , \tag{6}$$

$$U_0(\xi) = U_\infty\left[1 - \frac{2}{(\gamma - 1)M_\infty^2}\left\{\left[1 + \tfrac{1}{2}\gamma M_\infty^2 C_{p0}(\xi)\right]^{(\gamma-1)/\gamma} - 1\right\}\right]^{\frac{1}{2}} , \tag{7}$$

$$\xi = \left[x - x_L(\eta)\right]/c(\eta) \,, \tag{8}$$

and other basic quantities are defined in the List of Symbols.

The approximate method has achieved sufficient success in reproducing supercritical experimental pressure distributions to justify its application to the present flutter problem. As described briefly in Section 5 of Ref 7, the method has been programmed so that different modes, frequencies and mean incidences can be handled in the same calculation. Although the running time is relatively short, a lot of preliminary effort is needed in preparing the PLATEDATA and WINGDATA files.

The PLATEDATA file contains the results of previous calculations from lifting-surface theory for the appropriate modes, frequencies and Mach number. In the present work there has been a slight complication in that the method of Davies[3] is used in place of Ref 8. An extra program has been written to convert the pressures at the loading points into the quantities Γ_q and $\bar{\Gamma}_q$ required in equations (18) and (20) of Ref 7, which determine the respective quantities $\partial(\Delta C_p)/\partial\alpha$ in Eq. (3) and $\bar{K}(\xi)$ in Eq. (4). A further complication has arisen in the representation of modal data. The PLATEDATA files for the present work comprise the values of Γ_q for steady flow at a uniform incidence and for each value of the frequency parameter $\bar{\nu}$ the values of the real and imaginary parts of $\bar{\Gamma}_q$ for the following eight modes:

$$-z = \eta^{2m}(x/\bar{c})^n \qquad (m=0,1,2,3 \text{ and } n=0,1) \,. \tag{9}$$

The program is then run to give the generalized force coefficients as a pair of 8 × 8 matrices corresponding to the real and imaginary parts of

$$Q_{ij} = \frac{1}{2S\bar{c}}\iint(-z_i)(\Delta\bar{C}_p)_j dS \,, \tag{10}$$

where z_i is the downward vertical displacement from Eq. (9) for the appropriate mode and $(\Delta\bar{C}_p)_j$ is the complex loading for the appropriate mode of oscillation $z = z_j$ when the surface pressure coefficients $\bar{C}_{pu}$ and $\bar{C}_{p\ell}$ defined as in Eq. (1) are differenced to give

$$\Delta\bar{C}_p = \bar{C}_{p\ell} - \bar{C}_{pu} = \Delta C'_p + i\Delta C''_p \ . \tag{11}$$

A 5 × 8 matrix T' is formed to express each of the first five flexible modes of the flutter model to a sufficient approximation as a linear combination of the eight modes in Eq. (9). Then, if Q_1 denotes either of the 8 × 8 matrices, the required matrix for the flutter calculation is

$$Q_2 = T'Q_1T \ , \tag{12}$$

where T is the transpose of T' .

The WINGDATA file contains the steady-state data, either theoretical or experimental, at the given Mach number for an appropriate set of incidences. In the calculations of Ref 7 the choice lay between an early version of the transonic-small-perturbation (TSP) method for isolated wings and measured static pressures on the wind-tunnel model concerned. In the present investigation a later version of the TSP method is used, which incorporates two important new developments. The first, not relevant to the investigation, is the extension to treat wing-body combinations developed by Albone *et al*[9]. The second, to be discussed in Section 3.2, is the allowance for boundary layers due to Firmin[10]. Thus the inviscid steady flows for the isolated wing can be calculated with improved accuracy, and it is no longer necessary to have detailed experimental pressure plotting in order to represent viscous transonic flow in the WINGDATA file. Moreover, the effect of Reynolds number can be considered.

The present applications of the program of Ref 7 to the flutter model of Fig 1 cover Mach numbers and frequency parameters in the ranges $0.80 \leqslant M_\infty \leqslant 0.89$ and $0 < \bar{\nu} \leqslant 0.855$. Figs 6 and 7 illustrate the effects of these parameters on the inviscid oscillatory chordwise loading at an outboard station $\eta = 0.809$, when the wing at zero mean incidence is pitching about the axis through the root leading edge. With reference to Eq. (11) the distributions of $\Delta C'_p/\alpha_1$ and $\Delta C''_p/(\alpha_1\ \bar{\nu})$ are plotted, where α_1 is amplitude of oscillation in radians. In Fig 6 both distributions depart further and further from typical subsonic shapes as M_∞ increases from 0.80 to 0.88 and $\bar{\nu}$ is fixed at 0.428. As the shock wave develops in strength and moves aft with increasing M_∞ , so do the peaks until, at $M_\infty = 0.88$, $\Delta C'_p/\alpha_1$ reaches about 70 and $\Delta C''_p/(\alpha_1\ \bar{\nu})$ reaches about 100. At the higher stream Mach numbers of 0.885 and 0.89 the peak values are still large but decreasing; the evidence suggests that, although the shock wave continues to strengthen slightly and move aft, its smaller rate of movement with respect to α accounts for the falling peak values with increasing M_∞ .

The effect of frequency parameter, illustrated for $M_\infty = 0.86$ in Fig 7, stems primarily from the lifting-surface calculations of Ref 3. The high aspect ratio of the wing is responsible for large changes while the frequency parameter is fairly small, especially in $\Delta C''_p/(\alpha_1\ \bar{\nu})$. It looks as if the trends in both the real and imaginary quantities with increasing $\bar{\nu}$ have reversed over the forward part of the chord between $\bar{\nu} = 0$ and $\bar{\nu} = 0.855$. It is likely that the results for this highest frequency parameter suffer in accuracy because no account is taken of the decreasing shock-wave motion as frequency increases. But the frequency effects outside the shock-wave region should be realistic.

3.2 Effect of Boundary Layers

In the present investigation the TSP method of Ref 10 is used for both inviscid and viscous steady flows. The inviscid TSP calculations are more reliable than those used in Ref 7 on account of an improved relaxation scheme for solving the finite-difference equations of the flow field. The viscous TSP calculations allow for the boundary layers by modifications to the boundary conditions near the wing and wake. The modifications are introduced into the iterative scheme in steps as the calculation proceeds, but after each revision of the boundary-layer development the changes in boundary condition need to be under-relaxed to achieve convergence in the pressure distribution.

At the outset it is necessary to prescribe the location of transition from laminar to turbulent flow. The laminar or turbulent boundary layer is calculated from an attachment line. For use in the region between the transition front and the trailing edge the lag-entrainment method of Green *et al*[11] has been extended by Smith[12] to three-dimensional flow. Firmin[10] makes a further extension of the turbulent-boundary-layer method to calculate the wake.

There is no question that boundary-layer effects are important. Ref 10 allows for these reasonably well provided that the shock waves are not too strong and that the boundary layers remain attached. There are residual uncertainties about the accuracy of the boundary-layer theory in the region of any shock-wave boundary-layer interaction and as the trailing edge is approached. Moreover, the treatment of the wake does not allow for the strong vorticity near the wing tips or any subsequent rolling up into discrete trailing vortices. But, judged from the comparisons with experimental pressure distributions in Ref 10, the method has achieved a satisfactory measure of success.

Although there is little understanding of unsteady boundary layers in transonic flow, it is feasible now to allow for Reynolds number in three-dimensional steady flow subject to the transonic-small-perturbation approximation. Hence, by numerical differentiation with respect to incidence, the quasi-steady effect of the boundary layers can be calculated and used in the method of Ref 7. The primary effect is on $F(\xi)$ in Eq. (3) through the quantity $\partial C_p/\partial\alpha$ at $\alpha = \alpha_0$, but through their dependence on C_{p0} both $G(\xi)$ and $U_0(\xi)$ in Eqs. (6) and (7) are also changed by the boundary layers. All three functions influence $\bar{C}_p$ in Eq. (2) and thereby the generalized forces in Eqs. (10) and (11).

The results in Figs 8 to 10 illustrate the character and magnitude of the viscous effects. In Fig 8 the lift slope $\partial C_L/\partial\alpha$ and aerodynamic centre x_{ac} are calculated from the inviscid TSP solutions and are compared with the linear theoretical values for stream Mach numbers between 0.80 and 0.89. The effect of the 10% thick aerofoil section on $\partial C_L/\partial\alpha$ increases from 13% at $M_\infty = 0.80$ to 27% at $M_\infty = 0.875$, above which the percentage falls. The rearward shift in aerodynamic centre due to aerofoil thickness increases from $0.02\bar{c}$ to $0.18\bar{c}$ as M_∞ increases over the range. The influence of the boundary layers at the wind-tunnel Reynolds number of 3.4×10^6 with transition at 5% chord is shown in the range $0.86 \leqslant M_\infty \leqslant 0.885$. The loss in lift slope due to viscous effects is seen to increase with increasing M_∞ until it exceeds the large increase due to aerofoil section. The aerodynamic centre is found to lie somewhat closer to inviscid TSP theory than to linear theory. For $M_\infty = 0.86$ an extra calculation is made for a typical full-scale Reynolds number of 3.5×10^7 with transition still at 5% chord, and the results for both $\partial C_L/\partial\alpha$ and $x_{ac}/\bar{c}$ lie roughly midway between those for $R = 3.4 \times 10^6$ and for inviscid flow.

Fig 9 shows the symmetrical steady pressure distribution at $M_\infty = 0.88$ when $\alpha = 0$ and the quasi-steady lower-surface distribution

$$\partial C_{p\ell}/\partial\alpha = - \partial C_{pu}/\partial\alpha \qquad \text{when} \quad \alpha_0 = 0$$

for sections inboard at $\eta = 0.210$ and outboard at $\eta = 0.809$. The curves derived from the viscous TSP solutions for $R = 3.4 \times 10^6$ are compared with those from inviscid TSP solutions and from linear theory which gives $-C_{p0} \equiv 0$. The TSP curves all show the expected qualitative changes from the distributions given by linear theory. The behaviour of $\partial C_{p\ell}/\partial\alpha$ and the peaks associated with shock-wave movement are of primary importance as regards the calculations of oscillatory pressure. The inclusion of the boundary layer is seen to spread the recompression near the shock wave and to halve the peaks in $\partial C_{p\ell}/\partial\alpha$ at both sections. The shock wave is distinctly stronger at the outer section, which is the more important in relation to flutter.

For most of the stream conditions considered, the TSP solutions are carried out for only three incidences $\alpha = 0, \frac{1}{2}^\circ$ and 1°. Because of the symmetry of the aerofoil section these provide values of $C_{p\ell}$ (and C_{pu}) for the five incidences $\alpha = -1^\circ, -\frac{1}{2}^\circ, 0, \frac{1}{2}^\circ$ and 1°, from which to evaluate $\partial C_{p\ell}/\partial\alpha$ (and $\partial C_{pu}/\partial\alpha$). In the particular case of inviscid flow at $M_\infty = 0.86$ additional solutions are obtained for $\alpha = 1\frac{1}{2}^\circ, 2^\circ, 2\frac{1}{2}^\circ$ and 3°, so that the effect of mean incidence can be studied. It is interesting in Fig 10 to compare the relative effects of the changes from inviscid to viscous flow and from $\alpha_0 = 0$ to $\alpha_0 = 2^\circ$. The chordwise distributions of the real and imaginary parts of the oscillatory loading at $\eta = 0.809$ due to pitching motion about the axis through the root leading edge at $\bar{\nu} = 0.428$ show contrasting changes. The effect of viscosity is to weaken the peaks near midchord and to displace them upstream, while the increase in mean incidence from 0 to 2° strengthens the peaks and displaces them downstream. The consequences for flutter are surprising and will be discussed in Section 4.5.

4 FLUTTER CALCULATIONS

The wind-tunnel flutter test, described in Section 2, has yielded the experimental values of the equivalent air speed at flutter in Table 2 for the range of stream Mach number from 0.75 to 0.90. The aerodynamic theory, outlined in Section 3, is used to provide matrices of generalized force coefficients for the five modes included in Table 1. The solution of the flutter equations is discussed in Section 4.1.

The selection of flow conditions for the calculations is considered in Section 4.2. The primary aim is to evaluate the influence of the boundary layers on flutter speed at the Reynolds number of the experiment. A further objective is to examine the scale effect in increasing this Reynolds number to a value typical of full scale. As the flutter testing was all at zero mean incidence and there is the possibility of conducting further tests at small non-zero values of mean incidence α_0, a subsidiary aim is to assess the importance of α_0 as a flutter parameter.

Section 4.3 concerns the use of the three-dimensional TSP solutions in conjunction with strip theory as an alternative to Ref 7. The comparisons and discussion of the flutter characteristics follow in Sections 4.4 and 4.5.

4.1 Method of Analysis

The flutter equation to be solved is

$$\mathbf{A}\ddot{q} + \rho_\infty U_\infty \mathbf{B}\dot{q} + \rho_\infty U_\infty^2 \mathbf{C}q + \mathbf{E}q = 0 , \tag{13}$$

where **A** is the structural inertia matrix and **E** is the structural stiffness matrix for the first five flexible modes discussed in Section 2.2. The complex generalized force coefficients are first calculated as in Eq. (10) and are then transformed through Eq. (12) to a complex 5 × 5 matrix **Q** . The aerodynamic damping matrix **B** and the aerodynamic stiffness matrix **C** for prescribed values of M_∞ and $\bar{\nu}$ are given by

$$S\bar{c}\mathbf{Q} = \mathbf{C} + i\bar{\nu}\mathbf{B} . \tag{14}$$

The complex column matrix q represents the magnitudes and phases of oscillatory displacements in the five modes with frequency

$$f = U_\infty \bar{\nu}/(2\pi\bar{c}) . \tag{15}$$

A flutter condition occurs when Eq. (13) is satisfied for an undamped root with compatible values of the frequency parameter $\bar{\nu}$ and the stream density ρ_∞ , velocity U_∞ , Mach number M_∞ and stagnation temperature T_0 .

In the present analysis U_∞ is matched to the given wind-tunnel value of T_0 (= 298 K) and the prescribed value of M_∞ used to obtain the aerodynamic force matrices in Eq. (14). Then, for the prescribed value of $\bar{\nu}$, the density ρ_∞ and hence the equivalent air speed

$$V_c = U_\infty \sqrt{(\rho_\infty/\rho_0)} , \tag{16}$$

where ρ_0 is the standard air density at sea level, is increased until at $\rho_\infty = \rho_c$, say, Eq. (13) gives an undamped root of frequency f_c , say. If f_c exists, the corresponding frequency parameter $\bar{\nu}_c$ is then calculated from Eq. (15) and will, in general, be found to differ from the assumed frequency parameter $\bar{\nu}$. A matched critical flutter condition is obtained when

$$\bar{\nu}_c = \bar{\nu} = \bar{\nu}_f , \quad \text{say} . \tag{17}$$

A simple graphical procedure is used to determine this condition, the corresponding density $\rho_c = \rho_f$ and hence the equivalent air speed at flutter

$$V_f = U_\infty \sqrt{\rho_f/\rho_0} . \tag{18}$$

It is found that the most influential modes are fundamental bending (37 Hz) and fundamental torsion (326 Hz) designated as modes 1 and 4 in Table 1, while flutter was measured at about $\bar{\nu} = 0.4$ (90 Hz) . Aerodynamic force matrices $(\mathbf{C} + i\bar{\nu}\mathbf{B})$ for these two modes with $M_\infty = 0.88$ and $\bar{\nu} = 0.428$ are illustrated in Table 3. There are large variations between the calculated results

(a) from linear theory (Ref 3),
(b) by using Ref 7 with inviscid TSP data,
(c) by using Ref 7 with viscous TSP data.

The predicted values of V_f for $M_\infty = 0.88$ vary widely from 270 m/s with (a) to a value in excess of 400 m/s with (b). As the matrices seem to indicate, the viscous case (c) is found to give an intermediate flutter speed $V_f = 326$ m/s . The Appendix shows how a simplified binary analysis in terms of modes 1 and 4 can elicit the dominant aerodynamic influences.

4.2 Results

The range of the stream conditions in the present calculations is indicated in Fig 8. Lifting-surface calculations by the method of Ref 3 have been made for $M_\infty = 0.80, 0.84, 0.86, 0.88, 0.885$ and 0.89 for various frequency parameters in the range $0 < \bar{\nu} \leq 0.855$, the particular value $\bar{\nu} = 0.428$ being used for each M_∞ as it is close to the expected value at flutter. Table 4a gives the critical flutter speeds V_f and frequency parameters $\bar{\nu}_f$ from the calculations with lifting-surface aerodynamics at selected Mach numbers including $M_\infty = 0.75$ from the earlier calculations of Ref 2. It is only above $M_\infty = 0.86$ that the trends in the measured flutter speed in Table 2 become very different from the monotonic behaviour, a decrease as M_∞ increases, shown by these preliminary calculations.

The inviscid TSP calculations for $\alpha = 0, \frac{1}{2}^\circ$ and 1° have been made for each of the six values of M_∞ from 0.80 to 0.89. Table 4b shows that the flutter calculations for zero mean incidence based on inviscid TSP aerodynamics yield no flutter in the range of the experiments at $M_\infty = 0.88$; nor is it found at $M_\infty = 0.885$ and 0.89. The viscous TSP calculations for the wind-tunnel Reynolds number $R = 3.4 \times 10^6$ are confined to $M_\infty = 0.86$, 0.88 and 0.885 . This is the region of greatest interest, where the shock waves are well-developed and their locations are influenced by boundary-layer growth. The corresponding flutter calculations in Table 4b give a critical equivalent air speed at $M_\infty = 0.88$, but it has disappeared out of range at $M_\infty = 0.885$. An analysis of these results is made in Section 4.4.

To extend the information on boundary-layer effects, a further calculation with viscous TSP aerodynamics has been carried out for $M_\infty = 0.86$ at the Reynolds number 3.5×10^7 typical of full scale. Predictably this gives a flutter speed in Table 4b intermediate to those for $R = 3.4 \times 10^6$ and for inviscid flow. Also for $M_\infty = 0.86$ the steady inviscid TSP solutions are extended to $\alpha = 1\frac{1}{2}^\circ, 2^\circ, 2\frac{1}{2}^\circ$ and 3° to provide aerodynamic data for flutter calculations when the mean incidence is varied in the range $0 \leqslant \alpha_0 \leqslant 2^\circ$. The surprising result in Table 4b is that the equivalent air speed at flutter goes outside the experimental range as α_0 is increased from $1\frac{1}{2}^\circ$ to 2°. The effects of Reynolds number and mean incidence are discussed further in Section 4.5.

4.3 Strip-Theory Analysis

The TSP calculations, which form the basis of the Ref 7 approach, produce as a by-product spanwise lift and moment distributions due to rigid incidence. This information has been used to form simplified-strip-theory in-phase lift and moment flutter derivatives, along the span, and by means of Ref 13 to obtain the corresponding out-of-phase derivatives. Flutter calculations were carried out for comparison with the Ref 7 results and the experimental values.

Results of the calculations for zero mean incidence are listed in Table 4c and are shown plotted in Fig 11. The derivatives from the inviscid flow give the curve shown as a full line, whose shape is influenced by an upper flutter point for $M_\infty = 0.86$. This shape of curve is also apparent for the viscous case, in which no flutter instability was calculated for $M_\infty = 0.88$. Strip theory is seen to predict successfully the upturn in flutter speed with Mach number, but the estimation of flutter speeds at lower Mach numbers is seen to be low by approximately 15%. This mis-match is partially explained by the over-estimation of the aerodynamic forces as a result of using the rigid incidence load gradings from the steady TSP data. The estimation of flutter frequency is in error by some 50%, but improvements in the out-of-phase derivatives can reduce this error.

The flutter trends are better indicated by the local aerodynamic centre $\xi_{ac}(\eta)$ than by the overall quantity $x_{ac}/\bar{c}$ in Fig 8. The upper diagram of Fig 12 shows a strong early influence of supercritical flow on ξ_{ac} over the inner part of the wing, while the strong influence over the outer part is considerably delayed in Mach number. The inboard values of ξ_{ac} have the greater effect on $x_{ac}/\bar{c}$, but it is the rearward shift outboard that first deters and finally precludes flutter. Study of the lower diagram of Fig 12 therefore explains the adverse effect of viscosity on flutter in the present investigation and suggests that an increase in mean incidence may be favourable.

4.4 Comparison with Experiment

The experimental results in Table 2 comprise equivalent air speed V_f and frequency of oscillation f_f at critical flutter conditions. In the calculations the primary objective is to predict V_f . The quantity f_f is derived in the process and provides a secondary check.

The curve of V_f drawn as a full line in Fig 13, calculated with completely linearized theoretical aerodynamics, shows two characteristic differences when compared with the experimental data. Up to $M_\infty = 0.85$ the downward theoretical trend is too small, while above $M_\infty = 0.87$ the same gentle trend continues where a steep increase in flutter speed has been measured. The remaining points in Fig 13 are taken from Table 4b and correspond to aerodynamics based on Ref 7 as described in Section 3.1. With inviscid TSP data, the initial downward trend has become consistent in slope with the measurements; moreover, as with the strip-theory aerodynamics in Fig 11, the approximate allowance for the effects of supercritical flow have resulted in the prediction of the steep increase in V_f . But the lateral displacement of about 0.02 in M_∞ between the inviscid TSP and experimental curves shows that the calculated disappearance of flutter is premature. When the TSP data incorporate the calculated boundary layers with Reynolds number 3.4×10^6 and transition to turbulence at 5% chord as in the wind-tunnel tests, the lateral displacement is reduced to about 0.01 in M_∞ . Discrepancies are thus extremely small, and it may be said that the viscous TSP aerodynamics achieve an excellent measure of agreement with the experiment.

One aspect of the flutter tests that has called for explanation is the large increase in flutter frequency at $M_\infty = 0.889$ in Table 2. Fig 14 presents the information on f_f against M_∞ to correspond to Fig 13. The remarkable agreement between linear theory and experiment in the range $0.84 < M_\infty < 0.88$ is perhaps fortuitous. Although the frequencies based on TSP calculations in this range of M_∞ are 10 to 15% high, the discrepancy is reduced slightly when viscous effects are taken into account. It is also reassuring that, in supercritical flow where Fig 13 shows the rapid increase in V_f, Fig 14 shows the upward trend in f_f towards the high measured value of 120 Hz, whether or not the viscous effects are included in the TSP calculations. The matching procedure in the calculations (Section 4.1) is such that f_f is derived indirectly and can be quite sensitive to changes in the solution.

Since the structural characteristics in the calculations are independent of stream conditions, the disappearance of flutter at the higher supercritical Mach numbers is aerodynamic in origin. The Appendix describes how a simple explanation emerges from Niblett's[14] graphical representation of a binary approximation to the flutter equations. It is first verified that the overtone bending modes 2, 3 and 5 in Table 1 can be eliminated to leave binary flutter in modes 1 and 4 with similar characteristics, as shown in Table 5. Typical aerodynamic force matrices for $M_\infty = 0.88$ after this simplification are given in Table 3. It is in fact one of the smaller coefficients Q'_{44} (= −0.008 in Table 3b) that plays the dominant role; this aerodynamic stiffness in the torsion mode is strongly influenced by the rearward shift in aerodynamic centre x_{ac} as M_∞ increases in Fig 8, and more especially by the corresponding behaviour in local aerodynamic centre ξ_{ac} over the outer part of the span in the upper diagram of Fig 12. The direct stiffness and damping coefficients in the fundamental torsion mode, Q'_{44} and Q''_{44}, are plotted against M_∞ in Fig 15. While the variation in Q''_{44} against M_∞ is no greater with TSP theory than with linear theory, it is the fall in $-Q'_{44}$ inherent in the transonic flow conditions that matters. Moreover, the delay of this fall by about 0.01 in M_∞ when viscous effects are included brings the improved prediction of flutter speed in Fig 13.

To check the simple explanation in the Appendix, the flutter calculations for $M_\infty = 0.84$ with inviscid TSP aerodynamics have been repeated with identical aerodynamic data, except that the values of Q'_{44} are replaced by those for $M_\infty = 0.88$. The calculated flutter speed $V_f = 255$ m/s then increases to a value in excess of 400 m/s, just like the result for $M_\infty = 0.88$ with inviscid TSP aerodynamics. It is reasonable to suppose that the same mechanism was at work in the experiments.

4.5 Effects of Reynolds Number and Incidence

Having calculated critical flutter speeds for the wind-tunnel test conditions as far as available transonic theoretical techniques will permit, we now sample the effects of Reynolds number and mean incidence not covered by the experiments. As a preliminary we apply the arguments of the Appendix and consider what might be expected in the light of the calculated aerodynamic centres. Fig 8 shows that a factor of 10 on Reynolds number at $M_\infty = 0.86$ brings the value of x_{ac} roughly half-way towards the value for inviscid flow; a similar effect is expected in the local aerodynamic centres in lower diagram of Fig 12, where the bottom curve corresponds to the wind-tunnel conditions, and a rearward shift of about 0.02 in ξ_{ac} is envisaged. The effect of incidence in inviscid flow over the outer part of the span is a somewhat larger rearward shift of 0.05 in ξ_{ac} as α is increased from 0 to 2°. Thus, for the particular model, an increase in either Reynolds number or mean incidence should have a favourable influence on flutter speed.

The Reynolds number $R = 3.5 \times 10^7$ is chosen as typical of full scale, and boundary-layer transition is retained at 5% chord. The results of the flutter calculation are included on the right-hand side of Fig 16. The factor of 10 on Reynolds number at $M_\infty = 0.86$ raises flutter speed by only 1% and gives a marginal increase in flutter frequency, as Table 4b shows. The collected information with V_f plotted against $\log_{10}R$ in Fig 16 puts the various results for $M_\infty = 0.86$ and $\alpha_0 = 0$ into perspective and shows that strip-theory analysis (Section 4.3) underestimates the measured flutter speed where the use of Ref 7 leads to a much smaller over-estimate.

It would have been interesting to have calculated the effect of mean incidence in viscous flow, but even at $\alpha = 1^\circ$ the state of the boundary layer on the upper surface just aft of the shock wave is thought to be critically close to separation. Therefore the calculations are restricted to inviscid flow. Mean incidence was varied from $\alpha_0 = 0$ to 2° in steps of 0.5°, and the curve of V_f against α_0 on the left of Fig 16 is found to be roughly parabolic in shape. The increase in flutter speed is even larger than might have been expected from Fig 12 in contrast to the small effect of Reynolds number. The result emphasises the importance of the dependence of unsteady aerodynamic data upon mean flow conditions at transonic Mach numbers. The equivalent flutter speed has increased from 278 m/s to about 475 m/s beyond the range of the experiments as α_0 increases from 0 to 2°, that is as the mean lift coefficient C_L increases from

0 to 0.29. Practical restrictions on C_L in wind-tunnel flutter testing are therefore to be regretted.

5 CONCLUDING REMARKS

The flutter tests confirm both the usefulness and the shortcomings of completely linearized aerodynamics. In subsonic flows, calculated wing forces are often more realistic when both thickness and viscosity are neglected than when only one of these effects is taken into account. Indeed, the flutter calculations are reasonably successful in giving flutter speed within ±8% for stream Mach numbers M_∞ from 0.75 to 0.88. On the other hand, the predicted downward slope of equivalent flutter speed against M_∞ around 0.8 is less than half the slope from experimental data. Moreover, this gentle slope continues beyond $M_\infty = 0.86$ with no trace of the observed sharp rise in flutter speed and the rapid disappearance of flutter.

The effect of supercritical flow on the flutter model at zero lift is unlikely to be typical of lifting wings designed for this speed range. The investigation is viewed as a demonstrator of the order of magnitude of transonic effects on flutter, and more especially as an indirect test of aerodynamic calculations in the absence of pressure measurements. It would be interesting to make a comparable study for a supercritical wing at the design condition.

The simplest scheme of transonic calculation is to use the incremental spanwise loading and distribution of aerodynamic centre from TSP theory in conjunction with strip theory (Section 4.3) to modify the completely linearized aerodynamic force coefficients. Although the calculated flutter speeds are less good quantitatively, it is significant that the qualitative trend is now correct. This use of strip theory underestimates both the flutter speed at subcritical M_∞ and the value of M_∞ associated with the sharp rise in flutter speed, but this essential characteristic of the flutter tests is modelled.

The aerodynamic calculations by means of Ref 7 utilize the complete pressure distribution as distinct from the local lifts and moments from TSP theory. The allowance for frequency is fully three-dimensional and compatible with lifting-surface theory. When the steady and quasi-steady data are taken from inviscid TSP theory, the measured flutter speed is predicted within ±4% when $M_\infty < 0.855$, and the downward slope of the curve is also correct. Although the calculated sharp rise is premature by about 0.02 in Mach number, this discrepancy is roughly halved when viscous TSP theory is used instead with Reynolds number and transition position corresponding to the wind-tunnel conditions.

The availability of a steady three-dimensional viscous TSP theory (Ref 10) in conjunction with Ref 7 makes possible a flutter calculation for full-scale Reynolds number. A factor of ten on Reynolds number gives a marginal increase in flutter speed at $M_\infty = 0.86$. By contrast, the effect of mean incidence in inviscid flow at this Mach number is found to be large for the particular wing.

The calculated 25% increase in equivalent air speed at flutter as mean incidence is increased from 0 to 1.5° suggests that an extension of the experimental investigation to non-zero mean lift is desirable. There are opposing factors however, first that viscous TSP calculations at the higher incidence are likely to be unreliable at $M_\infty = 0.86$ because of shock-induced boundary-layer separation, and second that the stiffness of the flutter model is insufficient to prevent considerable static deformation. The fact remains that the lift dependence of transonic flutter characteristics needs attentive study.

It has been possible to isolate the particular aerodynamic force coefficient that has the greatest influence on flutter speed, and the quantity (Q'_{44}) is akin to a direct pitching moment. The gentle trend of decreasing flutter speed against M_∞ in the subsonic and low supercritical ranges is associated with an increasing lift slope. But the trend towards stability against flutter with increasing supercritical Mach number and with increasing mean incidence is allied to a rearward movement in local aerodynamic centre over the outer portion of the span.

Acknowledgment

The authors wish to acknowledge the contributions of their colleagues J.C.A. Baldock at the Royal Aircraft Establishment and R.E.J. Brazier at British Aerospace for the flutter analyses, and of V. Ansbergs at British Aerospace for running the computer program which produces the steady TSP results.

Appendix

THE REASON FOR THE LARGE INCREASE IN CRITICAL FLUTTER SPEED WITH MACH NUMBER

by

J. C. A. Baldock

The reason for the large increase in flutter speed has been investigated by using Niblett's[14] 'graphical representation' of binary flutter. This technique requires the flutter problem to be in two degrees of freedom with matrix equation

$$\mathbf{A}\ddot{q} + \sigma^{\frac{1}{2}}V\mathbf{B}\dot{q} + V^2\mathbf{C}q + \mathbf{E}q = 0 , \qquad \text{(A-1)}$$

where $V = U_\infty\sqrt{\rho_\infty/\rho_0}$ is the equivalent air speed,

$\sigma = \rho_\infty/\rho_0$ is air density relative to standard air density at sea level,

q corresponds to a set of normal modes.

The representation shows variations with V as parameter and requires constant matrices **A**, **B**, **C** and **E** and a constant value of σ. Techniques[15] are available for condensing a flutter condition from many degrees of freedom to a similar condition in two derived degrees of freedom, but they have not been necessary with this example. As will be seen, the two-degree-of-freedom system with the normal modes of fundamental bending and fundamental torsion gives a variation in flutter speed with Mach number similar to that with the basic five-degree-of-freedom system used in the main flutter calculations.

The form of Eq. (A-1) is different from the one in the main report in that Eq. (13) represents the model conditions in the wind tunnel where U_∞, M_∞ and stagnation temperature T_0 are constant and equivalent air speed V is varied by changing the air density. With Eq. (A-1) the effects of air density and equivalent air speed are separated. The aerodynamic matrices **B** and **C** are regarded as constant although they are functions of frequency parameter $\bar{\nu}$ as well as M_∞. For fixed M_∞ the aerodynamic matrices for $\bar{\nu} = 0.428$ nearest to the critical frequency parameter have been used for all V. As a further simplification an average value of σ has been used throughout. Table 5 shows that for inviscid flow the equivalent binary solutions give a similar variation of critical equivalent air speed V_f with Mach number.

In the 'graphical representation' of binary flutter, the real and imaginary parts of the characteristic equation at flutter are separated; with a suitable choice of coordinates, it is shown that flutter is given at the intersection of a conic and a straight line. Fig 17 shows a typical representation. Coordinate y is proportional to V^2 and coordinate ω^2 is proportional to the square of frequency. The conic labelled "$\sigma = 0$" is given by scaled coefficients of the matrices **A**, **C** and **E**, and the point marked FC gives the conditions at 'frequency coalescence' flutter, *ie* with $\sigma = 0$ in Eq. (A-1). Flutter at finite σ is given by the intersection of the other conic and a line, called the 'damping line' because it depends largely on the coefficients in the aerodynamic damping matrix **B**. The flutter point moves along the damping line towards the $\sigma = 0$ conic as the relative density σ is decreased. Properties of the conics can be related to the scaled aerodynamic coefficients, and some of those relevant to the present problem are shown on Fig 17; viz, the slopes of the $\sigma = 0$ conic at $y = 0$ are equal to the scaled direct aerodynamic stiffness coefficients c_{11} and c_{22}, and the differences between the conics is proportional to σb, where b is the determinant of the scaled matrix **B**.

The graphical representations for $M_\infty = 0.84$, 0.86 and 0.88 are shown in Figs 18 to 20. The most obvious differences between the graphs lie in the finite σ conics, and especially in the upper slopes of the conics at $y = 0$. As Mach number increases, there is some increase in the upper angle between the "$\sigma = 0$" and "finite σ" conics, indicating some increase in σb, but the largest differences are in the upper slopes of the $\sigma = 0$ conics, which equal c_{22} (Fig 17). The modes are numbered in increasing frequency, so that mode 1 is the fundamental bending mode and mode 2 is the fundamental torsion mode. Therefore c_{22} is the direct aerodynamic stiffness term for the torsion mode. The enormous increase in the turning-point values of y with finite σ, arising from the increased upper slopes, is not entirely matched, however, by similar increases in y for the flutter point; due to the low position of the damping line the intersections take place in the lower parts of the conic. The net result is that, for this particular application, the clue to variations in flutter speed lies in the intersections of the damping line and the $\sigma = 0$ conics.

The dependence on Mach number of the intersection with the $\sigma = 0$ conics resembles that for the turning value of y for the $\sigma = 0$ conics (FC in Fig 17). Therefore this turning value of y for 'frequency coalescence' relates closely to flutter speed. The turning value is given by the comparatively simple expression from Ref 14:

$$y_{FC} = \frac{(e_{22} - e_{11})}{(e_{22} + e_{11})\left[(c_{11} - c_{22}) + 2(-c_{12}c_{21})^{\frac{1}{2}}\right]} . \qquad \text{(A-2)}$$

When the values of these scaled coefficients for increasing M_∞ are inserted, it becomes clear that c_{22} is the most significant coefficient, variations in c_{11}, c_{12} and c_{21} tending to have smaller effects. Therefore c_{22} has been found to have two effects relating to the increased flutter speed through its influence on the turning value of y for the $\sigma = 0$ conics and on the upper slopes of these conics.

Coefficient c_{22} corresponds to the direct aerodynamic stiffness in the wing torsion mode, and its value obviously relates to the spanwise distributions of local lift curve slope and local aerodynamic centre, especially over the outer part of the span. Coefficient c_{12}, representing the force in the bending mode due to the torsional motion, will depend mostly on the values of the local lift curve slope. As M_∞ increases from 0.84 to 0.88, c_{12} is increased by about 22%, but the value of c_{22} is reduced to 18% of its value at $M_\infty = 0.84$. This reduction is associated primarily with a rearward shift of local aerodynamic centre which more than compensates for the effect of increased lift curve slope. Coefficient c_{21} from the force in the torsion mode due to wing bending is reduced to 43% of its $M_\infty = 0.84$ value as M_∞ is increased to 0.88. A reduction in this coefficient would also be expected from a rearward shift in local aerodynamic centre. It is concluded that the rearward shift in ξ_{ac} with increasing M_∞ in the upper diagram of Fig 12 is playing a large part in the increasing flutter speeds in Table 5.

The significance of the direct aerodynamic stiffness coefficient in the wing torsion mode could no doubt have been found by an automatic process of repeated flutter solutions with arbitrary variations in each of the aerodynamic damping and stiffness coefficients in the original five-degree-of-freedom calculation. The advantage of the graphical representation of Ref 14 is that the computation required is very much less. Moreover, the bird's-eye view of the problem is valuable for its indication of the flutter mechanism and for guidance on the effect of various coefficients in combination, which would usually result from physical changes in the aerodynamics.

Table 1

CALCULATED AND MEASURED MODES AND FREQUENCIES

Mode number	Mode description	Mode frequency (Hz)	
		Calculation	Experiment
1	Fundamental bending	37.3	36.8
2	First overtone bending	116.7	113.4
3	Second overtone bending	253.9	269.0
4	Fundamental torsion	323.6	326.5
5	Third overtone bending	446.9	406.5

Table 2

EXPERIMENTAL FLUTTER RESULTS

Root condition	M_∞	V_f (m/s) E.A.S.	$\sqrt{\sigma}$	f_f (Hz)	$\bar{\nu}_f$ (derived)
Free	0.749	304	1.237	116	0.57
Free	0.803	278	1.064	100	0.46
Locked	0.803	278	1.064	100	0.46
Free	0.843	260	0.955	89	0.40
Locked	0.852	257	0.935	88	0.39
Locked	0.871	257	0.917	86	0.37
Free	0.874	260	0.925	85	0.37
Free	0.889	334	1.171	120	0.51
Free	0.900	>352	>1.219	-	-

Table 3

AERODYNAMIC FORCE MATRICES FOR MODES 1 AND 4

$M_\infty = 0.88, \qquad \bar{\nu} = 0.428$

(a) Linear theory (Ref 3)

$$\begin{pmatrix} 0.210 & 0.493 \\ -0.024 & -0.034 \end{pmatrix} + i\bar{\nu}\begin{pmatrix} 0.604 & 0.007 \\ -0.010 & 0.070 \end{pmatrix}$$

(b) Ref 7 with inviscid TSP data

$$\begin{pmatrix} 0.304 & 0.730 \\ -0.013 & -0.008 \end{pmatrix} + i\bar{\nu}\begin{pmatrix} 0.955 & 0.130 \\ 0.019 & 0.063 \end{pmatrix}$$

(c) Ref 7 with viscous TSP data

$$\begin{pmatrix} 0.236 & 0.553 \\ -0.018 & -0.021 \end{pmatrix} + i\bar{\nu}\begin{pmatrix} 0.697 & 0.043 \\ -0.002 & 0.054 \end{pmatrix}$$

Table 4

CALCULATED EQUIVALENT AIR SPEEDS AT FLUTTER

(a) Lifting-surface aerodynamics

Aerodynamics	M_∞	α_0 (deg)	V_f (m/s)	$\bar{\nu}_f$
Lifting-surface	0.75	Any	296	0.53
	0.80	Any	282	0.46
	0.86	Any	273	0.38
	0.89	Any	268	0.37

(b) Aerodynamics by means of Ref 7

Aerodynamics	M_∞	α_0 (deg)	V_f (m/s)	$\bar{\nu}_f$
Inviscid TSP	0.80	0	272	0.47
	0.84	0	255	0.45
	0.86	0	278	0.46
	0.86	0.5	283	0.46
	0.86	1.0	308	0.46
	0.86	1.5	350	0.48
	0.86	2.0	(475)	(0.51)
	0.88	0	>400	-
TSP ($R = 3.4 \times 10^6$)	0.86	0	261	0.43
	0.88	0	326	0.45
	0.885	0	>450	-
TSP ($R = 3.5 \times 10^7$)	0.86	0	264	0.44

(c) Strip-theory aerodynamics

Aerodynamics	M_∞	α_0 (deg)	V_f (m/s)	$\bar{\nu}_f$
Inviscid TSP	0.80	0	241	0.70
	0.84	0	225	0.65
	0.86	0	288	0.56
TSP ($R = 3.4 \times 10^6$)	0.86	0	232	0.63
	0.88	0	-	-

Table 5

COMPARISON OF FLUTTER SPEEDS FROM FULL SOLUTIONS AND EQUIVALENT BINARY SOLUTIONS

Inviscid TSP	Values of V_f (m/s)		
	$M_\infty = 0.84$	$M_\infty = 0.86$	$M_\infty = 0.88$
Full solution	255	278	>400
Binary solution	265	294	398

REFERENCES

No.	Author	Title, etc
1	L. Martin	High aspect ratio wing flutter model. Unpublished report, 1976
2	R.E.J. Brazier	Theoretical and experimental flutter investigations on a high aspect ratio wing model. Unpublished report, 1977
3	D.E. Davies	Theoretical determination of subsonic oscillatory airforce coefficients. RAE Technical Report 76059, ARC R & M No.3804 (1976)
4	H. Tijdeman	Investigations of the transonic flow around oscillating airfoils. NLR TR 77090 U (1977)
5	W.H. Weatherill F.E. Ehlers J.D. Sebastian	Computation of the transonic perturbation flow fields around two- and three-dimensional oscillating wings. NASA CR-2599 (1975)
6	H.C. Garner	A practical approach to the prediction of oscillatory pressure distributions on wings in supercritical flow. RAE Technical Report 74181, ARC CP 1358 (1975)
7	H.C. Garner	A practical framework for the evaluation of oscillatory aerodynamic loading on wings in supercritical flow. AGARD-CP-226, Paper 16 (1977)
8	Doris E. Lehrian H.C. Garner	Theoretical calculation of generalized forces and load distribution on wings oscillating at general frequency in a subsonic stream. RAE Technical Report 71147, ARC R & M No.3710 (1971)
9	C.M. Albone M.G. Hall Gaynor Joyce	Numerical solutions for transonic flows past wing-body combinations. IUTAM Symposium Transonicum II, Göttingen, September 1975, pp 541-548, Springer-Verlag (1976)
10	M.C.P. Firmin	Calculations of transonic flow over wing/body combinations with an allowance for viscous effects. AGARD Fluid Dynamics Panel Symposium on Viscous-Inviscid Interactions, Colorado Springs, 29 September-1 October 1980
11	J.E. Green D.G. Weeks J.W.F. Brooman	Prediction of turbulent boundary layers and wakes in compressible flows by a lag-entrainment method. RAE Technical Report 72231, ARC R & M No.3791 (1972)
12	P.D. Smith	An integral prediction method for three-dimensional compressible turbulent boundary layers. RAE Technical Report 72228, ARC R & M No.3739 (1972)
13	R.E.J. Brazier	The prediction of flutter using an aerodynamic strip theory approach. Unpublished report, 1980
14	Ll. T. Niblett	A graphical representation of the binary flutter equations in normal co-ordinates. RAE Technical Report 66001, ARC R & M No.3496 (1966)
15	J.C.A. Baldock	A technique for analysing the results of a flutter calculation. RAE Technical Report 73168, ARC R & M No.3765 (1973)

Copyright ©, Controller HMSO, London 1980

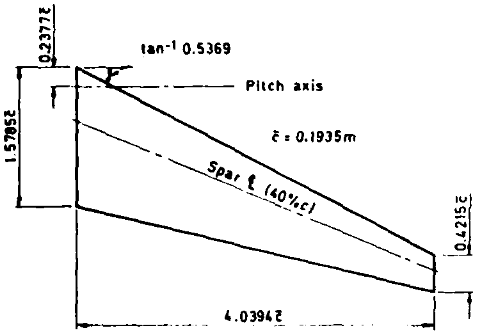
0.2377c̄
tan⁻¹ 0.5369
Pitch axis
1.5785c̄
c̄ = 0.1935m
Spar ℄ (40%c)
0.4215c̄
4.0394c̄

a Details of the planform

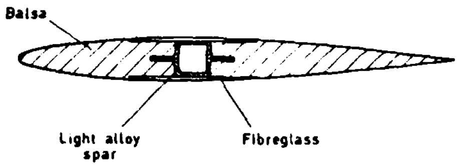
Balsa
Light alloy spar
Fibreglass

b Cross-section through the model (NACA64A010)

Fig 1 Geometry and construction of the flutter model

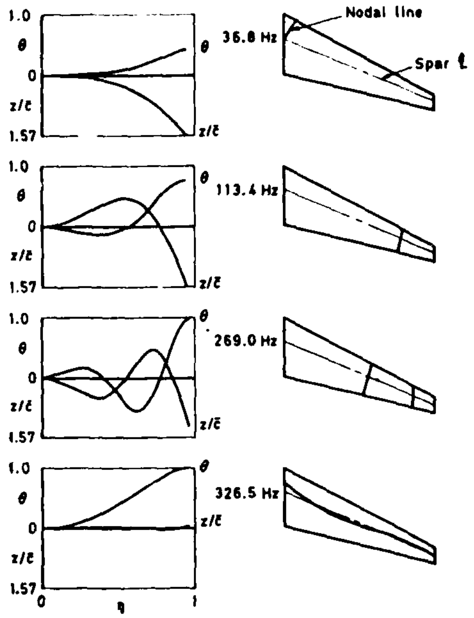

Fig 2 Measured modes with root mounting block free

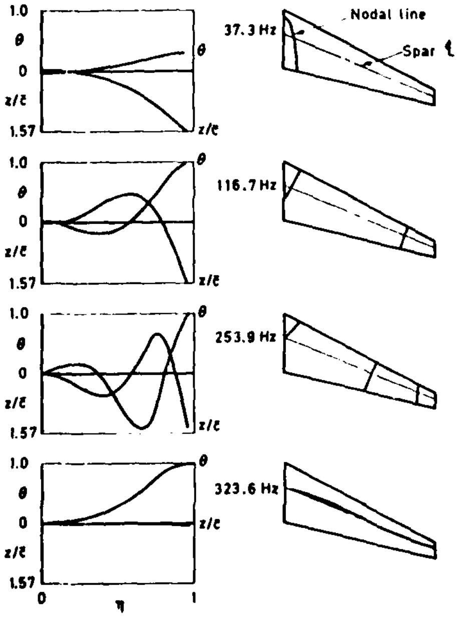

Fig 3 Calculated modes with root mounting block free

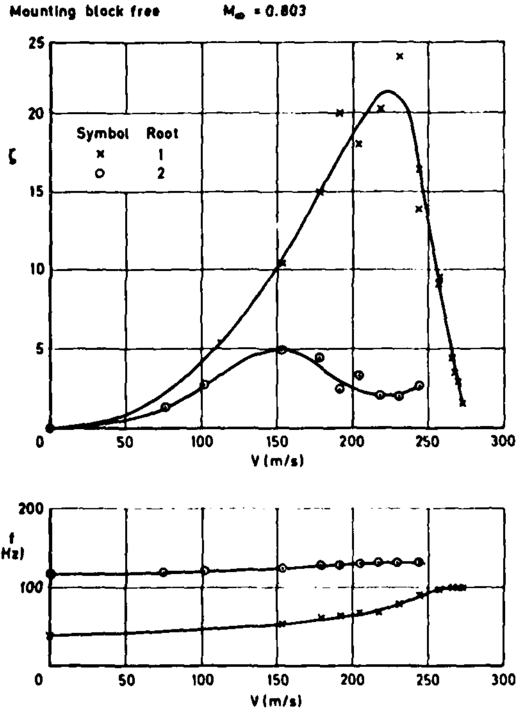

Fig 4 Measured critical damping and frequency of two bending modes

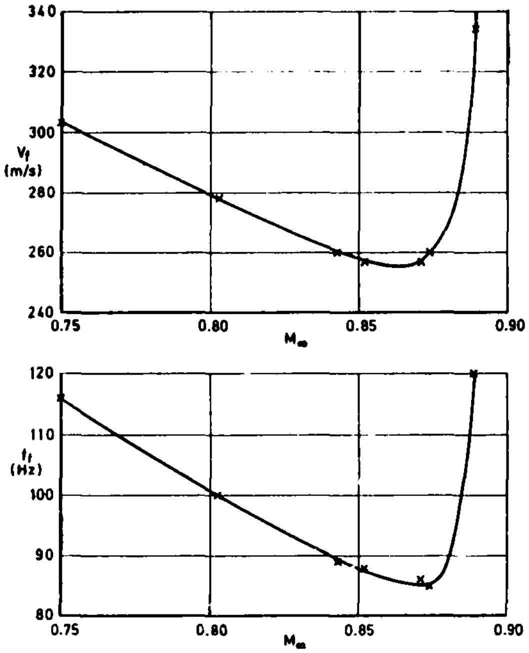

Fig 5 Measured flutter speed and frequency against Mach number

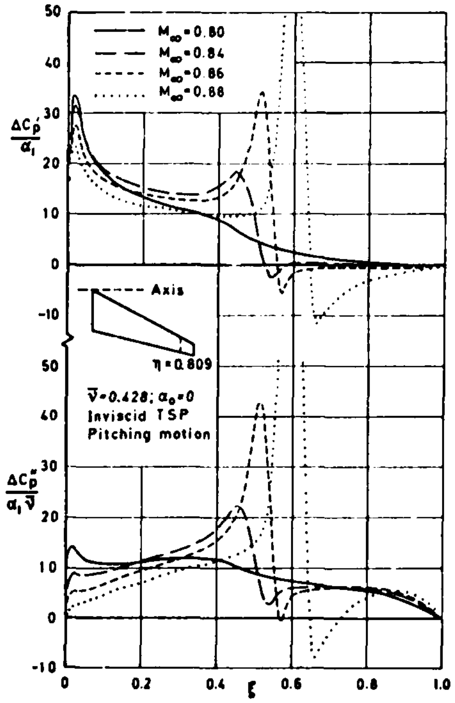

Fig 6 Calculated effect of Mach number on oscillatory chordwise loading

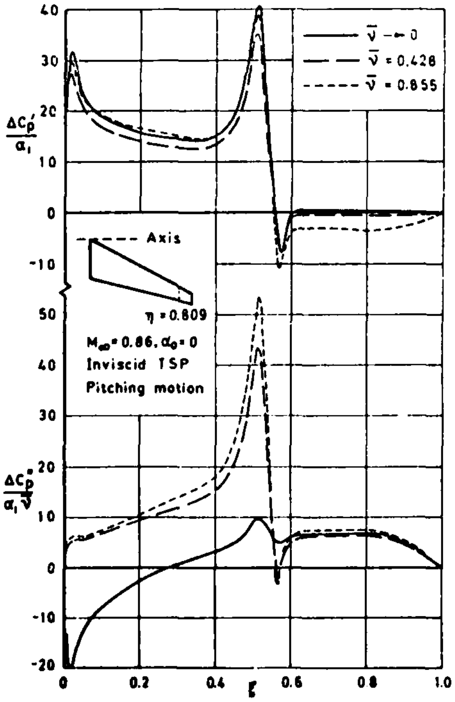

Fig 7 Calculated effect of frequency on chordwise loading

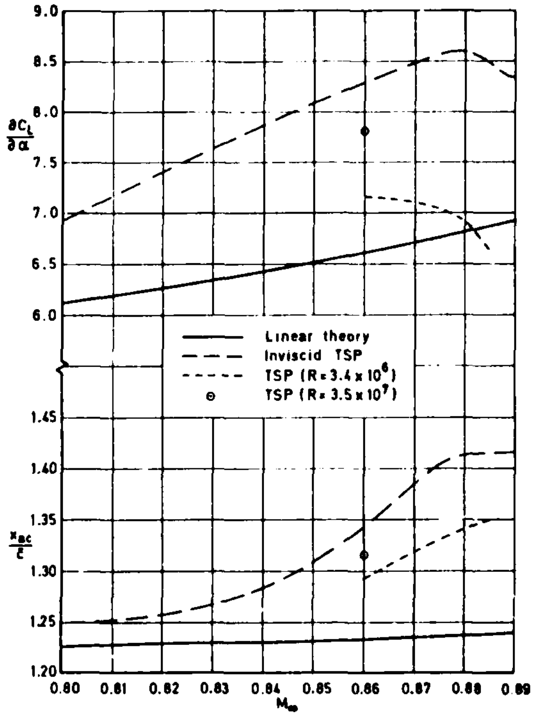

Fig 8 Calculated lift slope and aerodynamic centre against Mach number

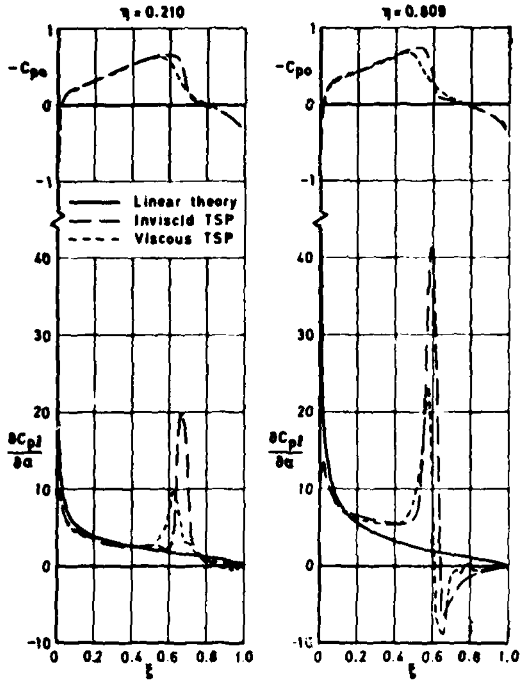

Fig 9 Calculated steady and quasi-steady pressure distributions (M_∞ = 0.88, α = 0)

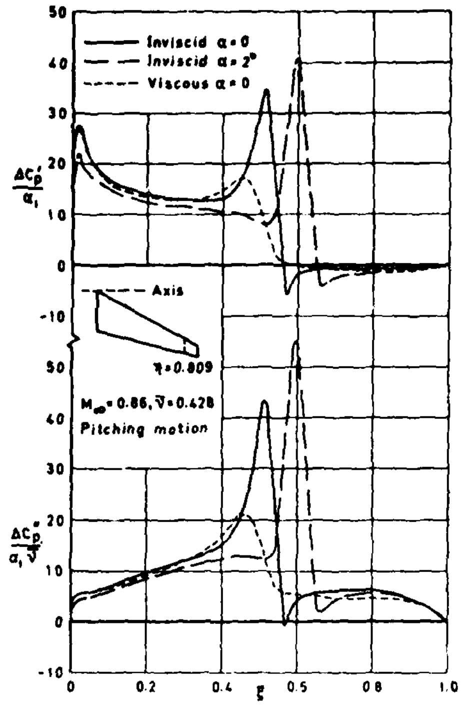

Fig 10 Calculated effects of viscosity and incidence on oscillatory loading

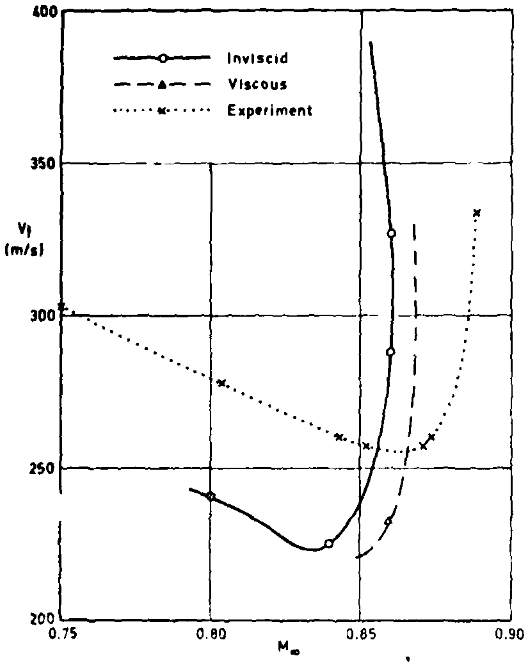

Fig 11 Flutter speeds predicted using strip-theory aerodynamics

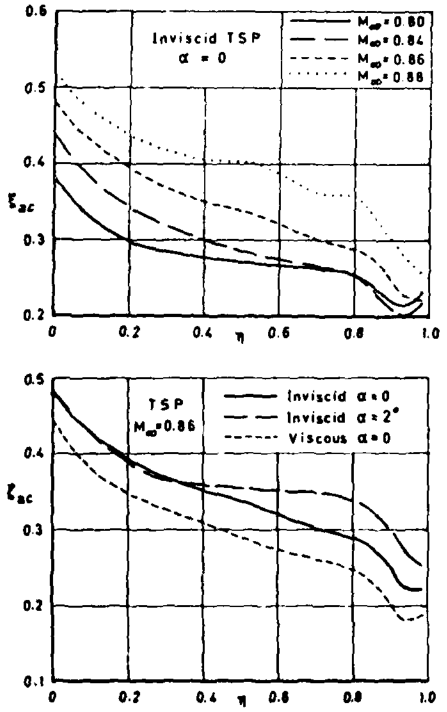

Fig 12 Local aerodynamic centres from various TSP solutions

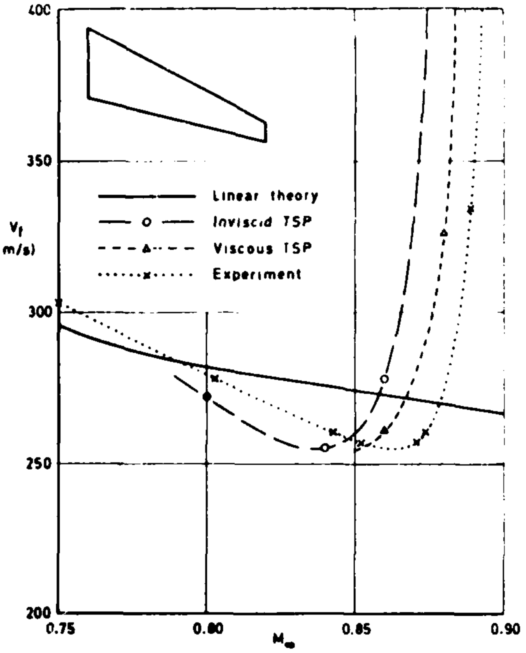

Fig 13 Calculated and measured equivalent air speed at flutter

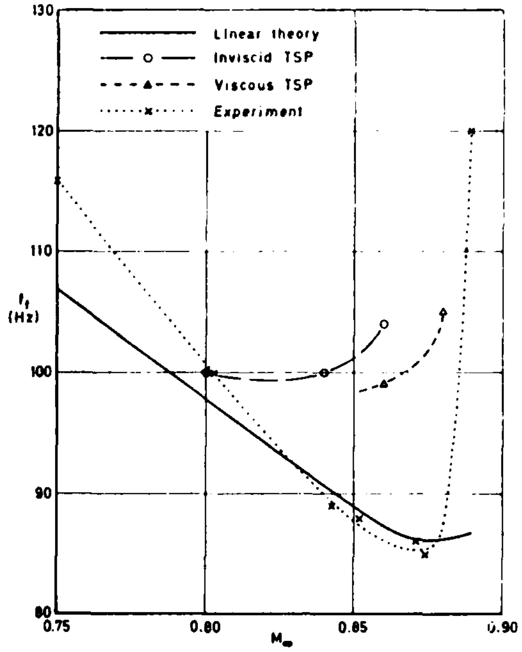

Fig 14 Calculated and measured frequency at flutter

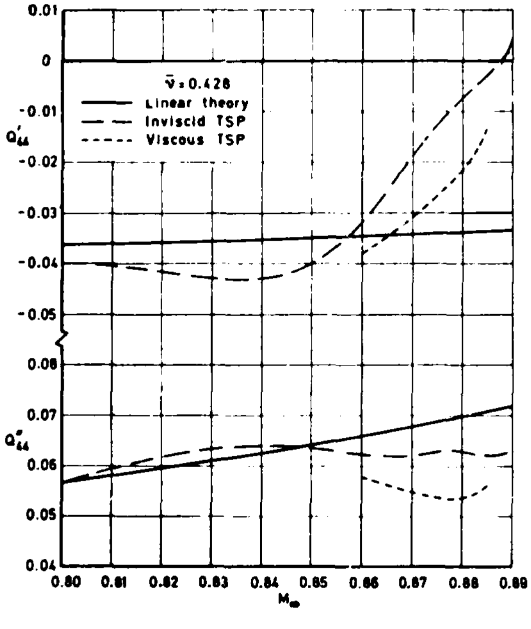

Fig 15 Calculated aerodynamic coefficients in fundamental torsion mode

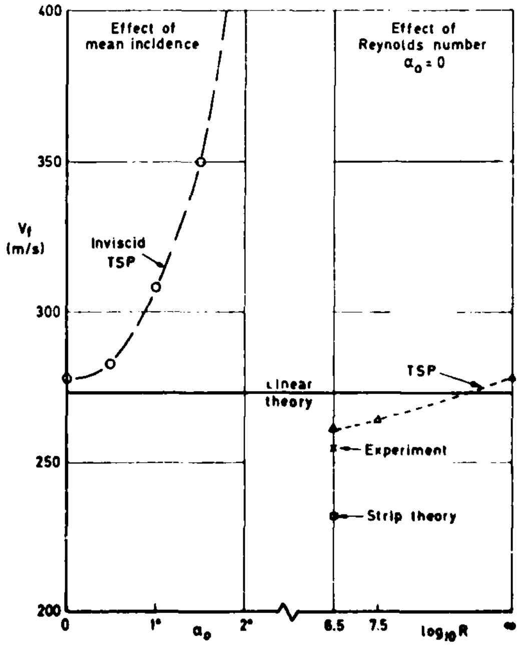

Fig 16 Estimated flutter speeds at $M_\infty = 0.86$

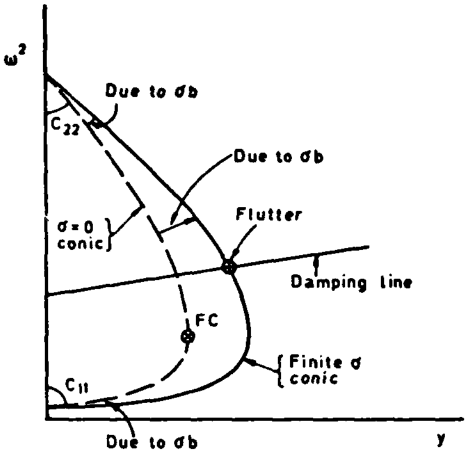
ω^2
Due to σb
C_{22}
Due to σb
Flutter
$\sigma = 0$ conic
Damping line
FC
Finite σ conic
C_{11}
Due to σb
y

Fig 17 Typical graphical representation

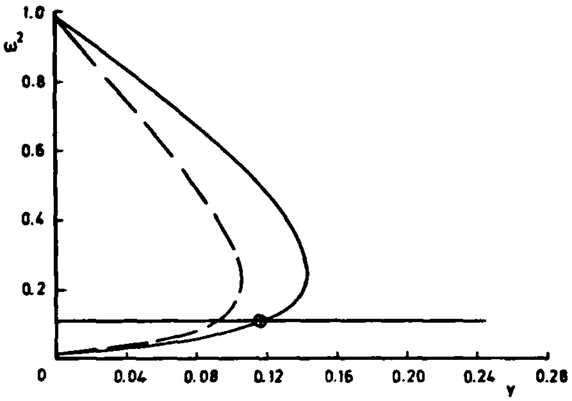

Fig 18 Graphical representation of flutter at $M_\infty = 0.84$

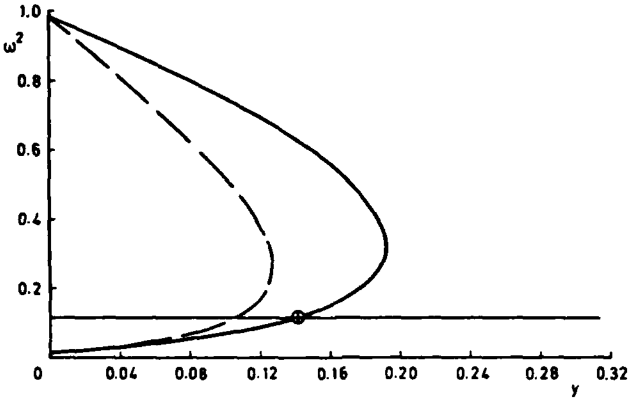

Fig 19 Graphical representation of flutter at $M_\infty = 0.86$

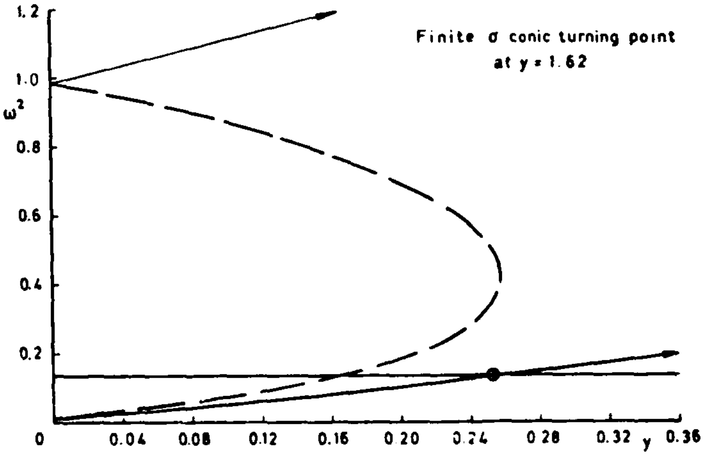

Fig 20 Graphical representation of flutter at $M_\infty = 0.88$

ANALYSIS OF TURBULENT FLOW ABOUT AN ISOLATED AIRFOIL USING A TIME-DEPENDENT NAVIER-STOKES PROCEDURE

by

S. J. Shamroth, Vice-President
H. J. Gibeling, Research Scientist
SCIENTIFIC RESEARCH ASSOCIATES, INC.
Glastonbury, Connecticut 06033, U.S.A.

SUMMARY

A compressible time-dependent Navier-Stokes calculation procedure which includes a transition turbulence model is applied to the isolated airfoil problem. The procedure solves the Navier-Stokes equations by the consistently split linearized block implicit method of Briley and McDonald in a body fitted coordinate system. The procedure is described and results are presented for flow about an airfoil whose incidence changes from 6 degrees to 19 degrees at a Reynolds number of one million and Mach number of 0.2. In addition, the unsteady flow about an airfoil held at a constant 19 degree incidence is examined and compared to data.

INTRODUCTION

The continued rapid development of computer hardware accompanied by rapid advances in numerical techniques have led to a very significant broadening of the practical choices available for analyzing viscous flow fields. Prior to recent computational advances predictive methods for viscous flow were confined primarily to empirical correlations or integral boundary layer solutions; however, computational techniques now allow routine solutions of the two-dimensional laminar and turbulent boundary layer equations. More recently attention has focused upon complex viscous flow fields which are not suited to analysis by two-dimensional boundary layer approaches and one important problem of this type is the general flow about a two-dimensional isolated airfoil.

The isolated airfoil flow problem is a classical problem of practical importance which arises in a variety of flow applications. Much of the initial impetus for predicting the isolated airfoil flow field was generated by the need to determine the lift characteristics of various airfoil shapes as a function of the incidence angle. Although initial studies focused upon the case of an airfoil at constant incidence, later studies include airfoils with time varying motion, and more recent efforts have begun to consider the aerodynamic flutter problem where aerodynamic and aeroelastic phenomena interact to determine the flow field solution.

If the airfoil flow field is well-behaved; i.e., if the boundary layer remains unseparated, then good predictions of lift for airfoils in steady flow can be obtained from a purely inviscid analysis. Obviously, an inviscid analysis does not contain a loss mechanism and if aerodynamic losses are required, they can be obtained from an empirical correlation or from a boundary layer type analysis. The prediction of the airfoil flow field at higher incidences where boundary layer separation occurs is more difficult.

When the viscous layer on the airfoil surface exhibits regions of significant separation, a purely inviscid analysis will not suffice even if only lift predictions are of interest. In the presence of significant separation, the observed pressure distribution will differ considerably from that predicted from inviscid flow considerations. The actual pressure distribution corresponds to that around a body equivalent in shape to the airfoil plus a displacement correction (for viscous displacement effects), and in the presence of large separated regions the displacement correction is not small. In such cases an analysis which is more complete than a purely inviscid analysis is required. One possibility for solving the separated airfoil flow field problem is the boundary layer strong interaction approach. In this approach an inviscid analysis and a boundary layer type analysis are solved so that the viscous displacement effects resulting from boundary layer growth influence the inviscid pressure distribution. Although this approach can give good results for some cases, it does have certain drawbacks. Usually, the approach requires an iteration between the two solutions and in the case of subsonic flow the iteration is a global one; i.e., the inviscid analysis is solved for a given displacement surface. The inviscid pressure distribution is then imposed upon the boundary layer equations and these equations are solved to predict the boundary layer development including a new displacement surface and the process is repeated. This iteration process may be difficult to converge under some circumstances, for example when large regions of separation occur or when the flow is transonic. Furthermore, assumptions may be required to treat the boundary layer equations in separated regions and normal pressure gradients must be assumed negligible in the viscous flow region. The drawbacks associated with boundary layer strong interaction techniques have led some investigators to seek an alternate means of predicting airfoil flow fields; one such alternate approach is a solution of the full Navier-Stokes equations.

One early application of the Navier-Stokes analysis to the isolated airfoil flow problem was performed by Mehta and Lavan (Ref. 1) who solved a stream function vorticity formulation of the laminar incompressible Navier-Stokes equations to predict flow about an impulsively started airfoil. Although this method required considerable computer run time, its excellent results convincingly demonstrated the practical benefits which could be realized from Navier-Stokes solutions. In another early investigation Lugt and Haussling (Ref. 2) utilized an incompressible stream function-vorticity approach to investigate flow about an abruptly started elliptical cylinder. More recent incompressible stream function-vorticity analyses have focused upon various aspects of the airfoil flow field problem. For example, Mehta (Ref. 3) used a numerical scheme considerably more efficient than that of Ref. 1 to solve incompressible laminar flow about an airfoil oscillating through incidence regimes in which stall occurs. Wu and Sampath (Ref. 4) and Wu, Sampath and Sankar (Ref. 5) applied the Wu-Thompson integro-differential formulation (Ref. 6) to both the impulsively started airfoil and the oscillating airfoil problem. In a similar vein Kinney and Cielak (Refs. 7 and 8) have investigated unsteady airfoil flow fields and Lugt and Haussling (Ref. 9) have investigated the time scale required to establish the Joukowski condition in incompressible flow. Finally, Thompson and his coworkers (e.g. Ref. 10) have calculated the flow about a variety of airfoil shapes and Hodge and Stone (Ref. 11) have investigated stalled airfoils using an incompressible primitive variable approach.

Although arguments can be made in favor of one of these procedures versus the other, it is clear that as a group these efforts have demonstrated that application of Navier-Stokes formulations to the airfoil problems are both feasible and practical. However, these procedures all have been limited by assumptions of (i) incompressibility and (ii) laminar flow. In regard to the first of these items, the preceding analyses all are incompressible and none except possibly that of Hodge and Stone can be extended readily to the compressible case. In regard to the second limitation, all these analyses assume the flow to be laminar, although presumably this assumption can be relieved in a straightforward manner if simple eddy viscosity and forced transition concepts are accepted.

The problem of eliminating the incompressible assumption from the full Navier-Stokes equations for airfoil flow field calculations has been the subject of a number of investigations. Verhoff (Ref. 12) applied MacCormack's fully explicit method (Ref. 13) to the airfoil problem; however, since the procedure is fully explicit, a small time step is necessary to maintain numerical stability as a result of the locally refined mesh in the boundary layer and long computer run times result. In this regard conditionally stable schemes such as fully explicit schemes are not an optimum choice when mesh refinement is required for boundary layer definition; in these schemes the maximum allowable time step size is limited by the spatial step size leading to large run times. The time-step limitation problem, which is severe even in laminar flows, is magnified considerably in turbulent flows where a much finer spatial resolution is required in the boundary layer. On the other hand, unconditionally stable schemes (in a linear sense) such as some of the implicit schemes do not uffer from this characteristic. Both Deiwert's (Ref. 14) and Levy's (Ref. 15) analyses are based upon MacCormack's more recent hybrid implicit-explicit-characteristics scheme (Ref. 16). By virtue of an enlarged stability bound this new procedure is more efficient than the original MacCormack procedure (Ref. 13) for airfoil calculations; however, it does present formidable coding problems. Implicit schemes, although more complicated to code than explicit schemes, do not present the formidable coding problems associated with the hybrid scheme. An implicit solution of the full Navier-Stokes equations has been developed by Gibeling, Shamroth and Eiseman (Ref. 17) who applied the Briley-McDonald (Ref. 18) numerical technique to the airfoil flow field. A similar approach has since been used by Sankar and Tassa (Ref. 19) to study an oscillating airfoil in a compressible low Reynolds number fluid. In another approach Steger (Ref. 20) used the thin shear layer equations in conjunction with the coordinate generation procedure of Thompson, Thames and Mastin (Ref. 21) to predict laminar flow about an airfoil. The equations solved in Ref. 20 are a reduced set of equations which retain only the viscous stress terms important in thin shear layer flows.

Although these various approaches have focused upon the compressible problem, they have been confined to laminar flow whereas most flow fields of practical interest are turbulent. In principle a laminar procedure can be extended to turbulent flow in a straight forward manner if eddy viscosity and forced transition concepts are accepted. However, in the general airfoil flow field the eddy viscosity assumption which relates the eddy viscosity to the mean flow via an algebraic equation is expected to be inadequate. The eddy viscosity assumption is particularly suspect in regions of strong pressure gradients and may be inappropriate in regions of separated flow. In addition, an important component of the flow field development may be the transition process since early transition may inhibit separation. In this regard a forced transition model, where the transition location is uniquely related to some mean flow parameter such as a boundary layer integral thickness, may lead to serious errors in the predicted results. Thus, a more general turbulence model is sought. Finally, the airfoil flow field contains regions of laminar, transitional and turbulent flow and, therefore, any model used must be appropriate for all three flow regimes. Such a model has been applied by Shamroth and Gibeling to the airfoil flow field problem (Ref. 22). The model used combines a turbulence energy partial differential equation with an algebraic length scale equation, and in Ref. 22 the model was used to predict airfoil flow fields at both zero and six degrees incidence. Although the predicted results at these incidence angles were encouraging, they did not address the problem of the stalled airfoil in a high Reynolds number turbulent flow. The present paper focuses upon the airfoil at high incidence angle as it considers flow about an airfoil in ramping motion as well as flow about an airfoil at high incidence.

ANALYSIS

The Coordinate System

The presence of bounding surfaces of a computational domain which do not fall upon coordinate lines presents significant difficulties for numerical techniques which solve the Navier-Stokes equations. If a bounding surface (such as the airfoil surface) does not coincide with a coordinate line, serious numerical errors may arise in the application of boundary conditions and considerable effort may be required to reduce these errors to an acceptable level. Although this problem arises in both viscous and inviscid flows, it is more severe in viscous flows where no-slip conditions on solid walls can combine with boundary condition truncation error to produce numerical solutions which are both qualitatively and quantitatively in error. Thus coordinate systems are sought in which each no-slip surface of the specific problem falls on a coordinate line. Such a system is termed a body-fitted coordinate system. Several approaches are available to form a body-fitted coordinate system. Among the coordinate system candidates are conformal coordinate systems such as that used by Mehta (Ref. 3), systems based upon solution of a Poisson equation such as those developed by Thompson and his coworkers (e.g. Ref. 21) or Haussling (Ref. 23) and a constructive system.

The approach used in the present effort is a constructive approach in which the required airfoil is by definition a coordinate line and in which grid point placement is specified by the user. The procedure was developed originally for the isolated airfoil problem by Gibeling, Shamroth and Eiseman (Ref. 17) and extended to the cascade by Eiseman (Ref. 24); the application of the procedure to the airfoil problem is described in Ref. 25. The coordinate system generated by the constructive process has several advantages. The system allows packing of grid points in regions where high grid resolution is required. In general, the high resolution regions are required near the airfoil surface (where the boundary layer is found) and in the vicinity of the airfoil leading edge where rapid streamwise changes are present. In addition, although the grid has a branch cut emanating from the airfoil trailing edge, metric data is continuous across the branch cut. Furthermore, although the grid is nonorthogonal, the amount of nonorthogonality is not large. Finally, as applied to the airfoil problem the metric data remains smooth from grid point to grid point. A sketch of the coordinate system is shown in Fig. 1 and a fuller discussion is presented in Refs. 24 and 25.

Mean Flow Equations

A solution of the compressible, time-dependent Navier-Stokes equations in conjunction with a suitable turbulence model would serve to predict the flow field for both laminar and turbulent flows. The form of the equations expressed in the more common coordinate systems can be found in standard fluid dynamic texts and the equations themselves have been derived in general tensor form by McVitte (Ref. 26) for inviscid flow and by Walkden (Ref. 27) for viscous flow.

One possible approach for solving the equations in general nonorthogonal form is the strong conservation approach such as that used by Steger (Ref. 20) and Thomas and Lombard (Ref. 28). A second possible approach solves a set of equations in which the metric coefficients do not appear within derivatives (quasilinear form). In both cases the independent spatial variables are transformed from the Cartesian coordinates (x,y) to a new set of coordinates (ξ,η) where

$$\begin{aligned} \xi &= \xi(x,y,t) \\ \eta &= \eta(x,y,t) \\ \tau &= t \end{aligned} \tag{1}$$

The stong conservation form of the equations then becomes

$$\begin{aligned} &\frac{\partial W/D}{\partial \tau} + \frac{\partial}{\partial \xi}\left[\frac{W\xi_t}{D} + \frac{F\xi_x}{D} + \frac{G\xi_y}{D}\right] + \frac{\partial}{\partial \eta}\left[\frac{W\eta_t}{D} + \frac{F\eta_x}{D} + \frac{G\eta_y}{D}\right] \\ &= \frac{1}{Re}\left[\frac{\partial}{\partial \xi}\left(\frac{F_1\xi_x}{D} + \frac{G_1\xi_y}{D}\right) + \frac{\partial}{\partial \eta}\left(\frac{F_1\eta_x}{D} + \frac{G_1\eta_y}{D}\right)\right] \end{aligned} \tag{2}$$

where

$$D = \xi_x\eta_y - \xi_y\eta_x$$

$$W = \begin{pmatrix} \rho \\ \rho u \\ \rho v \end{pmatrix}, \quad F = \begin{pmatrix} \rho u \\ \rho u^2 + p \\ \rho uv \end{pmatrix}, \quad G = \begin{pmatrix} \rho v \\ \rho uv \\ \rho v^2 + p \end{pmatrix} \quad F_1 = \begin{pmatrix} 0 \\ \tau_{xx} \\ \tau_{xy} \end{pmatrix} \quad G_1 = \begin{pmatrix} 0 \\ \tau_{xy} \\ \tau_{yy} \end{pmatrix} \tag{3}$$

The quasilinear form of the equations is expressed as

$$\begin{aligned} &\frac{\partial W}{\partial \tau} + \xi_t\frac{\partial W}{\partial \xi} + \xi_x\frac{\partial F}{\partial \xi} + \xi_y\frac{\partial G}{\partial \xi} + \eta_t\frac{\partial W}{\partial \eta} + \eta_x\frac{\partial F}{\partial \eta} + \eta_y\frac{\partial G}{\partial \eta} \\ &= \frac{1}{Re}\left[\xi_x\frac{\partial F_1}{\partial \xi} + \eta_x\frac{\partial F_1}{\partial \eta} + \xi_y\frac{\partial G_1}{\partial \xi} + \eta_y\frac{\partial G_1}{\partial \eta}\right] \end{aligned} \tag{4}$$

It should be noted that in both approaches the dependent variables are the density, ρ, and the Cartesian velocity components.

The problem of proper equation form in non-Cartesian spatial variables has been discussed by several investigators (e.g., Refs. 22 and 28). If the strong conservation form of the equations is to be used then care must be taken to evaluate the metric data by a method which is consistent with a control volume approach (Ref. 28). Usually this requires numerical evaluation of the metric data even if an analytic functional relationship for the transformation is available. The analytic representation of the metric data, ξ_x, ξ_y, etc., when combined with the strong conservation form of the equations leads to significant error for as straightforward a calculation as low Reynolds number flow about a circular cylinder (Ref. 22). In a private communication (Ref. 29) Thompson has suggested that the discrepancy shown in Ref. 22 would be decreased or eliminated by use of numerically evaluated metric coefficients. Thus in the case of a time-independent Jacobian, either approach can be expected to yield satisfactory results. The quasilinear form was used in the present effort.

The Turbulence Model

Since the present effort addresses the problem of turbulent flow, it is necessary to specify a turbulence model suitable for this problem. One complicating factor in hypothesizing and applying a turbulence model for the isolated airfoil flow field is that the flow is not turbulent everywhere. Far from the airfoil the flow is inviscid and irrotational. In addition, even near the airfoil surface the flow is laminar in the vicinity of the airfoil leading edge. Thus any proposed model must be capable of dealing with laminar, transitional and turbulent flow. Although a turbulent calculation could be obtained by assuming an eddy viscosity model, eddy viscosity (or equilibrium mixing length) models are not appropriate for flows containing large separated regions (e.g. Ref. 30). In addition, if an eddy viscosity model were to be used, then the transition location must be specified and the various transition location correlations may not be appropriate for the very strong pressure gradients found in flow about airfoils at incidence.

The approach taken in the present effort assumes an isotropic turbulent viscosity, μ_T, relating the Reynolds stress tensor to mean flow gradients.

$$-\overline{\rho u_i' u_j'} = \mu_T\left[\left(\frac{\partial u_i}{\partial x_j} + \frac{\partial u_j}{\partial x_i}\right) - \frac{2}{3}\frac{\partial u_k}{\partial x_k}\delta_{ij}\right] \tag{5}$$

The turbulent viscosity is related to the turbulence energy, k, and the turbulence energy dissipation rate, ε, via the Prandtl-Kolmogorov constitutive equation

$$\mu_T = \rho C_\mu k^2/\epsilon \; f(y/\delta) \tag{6}$$

where C_μ is a turbulence structural coefficient and $f(y/\delta)$ is a factor used to ensure small turbulent viscosities at locations far from the airfoil. The function $f(y/\delta)$ is taken as

$$\begin{aligned} f(y/\delta) &= 1.0 \qquad y \le \delta \\ f(y/\delta) &= e^{-b(y/\delta - 1.0)} \qquad y > \delta \end{aligned} \tag{7}$$

where b is a constant. The present approach utilizes the turbulence energy equation, an algebraic length scale equation and a functional form for C_μ in which C_μ is dependent upon turbulence Reynolds number. When this model is used in conjunction with the mean flow equations, both the mean flow and turbulent viscosity emerge from the solution.

The turbulence energy equation has been given by many investigators (e.g. Ref. 31) and can be written as

$$\begin{aligned} \frac{\partial \rho k}{\partial t} + \frac{\partial \rho u k}{\partial x} + \frac{\partial \rho u k}{\partial y} &= \frac{\partial}{\partial x_k}\left[\left(\mu + \frac{\mu_T}{\sigma_k}\right)\frac{\partial k}{\partial x_k}\right] \\ &+ \mu_T\left(\frac{\partial u_i}{\partial x_k} + \frac{\partial u_k}{\partial x_i}\right)\frac{\partial u_i}{\partial x_k} - \rho\epsilon - 2\mu\frac{\partial k^{1/2}}{\partial x_j}\frac{\partial k^{1/2}}{\partial x_j} \end{aligned} \tag{8}$$

The turbulence energy dissipation rate ε, is related to a length scale ℓ, the turbulence energy k, and the structural coefficient C_μ via the equation

$$\epsilon = C_\mu^{3/4}\frac{k^{3/2}}{\ell} \tag{9}$$

The length scale is taken as a minimum value of two lengths; a wall length and a wake length. The wall length is assumed to be given by a conventional wall damped Prandtl's mixing length, via

$$\ell = \kappa y_s\left(1 - e^{-y_s^+/27}\right) \tag{10}$$

with a maximum value of 0.09 δ. In Eq. (10) κ is the von Karman constant taken as 0.43, y^+ is the dimensionless distance from the airfoil surface and δ is the boundary layer thickness. The wake length scale was taken as $\ell = .05\delta$ where δ is the wake thickness. In regions of separated flow the length scale is modified so that $\ell \ge \ell_{min}$ where

$$\ell_{MIN} = 0\ 1h\left(1 - e^{-y^+/27}\right) \tag{11}$$

where h is the local height of the separated region.

Finally, the coefficient C_μ is evaluated following the procedure of McDonald and his coworkers (Refs. 32-34) which has been very successful in predicting boundary layers in forward and reverse transition. This approach relates C_μ to a new coefficient a_1 where

$$a_1 = C_\mu^{1/2}/2 \tag{12}$$

and a_1 is taken as a function of a turbulence Reynolds number, R_τ, of the form

$$a_1 = a_0\left[\frac{f(R_\tau)}{100}\right] \Big/ \left\{1.0 + 6.66\, a_0\left[\frac{f(R_\tau)}{100} - 1\right]\right\} \tag{13}$$

where

$$\begin{aligned} a_0 &= .0115 \\ f(R_\tau) &= 100.\, R_\tau^{0.22} \qquad R_\tau \le 1 \\ f(R_\tau) &= 68\,1\, R_\tau + 614.3 \qquad R_\tau \ge 40 \end{aligned} \tag{14}$$

and a cubic curve is fit for values of R_τ between 1 and 40.

It should be noted that with the current turbulence model the turbulence equations are solved in conjunction with the mean flow equations throughout the flow field. The analysis predicts some regions having a turbulent viscosity much larger than the laminar viscosity (turbulent regions), other regions having a turbulent viscosity on the order of the laminar viscosity (transitional regions), and finally, some regions having turbulent viscosity less than the laminar viscosity (laminar regions). No transition location is input into the analysis.

The Numerical Procedure

The numerical procedure used to solve the governing equations is a consistently split linearized block implicit scheme originally developed by Briley and McDonald (Ref. 18) which is embodied in a computer code termed MINT, an acronym for Multi-dimensional Implicit Nonlinear Time-dependent. The basic algorithm was further developed and applied to both laminar and turbulent flows in a variety of studies (e.g. Refs. 22, 35, 36). A recent comprehensive description of the method is given by Briley and McDonald in Ref. 37.

The method can be outlined as follows: the governing equations are replaced by an implicit time difference approximation, optionally a backward difference or Crank-Nicolson scheme; the backward difference approach was used in the present calculations. Terms involving nonlinearities at the implicit time level are linearized by Taylor expansion about the solution at the known time level, and spatial difference approximations are introduced. The result is a system of multidimensional coupled (but linear) difference equations for the dependent variables at the unknown or implicit time level. To solve these difference equations, the Douglas-Gunn (Ref. 38) procedure for generating alternating-direction implicit (ADI) schemes as perturbations of fundamental implicit difference schemes is introduced in its natural extension to systems of partial differential equations. This technique leads to systems of coupled linear difference equations having narrow block-banded matrix structures which can be solved efficiently by standard block-elimination methods. Details of the procedure are given in Refs. 18, 22 and 37.

Boundary Conditions

An important component of the airfoil analysis concerns specification of boundary conditions. The present analysis requires boundary conditions to be set along the lines $\xi=\xi_{min}$, $\xi=\xi_{max}$, $\eta=\eta_{min}$ and $\eta=\eta_{max}$. With the coordinate system sketched in Fig. 1, $\xi=\xi_{min}$ (line EH) and $\xi=\xi_{max}$ (line DF) are downstream boundaries. In the original formulation (Refs. 17 and 22) first derivatives of all quantities were set to zero along these lines and function conditions for all variables were set on the outer boundary HJNKF. On the airfoil surface no-slip conditions were used in conjunction with an inviscid momentum equation (which for no motion reduced to zero pressure gradient) as boundary conditions and either the turbulence energy or its derivative was specified at the surface. The results presented in Refs. 17 and 22 were obtained with these boundary conditions. More recently the boundary conditions were modified based upon a suggestion by Briley and McDonald (Ref. 36). Following this suggestion, static pressure is specified along with velocity derivatives along the downstream boundaries (lines EH and DF) and along the aft portion of the outer boundary (line segments HJ and KF). Total pressure, angle of incidence and the density derivative are specified along the outer boundary segment JNK. This approach was used successfully by Shamroth, Gibeling and McDonald (Ref. 39) in a Navier-Stokes solution to the cascade problem and has since been incorporated into the airfoil analysis. The ramp motion and nineteen degree incidence results presented here were obtained with this latter set of boundary conditions.

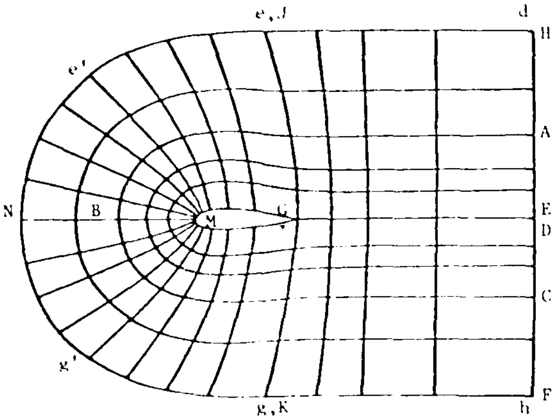

Figure 1. - Sketch of coordinate system.

Grid Spacing and Artificial Viscosity

The solution of the Navier-Stokes equations for an isolated airfoil at high Reynolds number presents a formidable grid resolution problem. If the regions having rapid changes in dependent variables are to be adequately resolved and if the outer boundary is to be placed in a region only modestly perturbed by the airfoil flow field, then considerable grid stretching must be used. In the present calculations the grid was very highly resolved in the vicinity of the airfoil where the first grid point was placed 0.00002 chords from the airfoil surface. In contrast, the grid spacing in the outer region of the flow was of the order of 0.6 chords. Similarly grid points were concentrated in the airfoil leading edge region. Hence, high resolution was obtained in regions where the dependent variables changed rapidly.

A second problem which arises in high Reynolds number flow is the spurious oscillations associated with the so-called "cell Reynolds number problem". In the present approach these oscillations were damped by adding a normal diffusion term to the equations in which the diffusive coefficient μ_a was set by the criterion that the cell Reynolds number be less than or equal to 2. The cell Reynolds number is defined as $\rho u_i \Delta x_i/\mu_a$ where u_i is the velocity component in the ith direction and Δx_i is the grid spacing in the ith direction. If the cell Reynolds number at a given location is less than 2, no artificial diffusion term is added at that location. In the present calculations the cell Reynolds number in the direction normal to the airfoil surface is less than two in the vicinity of the airfoil and, therefore, no artificial diffusion term need be added to the momenta equations in this region. Therefore, the major diffusion process in the calculation is not altered by this artificial damping term.

RESULTS

Low Incidence Cases

A preliminary assessment of the code was made by calculating flow about a NACA0012 airfoil at zero degrees incidence. The Reynolds number for this case was 10^6 and the Mach number was 0.147. Two calculations were made: the first calculation used a coordinate grid of 41x30 points to calculate flow about one-half the symmetric airfoil flow field. The second calculation did not assume symmetry and utilized a grid which gives better resolution in the vicinity of the airfoil. The grid in this case consisted of 81 pseudo-radial lines and 39 pseudo-azimuthal lines with the first pseudo-radial grid point located 0.00002 chords from the airfoil surface and the last pseudo-radial grid point (the outer boundary) located approximately four chords from the airfoil surface. The low incidence calculations were initiated from an approximate inviscid solution with a simple overwrite near the airfoil surface bringing the flow field to a no-slip condition. Convergence was obtained in approximately 150 time steps.

The predicted pressure distribution for the full airfoil calculation along with the results of Mehta (Ref. 3) and the data of Gregory and O'Reilly (Ref. 40) are shown in Fig. 2. As can be seen in Fig. 2, the results of the present calculation are in good agreement with the data except in the aft region of the airfoil. In this region the difference between Mehta's results and the data may result from Mehta's analysis (Ref. 3) being laminar and the data being taken in the turbulent regime. A laminar boundary layer is more susceptible to separation than a turbulent one and indeed, the prediction of Mehta does show separation upstream of the trailing edge whereas the data show the boundary layer to remain attached over the entire suction surface. Therefore, the discrepancy between the data of Ref.40 and the analysis of Mehta could be the result of the computed laminar boundary layer separating and modifying the trailing edge pressure distribution. Likewise, although the present prediction includes a turbulence model, the grid resolution in the vicinity of the airfoil surface still may not be sufficiently fine; consequently a discrepancy in the predicted surface pressure distribution may result. This possibility is given weight in Ref. 22 where an improvement in the aft region surface pressure distribution with increased boundary layer resolution is noted.

Following the zero incidence calculation attention was focused upon prediction of the airfoil flow field at six degrees incidence. Once again the Reynolds number was 10^6 and the Mach number was 0.147. The predicted pressure distribution is compared with the data of Gregory and O'Reilly (Ref. 40) taken for a Reynolds number 2.8×10^6 in Fig. 3. As shown in Fig. 3 the major discrepancy between data and analytic prediction occurs in the leading edge region where the analysis fails to predict the correct suction peak. This discrepancy is at least partially a result of grid resolution. The strong favorable pressure gradient region leading to the suction peak occurs in a very limited region of the flow field between $0\leq x/c\leq 0.01$. This region extends over only one percent of the airfoil chord and only one tenth of one percent of the entire grid extent. In interest of computer run time economy the grid was limited to 81x30 points (a total of 2430 grid points) and even though points were packed into the leading edge region, only four pseudo-radial lines were placed within the favorable pressure gradient region. Thus even with a total of 2430 grid

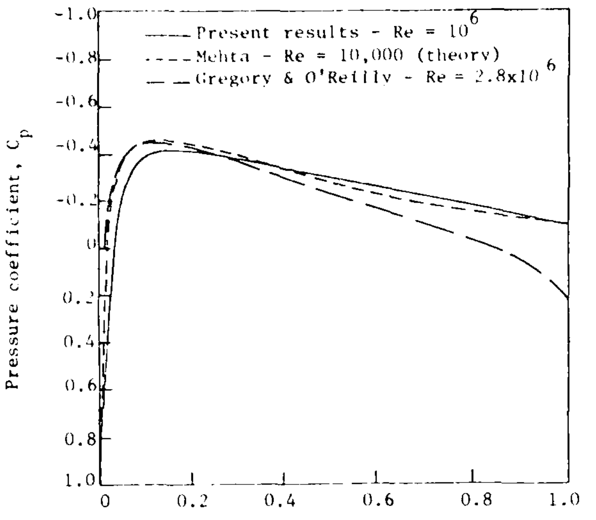

Figure 2. - Surface pressure distribution for NACA 0012 airfoil at zero incidence (full airfoil calculation)

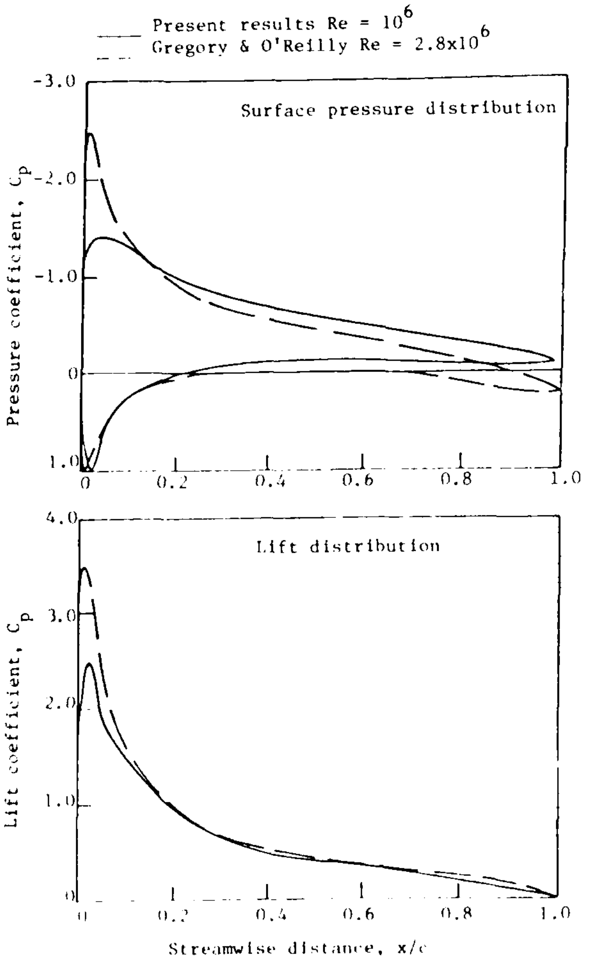

Figure 3. - Surface pressure distribution for NACA 0012 airfoil at 6° **incidence**.

points and significant leading edge grid packing, resolution in this region was marginal. It is expected that increased resolution would result in better agreement with the data.

In regard to other aspects of the flow field the predicted suction surface transition location occurs at $x/c \approx 0.08$. The data of Gregory and O'Reilly gives transition at $x/c \approx 0.04$ for a Reynolds number of 2.8×10^6 and $x/c \approx 0.08$ for a Reynolds number of 1.48×10^6. Thus the predicted transition location is in excellent agreement with data. The transition location predicted on the pressure surface is $x/c \approx 0.30$; thus the pressure surface boundary layer remains laminar considerably longer than does the suction surface boundary layer, as expected. In addition, as shown in detail in Ref. 22, the analysis gives many of the experimentally observed flow phenomena including rapid acceleration around the leading edge, different development of pressure and suction surface boundary layers and different development of pressure and suction surface turbulence energy fields.

Airfoil in Ramp Motion

The next case considered is the NACA0012 airfoil in ramp motion. In this case the Reynolds number was taken as 10^6 and the Mach number as 0.147. A solution was allowed to develop for an airfoil at six degrees incidence and when the flow approached steady state the incidence was changed from 6 to 19 degrees via the equation

$$\alpha=\alpha_0+\frac{(\Delta\alpha)}{2}\,[1.0-\cos\omega(t-t_0)] \qquad t_0<t<(t_0+\Pi)/\omega$$

where

$$a_0=6^\circ,\ \Delta\alpha=13^\circ,\ \omega=5,\ t_0=1.20$$

For $t>(t_0+\Pi)/\omega$, the incidence was held constant at

$$\alpha=\alpha_0+\Delta\alpha$$

The results of the calculation during the ramping period are presented in Figs. 4 and 5. Figure 4 shows the pressure coefficient distribution at various incidence angles. At six degrees the pressure distribution is typical of that found for a steady airfoil; the suction peak has been smeared and diminished due to insufficient streamwise resolution as discussed previously. As the incidence changes from 6 to 9 degrees the rapid motion, particularly in the trailing edge region, causes high pressure to appear on the lower side of the airfoil and low pressures to appear on the upper side. It should be noted that the velocity of the airfoil trailing edge relative to the inertial frame reaches a maximum value of 0.4 U_∞ and, therefore, large deviations from the steady solution are to be expected. The situation becomes more pronounced at 12.5 degrees; however, by 14 degrees a tendency to return to the usual static airfoil pressure distribution appears. Finally, at the last incidence angle, 19 degrees, (t=1.93), the basic pressure distribution is approaching the type expected for a steady airfoil with no evidence of stall. The location of the separation points is presented in Fig. 5. At the initiation of the ramp motion no separated flow was present; however, separation appeared soon after the ramp motion began and the trailing edge separation point moves continuously upstream as shown in the figure. During this process the separated region remains very thin and has only a minimum viscous displacement effect upon the outer nominally inviscid flow.

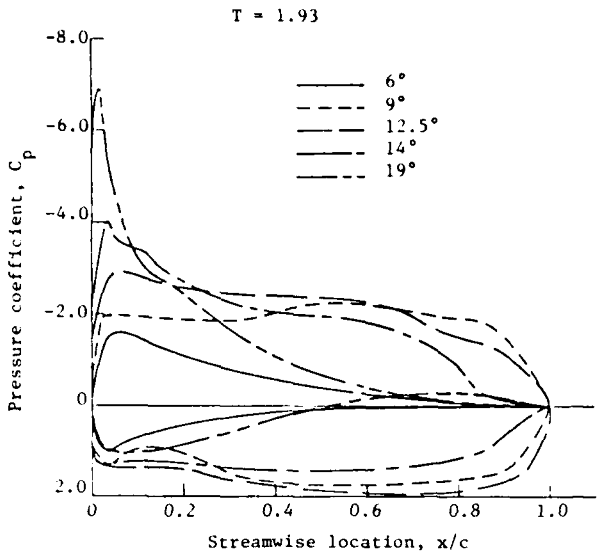

Figure 4. - Pressure coefficient for airfoil in ramp motion.

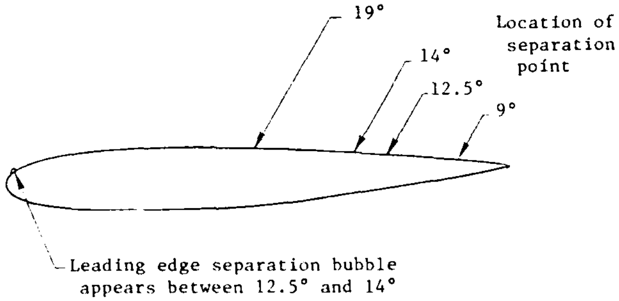
19°
14°
12.5°
9°
Location of separation point
Leading edge separation bubble appears between 12.5° and 14°

Figure 5. - Location of separation points for airfoil in ramp motion.

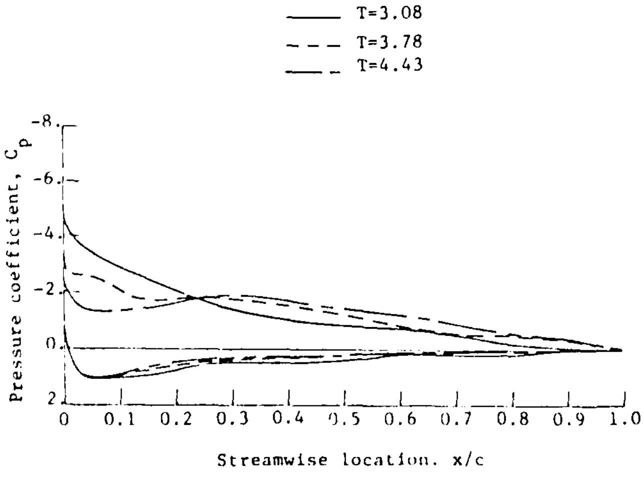

Figure 6. - Pressure distribution for 19° airfoil after cessation of airfoil motion (airfoil motion ceases at T=1.83).

After cessation of the motion the flow continues to develop and the pressure distribution undergoes radical changes as shown in Figs. 6 and 7. The major changes occur in the airfoil leading edge region where the suction peak appearing on the airfoil upper surface continues to drop in magnitude from a value of approximately 6.8 at t=1.83 (just after the cessation of airfoil motion) to a value of approximately 1.2 at t=5.38. A unit increment in t represents the time required for a particle moving at free stream velocity to traverse a distance of one chord. The drop in the suction peak and the accompanying decrease in airfoil lift exhibited in Figs. 4, 6 and 7 are consistent with the development of airfoil stall. The calculation also predicts a minor movement of the airfoil front stagnation point towards the geometric leading edge. In addition to the loss of lift, the analysis predicts a pressure perturbation to initiate at t ≈ 3.7 (see Fig. 6) and then move downstream at a speed of approximately 36% free stream velocity. Although quantitative comparisons between this prediction and data are not available, the predicted flow seems physically realistic.

The Stalled Airfoil - 19 Degrees Incidence

Upon reaching 19 degrees, the motion ceased and as discussed in the previous section the airfoil flow field was allowed to develop at 19°. A comparison of the calculated results and the measured data of Young, Meyers and Hoad (Ref. 41) for an airfoil at 19.4° incidence is presented in Fig. 8. Figure 8 compares the predicted and measured values of the zero velocity line. Below this line the flow is directed toward the leading edge and above this line the flow is directed toward the trailing edge. The predicted values are shown as a function of time. During the ramping process the separated region present was too thin to be shown on the scale of Fig. 8 and the results shown are at times well past the cessation of the ramping motion which ceases at t ≈ 1.9. The results presented in Fig. 8 show the growth of the backflow velocity zone with time, and at the latter times shown the backflow zone position has converged over most of the airfoil as continued growth is confined to regions in the vicinity of the airfoil trailing edge. As can be seen the comparison between predicted zone location and that measured by Young, Meyers and Hoad (Ref. 41) is very encouraging.

A vector plot of the velocity field as measured by Young, Meyers and Hoad is shown in Fig. 9. These results show a large separated region to be present over the airfoil upper surface with separation initiating in the immediate vicinity of the airfoil leading edge. A vortex appears to be centered at roughly the eighty percent chord location. The data (not shown on this figure) indicated that the wake closure point was located well downstream of the airfoil trailing edge and above the airfoil suction surface. Another feature is the appearance of a very strong shear layer in the airfoil trailing edge vicinity where the suction surface and pressure surface flow fields meet. Finally, the calculated results indicate that flow is entrained into the recirculation region from two sources. One source is the flow region above the recirculation zone. The second source is the flow which originates on the airfoil pressure surface, then passes into the mixing layer which forms at the airfoil trailing edge and finally is entrained into the recirculation region from below.

Predicted velocity vector fields are shown in Figs. 10 and 11. These figures represent the flow field at times t_1 and $t_1+\Delta t$ where Δt is the time required for a free stream particle to move a distance of one chord length. As can be seen in the figures, the analysis predicts the formation of a large separation region which initiates very near the airfoil leading edge; this is in agreement with the data shown in Fig. 8. Other similarities between data and analytic prediction can be found in the vortex formation and in the strong shear layer which appears at the airfoil trailing edge. In addition, the calculated flow field was characterized by significant flow unsteadiness in the leading edge region which limited the permissible maximum time step. This characteristic of unsteady leading edge flow also appeared in the experimental study.

In regard to other features the analysis showed the vortex to be moving downstream at a velocity of approximately 0.2 U_∞; however, no regular shedding pattern was observed in the experiment. Some comments on this are in order. First of all the calculation has not yet been run long enough to determine if a regular shedding will result although the first vortex being formed definitely appears to be in the process of shedding. Secondly, although the experiment did not detect any regular shedding pattern, it is possible that an irregular shedding did occur. Finally, the turbulence model used may cause a spurious prediction of shedding.

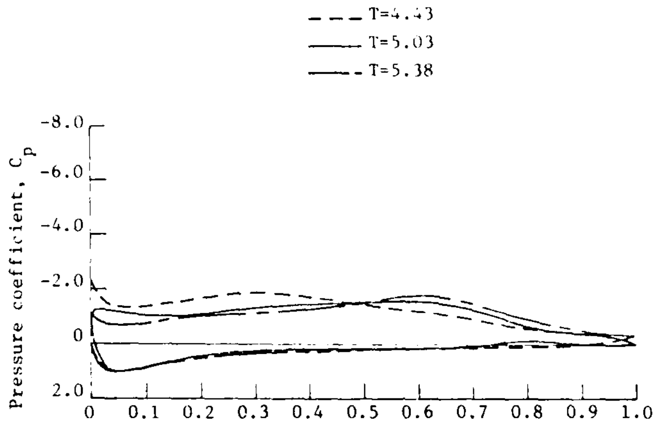

Figure 7. - Pressure distribution for 19° airfoil after cessation of airfoil motion (airfoil motion ceases at T=1.83).

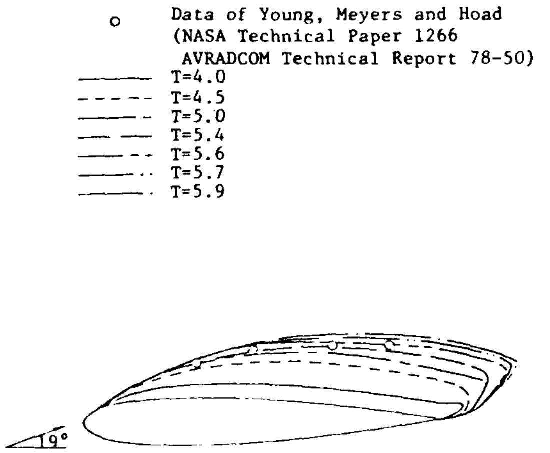
o Data of Young, Meyers and Hoad
(NASA Technical Paper 1266
AVRADCOM Technical Report 78-50)
T=4.0
T=4.5
T=5.0
T=5.4
T=5.6
T=5.7
T=5.9
19°

Figure 8. - Development of backflow velocity zone for airfoil at 19°.

A second feature to be considered is the backflow velocity. The maximum reversed flow velocity measured in the experiment was of the order 0.25 U_∞. The maximum backflow values shown in Fig. 10 are approximately 0.50 U_∞. Although this value is high, modifications in the choice of the separated zone turbulence length scale could decrease this quantity. In calculations performed during this study modifying this length scale significantly changed the backflow velocity without significantly changing other flow features. Finally, it should be noted that the length of the separated zone is still increasing as the wake reattachment point is continuing to move downstream (see Fig. 8). As the separated zone becomes longer, it is possible that the predicted backflow velocity will decrease.

Calculated vorticity contours at the two times are shown in Figs. 12 and 13. The vorticity contours presented correspond to normalized values of -100, -25, -10, -5, 0, 5, 10, 25, 100. In both figures the vorticity on the airfoil pressure surface is confined to the boundary layer whereas that on the suction surfaces occurs in two locations. One region of vorticity is located in the wall layer close to the airfoil surface; the second region is a 'tongue-like' region extending from the vicinity of the airfoil leading edge into the 'free stream'. This contour line represented by the value 5 is a region of a local maximum vorticity. As can be seen by comparing Figs. 12 and 13, the tongue-like region of vorticity appears to break off and be convected downstream as a local concentrated region (See Fig. 13). This may be interpreted as the initiation of a shed vortex. A third area of high vorticity concentration occurs at the airfoil trailing edge where the sharp mixing layer is present. The two contour lines in each figure which are upstream of the airfoil are the locus of zero vorticity and these lines separate regions of very low positive and very low negative vorticity present in the calculation.

A closer examination of the predicted flow field shows the emergence of an inner counterclockwise rotating separation zone which occurs under the main suction surface separation zone. As can be seen in Figs. 9-11, the major separated region is a large region of clockwise rotation. However, a detailed vector plot of the mid-chord portion of the suction surface presented in Fig. 14 shows a secondary separation region of counter-clockwise rotation developing very close to the surface. This region is characterized by having flow in the immediate vicinity of the airfoil surface directed in the downstream direction and the region is completely embedded within the primary separation zone. A final velocity vector plot is shown in Fig. 15 which details the leading edge region. The stagnation point location, the flow separation at the stagnation point, the acceleration about the leading edge and the initiation of flow separation are all shown clearly.

Plots of static pressure contours are presented in Figs. 16 and 17. The results correspond to physical times t_1 and $t_1+\Delta t_1$ where Δt_1 is the time required for a free stream particle to travel one chord in distance; these items are identical to those used for the velocity vector plots, Figs. 10 and 11, and the vorticity contour plots, Figs. 12 and 13. The contours plotted represent values of $(p-p_\infty)/(p^o_\infty-p_\infty)$ where p is the local static pressure, p_∞ is the undisturbed free stream static pressure and p^o_∞ is the undisturbed free stream

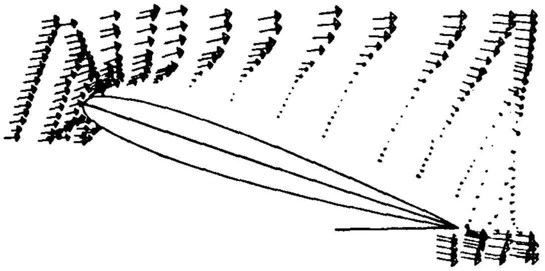

Figure 9. - Experimentally measured velocity field, α= 19.4°. (Data of Young, Meyers and Hoad)

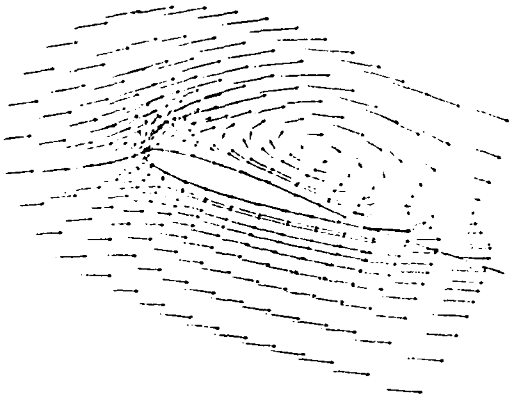

Figure 10. - Computed velocity vector field, $\alpha = 19°$, $t = t_1$.

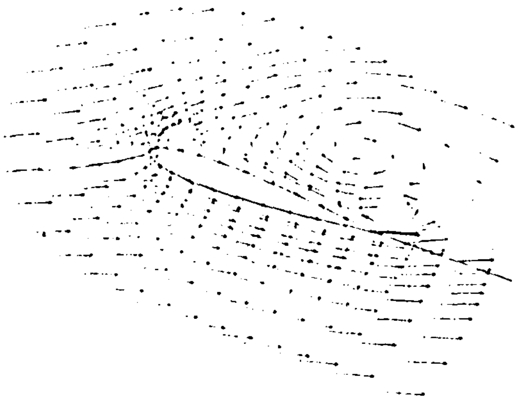

Figure 11. - Computed velocity vector field, $\alpha = 19°$, $t = t_1 + \Delta t$, $\Delta t = 1.0$.

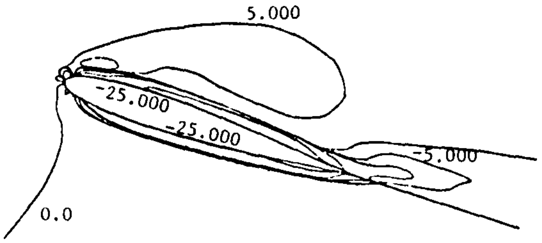

Figure 12. - Vorticity contours, $\alpha = 19°$, $t = t_1$.

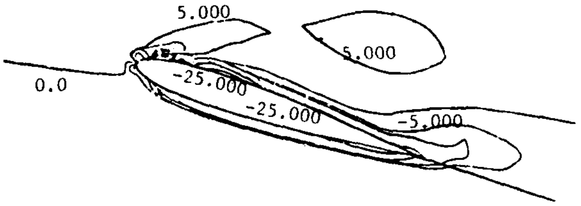

Figure 13. - Vorticity contours, $\alpha = 19°$, $t = t_1 + \Delta t$, $\Delta t = 1.0$.

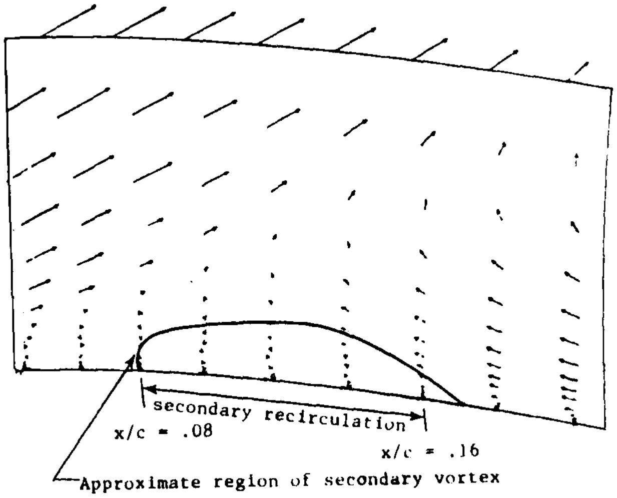

Figure 14. - Velocity vector plot, detail of suction surface, $\alpha = 19°$.

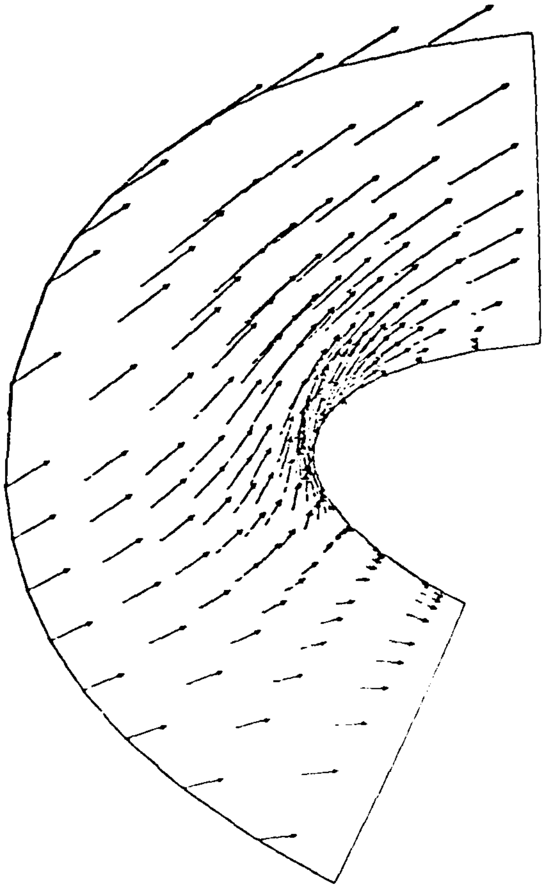

Figure 15. - Velocity vector plot, detail of leading edge region, $\alpha = 19°$

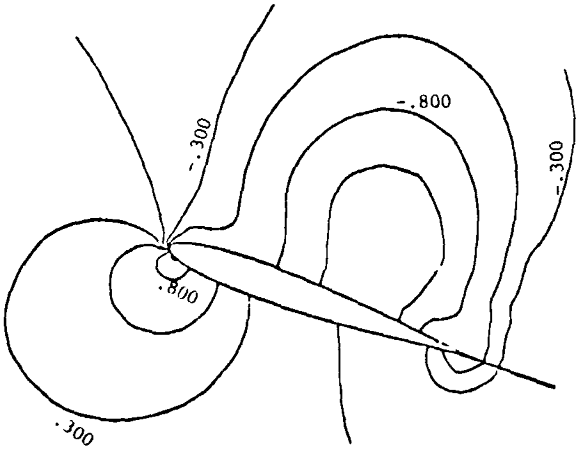

Figure 16. - Static pressure contours, $\alpha = 19°$, $t = t_1$.

stagnation pressure. The two pressure contours are remarkably alike with the major difference being a convection of the pressure field in the downstream direction. The convection velocity is approximately 0.25 U_∞. Contour lines of $(p-p_\infty)/(p_\infty^o-p_\infty)$ are plotted for values 1.0, .8, .5, .3, 0, -.3, -.5, -.8, -1.0. The increase in static pressure as the flow approaches the front stagnation point is clearly shown in both figures. In addition no sharp suction peak occurs on the airfoil upper surface. Rather a gradual pressure drop occurs over the front portion of the suction surface and this is followed by a pressure rise. The pressure field is consistent with a stalled airfoil.

Measurements of the resultant standard deviation of velocity as given by Young, Meyers and Hoad (Ref. 41) are presented in Fig. 18. The results represent lines of constant $(u'^2/U_\infty^2+v'^2/U_\infty^2)^{1/2}$ and include all non-steady contributions; i.e., contributions due to large scale unsteadiness as well as turbulence. Furthermore, only the contributions of two fluctuating velocity components were measured. Finally, the free stream value of the resultant standard deviation measured in the tunnel is approximately 0.04.

If it is assumed $w' \approx u' \approx v'$ then the maximum value of $k=(u'^2+v'^2+w'^2)/2U_\infty^2$ is approximately equal to 0.09. As shown in Fig. 18 measured regions of high resultant standard deviation occur in the vicinity of the free mixing region; a second region of high resultant standard deviation values occurs at the airfoil trailing edge. Predicted values of k are shown in the contour plot of Fig. 19. The contour line values plotted are 0.001, 0.005, 0.01, 0.02, 0.03, 0.04, 0.05, 0.06. The locus of the line having the maximum turbulence energy at each streamwise station is also shown in Fig. 19. It should be noted that this line has the same general shape as that experimentally measured; it is nearly parallel to the free stream over most of the airfoil and then turns downward at a streamwise location in the vicinity of the trailing edge. The magnitude of k on this line varies between 0.02 and 0.03; however, the measured velocity resultant standard deviation includes all unsteadiness and the calculation includes only that unsteadiness associated with turbulence. Furthermore, the measured free stream resultant standard deviation was 0.04 and the free stream turbulence level used in the calculation was 0.001. Therefore, the measured data and predicted values are consistent and even appear to be in reasonable agreement.

CONCLUSION

The present paper describes the application of a time-dependent, compressible Navier-Stokes calculation procedure to the isolated airfoil problem. The analysis solves the full Navier-Stokes equations in conjunction with a turbulence energy model to predict the flow field development. When applied to airfoils at relatively low incidence, solutions obtained within 150 time steps showed good general agreement with data and exhibited many of the experimentally observed flow phenomena. Discrepancies between the calculated results and data appear due primarily to grid resolution and turbulence modeling effects. The analysis also was applied to ramp motion between 6 and 19 degrees and to an airfoil held at 19 degrees incidence. Although no comparisons were made with data for the ramp motion case, the computed flow field appears to be physically realistic. The 19 degree case was compared with experi-

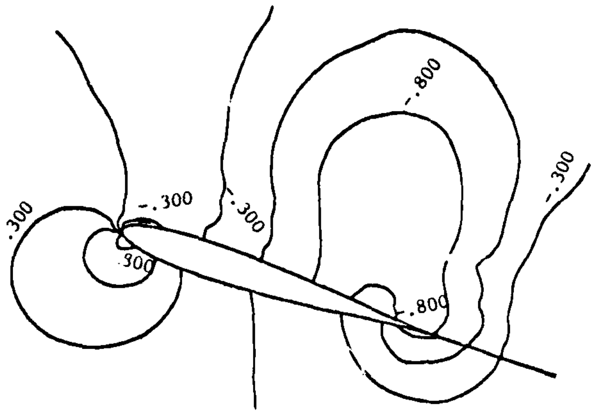

Figure 17. - Static pressure contours, $\alpha = 19°$, $t = t_1 + \Delta t$, $\Delta t = 1.0$.

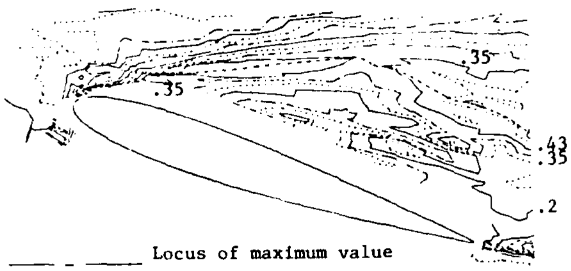

Figure 18. - Measured resultant standard deviation of velocity (Young, Meyers and Hoad).

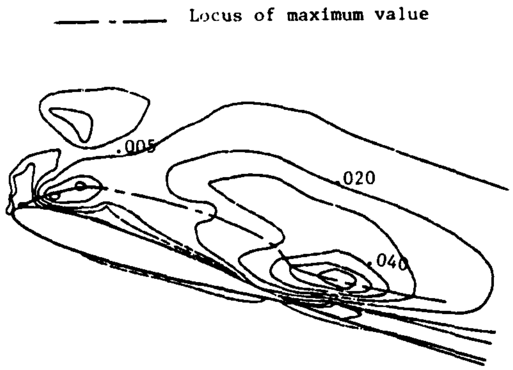

Figure 19. - Turbulence energy contours, $\alpha = 19°$.

mental data and the results were very encouraging as the calculated flow field was in good qualitative agreement with the measurements. In particular, both the calculation and data showed the appearance of a large separated region initiating in the immediate vicinity of the airfoil leading edge, leading edge unsteadiness, a strong shear region at the airfoil trailing edge and the same general level and location of the maximum turbulence energy region. In addition, it should be noted that the calculated wake closure point was still moving downstream and further development of the calculation may lead to improved agreement.

ACKNOWLEDGMENT

This work was supported under a joint NASA/Army program between the Structures Laboratory, U. S. Army Research and Technology Laboratory (AVRADCOM) and NASA Langley Research Center under Contract NAS1-15214.

REFERENCES

1. Mehta, U. B. and Lavan, Z.: Starting Vortex, Separation Bubble and Stall: A Numerical Study of Laminar Unsteady Flow about an Airfoil. J. Fluid Mech., Vol. 67, 1975, pp. 227-256.

2. Lugt, H. J. and Haussling, H. J.: Laminar Flow about an Abruptly Accelerated Elliptic Cylinder at 45° Incidence. J. Fluid Mech., Vol. 65, 1974, pp. 711-734.

3. Mehta, U. B.: Dynamic Stall of an Oscillating Airfoil. Proceedings of AGARD Conference on Unsteady Aerodynamics, September 1977.

4. Wu, J. C. and Sampath, S.: A Numerical Study of Viscous Flow About an Airfoil. AIAA Paper 76-337, 1976.

5. Wu, J. C., Sampath, S. and Sankar, N. L.: A Numerical Study of Unsteady Viscous Flows Around Airfoils. Proceedings of AGARD Conference on Unsteady Aerodynamics, September 1977.

6. Wu, J. C. and Thompson, J. F.: Numerical Solutions of Time-Dependent Incompressible Navier-Stokes Equations Using an Integro-Differential Formulation. Computers and Fluids, Vol. 1, 1973, pp. 197-215.

7. Kinney, R. B. and Cielak, Z. M.: Analysis of Unsteady Viscous Flow Past an Airfoil: Part I - Theoretical Development. AIAA Journal, Vol. 15, No. 12, December 1977, pp. 1714-1719.

8. Cielak, Z. M. and Kinney, R. B.: Analysis of Unsteady Viscous Flow Past an Airfoil: Part II - Numerical Formulation and Results. AIAA Journal, Vol. 16, No. 2, February 1978, pp. 105-110.

9. Lugt, H. J. and Haussling, H. J.: The Acceleration of Thin Cylindrical Bodies in a Viscous Fluid. Journal of Appl. Mech., Vol. 45, 1978, pp. 1-6.

10. Thames, F. C., Thompson, J. F., Mastin, C. W. and Walker, R. L.: Numerical Solutions for Viscous and Potential Flow about Arbitrary Two-Dimensional Bodies Using Body Fitted Coordinate Systems. Journal of Comp. Phys., Vol. 24, 1977, pp. 245-273.

11. Hodge, J. K. and Stone, A. L.: Numerical Solution for Airfoils Near Stall in Optimized Body Fitted Curvilinear Coordinates. AIAA Paper 78-284, 1978.

12. Verhoff, A.: Numerical Solution of Subsonic Viscous Inviscid Interacting Flows. AFFDL-TR-76-64, July 1976.

13. MacCormack, R. W.: The Effect of Viscosity in Hypervelocity Impact Cratering. AIAA Paper No. 69-354, 1967.

14. Deiwert, G. S.: Recent Computation of Viscous Effects in Transonic Flow. Proceedings of the Fifth International Conference on Numerical Methods in Fluid Dynamics, Springer-Verlag, New York, 1976.

15. Levy, L. L., Jr.: An Experimental and Computational Investigation of the Steady and Unsteady Transonic Flow Fields about an Airfoil in a Solid Wall Test Channel. AIAA Paper 77-678, 1977.

16. MacCormack, R. W.: An Efficient Explicit-Implicit Characteristic Method for Solving the Compressible Navier-Stokes Equations. SIAM-AMS Proceedings of the Symposium on Computational Fluid Dynamics, 1977.

17. Gibeling, H. J., Shamroth, S. J. and Eiseman, P. R.: Analysis of Strong-Interaction Dynamic Stall for Laminar Flow on Airfoils. NASA CR-2969, April 1978.

18. Briley, W. R. and McDonald, H.: Solution of the Multidimensional Compressible Navier-Stokes Equations by a Generalized Implicit Method. J. Comp. Physics, Vol. 24, No. 4, August 1977, p. 372.

19. Sankar, N. L. and Tassa, Y.: Reynolds Number and Stability Effects on Dynamic Stall of an NACA0012 Airfoil. AIAA Paper No. 80-0010, 1980.

20. Steger, J. L.: Implicit Finite Difference Simulation of Flow About Arbitrary Two-Dimensional Geometries. AIAA Journal, Vol. 16, 1978, pp. 679-686.

21. Thompson, J. F., Thames, F. C. and Mastin, C. W.: Automatic Numerical Generation of Body Fitted Curvilinear Coordinate System for Field Containing Any Number of Arbitrary Two-Dimensional Bodies. J. Comp. Physics, Vol. 15, 1974, pp. 299-319.

22. Shamroth, S. J. and Gibeling, H. J.: A Compressible Solution of the Navier-Stokes Equations for Turbulent Flow About an Airfoil. NASA CR-3183, 1979. (See also AIAA Paper 79-1543).

23. Haussling, H. J.: Body Fitted Coordinates for Accurate Numerical Solution of Multibody Flow Problems. Journal of Comp. Phys., Vol. 30, 1979, pp. 107-124.

24. Eiseman, P. R.: A Coordinate System for a Viscous Transonic Cascade Analysis. J. Comp. Physics, Vol. 26, March 1978, pp. 307-338.

25. Shamroth, S. J. and Levy, R.: Description of a Constructive Coordinate System Generation Computer Code for Isolated Airfoils. Scientific Research Associates Rpt. R80-1, 1980.

26. McVitte, G. C.: A Systematic Treatment of Moving Axes in Hydrodynamics. Proceedings of the Royal Society A, 1965, pp. 285-300.

27. Walkden, F.: The Equations of Motion of a Viscous, Compressible Gas Referred to an Arbitrarily Moving Coordinate System. Royal Aircraft Establishment, Technical Report No. 66140, April 1966.

28. Thomas, P. D. and Lombard, C. K.: Geometric Conservation Law and Its Application to Flow Computations on Moving Grids. AIAA Journal, Vol. 17, 1979, pp. 1030-1037.

29. Thompson, J. F.: Private Communication, 1979.

30. Simpson, R. L.: A Review of Some Phenomena in Turbulent Flow Separation. ASME Symposium on Turbulent Boundary Layers, 1979, pp. 1-14.

31. Launder, B. E. and Spalding, D. B.: The Numerical Computation of Turbulent Flows. Computer Methods in Applied Mechanics and Engineering, Vol. 3, 1974, pp. 269-289.

32. McDonald, H. and Fish, R. W.: Practical Calculation of Transitional Boundary Layers. Int. J. Heat and Mass Transfer, Vol. 16, No. 9, 1973, pp. 1729-1744.

33. Shamroth, S. J. and McDonald, H.: Assessment of a Transitional Boundary Layer Theory at Low Hypersonic Mach Numbers. Int. J. Heat and Mass Transfer, Vol. 18, 1975, pp. 1277-1284.

34. Kreskovsky, J. P., Shamroth, S. J. and McDonald, H.: Application of a General Boundary Layer Analysis to Turbulent Boundary Layers Subjected to Strong Favorable Pressure Gradients. J. Fluid Eng., Vol. 97, June 1975, pp. 217-224.

35. Gibeling, H. J., Buggeln, R. C. and McDonald, H.: Development of a Two-Dimensional Implicit Interior Ballistics Code. Army Ballistics Research Laboratory Rpt. ARBRL-CR-00411, 1980.

36. Briley, W. R. and McDonald, H.: Computation of Three-Dimensional Horseshoe Vortex Flow Using the Navier-Stokes Equations. Seventh International Conference on Numerical Methods in Fluid Dynamics, 1980.

37. Briley, W. R. and McDonald, H.: On the Structure and Use of Linearized Block Implicit Schemes. Journal of Comp. Phys., Vol. 34, 1980, pp. 54-73.

38. Douglas, J. and Gunn, J. E.: A General Formulation of Alternating Direction Methods. Numerische Math., Vol. 6, 1964, pp. 428-453.

39. Shamroth, S. J., Gibeling, H. J. and McDonald, H.: A Navier-Stokes Solution for Laminar and Turbulent Flow Through a Cascade of Airfoils. AIAA Paper 80-1426, 1980.

40. Gregory, N. and O'Reilly, C. L.: Low Speed Aerodynamic Characteristics of NACA0012 Airfoil Section, Including the Effects of Upper Surface Roughness Simulating Hoarfrost. Aero Report 1308, National Physics Laboratory, 1970.

41. Young, W. H., Jr., Meyers, J. F. and Hoad, D. R.: A Laser Velocimeter Flow Survey Above a Stalled Wing, NASA Technical Paper 1266, AVRADCOM Technical Report 78-50, 1978.

EXPERIMENTAL STUDIES OF SCALE EFFECTS ON OSCILLATING AIRFOILS AT TRANSONIC SPEEDS

Sanford S. Davis
Aerodynamic Research Branch
Aerodynamics Division
Ames Research Center, NASA
Moffett Field, California 94035, U.S.A.

SUMMARY

Experimental data are presented on the effect of Reynolds number on unsteady pressures induced by the pitching motion of an oscillating airfoil. Scale effects are discussed with reference to a conventional airfoil (NACA 64A010) and a supercritical airfoil (NLR 7301) at mean-flow conditions that support both weak and strong shock waves. During the experiment the Reynolds number was varied from 3×10^6 to 12×10^6 at a Mach number and incidence necessary to induce the required flow. Both fundamental frequency and complete time history data are presented over the range of reduced frequencies that is important in aeroelastic applications. The experimental data show that viscous effects are important in the case of the supercritical airfoil at all flow conditions and in the case of the conventional airfoil under strong shock-wave conditions. Some frequency-dependent viscous effects were also observed.

LIST OF SYMBOLS

C_p	static pressure coefficient, (P - PINF)/QINF
$C_p(x,t)$	instantaneous pressure coefficient
$C_{p,\alpha}(x)$	first harmonic complex amplitude of the unsteady pressure, per radian
c	chord of wing, 0.5 m
$\exp(-i\omega t)$	$\cos \omega t - i \sin \omega t$
f	frequency, Hz, fT = 1
$I_q(t)$	qth moment of the instantaneous pressure coefficient
$I_{0,\alpha}$	first harmonic complex amplitude of the upper surface loading, per radian
k	reduced frequency, $\omega c/2U$
M	free-stream Mach number
P(x,t)	instantaneous pressure, N/m^2
PINF	free-stream static pressure, N/m^2
QINF	free-stream dynamic pressure, N/m^2
Re	chord Reynolds number
T	period of the motion, sec
t	time, sec
U	free-stream velocity, m/sec
x	distance along airfoil, m
α	complex amplitude of the unsteady angle of attack
α_m	mean angle of attack
$\alpha(t)$	instantaneous angle of attack
ω	radian frequency, 1/sec

Complex notations:

Im[ ]	imaginary part of [ ]
Mag[ ]	magnitude of [ ]
Ph[ ]	phase of [ ], deg
Re[ ]	real part of [ ]

1. INTRODUCTION

Scale effects have been considered an important element in aerodynamics research for many years. In early experimental studies of steady transonic flows in the 1940s, the Reynolds number, as it affected the state of the boundary layer approaching a shock wave, was recognized as a critical parameter (Ref. 1). In the 1950s the boundary-layer-trip technique was developed to simulate high Reynolds number flows in the wind tunnel (Ref. 2). With the development of thicker and more highly loaded airfoil sections in the 1960s, more complicated scale effects due to local flow separations were discovered (Ref. 3), and extensive experimental programs were developed to quantify these viscous interactions (Refs. 4, 5). Even today, a concerted effort is under way to understand the effect of Reynolds number on modern supercritical airfoil sections (see Gessow's introductory remarks to a recent NASA conference, Ref. 6).

In the field of unsteady transonic aerodynamics, the scale effect has hardly been seriously considered, either experimentally or analytically. In the original chapter on boundary-layer effects in the AGARD Manual on Aeroelasticity (Ref. 7), the authors of that work found no studies that considered the coupling of a boundary layer to the unsteady-pressure field. In Jones' review of unsteady aerodynamics in 1963 (Ref. 8), the need for such research was reiterated; current review articles continue to cite the need for such research (Refs. 9, 10).

Recently, numerical solutions to the Navier-Stokes equations were applied to unsteady transonic flow problems (Refs. 11-13). They were used to model passively excited oscillations where good qualitative agreement with experiment was demonstrated. Computations for a forced oscillation problem, including viscous effects, were reported in Ref. 14. All these codes, mostly concerned with mild transonic interactions where simple turbulence models suffice, are limited by long executing times, even on powerful computers. Future applications of the numerical method, guided by experimental data, better turbulence models, and the availability of faster computers will certainly contribute to our understanding of scale effects on unsteady aerodynamic response.

Experimentally, Tijdeman (Ref. 15) analyzed some of the NLR oscillatory data for scale effect. He accounted for the boundary layer by including the displacement effect in the calculated pressure distributions. For subsonic flows, his results show that thickness and boundary-layer effects tend to counteract one another in the sense that measured unsteady-pressure distributions tend to follow classical flat-plate theory. For transonic flows, his analysis showed that the boundary layer had a profound effect on both the mean shock-wave location and the characteristic unsteady-pressure peak at the mean shock locations. Tijdeman showed that inviscid theories are inadequate for predicting unsteady transonic flows, but his data, measured in an atmospheric wind tunnel, did not address the effect of Reynolds number directly. Similar comparisons and conclusions were reported by Grenon et al. (Ref. 16) in their oscillating flap studies.

In this paper experimental data from tests in the 11- by 11-Foot Transonic Wind Tunnel at Ames Research Center are used to illustrate the importance of scale effects on the unsteady aerodynamics of both conventional and supercritical airfoils. First, the integrated upper-surface unsteady-pressure distributions are used to assess global variations (Sec. 3.1). More detailed information is presented with the aid of the fundamental frequency pressure data (Sec. 3.2), and ultimately with the instantaneous time histories (Sec. 3.3). Many of the effects involve complex unsteady viscous interactions that are not yet completely understood nor easily modeled; as a result, theoretical comparisons will be restricted to linearized, inviscid, unsteady aerodynamic theory.

2. EXPERIMENTAL APPARATUS AND TEST CONDITIONS

The experiment was conducted during the early part of 1978. The 11- by 11-Foot Transonic Wind Tunnel is a continuous flow facility that can be pressurized between 50 and 200 kPa for independent control of Mach and Reynolds number. The test wings – an NACA 64A010 conventional airfoil section and an NLR 7301 supercritical airfoil section – were mounted between two floor-to-ceiling splitter plates installed in the 3.35- by 3.35-m slotted test section. The 0.5-m-chord by 1.35-m-span wings were fabricated from a lightweight graphite-epoxy composite material. A sketch of the test apparatus is shown in Fig. 1, and a complete description of the test hardware, motion generators, and models is given in Ref. 17. The chord Reynolds number range was approximately 3×10^6 to 12×10^6. No boundary-layer trips were used in this test.

The data reported in this paper form a small portion of the extensive data base that was collected during the test. Some of the data were previously reported in Refs. 18 and 19, and a discussion of the method used to acquire and validate the unsteady data is presented in Ref. 20. The data subset relating to scale effects is presented in Table 1. Two broad categories are represented: conditions 1 to 3 represent attached flows and conditions 4 and 5 are examples of separated flows. As will be shown presently, both classes of flows can exhibit scale effects, with the separated flow data indicating a more erratic behavior.

3. PRESENTATION OF DATA AND DISCUSSION

3.1 Variation of the Global Parameter [illegible] with Frequency

A convenient measure of the load on the upper surface is the chordwise integral of the airfoil pressure distribution. As introduced in Ref. 19, this parameter is defined as

$$\int [illegible]$$

where [illegible] is a measure of the lift attributed to the upper surface with [illegible] decomposition of [illegible] defines the amplitude of the first harmonic [illegible]

$$\int [illegible]$$

Considering first the attached flows, conditions 1 to 3 in Table 1, the variation of the [illegible] with frequency is shown in Table [illegible], with Reynolds number as parameter. Values from subsonic [illegible] unsteady aerodynamic theory (Ref. [illegible]) are also shown for comparison. The frequency variation [illegible] attached transonic flows (decreasing amplitude with increasing frequency) persists at all Reynolds numbers. The data also show decreasing amplitudes with increasing Reynolds numbers at most frequencies. [illegible] the subsonic flow (M = 0.500), the variations are minimal and can probably be accounted for by simple [illegible]sion of the boundary layer displacement. The transonic flows, being sensitive to shock-wave/boundary-layer interactions, show slightly more severe scale effects.

A graphic summary of the scale effect for conditions 1-3 is shown in Fig. 2 where the variation of the complex amplitude with Reynolds number is presented at a reduced frequency k = 0.05. As expected, the subsonic flow condition is least affected by Reynolds number. The trend for both the conventional and supercritical data at transonic Mach numbers is toward decreasing in-phase and out-of-phase (Re and Im) components with Reynolds number. It is noteworthy that, for each flow condition, the phase does not change by more than 5° over the Reynolds numbers range considered.

In Refs. 18 and 19 it was shown that the aerodynamic transfer function (variation of load with frequency) was not even qualitatively consistent with linear theory wh[illegible]ck wave was strong enough to separate the boundary layer. The separated boundary layer had a ma[illegible]ct on the loads, and it is expected that scale effects would also be very important. Table 3 shows the magnitude of the complex amplitudes for conditions where strong unsteady shock-wave/boundary-layer interactions are encountered. No discernible trends are evident from these data. In fact, the magnitudes undergo alarming variations with Reynolds number when compared with the attached-flow data. Due to this complex behavior, further information must be gleaned from the unsteady-pressure data itself.

3.2 Unsteady-Pressure Distributions

The first harmonic complex unsteady pressure is defined by the following expression:

$$\alpha C_{p,\alpha}(x) = \frac{1}{T}\int_0^T C_p(x,t)\exp(-i\omega t)dt$$

An analysis of the in-phase and out-of-phase (Re and Im) component of $C_{p,\alpha}$ will show that the distributions for attached-flow conditions are qualitatively consistent with the simplest theoretical models that include viscous effects by consideration of the boundary-layer displacement. The separated flow, however, shows important unsteady effects that are attributed to both the steady-flow scale effect and the unsteady viscous response of the boundary layer.

The data for attached-flow conditions 1-3 are shown in Figs. 3-5, respectively. For each frequency, the mean, in-phase, and out-of-phase components of the unsteady-pressure distribution are presented. Figure 3 shows that the subsonic flow ($\alpha = 0$, $M = 0.5$) has minimal scale effect. The only difference between Reynolds numbers is the slight dip in the in-phase component at wing station $x/c = 0.5$. Sublimation photographs showed that transition occurred at this location at $Re = 2.5 \times 10^6$; at $Re = 10 \times 10^6$, transition was very close to the leading edge. In any event, the state of the boundary layer has no effect on the unsteady-pressure distribution, which assumes the classical shape that was predicted many years ago from linearized subsonic theory. The same airfoil at transonic speeds in Fig. 4 ($\alpha = 0$, $M = 0.8$) shows that scale effect is also quite minimal. Aside from a slight upwind movement of the mean shock position that affects the chordwise location of the unsteady-pressure peak, the effect is minor. Sublimation photographs at this condition showed that transition occurs at the shock wave at $Re = 3.3 \times 10^6$; while leading-edge transition was observed at $Re = 12.6 \times 10^6$. The last attached flow condition, shown in Fig. 5 for the NLR 7301 supercritical airfoil, exhibits more severe scale effects. Although the region of rapid compression (probably not a shock wave at this supercritical design condition) moves only slightly, the unsteady pressure is quite different at the three Reynolds numbers indicated. These differences are probably due to the large extent of supercritical flow on the upper surface that is affected by the change in effective airfoil shape due to the unsteady boundary-layer growth. The difficulty in distinguishing differences by examining the integrated values shown previously is obvious because of the varying contribution to the loads from positive and negative lobes of the unsteady pressures.

The data for shock-induced separation are more difficult to analyze. These data are shown in Figs. 6 and 7. Figure 6 shows the large effect of Reynolds number for the NACA 64A010 at $\alpha = 4°$, $M = 0.8$ (condition 4 in Table 1). The mean flow differs not so much in the shock position as in the extent of separated flow downstream of the shock. This separated flow has a marked effect on the in-phase unsteady pressure at the shock wave and beyond. The out-of-phase pressures are not very much different at the two Reynolds numbers shown. The mechanisms whereby the in-phase pressures are more sensitive than the out-of-phase pressures have yet to be explained. Figure 7 shows similar data for the supercritical airfoil at a Mach number beyond its design point (condition 5 in Table 1). The mean flow differs from the previous case in the absence of any discernible training-edge pressure recovery downstream of the shock wave. This indicates a more severe flow separation. The data for the unsteady components of the pressure distribution also show a significant sensitivity to Reynolds number. For the in-phase component, especially, variations in the negative contribution to the load change rapidly with Reynolds number. This large variation gives rise to the confusing trends in the unsteady loads shown in Table 3. Again, it should be noted that the in-phase components appear to be more sensitive to Reynolds number than the out-of-phase components.

It is clear from the preceding discussion that a more fundamental data set needs to be examined to clarify the underlying physical mechanisms behind the scale effect. The final sequence of data will show how the Reynolds number effects the instantaneous unsteady-pressure time histories.

3.3 Instantaneous Pressure Data

The measured unsteady-pressure coefficients $C_p(x,t)$ are presented in Figs. 8 to 12 for the five flow conditions listed in Table 1. At each chordwise station (identified by a numerical key), data are shown at two Reynolds numbers. The mean portion of the instantaneous pressure coefficient was suppressed for clarity. (The reference line for each trace is the corresponding tic mark on the airfoil contour.) As explained in Ref. 20, the dynamic data have been processed to eliminate all asynchronous signals. Thus, all of the dips and bulges shown in the data are truly periodic. Whether they can be traced to a particular fluid-mechanical event at that instant is argumentative, but they are included here for completeness. The input motion is the same for both Reynolds numbers and can be used as the phase reference ($\omega t = 0$ when $\alpha = \alpha_{max}$) For the most part, data are shown at the low, reduced frequency $k = 0.05$.

The subsonic flow (condition 1) is presented in Fig. 8, and, as expected, scale effect is minimal. The usual trend of decreasing amplitude with increasing chordwise location is obvious. The distorted signal at $Re = 2.5 \times 10^6$ in traces 9 and 10 is apparently caused by the transitional boundary layer. The noise on traces 15 and 16 at low Reynolds number has no discernible fluid-mechanical origin.

The effect of increasing the Mach number to 0.80 is shown in Fig. 9. The presence of the shock wave is apparent by its distortion of the pressure signal of both Reynolds numbers, causing a severe local scale effect. However, both upstream and downstream of the shock wave, the Reynolds number does not have a significant effect. The global ramifications of these local effects were tabulated in Table 2.

Data from the supercritical airfoil at its shock-free design condition are shown in Figs. 10a and 10b. Data are presented at two frequencies to show the complicated cross-coupling between frequency and scale effects that was not present in the previous cases. In Fig. 10a data at the low reduced frequency of [illegible] show very significant scale effects in the supercritical flow region. At $Re = 12.6 \times 10^6$ there is a higher amplitude, more distortion, and significant phase shifting. Whether these effects can be explained by simple boundary-layer displacement corrections remains to be answered. In Fig. 10b there is a surprising trend toward reduced harmonic distortions at higher Reynolds numbers (traces 5-9), although there are still significant phase shifts attributable to scale effect. At the "shock wave" (which appears during the cycle), the effect of Reynolds number is apparent. Consistent with the previous attached flow data, there is minimal response near the trailing edge at both frequencies.

Data pertaining to the second flow regime (e.g., shock-induced separation), are presented in Figs. 11 and 12. In Fig. 11 the scale effect is most prominent at the shock-wave location (traces 8 and 9). The fundamental frequency data shown in Fig. 6 indicate that the in-phase component is most severely affected by the Reynolds number. The large change in the unsteady pressure is apparent. Upstream, there is a significant increased phase lag with increasing Reynolds number. This phase lag persists into the separated-flow region aft of the shock. Unfortunately, no data are available at $k = 0.05$.

In Fig. 12 the well-separated flow over the supercritical airfoil does not induce large unsteady disturbances downstream of the shock. This seems to ameliorate the scale effect in the leading-edge region, but not at the shock itself. Data at $k = 0.05$ show similar trends.

This cursory examination of the unsteady-pressure traces indicates the sensitivity of the flow patterns to geometry, frequency, mean-flow conditions, and Reynolds number. It is clear that predictive schemes must include, as a minimum, physical models of all of these parameters.

4. CONCLUDING REMARKS

Examination of some of the data from a series of tests on oscillating airfoils in the Ames 11- by 11-Foot Transonic Wind Tunnel showed that scale effects could be a very important factor in the unsteady aerodynamic behavior of the airfoils. Configurations with mean flows that support fully attached boundary layers and weak shock waves have unsteady response characteristics that are mild functions of Reynolds number. These configurations can probably be modeled with currently available computational tools. An exception, perhaps, is airfoils that possess mean flows with extensive regions of supercritical flow. The detailed pressure distributions contain substantial scale effects, but the overall loads may not be so severely affected.

Configurations with mean flows having detached boundary layers are enigmatic. As reported in Refs. 18 and 19, the contribution to the unsteady load may be caused by a delicate balancing of positive and negative lobes in the unsteady pressures (see Fig. 7). For these conditions, shape changes caused by scale effects may have severe ramifications. The erratic behavior of the unsteady loads shown in Table 3 is illustrative of this effect. The major technological application of unsteady aerodynamics is to aeroelastic analysis and design. The sensitivity of flutter boundaries and stability margins to scale effects must be considered in those situations.

In the mathematical modeling of unsteady transonic aerodynamics, it is clear that the Reynolds number needs to be included as a primary parameter. Progress in computational research during the past decade was characterized by the inclusion of nonlinear thickness effects, and it is hoped that this and other experimental data, along with new computational efforts, will advance our knowledge well beyond the inviscid approximation.

REFERENCES

1. Ackeret, J.; Feldmann, F.; and Rott, N.: Investigations of Compression Shocks and Boundary Layers in Gases Moving at High Speed. NACA TM-1113, 1947.

2. Holder, D. W.: The Transonic Flow Past Two-Dimensional Airfoils. J. Royal Aero. Soc., vol. 68, Aug. 1964, pp. 501-516

3. Pearcy, H. H.; Haines, A. B.; and Osborne, J.: The Interactions between Local Effects at the Shock and Rear Separation. Transonic Aerodynamics, AGARD CP-35, Sept. 1968, pp. 11-1 to 11-23.

4. Blackwell, J. A.: Effect of Reynolds Number and Boundary-Layer Transition Location on Shock-Induced Separations. Transonic Aerodynamics, AGARD CP-35, Sept. 1968, pp. 21-1 to 21-10.

5. Blackerby, W. T.; and Cahill, J. F.: High Reynolds Number Tests of a C-141A Aircraft Semispan Model to Investigate Shock-Induced Separation. NASA CR-2604, 1975.

6. Gessow, A.: NASA Research Objectives and Roles. Advanced Technology Airfoil Research, NASA CP-2045, 1979.

7. Ashley, H.; and Zartarian, G.: Thickness and Boundary-Layer Effects. AGARD Manual on Aeroelasticity, vol. II, Chap. 9., Nov. 1960.

8. Jones, W. P.: Trends in Unsteady Aerodynamics. J. Royal Aeronaut. Soc., vol. 67, no. 627, 1963, pp. 137-151.

9. McCroskey, W. J.: Some Current Research in Unsteady Fluid Dynamics. Trans. ASME. J. Fluids Eng., vol. 99, Mar. 1977, pp. 8-39.

10. Tijdeman, H.; and Seebass, R.: Transonic Flow Past Oscillating Airfoils. Annual Review of Fluid Mechanics, vol. 12, Annual Reviews Inc., Palo Alto, Calif., 1980, pp. 181-222.

11. Levy, L. L., Jr.: Experimental and Computational Steady and Unsteady Transonic Flows about a Thick Airfoil. AIAA J., vol. 16, June 1978, pp. 564-572.

12. Steger, J.: Implicit Finite-Difference Simulation of Flow About Arbitrary Two-Dimensional Geometrics. AIAA J., vol. 16, July 1978, pp. 679-686.

13. Steger, J.; and Bailey, H. E.: Calculation of Transonic Aileron Buzz. AIAA J., vol. 18, Mar. 1980, pp. 249-255.

14. Chyu, W.; and Davis, S.: Calculation of Unsteady Transonic Flow over an Arbitrary Airfoil. AIAA Paper 79-1554, Williamsburg, VA, July 1979.

15. Tijdeman, H.: Investigations of the Transonic Flow Around Oscillating Airfoils. NLR TR-77090U, Oct. 1977.

16. Grenon, R.; Desopper, A.; and Sides, J.: Unsteady Effects of a Control Surface in Two-Dimensional Subsonic and Transonic Flow. Aerodynamic Characteristics of Controls, AGARD CPP-262, May 1979, pp. 19-1 to 19-13.

17. Malcolm, G.; and Davis, S.: New NASA-Ames Wind Tunnel Techniques for Studying Airplane Spin and Two-Dimensional Unsteady Aerodynamics. Dynamic Stability Parameters, AGARD CP-235, Nov. 1978, pp. 3-1 to 3-12.

18. Davis, S.; and Malcolm, G.: Experiments in Unsteady Transonic Flow. AIAA Paper 79-769, St. Louis, MO, Apr. 1979.

19. Davis, S.; and Malcolm, G.: Unsteady Aerodynamics of Conventional and Supercritical Airfoils. AIAA Paper 80-734, Seattle, WA, May 1980.

20. Davis, S.: Computer/Experiment Integration for Unsteady Aerodynamic Research. Int. Congress on Instrumentation in Aerospace Simulation Facilities, ICIASF '79 Record, Sept. 1979, pp. 237-250.

21. Bispinghoff, R.; and Ashley, H.: Principles of Aeroelasticity. J. Wiley and Sons, New York, 1962, p. 106.

TABLE 1.- RANGE OF FLOW CONDITIONS CONSIDERED

Flow condition	Airfoil	M	α_m	Motion
1	NACA 64A010	0.500	0	Pitching ±1° at 0.25 c
2	NACA 64A010	0.796	0	Pitching ±1° at 0.25 c
3	NLR 7301	0.752	0.37	Pitching ±0.5° at 0.40 c
4	NACA 64A010	0.789	4.0	Pitching ±1° at 0.25 c
5	NLR 7301	0.807	0.38	Pitching ±0.5° at 0.40 c

TABLE 2.- MAGNITUDE OF UNSTEADY LOADING ATTRIBUTED TO UPPER SURFACE — ATTACHED FLOW

$Re \times 10^{-6}$	Mag $I_{0,\alpha}$							
	k = 0	k = 0.025	k = 0.05	k = 0.10	k = 0.15	k = 0.20	k = 0.25	k = 0.30
Flow condition 1 (M = 0.500)								
2.5	3.7	3.67	3.59	3.27	2.97	2.83	-	-
5	3.8	-	-	-	-	2.45	-	-
10	-	-	3.43	3.19	2.91	2.74	2.58	-
Inviscid theory	3.64	3.42	3.22	2.91	2.69	2.52	2.44	2.38
Flow condition 2 (M = 0.796)								
3.3	5.5	-	4.87	-	3.19	2.84	2.24	-
6.7	5.7	-	-	-	-	2.67	-	-
12.6	-	4.62	4.41	3.80	2.90	2.68	2.16	2.16
Inviscid theory	5.25	4.61	4.12	3.46	3.07	2.84	2.71	2.63
Flow condition 3 (M = 0.752)								
3.3	-	-	6.46	-	-	2.98	-	-
6.2	-	6.56	6.19	4.80	-	3.67	-	2.01
11.5	-	6.05	5.62	4.63	3.65	3.12	-	1.94
Inviscid theory	4.76	4.23	3.88	3.22	2.97	2.75	2.62	2.54

TABLE 3.- MAGNITUDE OF UNSTEADY LOADING ATTRIBUTED TO UPPER SURFACE — SEPARATED FLOW

$Re \times 10^{-6}$	Mag $I_{0,\alpha}$	
	k = 0.05	k = 0.20
Flow condition 4 (M = 0.789)		
6.2	-	4.48
11.9	1.67	5.57
Inviscid theory	4.12	2.84
Flow condition 5 (M = 0.807)		
3.3	2.39	1.53
6.3	0.44	0.69
11.7	1.08	0.88
Inviscid theory	4.13	2.82

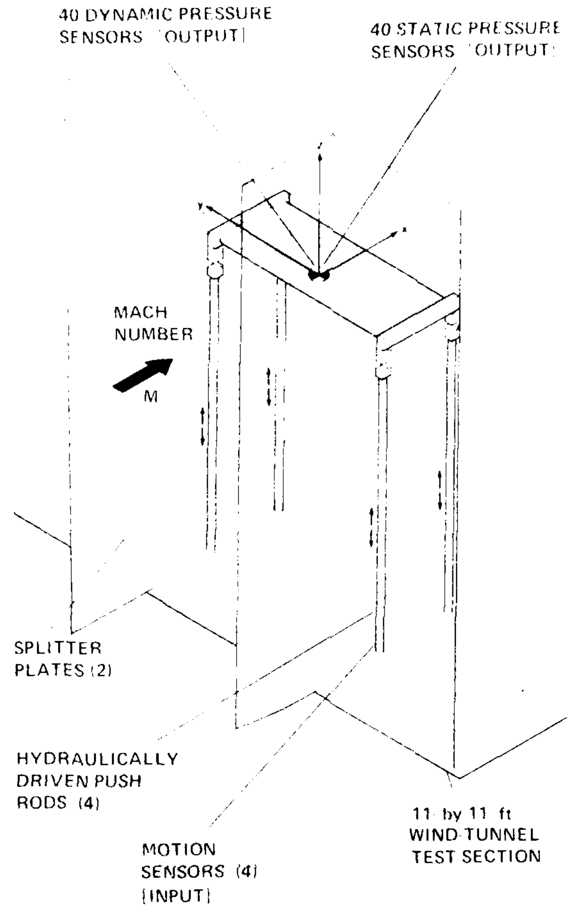
40 DYNAMIC PRESSURE SENSORS (OUTPUT)
40 STATIC PRESSURE SENSORS (OUTPUT)
z
y
x
MACH NUMBER
M
SPLITTER PLATES (2)
HYDRAULICALLY DRIVEN PUSH RODS (4)
MOTION SENSORS (4) (INPUT)
11 by 11 ft WIND-TUNNEL TEST SECTION

Fig. 1. Oscillating airfoil test apparatus installed in the 11- by 11-Foot (3.4 by 3.4 m) Transonic Wind Tunnel at Ames Research Center.

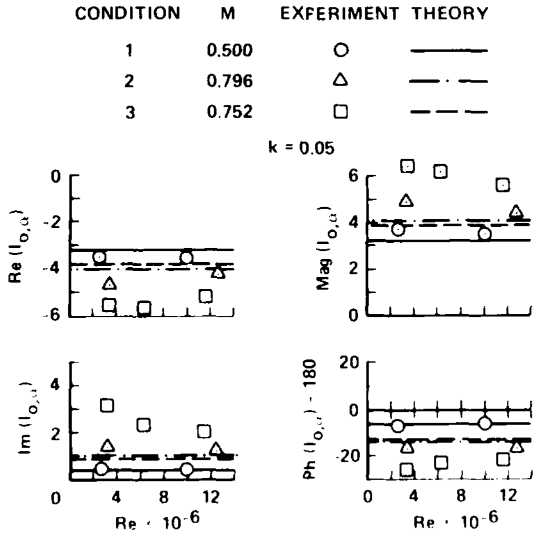

Fig. 2. Variation of the unsteady loading attributed to the upper surface with Reynolds number; low-frequency data, k = 0.05.

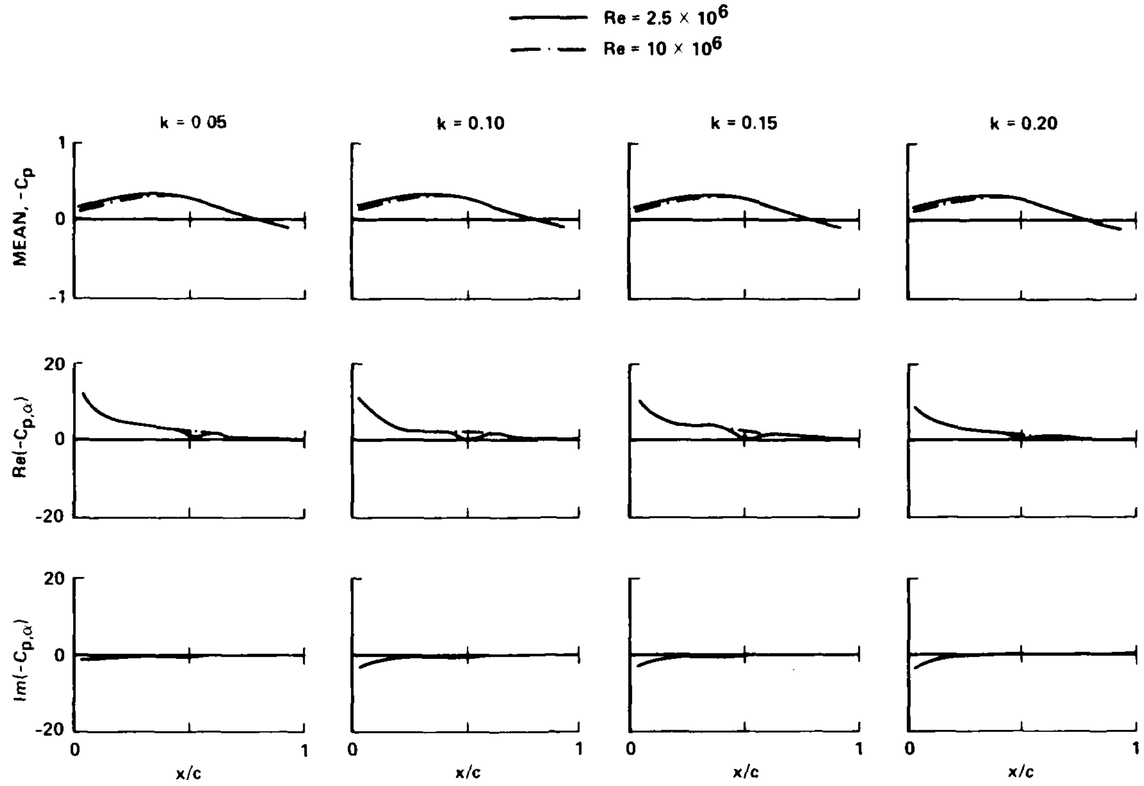

Fig. 3. Unsteady-pressure distribution on oscillating NACA 64A010 airfoil; mean and first harmonic component, M = 0.500, α_m = 0°, pitching ±1° at 0.25 c.

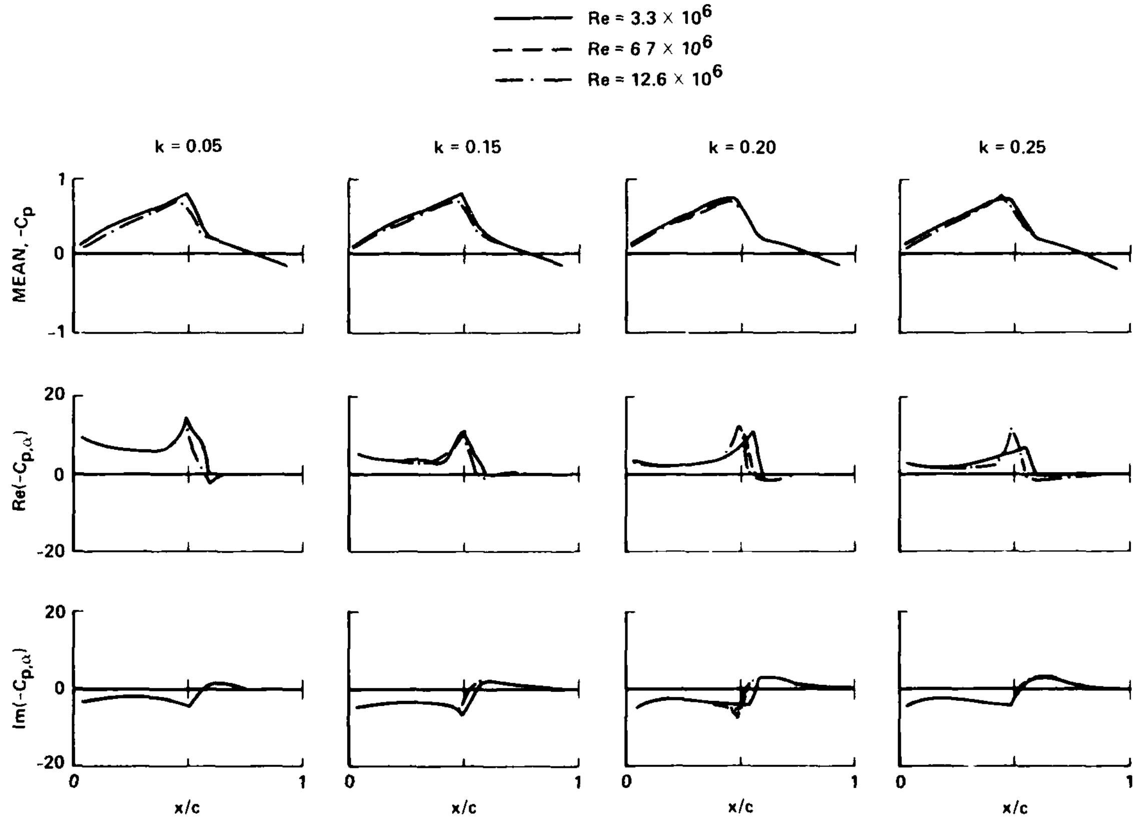

Fig. 4. Unsteady-pressure distribution on oscillating NACA 64A010 airfoil; mean and first harmonic component, M = 0.796, α_m = 0°, pitching ±1° at 0.25 c.

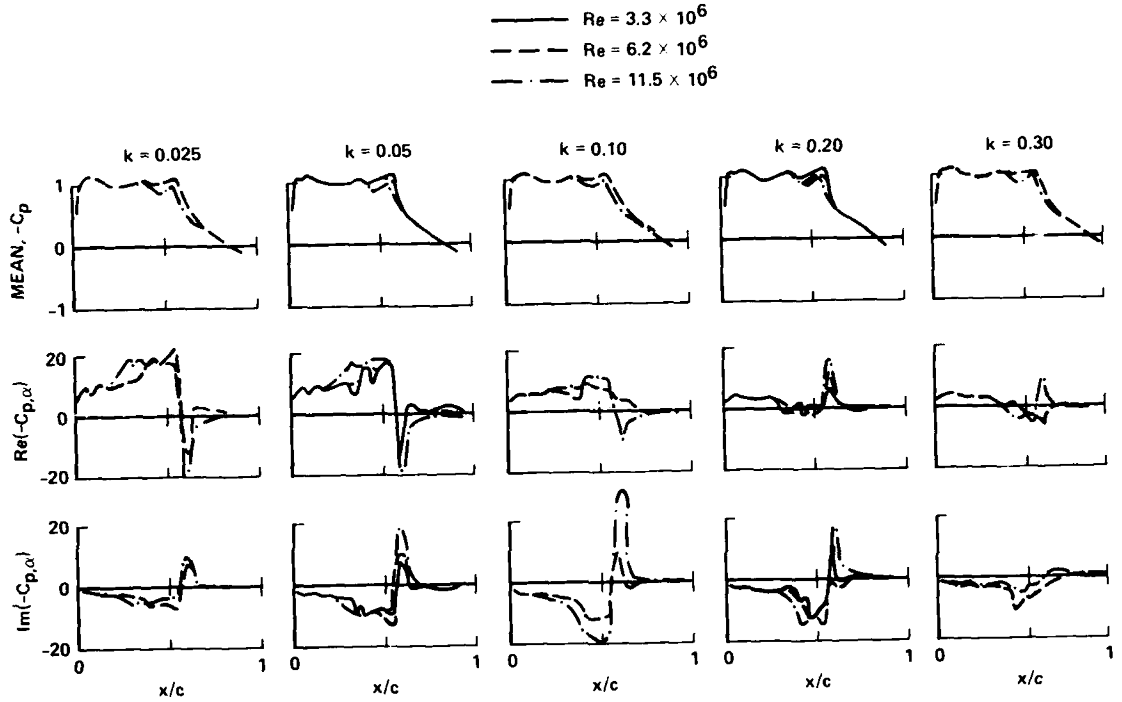

Fig. 5. Unsteady-pressure distribution on oscillating NLR 7301 airfoil; mean and first harmonic component, M = 0.752, α_m = 0.37°, pitching ±0.5° at 0.40 c.

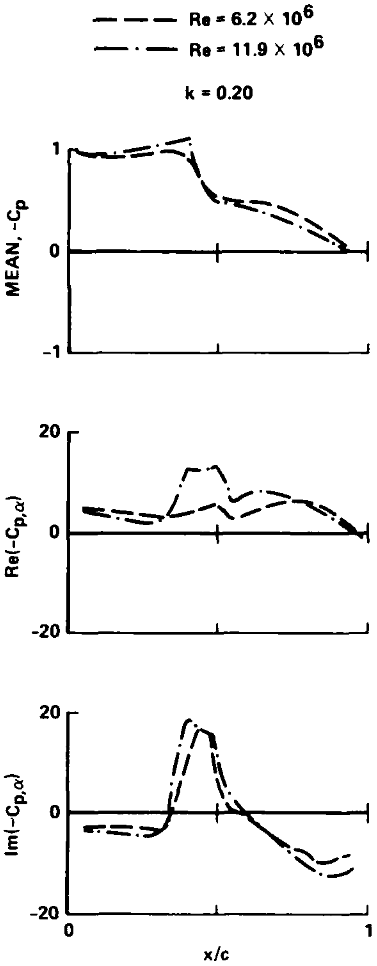

Fig. 6. Unsteady-pressure distribution on oscillating NACA 64A010 airfoil; mean and first harmonic component, M = 0.789, α_m = 4°, pitching ±1° at 0.25 c.

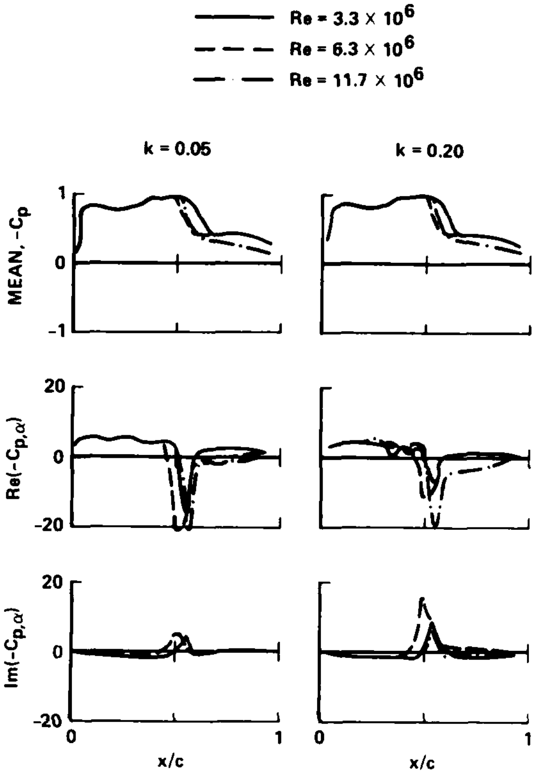

Fig. 7. Unsteady-pressure distribution on oscillating NLR 7301 airfoil; mean and first harmonic component, M = 0.807, α_m = 0.38°, pitching ±0.5° at 0.40 c.

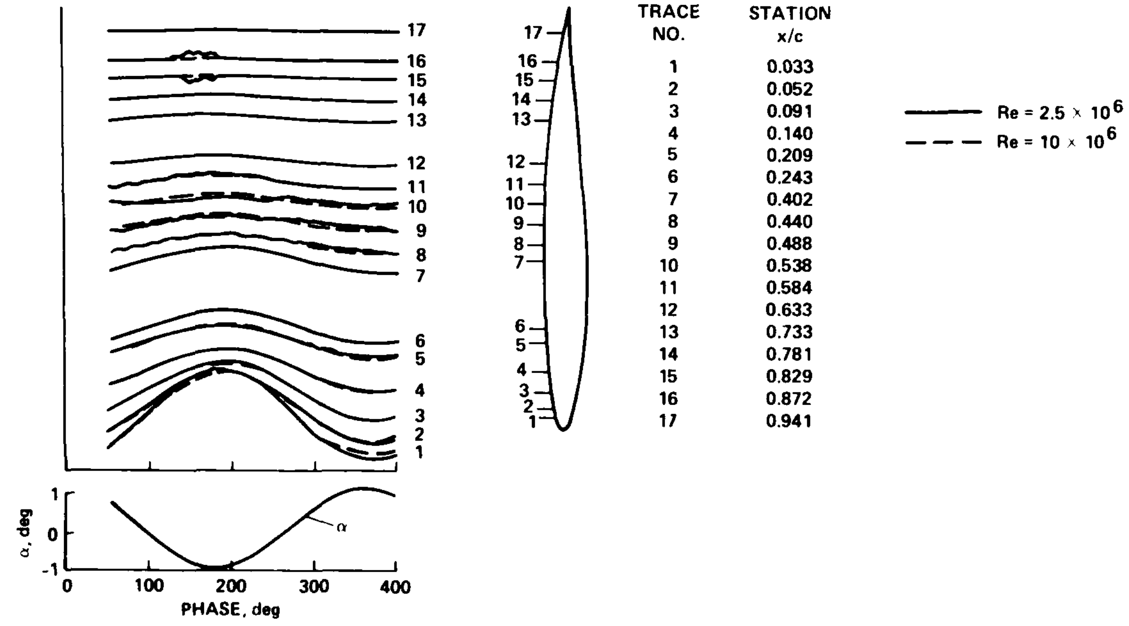

TRACE NO.	STATION x/c
1	0.033
2	0.052
3	0.091
4	0.140
5	0.209
6	0.243
7	0.402
8	0.440
9	0.488
10	0.538
11	0.584
12	0.633
13	0.733
14	0.781
15	0.829
16	0.872
17	0.941

Fig. 8. Complete time histories of unsteady-pressure data; M = 0.500, α_m = 0°, pitching ±1° at 0.25 c, k = 0.05.

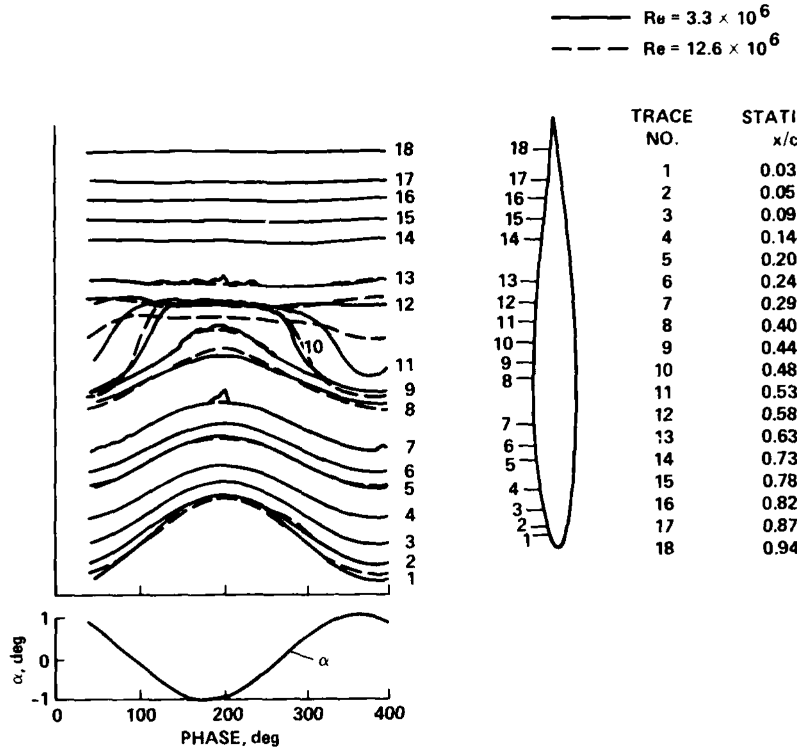

TRACE NO.	STATION x/c
1	0.033
2	0.052
3	0.091
4	0.140
5	0.209
6	0.243
7	0.294
8	0.402
9	0.440
10	0.488
11	0.538
12	0.584
13	0.633
14	0.733
15	0.781
16	0.829
17	0.872
18	0.941

Fig. 9. Complete time histories of unsteady-pressure data; $M = 0.796$, $\alpha_m = 0°$, pitching ±1° at 0.25 c, $k = 0.05$.

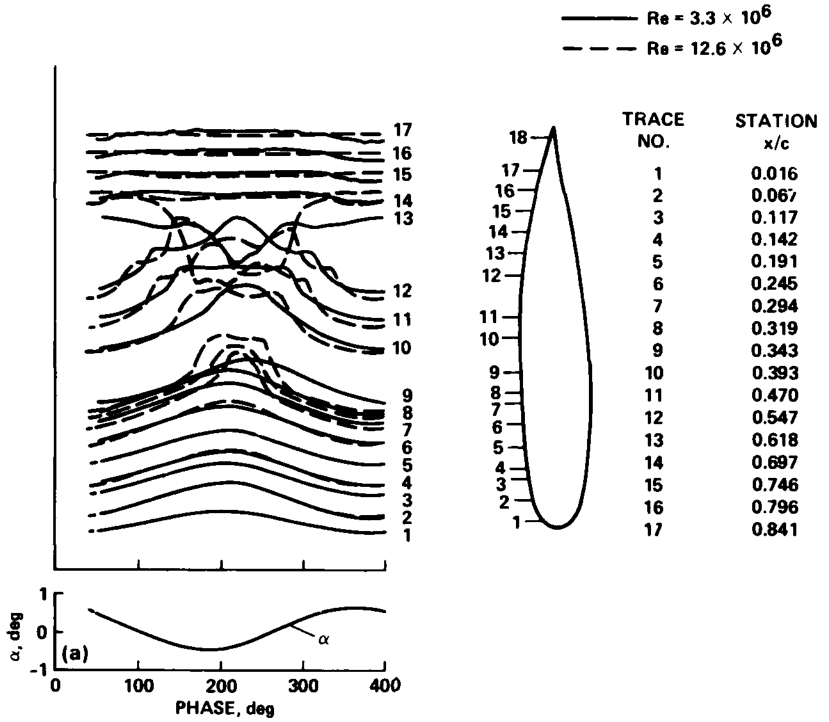

TRACE NO.	STATION x/c
1	0.016
2	0.067
3	0.117
4	0.142
5	0.191
6	0.245
7	0.294
8	0.319
9	0.343
10	0.393
11	0.470
12	0.547
13	0.618
14	0.697
15	0.746
16	0.796
17	0.841

k = 0.05

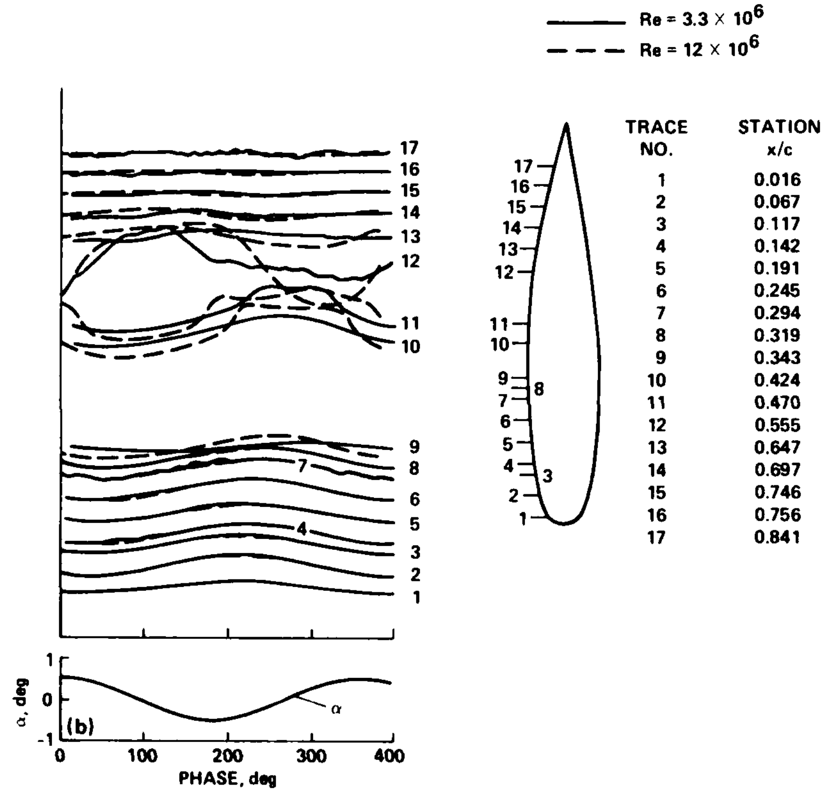

TRACE NO.	STATION x/c
1	0.016
2	0.067
3	0.117
4	0.142
5	0.191
6	0.245
7	0.294
8	0.319
9	0.343
10	0.424
11	0.470
12	0.555
13	0.647
14	0.697
15	0.746
16	0.756
17	0.841

k = 0.20

Fig. 10. Complete time histories of unsteady-pressure data; M = 0.752, α_m = 0.37°, pitching ±0.5° at 0.40 c.

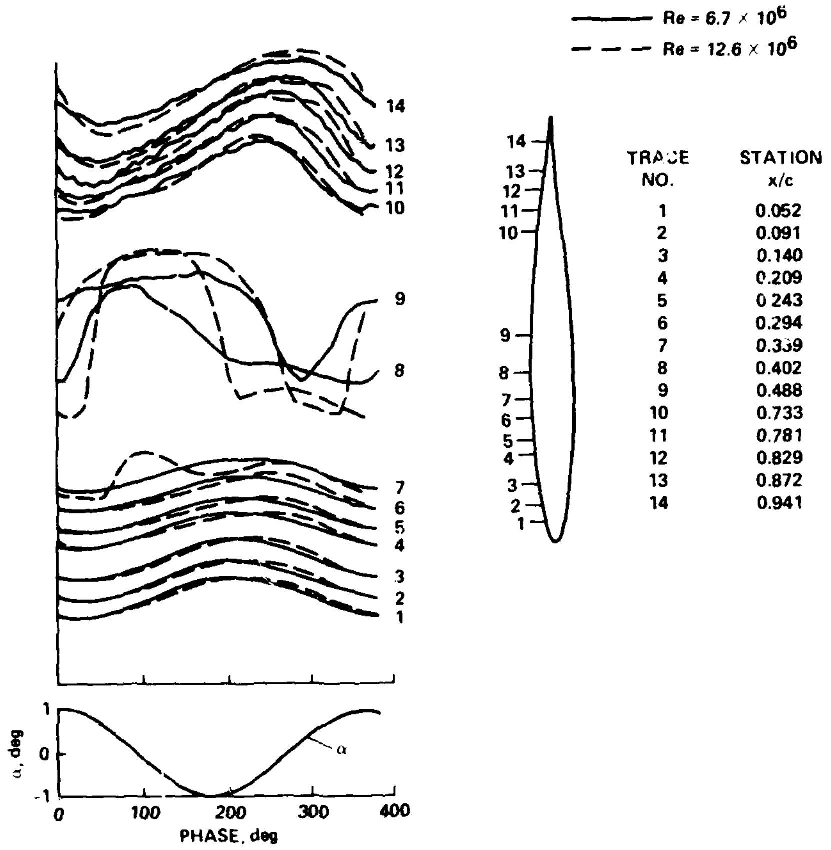

TRACE NO.	STATION x/c
1	0.052
2	0.091
3	0.140
4	0.209
5	0.243
6	0.294
7	0.339
8	0.402
9	0.488
10	0.733
11	0.781
12	0.829
13	0.872
14	0.941

Fig. 11. Complete time histories of unsteady-pressure data; M = 0.789, α_m = 4°, pitching ±1° at 0.25 c, k = 0.20.

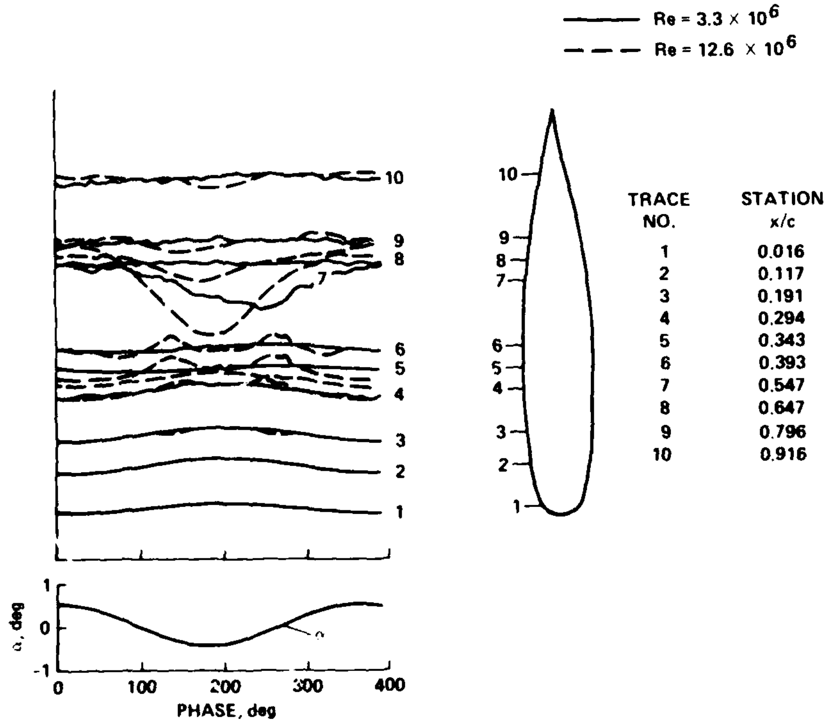

TRACE NO.	STATION x/c
1	0.016
2	0.117
3	0.191
4	0.294
5	0.343
6	0.393
7	0.547
8	0.647
9	0.796
10	0.916

Fig. 12. Complete time histories of unsteady-pressure data; M = 0.807, α_m = 0.38°, pitching ±0.5° at 0.40 c, k = 0.20.

SOME REMARKS ON THE UNSTEADY AIRLOADS ON OSCILLATING CONTROL SURFACES IN SUBSONIC FLOW

by

H. Försching
DFVLR - AVA Göttingen
Institut für Aeroelastik
Bunsenstr. 10, 3400 Göttingen, Germany

Summary

Parameters which are neglected within the framework of linearized potential flow theory, but which are highly influential in the development of unsteady airloads on oscillating control surfaces in subsonic flow are discussed. Based on theoretical and experimental results the effects of gap width and slot geometry, finite thickness, flow viscosity, and incidence of both wing and control surface are explained. Some topics for further research work with regard to active control applications are indicated.

Nomenclature

x, y, z	Cartesian coordinates
L	Lift per unit span
Ma	Mach number
M_α	Wing moment per unit span
M_β	Control moment per unit span, about hinge axis
V	Flow velocity
b	Wing semi-span
c	Wing half-chord
c_β	Chord of control surface
c_p	Unsteady pressure coefficient $= (p - p_\infty) / q$
h	Amplitude of bending deflection
p_∞	Static pressure of undisturbed flow
q	Dynamic pressure $= 1/2\ \rho\ V^2$
Δc_p	Pressure difference between upper and lower surface
f	Frequency of oscillation
k	Reduced frequency $= \omega c / V$
k_a, k_b	Unsteady aerodynamic lift coefficients due to L and M_α
m_a, m_b	Unsteady aerodynamic moment coefficients due to L and M_α
n_c	Unsteady aerodynamic moment coefficient due to M_β
t	Time
α	Amplitude of pitch oscillation
α_o	Steady mean incidence of wing
β	Amplitude of control surface rotation
β_o	Steady mean incidence of control surface
ϵ	Gap parameter (gap width / wing chord)
ρ	Air density
τ	Control surface chord parameter $= 2c / c_\beta$
ω	Circular frequency $= 2\pi f$

1. Introduction

The knowledge of the unsteady aerodynamic loading on oscillating wings with control surfaces is of special concern in aeroelastic investigations and in determining power requirements in active control systems for load alleviation and flutter suppression. In view of the long-recognized inadequacy of linearized methods for the prediction of unsteady airloads on oscillating trailing-edge control surfaces, questions can be raised about the possibilities of further theoretical improvements. One tentative response would point to the attendent possibility of introducing into the theory such effects as boundary layer, transonic shocks near the wing surface, or local variations of flow properties due to thickness and slot geometry. Indeed, from experimental studies it is known that these effects, which are neglected within the framework of linearized potential theory, are highly influential in the development of unsteady airloads on oscillating controls.

This paper elucidates the situation of our present knowledge of the unsteady airloads on oscillating controls, and indicates some topics for further research work, particularly with regard to active control application, and to investigation of the flutter stability of high-performance aircraft during operation at large angles of attack. Based on theoretical and experimental results it is indicated how profile thickness, gap width and slot geometry, incidence of both wing and control and, finally, flow viscosity affect the unsteady airloads on oscillating wing-control systems.

2. Parameters influencing the development of unsteady airloads on oscillating control surfaces

2.1 General remarks

If an aerodynamically unbalanced control is deflected so as to produce a discontinuity in mean surface slope along its leading and side edges, linearized lifting surface potential theory shows that the lifting pressure difference is logarithmically singular along any subsonic leading edge, and that the spanwise lift distribution has a logarithmically infinite derivative at the sides. In analytical predictions based on linearized lifting surface theory, this peculiar behavior of pressure distribution around oscillating controls is taken into account by choosing corresponding pressure functions in applying kernel function collocation methods, and by providing an accumulation of panels around the leading and side edges when panel procedures are applied. As long as the wing is at zero angle of attack and the control surface oscillates around this steady position, and when the gap between the wing and control is closed, experiments have shown that the measured unsteady airloads are in reasonable agreement with theoretical results. But we also know from experiments that the type of pressure distribution in the vicinity of the leading edge of an oscillating control, and thus the related overall unsteady aerodynamic hinge moment coefficients, are extremely sensitive to even small changes in geometric shape. Whereas satisfactory correlation has generally been found between linearized "flat plate" theory and experiment for the unsteady two-dimensional aerodynamic coefficients of oscillating wings (at zero incidence) in subsonic flow, this is not the case for the relating coefficients of oscillating control surfaces, as shown in Fig.1 . It is seen that there is a discrepancy between linearized "flat plate" theory and experiment by roughly 100% , and that the theoretical values are too large.

For this unsatisfactory situation several parameters are known to be of primary influence. As previously mentioned, the geometry of the slot between the main surface and the control, and with it the definition of the effective location of the hinge axis in context with an aerodynamically unbalanced control surface, is of considerable importance. Other important geometric effects may be seen in the gap width, in the finite thickness, and in the static incidence of both the main surface and the control itself. Furthermore, the influence of flow viscosity expressed in boundary layer effects or Reynolds number effects, etc., may be of importance. Although our knowledge about these effects upon the development of unsteady airloads on oscillating wing-flap systems is still rather poor, some general statements can be made from what we have learned so far mainly from wind tunnel measurements.

2.2 Effects of gap width and slot geometry

Concerning the effects of the slot geometry between wing and flap, the leading edge radius, the eccentricity and chordwise location of the hinge, the slot extension and the gap width are of decisive importance. In practical calculations, as shown in Fig.2 , the question whether the translatory part of the control surface motion should be treated as a closed or open slot poses considerable difficulties. Whereas in the real part an open slot yields no pressure singularity at all, a closed slot induces a pressure singularity of the order $1/(x - x_{hinge})$. It can be seen that the character of both pressure distributions is completely different.

A strong pressure sensitivity can also be observed in connection with the gap width between the main surface and the control. This was shown for steady flow by M.Landahl [1] many years ago, and is illustrated in Fig.3 . Starting with a logarithmic singularity at the hinge line, the pressure very quickly changes there to a zero pressure difference at the trailing edge of the fixed wing and a square root singularity at the flap leading edge. It is seen from Fig.3 that this change of pressure singularity appears even for gap parameters ϵ which are only 0.1 to 1% Evidently this is also the case for an oscillating flap with an open gap, as can clearly be seen in Fig.4 . The typical change of the pressure singularity and the increase of pressure on the flap indicated in Fig.3 is also shown in Fig.4 , yielding a corresponding increase of the unsteady hinge moment. This has in fact been observed in wind tunnel measurements, when the gap width has been systematically increased, see Ref. [3] .

Therefore it becomes obvious that, in treating the unsteady aerodynamic problem of the oscillating wing with control, we have to deal basically with an aerodynamic interference problem of two lifting systems when the gap is unsealed, as is the case with real aircraft wings. The same condition of course holds true also for a wing with a leading edge flap.

On the other hand, in wind tunnel model measurements, the slot geometry between wing and control surface is usually made up of two concentric circles, i.e. there is no eccentricity and practically no aerodynamic balance. Thus, the gap parameter ϵ is usually smaller than 0.3% . In reality aircraft wings with control surfaces exhibit rather asymmetric slot geometries which may considerably affect both the steady and unsteady airloads on the lifting system. In particular this is the case when the wing and/or the control surface have a steady mean incidence, as will be shown later.

There is a need for more detailed theoretical and experimental investigations of these effects of slot geometry and gap width. With the possibilities given by the application of panel procedures it may be expected that at least potential-type theoretical solutions of the two-dimensional problem will be elaborated in the near future, as already pointed out by Dr. Geissler in his paper.

2.3 Effects of finite thickness and steady incidence

If the control surface is not coplanar with the fixed wing but is rather oscillating about a steady mean incidence, drastic effects on the development of the unsteady pressure distributions have also been observed. Apart from an increase in the load distribution with increasing mean flap incidence β_0 , the type of pressure singularity is also changing. In particular, the imaginary part of the pressure distribution, which is non-singular if the wing and the flap are coplanar, has been found to become discontinuous or even singular at the hinge point location at non-zero mean flap incidences when the gap is closed; see Ref. [2].

On the other hand, it is well known from theoretical investigations on a series of airfoils with finite thickness that the development of the unsteady flow on oscillating airfoils may be changed remarkably by thickness effects, see Ref. [4]. This fact is obvious in Fig.5, where the unsteady two-dimensional aerodynamic lift and moment coefficients of a Joukowski airfoil pitching about its mean chord in incompressible flow are illustrated. For wings of moderate thickness (smaller than 10%) and in the reduced frequency range of interest ($0.1 < k < 2$), the thickness effect in Fig.5 is relatively small, i.e. of the order of only a small percentage.

It is not adequately known to what extent finite thickness affects the development of unsteady airloads on oscillating control surfaces, and hence the related two-dimensional unsteady aerodynamic coefficients widely used in strip analyses. The same holds true for the influence of the steady angle of attack which is also neglected in the process of linearization of the potential equation within the framework of small-perturbation theory. In fact, inviscid linearized small-perturbation lifting surface theory has served the aeroelastician well in a majority of the aircraft design applications, and it has been carried now to a high level of mathematical and numerical development. For oscillating wings without controls in subsonic flow the effects of thickness and steady angle of attack on the unsteady airloads seem to be of only minor importance. However, there is evidence that the effect of these parameters is indeed important, in conjunction with the slot geometry and the open gap on the unsteady airloads of oscillating control surfaces. This conclusion has been drawn from wind tunnel measurements on an oscillating wing-flap system in two-dimensional incompressible flow, which have been performed recently at DFVLR in Göttingen [4], some results of which are shown in the following figures.

Fig.6 illustrates the profile geometry of the investigated airfoil with flap. The airfoil has a NACA 0012-profile, the flap has a chord ratio of 30%, and the control hinge is at 75% of the wing chord. The slot geometry is asymmetric and hence typical for a slot usually found in real aircraft. Fig.6 also shows a comparison between the calculated and measured chordwise unsteady pressure distribution for the case that the airfoil with flap is at zero incidence ($\alpha_0 = 0$ and $\beta_0 = 0$), the wing is at rest and the flap is undergoing harmonic oscillations about its hinge axis, and the gap is closed. As can be seen, there is a reasonably good correlation between linearized "flat plate" theory and experiment, although a small slot effect becomes obvious even when the gap is closed.

However, when the flap oscillates about steady mean incidences $\beta_0 \neq 0$ and the gap is not closed, drastic changes in the unsteady pressure distributions occur, as illustrated in Fig.7. The same condition has been observed when the angle of attack $\alpha_0 \neq 0$, as illustrated in Fig.8. Finally, Fig.9 shows the effects of steady mean incidence of both the wing (α_0) and the flap (β_0) upon the unsteady aerodynamic pressure distribution, together with the effect of the open and closed gap. It is clear that the closed gap yields a completely different pressure distribution and even a flow separation at the trailing edge of the flap. There is practically no agreement with linearized "flat plate" predictions here, particularly on the fixed wing and surprisingly even when the gap is closed.

A striking feature of all these pressure distributions near the flap leading edge is that two rather pronounced pressure peaks always appear when the gap is open, thus indicating that the aerodynamic wing-flap problem in this case is in fact an aerodynamic interference problem.

Perhaps the most important practical consequences of these incidence and slot geometry effects with regard to active control applications are manifested in the related control hinge moments, as illustrated in Fig.10. It can be seen that the unsteady hinge moment coefficients n_c are changing completely when the gap is closed. Linearized "flat plate" theory yields rather unrealistic results and the relatively good agreement in the imaginary part at small reduced frequencies must be considered a mere coincidence.

2.4 Effect of flow viscosity

It is often argued that thickness effects are roughly compensated for by boundary layer effects, explaining the good agreement frequently found when comparing experimental aerodynamic results with the theoretical ones which neglect wing thickness and fluid viscosity. To what extent this argument is really true is not definitely clear, and as long as no results are available from systematic wind tunnel measurements in a wide range of Reynolds numbers, this reasoning should be applied with care. In fact, there is some evidence that the boundary layer or the Reynolds number effect is of minor importance in treating unsteady aerodynamic problems of oscillating wings without controls at least in subsonic flow at small incidences. Application of transition strips is a common practice to simulate a turbulent boundary layer and a transcritical Reynolds number in wind tunnel model tests. However, from the very few test results available for oscillating control surfaces at various Reynolds numbers, we know (see Ref.[5]) that hinge moments of oscillating flaps are decisively dependent upon the Reynolds number. Test results at moderate Mach numbers show deviations from potential theory calculations up to 100%, even in the case of zero mean angle of attack (see also Fig.1). It is difficult to say to what extent these discrepancies may be attributed to flow viscosity effects. For oscillating control surfaces, we must keep in mind that effects of gap geometry and incidence are at least of the same order of magnitude, as shown in the previous discussion. On the other hand, it must be assumed that an interaction takes place between the boundary layer and the very complicated flow processes at the flap leading edge for those (open) gap geometries as they indeed exist on slotted aircraft wings, in particular when the wing-flap lifting system is operating at non-zero incidences. All these effects are widely unknown and there is an urgent need for detailed theoretical experimental investigations.

As Dr. Geissler has mentioned in his paper, there is work underway at DFVLR to gain more insight into these rather complicated aerodynamic problems. By applying a potential velocity panel procedure, an elaboration of theoretical results for the unsteady airloads on oscillating control surfaces is attempted, taking into account the effects of finite thickness, gap geometry and incidence. On the other hand, systematic wind tunnel measurements of two-dimensional unsteady aerodynamic hinge derivatives in the Reynolds number range 10^5 to 10^7 are in preparation in a new type of compressed-air wind tunnel. It is hoped that these investigations will provide a better understanding of the unsteady airloads on oscillating controls in context with real aircraft wing-control geometries and Reynolds numbers.

3. Conclusion

From the discussions it became apparent that those parameters neglected within the framework of linearized potential flow theory may be highly influential in the development of unsteady airloads on oscillating control surfaces in subsonic flow. In particular, the effects of slot geometry and gap width, finite thickness, steady mean incidence of both wing and flap, and flow viscosity have been shown to be of decisive importance. Since most of what we know today about these effects has been learned from wind tunnel studies, efforts should be made to elaborate at least potential-type theoretical solutions. Application of panel procedures may serve in this intention well.

Almost nothing is known about the influence of flow viscosity, and there is an urgent need for systematic wind tunnel investigations on this subject with a wide range of Reynolds numbers. Since the development of unsteady airloads on oscillating control surfaces in all its detail is still not thoroughly understood, much research work on this practical important topic of unsteady aerodynamics is necessary in the future, especially with regard to active control applications.

4. References

[1]	White, R.B. Landahl, M.	Effect of Gaps on the Loading Distribution of Planar Lifting Surfaces. AIAA Journal, Vol.6, No.4, 1968, pp.626-631
[2]	Laschka, B.	Unsteady Aerodynamic Prediction Methods Applied in Aeroelasticity. AGARD Rep. No.45, 1975, pp.1-7 to 1-31
[3]	Bergh, H.	Experimental Determination of the Aerodynamic Forces on an Oscillating Wing with Control Surface in Incompressible Two-Dimensional Flow. NLL-Report F.175, 1955
[4]	Küssner, H.G.	Non-Stationary Theory of Airfoils of Finite Thickness in Incompressible Flow. AGARD Manual on Aeroelasticity, Part II, Chapter 8
[5]	Kienappel, K. Round, D.	Analysis of Unsteady Pressure Measurement on an Airfoil Section with an Harmonically Oscillating Slotted Flap. To be published shortly as DLR-FB 80-22
[6]	Gray, R. Davies, D.E.	Comparison of Experimentally and Theoretically Determined Values of Oscillatory Aerodynamic Control Surface Hinge Moment Coefficients. RAE Techn. Report 72023, March 1972

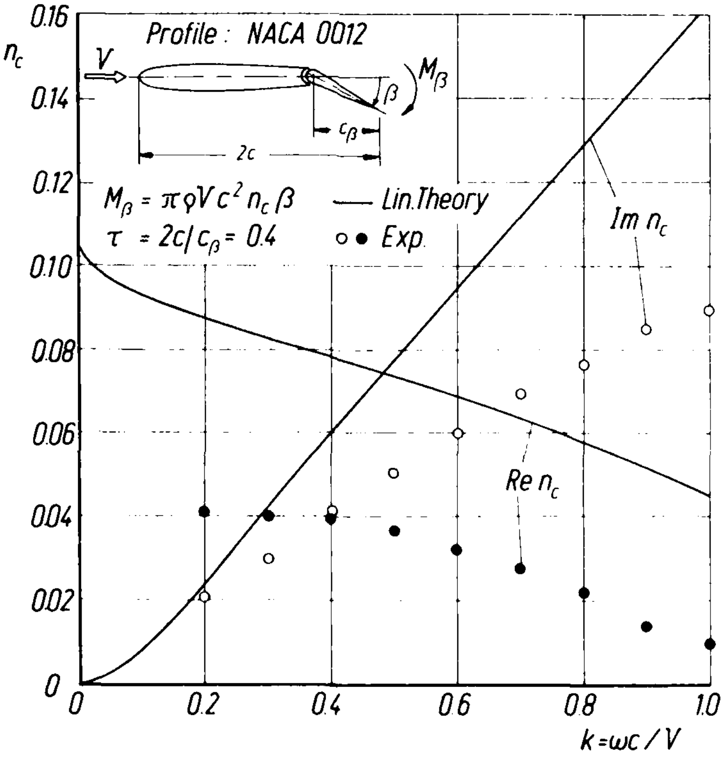

Figure 1: Comparison of theoretically predicted and measured unsteady aerodynamic hinge moment coefficients of an oscillating flap.

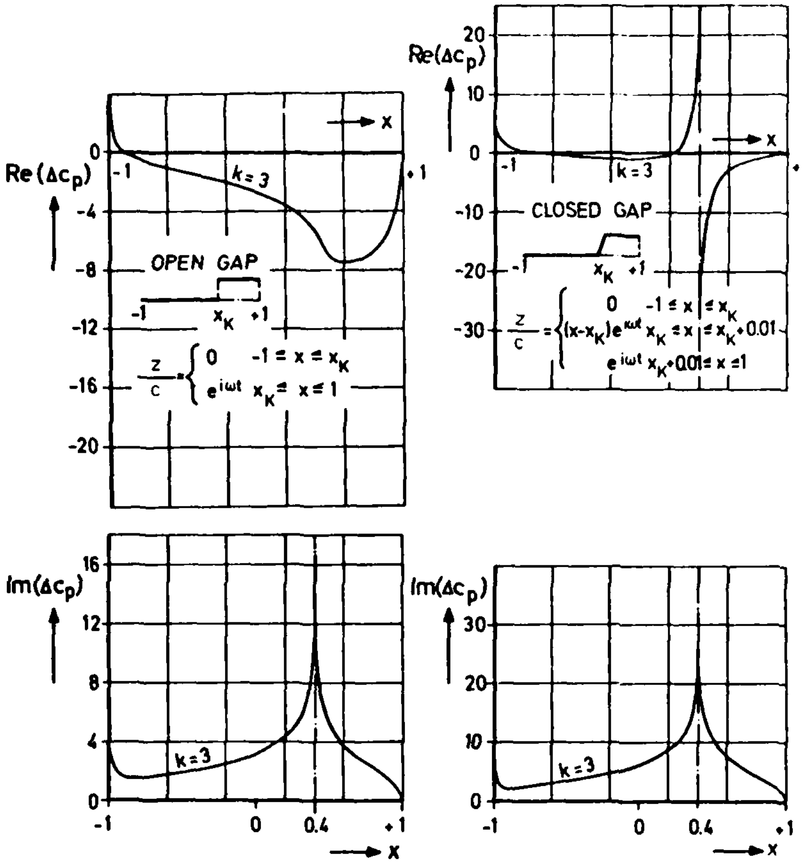

Figure 2: Effect of gap geometry on the unsteady pressures of wings with control surfaces performing translational oscillations. (Ref. [2])

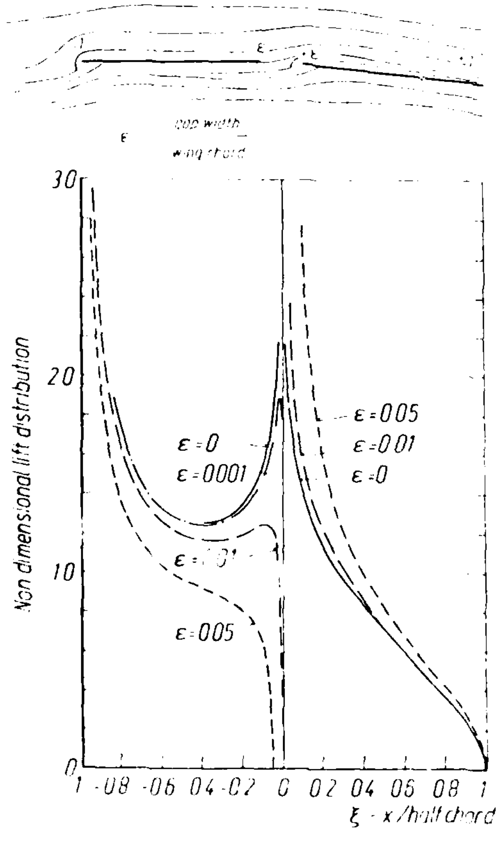

Figure 3: Effect of gap size on chordwise pressure distribution of an airfoil in steady incompressible flow. (Ref. [1])

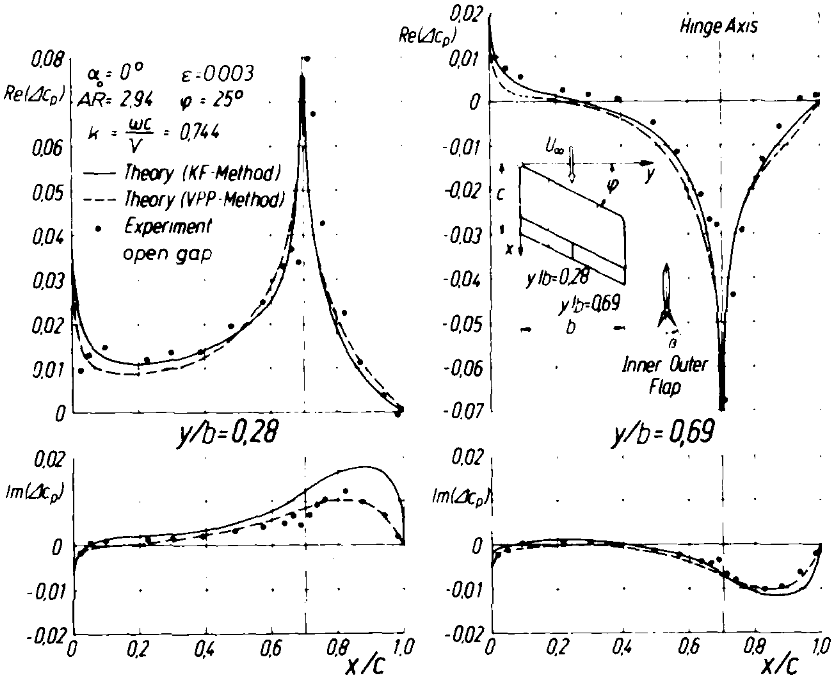

Figure 4: Measured and calculated unsteady aerodynamic pressure distributions at two specified spanwise sections on a fixed, constant-chord, swept half-wing with a NACA 0012-profile, and with two controls oscillating harmonically with equal amplitude in antiphase, in incompressible flow.

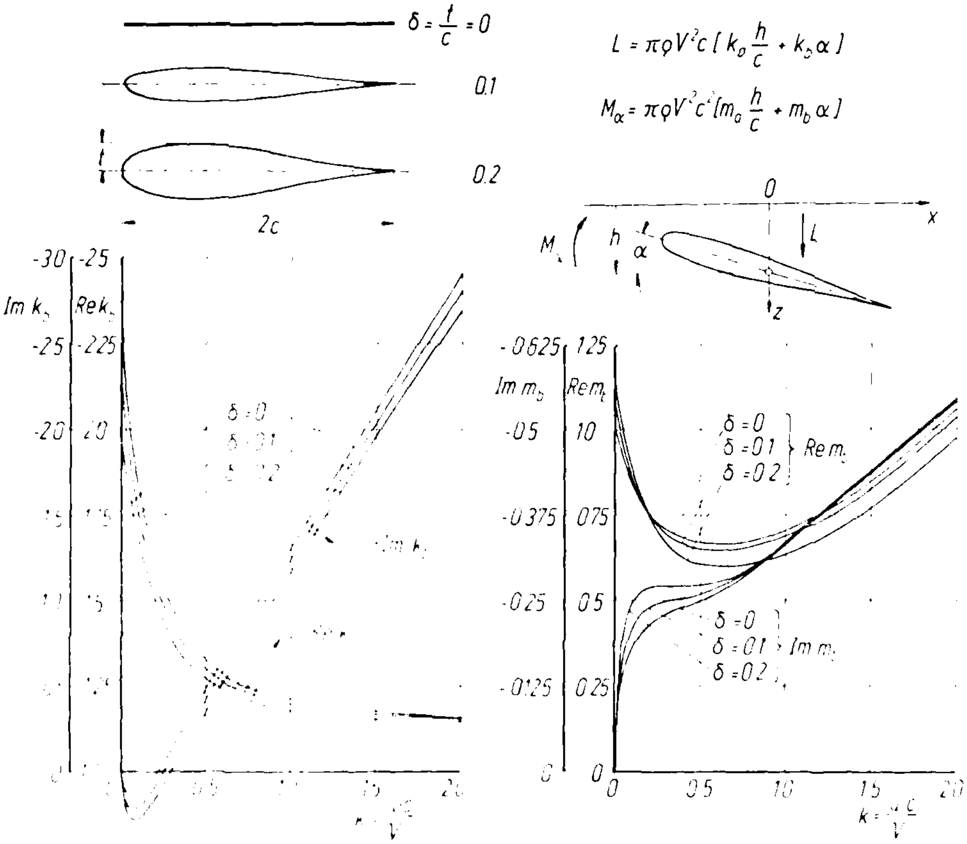

Figure 5: Influence of thickness on lift and moment coefficients of a Joukowsky-profile pitching about its mean chord (Ma 0).

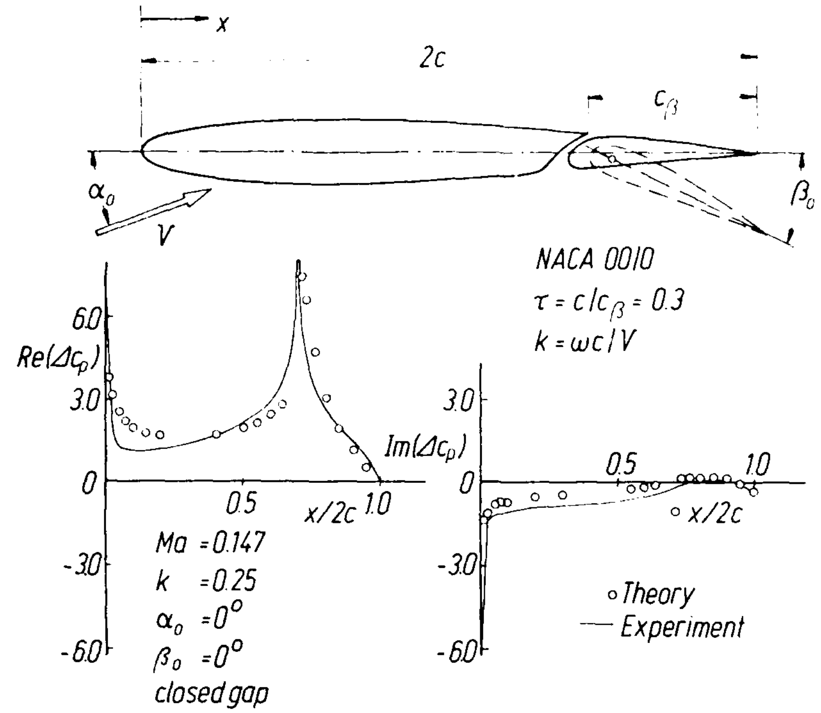

Figure 6: Profile and comparison between theory and experiment of the investigated two-dimensional wing-flap system, when the flap is undergoing harmonic oscillations about its hinge axis.

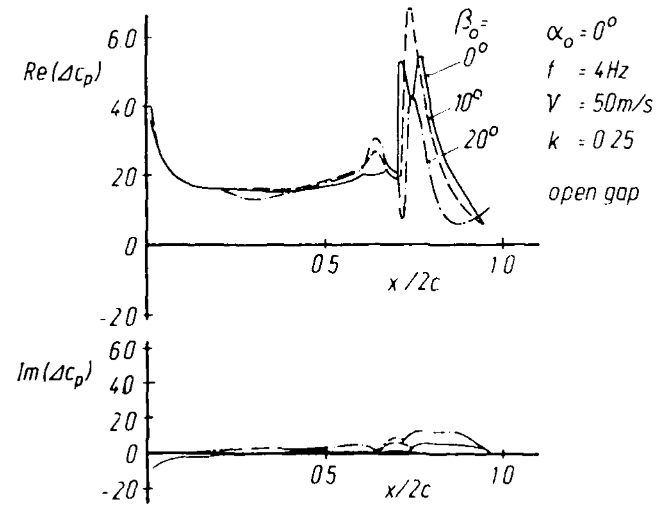

Figure 7: Unsteady aerodynamic pressure distributions of the wing-flap system, when the flap oscillates harmonically about several steady mean incidences β_0 and the gap is open.

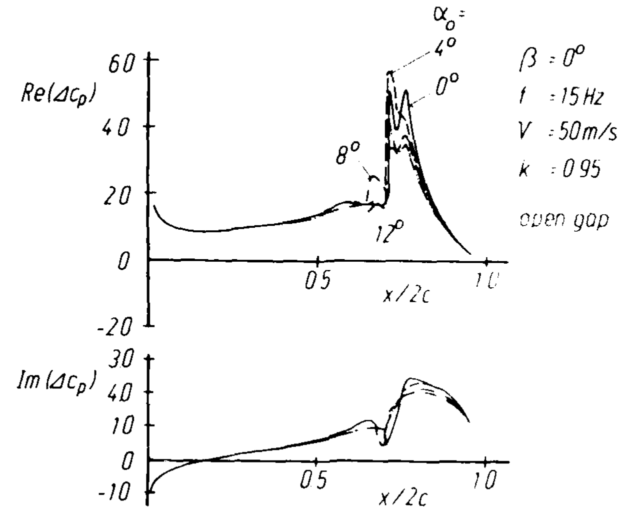

Figure 8: Unsteady aerodynamic pressure distributions of the wing-flap system of different steady mean angies of attack α_0 , when the flap oscillates harmonically and the gap is open.

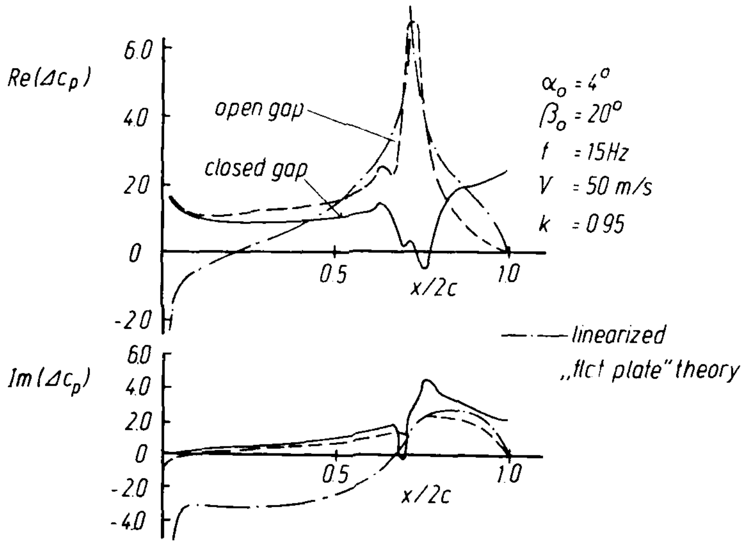

Figure 9: Effects of steady mean incidences α_0 and β_0 , and sealing of the gap upon the unsteady aerodynamic pressure distributions of the wing-flap system, when the flap oscillates harmonically about its hinge axis.

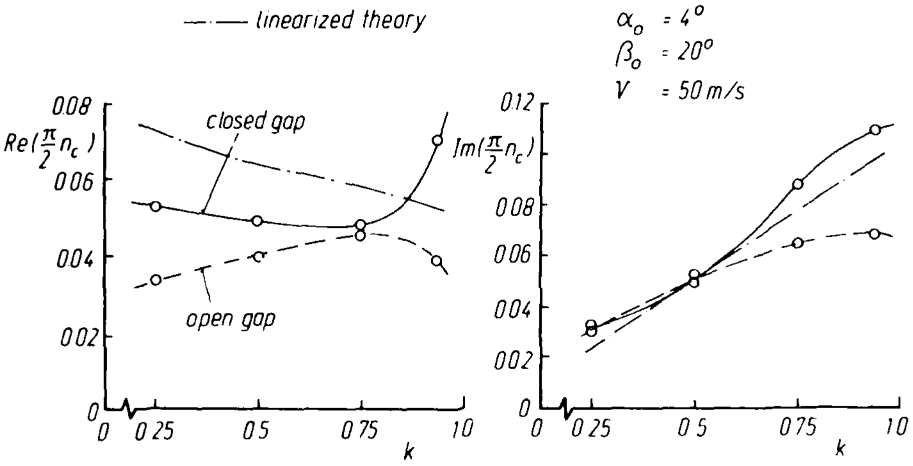

Figure 10: Influence of slot geometry on the unsteady hinge moment coefficient n_c , when the flap oscillates harmonically about its hinge axis.

OSCILLATORY FLOWS FROM SHOCK-INDUCED SEPARATIONS ON BICONVEX AEROFOILS OF VARYING THICKNESS IN VENTILATED WIND TUNNELS

D. G. Mabey

Structures Department, Royal Aircraft Establishment, Bedford, UK

SUMMARY

Previous tests of biconvex aerofoils at zero incidence at transonic speeds have sometimes shown a narrow Mach number range within which the flow is periodic. Within this range large surface pressure fluctuations are developed at a discrete frequency, $\omega c/U$ of order 1, which would strongly influence the buffeting of any aerodynamic component with this section. Similar instabilities at transonic speeds have also been observed on other aerofoils for thickness/chord ratios greater than about 10%.

Recently the flow instability boundaries on a series of biconvex aerofoils with thickness/chord ratios varying from 10 to 20%, set at zero incidence, were measured in a small transonic tunnel. The region of flow instability with laminar boundary layer/shock wave interactions was a little wider than the corresponding region with turbulent boundary layer/shock wave interactions. A criterion for the occurrence of the instability was developed from the measurements.

Some interesting examples of dynamic wall-interference effects were observed in the slotted working sections with hard slats, which were greatly reduced in the alternative slotted working sections with slats made from sound-absorbing laminate. Interesting examples of dynamic interference were also observed in special comparative tests in closed working sections formed by hard or laminate walls.

LIST OF SYMBOLS

A	empirical expression for $\omega \ell/U$
C_L	lift coefficient
c	aerofoil chord
C_A, C_H	aerodynamic and elastic hinge stiffnesses (eqn 4)
d	total plenum chamber depth/tunnel height
f	frequency of instability (Hz)
H	tunnel height
I	flap inertia
K	transonic similarity parameter (eqn 1)
K_e	equivalent transonic similarity parameter
ℓ	distance from terminal shock wave to trailing edge
M	free stream Mach number
M_{crit}	critical Mach number
M_e	equivalent Mach number associated with K_e
M_1	Mach number just upstream of terminal shock
$\bar{p}$	rms pressure fluctuation
q	free stream kinetic pressure
R	Reynolds number based on c
t	aerofoil thickness
T	time
U	free stream velocity
x, y	coordinates (Fig 2)
α	angle of incidence (degrees)
γ	ratio of specific heats
ω	circular frequency, $2\pi f$ (radians/second)

1 INTRODUCTION

Recently there has been renewed interest in the use of thick wing sections (with thickness/chord ratios, t/c, greater than say 10%) for civil aircraft operating at high subsonic speeds (say from $M = 0.75$ to 0.85). Thus a wing section 15.1% thick will be used at the root of the A310B aircraft. These thick sections allow reduced wing structural weight or increased aspect ratio, and may also be conveniently combined with advanced sections which incorporate some degree of supercritical flow.

One possible difficulty with such thick sections at transonic speeds and low angles of incidence is the occurrence of periodic pressure fluctuations at frequency parameters, $\omega c/U$, of order 1. Some time ago Lambourne[1] collected limited evidence for such relatively low excitation frequencies at transonic speeds on a number of conventional aerofoil sections with thickness/chord ratios higher than 10%. Recently Roos and Riddle[2] found a low level of discrete excitation at a frequency parameter of about 0.4 on a supercritical wing of thickness/chord ratio 11%. At the design lift coefficient (of about $C_L = 0.5$) the discrete excitation persisted over the wide Mach number range from $M = 0.60$ to $M = 0.87$ (see Ref 2, Fig 22).

Thick biconvex aerofoils set at zero incidence are interesting because these produce discrete excitation over a narrow range of Mach numbers at transonic speeds. Thus McDevitt *et al*[3] found a narrow region of oscillatory flow in an 18% thick biconvex aerofoil (see Fig 1), which persisted over a wide range of Reynolds number. The region of oscillatory flow was wider when the Mach number was decreased ($dM/dT < 0$) because of flow hysteresis. This oscillatory flow is generated by the upstream and downstream movement of the terminal shock and oscillatory vortex shedding in the wake. The phenomenon has subsequently been predicted[4,5], from a numerical solution of the full Navier-Stokes equations with an appropriate turbulence model. However no simple prediction method or adequate physical explanation for the self-excited shock wave oscillation is yet available.

The present note provides the measured instability boundaries for biconvex aerofoils with thickness/chord ratios varying from 10 to 20%. Analysis of the measurements suggests features of the pressure fields which might produce flow instability on conventional aerofoil sections. The measurements may also stimulate further theoretical studies.

2 EXPERIMENTAL DETAILS

The slotted transonic working section of the RAE 4 in × 4 in tunnel (H = 101 mm) was used for these tests (Fig 2). Tests were made with both hard and laminate (sound-absorbing) liners[6,7]. Most of the tests were made with a total dimensionless plenum chamber depth, $d = 0.67$, as illustrated in Fig 2, but a few comparative tests were made with a total plenum chamber depth of $d = 4.0$. A few special tests were made with hard and laminate closed working sections.

The biconvex aerofoils were made of wood and spanned the tunnel centrally. For the aerofoils with thickness/chord ratios of 10, 12, 14, 16 and 18% the chords selected were $c = 32$ mm and 50 mm. For the aerofoils with thickness/chord ratio 20% the chords were reduced to 25 mm and 41 mm to reduce the blockage. For brevity this reduction in chord is ignored in figures where measurements for thickness/chord ratios of 20% are included.

For simplicity no pressure transducers were generally installed in a model. Instead, six pressure transducers used in previous tests[6,7] were mounted on one sidewall close to the model and ahead of it (Fig 2). Five transducers distant 0.5H upstream of the model were used to check the wave form of the tunnel resonance excited by the unstable flow on the model. Note that one transducer was in the top plenum chamber. A single transducer adjacent to the model centre line, but displaced 0.25H below it, was used initially to detect the onset of flow instability. Later this transducer was supplemented by another closer to the model ($y/H = -0.05$), and by another actually flush mounted on the 18% thick aerofoil with $c = 50$ mm at 78% chord ($y/H = 0$).

The tunnel total pressure and total temperature cannot be independently controlled. The tunnel total pressure is always a little lower than ambient static pressure and the tunnel total temperature lies in the range from 10°C to 15°C. For the small aerofoils used in the present tests ($c = 32$ mm and 50 mm) this only gives Reynolds numbers of about 0.4×10^6 and 0.6×10^6 respectively. These low Reynolds numbers ensured that laminar boundary layer/shock wave interactions were achieved on the smaller aerofoils. Turbulent boundary layer/shock wave interactions were ensured by fixing transition 2.5 mm downstream of the leading edge with a narrow band of ballotini (small glass spheres) of dia. 0.25 mm.

3 RESULTS

3.1 Determination of flow instability boundaries and resonances

Fig 3 shows some initial test results with free transition and a laminar boundary layer/shock wave interaction for the 18% thick aerofoil with a chord of 32 mm. Fig 3a shows that the Mach number range for flow instability is easily measured on the sidewall below the model (at $y/H = -0.25$), although the pressure transducer is located a significant distance (0.78c) below the aerofoil. The lower Mach number limit to the range of flow instability is rather ill-defined because of flow hysteresis similar to that observed by McDevitt (Fig 1). The curve for the laminate slats is about 0.02 lower in nominal Mach number compared to the hard slats. This displacement is probably caused by the increased boundary layer growth on the relatively rough surface of the laminate slats compared to the smooth, hard slats, for the increased boundary layer growth should increase the local free stream Mach number for a fixed nominal Mach number.

The pressure fluctuation measurements upstream of the model given in Fig 3b show that the flow instability on this aerofoil at a Mach number of 0.78 excites a stronger resonance in the working section with hard slats. This is because the discrete frequency of the excitation has been made to coincide with the fundamental transverse resonance frequency of the working section by the deliberate choice of a chord length of 32 mm. The resonance frequency (1100 Hz) had been excited previously by a loud speaker mounted in the plenum chamber and predicted according to a new theory[7]. This resonance condition is particularly interesting, because although Fig 3a shows that the strength of the excitation is virtually unaltered by the change from hard slats to laminate slats, Fig 3b shows that the strength of the resonance is significantly reduced. Fig 3b thus provides an example of the superiority of sound-absorbing slats for dynamic tests of aircraft models at transonic speeds.

Fig 3b also illustrates an interesting feature of the sound-absorbing slats. The resonance frequency (1070 Hz) is a little lower than with hard slats (1100 Hz). The lower resonance frequency is attributed to a small increase in the effective acoustic height of the working section, due to the movement of air into the laminate. Lower resonance frequencies with laminate liners were observed previously both with these liners in the 4 in × 4 in tunnel[7] and with comparative 'mock-up' liners in the RAE 3 ft tunnel[8].

Fig 4 shows some typical results for the same aerofoil with fixed transition. Fig 4a shows that the Mach number range for flow instability is still well defined, although the level of pressure fluctuations is only about 20% of that measured previously with free transition (*cf* the change of scale between Fig 4a and Fig 3a). Fig 4b shows that at this reduced level of excitation, no resonance mode can be detected, even in the working section with hard slats.

Fig 5 illustrates an interesting oscillation observed with free transition on the 10% thick aerofoil with a chord of 32 mm at a higher Mach number, about M = 0.90. Fig 5a indicates that the range of Mach number for flow instability ($0.88 < M < 0.91$) is much the same with hard slats as with laminate slats.

However the oscillation frequency changes radically between the hard and laminate slats. With the hard slats the frequency observed (1000 Hz) coincides with the fundamental transverse resonance frequencies previously measured[7] with acoustic excitation. However, this gives too low a frequency parameter (0.77) compared with previous measurements on a nominally identical model with free transition in a much larger slotted tunnel[9]. When the hard slats are replaced by laminate slats the frequency observed is much higher (1370 Hz), and the higher frequency parameter (1.05) is in better agreement with the previous measurements [9] (see Fig 7). We may infer that with the hard slats the shock oscillation is locked to the tunnel resonance frequency and is therefore best regarded as a forced oscillation. This hypothesis is supported by the relatively high pressure fluctuations measured upstream of the model with the hard slats in comparison with the low pressure fluctuations measured with laminate slats (Fig 5b). The measurements in Fig 5 thus represent a severe, though admittedly rather unusual, example of dynamic interference.

Similar but smaller increases in the oscillation frequency were also noticed for the 12% aerofoils with chord 50 mm (with both transition free and fixed) and these have been indicated later (Fig 7). For the thicker aerofoils ($t/c \geqslant 14\%$), alteration of the slats did not change the oscillation frequency. Hence most of the measurements are probably free of dynamic interference, except when the oscillation frequency actually coincides with a tunnel resonance frequency, as previously discussed (*eg* Fig 3).

3.2 Boundaries for flow instability

Fig 6 shows the flow instability boundaries measured on biconvex aerofoils of both groups.

For the short chord aerofoils with free transition the boundary layer/shock wave interaction is laminar at these low Reynolds numbers and there is a range of Mach number of about 0.04 over which the flow is unstable. For the thinnest aerofoil, with t/c = 10%, the measured range of instability is in excellent agreement with that observed with free transition by Karashima[9]. With fixed transition the flow is stable for t/c = 10% (just as in Karashima's tests) and is also stable for t/c = 12%. For $t/c \geqslant 14\%$ the flow is unstable over a smaller range of Mach number of about 0.02.

For the long chord aerofoils, giving the higher Reynolds numbers, the boundaries for flow instability with transition free and transition fixed are quite similar. No instability was observed for t/c = 10%. However, with t/c = 12% there was a well marked instability with free transition and a weak instability with fixed transition; oil flow tests established that with free transition there was a shock induced separation at about $x_s = 0.7c$, which was eliminated with fixed transition.

When due allowance is made for the scatter in the measurements, inevitable because of flow hysteresis, the results for both groups of aerofoils are in good agreement for thickness/chord ratios above 12%. However for the lowest thickness/chord ratio (10%) the instability is only found for the short chord aerofoil with a laminar boundary layer/shock wave interaction. Hence wall interference on these flow instability boundaries is probably fairly small, despite the large blockage ratios of the models.

In addition the present instability range for the long chord aerofoil with t/c = 18% and fixed transition are in excellent agreement with the instability observed at the same low Reynolds number in a closed working section with carefully contoured liners[10]. In contrast, the present instability range for t/c = 20% does not agree with the instability observed previously[11] at an indicated Mach number of 0.71.

3.3 Frequency parameters for instability and dynamic interference

Fig 7 shows the frequency parameters, $\omega c/U$, measured on both groups of models with transition free and transition fixed. These measurements were made in the slotted working section with hard slats, except where there is tunnel resonance and the results for laminate slats are preferred as having less wall interference (section 3.1).

For the short chord aerofoils (Fig 7a) with free transition the frequency parameters lie in the range from about 0.72 to 1.04. The two frequency parameters observed for $t/c = 10\%$ with the hard and the laminate slats correspond with the measurements presented in Fig 5. With the laminate slats the frequency parameter is in better agreement with Karashima's measurements[9]. With transition fixed the frequency parameters are a little lower than with transition free, but no oscillation is observed for $t/c = 10\%$ and 12%.

For the long chord aerofoils (Fig 7b) the frequency parameters lie in the range from 0.85 to 1.15, significantly higher than for the short chord aerofoils. If we tentatively assume that the frequency parameter is controlled primarily by the shock position, the lower frequency parameter at the lower Reynolds number suggests that with thicker boundary layers the mean shock position is further upstream. This hypothesis is consistent with the observation that with fixed transition, and excessively thick turbulent boundary layers, the frequency parameters are again a little lower than with free transition.

The measurements made with transition free on the long chord aerofoil make an interesting comparison with other measurements made on thick biconvex aerofoils. Thus for $t/c = 18\%$, the frequency parameter in the present tests is about 1.07, compared to the somewhat lower value of 0.98 observed over a wide range of Reynolds number by McDevitt[3]. McDevitt's measurements may be subject to some dynamic interference from the hard walls of the closed working section which lowers the frequency of the instability, even in the absence of a tunnel resonance.

Special tests with the present 18% thick aerofoils in alternative closed working sections made with hard and laminate top and bottom walls were made to confirm this hypothesis. These walls were uncontoured (in contrast with McDevitt's experiment) so that the flow choked at comparatively low Mach numbers. However, just before choking a range of flow instability was observed, as in the slotted working sections at higher Mach numbers. For the aerofoil with c = 50 mm, the flow choked at about M = 0.71 in the closed working sections, and the range of instability was about

$$0.68 < M < 0.70 \quad ,$$

(*cf* $0.76 < M < 0.79$ for the hard slotted working section). However, with the hard walls the frequency of the instability (830 Hz) was appreciably lower than with laminate walls (1000 Hz), although the level of fluctuation was almost unaltered. With these closed laminate walls the frequency (1000 Hz) was thus a little higher than the frequency (890 Hz) in the unchoked slotted working section at much higher speeds. This change in frequency thus illustrates an interesting consequence of the approach to choking in a closed working section.

Similarly, for the 18% thick aerofoil with c = 32 mm the flow choked in the closed working sections at about M = 0.77, and the range of instability was from about

$$0.73 < M < 0.74 \quad ,$$

(*cf* $0.78 < M < 0.81$ in the hard slotted working section). However with the hard closed walls the frequency (1030 Hz) was appreciably lower than with the laminate walls (1130 Hz). Again with the closed laminate walls the frequency was almost the same as in the hard slotted working section (1100 Hz) at much higher speeds.

Now in McDevitt's experiments the ratio, H/c, of the tunnel height to the aerofoil chord, was 1.9, compared to 2.0 and 3.1 in the present tests for the aerofoils with c = 50 mm and 32 mm. Hence the frequency observed with the hard contoured walls is probably about 10 to 20% lower than would be obtained in an unconstrained flow, or with contoured walls made of sound-absorbing laminate.

An investigation of the instability on the 12% thick aerofoil with c = 50 mm and free transition gave similar results. The range of instability from both closed working sections was from

$$0.75 < M < 0.76 \quad ,$$

(*cf* $0.85 < M < 0.86$ in the hard slotted section), but the frequency was only 690 Hz with the closed hard walls compared to 870 Hz with the closed laminate walls. The corresponding frequency in the hard slotted section was 820 Hz. Even with slotted walls we have seen in section 3.1 that the frequency parameter on this aerofoil increased significantly when the hard slats were replaced by sound-absorbing slats.

Of course, if closed walls are used much further away from the models dynamic interference can be reduced. Thus Finke[11] measured a frequency parameter of 1.13 for an aerofoil with $t/c = 20\%$ in a closed section with hard walls and $H/c = 8$, in good agreement with the present measurements for $H/c = 2.4$ in the slotted working sections.

3.4 Level of excitation

The small size of these models prevented the general installation of pressure transducers to measure the excitation directly. However, the rms pressure fluctuations, $\bar{p}$, on the sidewall adjacent to the centre line of the models (at $x/H = 2.5$ in Fig 2) were used initially to indicate the variation of the excitation of the model with thickness/chord ratio and boundary layer thickness.

Fig 8 shows as functions of the thickness/chord ratio three typical sets of measurements of the maximum sidewall pressure fluctuations over the range of Mach number. This maximum generally occurs close to the middle, or just below the middle, of the unstable flow regions shown in Fig 6. Fig 8a shows that for the short chord aerofoils the maximum pressure fluctuations are significantly higher with free transition than with fixed transition. Now a laminar boundary layer/shock wave interaction would generally be of much greater extent than a turbulent interaction. Hence in an unsteady flow wider shock excursions, giving larger pressure fluctuations, would be expected with a laminar boundary layer than with a turbulent boundary layer. A similar difference between the surface pressure fluctuations observed with laminar and turbulent boundary layer/shock wave interactions was previously noticed for nominally steady, attached flow on a swept wing at $M = 0.90$. (See discussion on Fig 11b in Ref 12.) The dotted curves in Fig 8a indicate the approximate level of pressure fluctuations which might have been expected for $t/c = 18\%$ and 10% in the absence of the resonances discussed in Figs 3 and 5.

The measurements shown in Fig 8a relate to hard slats. With laminate slats (Fig 8b) the maximum pressure fluctuations on the sidewall are a little lower, but the general character is unaltered. Upstream of the model (at $x/H = 2.0$) the pressure fluctuations are appreciably lower with the laminate slats than with the hard slats. This is because the laminate slats weaken the forward propagation of the pressure fluctuations, rather than alter the excitation at source.

Fig 8c shows corresponding measurements for the longer chord aerofoils tested with hard slats. Again the pressure fluctuations are significantly higher for the thin boundary layer obtained transition free than for the thick turbulent boundary layer obtained transition fixed, and may give the better indication of the level of pressure fluctuations at high Reynolds numbers. These sidewall pressure fluctuation measurements with transition free and fixed are both a little lower than the corresponding measurements on the shorter chord aerofoils shown in Fig 8a. At first sight this is an anomalous result, because for the longer chord model the sidewall static pressure fluctuation measurements (at the fixed point $x = 2.0H$, $y = -0.25H$) are relatively closer to the aerofoil ($y/c = -0.50$ for $c = 50$ mm compared to $y/c = -0.78$ for $c = 32$ mm). However, because of the form of the unsteady boundary layer/shock wave interaction (see the shadowgraph in Fig 14 of Ref 10), the sidewall pressure fluctuations probably do not decay uniformly with distance from the aerofoil. In the attached flow at $y/c = -0.50$ the terminal shock is oblique and weak, so that the flow downstream is still supersonic. Thus the pressure change across the shock would be comparatively small, giving relatively small pressure fluctuations in the unsteady flow. Further away from the aerofoil at $y/c = -0.78$ the shock wave becomes normal and the downstream flow is subsonic. Hence the pressure change across the shock is comparatively large, giving relatively large pressure fluctuations in the unsteady flow. Even further away from the aerofoil the shock wave disappears and the pressure is continuous, giving small pressure fluctuations in the unsteady flow.

In an attempt to get a better indication of the level of the excitation closer to the aerofoils, the pressure transducer in the sidewall adjacent to the centre of the aerofoils was moved from $x = 2.5H$, $y = -0.25H$ to $x = 2.64H$, $y = -0.05H$ (Fig 2). Thus for the aerofoils with $c = 50$ mm, this transducer was located at 78% of the local chord, and at $y/c = -0.10$. Comparing Fig 9a with Fig 8c, we see that the pressure fluctuations are significantly higher closer to the model, as we would expect, but they may be influenced by local flow separations in the aerofoil/sidewall junction.

We have seen that the sidewall pressure fluctuation measurements increase as the boundary layer thickness decreases (Fig 8). In McDevitt's experiments on the 18% thick aerofoil (Ref 10, Fig 13) the rms surface pressure fluctuations are at the remarkably high level of $\bar{p}/q = 40\%$ and increase monotonically as the Reynolds number increases from $R = 1 \times 10^6$ to $R = 7 \times 10^6$ (Fig 9b). McDevitt is confident that tunnel resonance did not occur (see discussion of Fig 11 in Ref 3). Similarly, no strong resonances were excited in the low Reynolds number (0.7×10^6) tests in the closed working sections briefly described in section 3.3 above.

In order to bridge the gap between the present sidewall pressure fluctuation measurements at low Reynolds number and the surface pressure fluctuation measurements of Ref 10, two special tests were made. The results of these special tests are included in Fig 9b. For the first test a pressure transducer was mounted on the top surface of the 18% thick aerofoil with $c = 50$ mm, giving pressure fluctuations at 78% chord ($y = 0$) in the central plane. The back of the transducer projected from the bottom surface of the aerofoil, but was covered by a small fairing. The surface pressure fluctuations with both free and fixed transition were about $\bar{p}/q \approx 10\%$ and approximately twice the corresponding sidewall measurements. For the second test an 18% thick biconvex wing with a chord of 200 mm and an aspect ratio of 2 was briefly tested in the top and bottom slotted ($H = 640$ mm) working section of the RAE 3 ft tunnel. With free transition the pressure fluctuations at mid-semispan (where an oil flow photograph indicated that the local flow was almost two-dimensional) increased steadily from $\bar{p}/q \approx 16\%$ at $R \approx 0.4 \times 10^6$ to $\bar{p}/q \approx 25\%$ at $R = 0.7 \times 10^6$. With fixed transition the levels were appreciably lower (from 3% to 6%), omitted from Fig 9b for clarity. Tests at higher Reynolds numbers were not possible because of the large amplitude motion of the model on the sting.

Surface pressure fluctuation levels of $\bar{p}/q$ above 10% would generally be accompanied by severe buffeting on aircraft components, even with the usual broadband spectrum.

In addition it is easy to show that this type of instability, with anti-phase shock oscillations on the upper and lower surfaces, can produce significant oscillatory pitching moments. Let us assume that the rms level of the pressure fluctuations between $x/c = 0.80$ and 1.00 is about 20%q (a conservative assumption in view of Fig 9b), and that these fluctuations are perfectly correlated spanwise and chordwise. Then the rms lift over this area/unit span is $(0.40q \times 0.2c)$ and acts at $x/c = 0.90$. Hence the rms moment about $x/c = 0.25$ is $(0.40q \times 0.20)(0.65c)$ so that the rms moment coefficient is about

$$\bar{C}_M = 0.05$$

and the amplitude about $C_M = 0.1$ (because of the nearly triangular wave form). This torsion moment is concentrated at a discrete frequency in the flutter range. It could be potentially serious if it coincided with a structural mode such as the first wing torsion mode, which is normally in the range from $\omega c/U$ from 0.5 to 1.0.

4 ORIGIN OF THE INSTABILITY

We have established that over a narrow range of transonic Mach numbers there is an unusual form of periodic flow on thick biconvex aerofoils, but we have not identified what criteria control the oscillation.

Finke[11] gives a comprehensive review of possible theoretical models which might explain oscillations of this type. Finke's suggested analogy between wake oscillation and Eckhaus' theory[13] of transonic rudder flutter is interesting, but invokes an inviscid flow model. The theory predicts a wide range of frequencies and Mach numbers over which flow instability is possible (Ref 11, Fig 51), but manifestly this prediction is incompatible both with the experiments cited there and with the narrow range of frequencies and Mach numbers observed in the present tests. Finke showed that with laminar boundary layer/shock wave interactions the theories of Karishima[9] and Dvorak[14] correctly predict the frequency, but that the theories are restricted to small-amplitude shock oscillations and are inapplicable to turbulent boundary layers.

Recently McDevitt[10] has clearly established that on a biconvex aerofoil with $t/c = 18\%$ and a turbulent boundary layer/shock wave interaction, the shock does not generally oscillate about a mean position. Instead, for most of the region of unsteady flow, successive shock waves move upstream from the trailing edge, alternating between the top and bottom surfaces. McDevitt suggests that this is a special form of oscillatory flow, classified as a type C motion by Tijdeman[15]. Within a narrow range of Mach number a shock wave motion of this type has been predicted from a numerical solution of the full Navier-Stokes equations[4,5]. However the computations took 7.5 hours on a CDC 7600 computer and even with more powerful computers it is unlikely that this method could be applied for routine calculations on more realistic aerofoil sections.

An alternative approach is to ask whether the present measurements suggest well-defined conditions for the onset and termination of the instability, which might be applicable to other aerofoils, and also provide a clue as to the physical cause of the oscillation. This question is prompted by the observation that the narrow region of flow instability shown in Fig 6 is displaced roughly 0.1 in Mach number above the curve for critical Mach number as a function of thickness/chord ratio, derived from the transonic similarity solutions given by Spreiter[16] and confirmed by recent measurements (e.g. Fig 13 of Ref 17).

As a first attempt to explain the phenomenon, the flow instability boundaries given in Fig 6 are replotted in Fig 10 in terms of the transonic similarity parameter:

$$K = (M^2 - 1)/[M^{4/3}(\gamma + 1)^{2/3}(t/c)^{2/3}] \quad . \qquad (1)$$

The critical Mach number now occurs along the straight line $K = -1.42$, corresponding with the curve of M_{crit} in Fig 6. Fig 10 shows that the values of K for the onset and termination of the instability vary appreciably with thickness/chord ratio. The instability is unlikely to be inherent in the transonic inviscid flow, for such an instability would always start and stop at particular values of the transonic similarity parameter. Hence the instability probably results from a critical phenomenon in the viscous transonic flow. This conclusion is supported by numerical solutions of the full Navier-Stokes equations already available for $t/c = 12\%$ (Ref 17) and for $t/c = 18\%$ (Refs 4 and 5). The steady solutions (marked by triangles in Fig 10 and joined by dotted lines) roughly enclose the unstable flow region found with fixed transition, and thus indicate that there are unlikely to be fixed values of K controlling the instability. In addition, the oscillatory solution found for $t/c = 18\%$ disappeared when the viscosity was eliminated.

A simple explanation of the phenomenon might be that the boundaries of Fig 6 correspond to local Mach numbers for the start and stop of the instability, which might be almost independent of the thickness/chord ratio. These constant Mach numbers would be determined by some as yet unidentified feature of the boundary layer/shock wave interaction. Now the local Mach numbers upstream of the shock wave could not be easily measured on these small models, but approximate Mach numbers upstream of the shock can be obtained from the measured shock position and Ref 16, as we shall indicate. This approach is reasonable, because the shock position must be a crucial factor in determining the instability, and we have already suggested in section 3.3 that the shock position controls the oscillation frequency.

Fig 11a shows the steady shock position previously measured[9,18,19] in different wind tunnels on a number of thin biconvex aerofoils with attached flow, plotted against the transonic similarity parameter. Even for these thin aerofoils the shock position is upstream of that according to Spreiter's theory for a given value of K. This discrepancy must be attributed to the fact that Spreiter had to use the inviscid shock jump relationship, whereas in the real viscous flow the local thickening of the boundary layer at the foot of the shock produces an appreciably smaller increase in pressure. Oil flow studies on the present, generally thicker, models show in Fig 11b that both close to the onset and completion of the instability the shock positions straddle the mean line for the thin aerofoils taken from Fig 11a.

The method devised to predict the approximate local Mach number immediately upstream of the shock utilizes the mean line of Fig 11. For a particular aerofoil at transonic speeds the pair of free stream Mach numbers for the onset and completion of the instability define a pair of values of K, and hence particular values of x_s/c from the mean line. For the same shock positions, Spreiter's theory determines a pair of equivalent values, K_e, and hence equivalent free stream Mach numbers, M_e. From these values of K_e, M_e and the results of Spreiter's theory in Table 1c of Ref 16, approximate local Mach numbers upstream of the shock may be calculated for a particular thickness/chord ratio.

Concerning first the predictions for a turbulent boundary layer/shock wave interaction, Fig 12 shows that the local Mach number for the onset of the instability varies from 1.24 for t/c = 12% to 1.15 for t/c = 20%. In contrast, the constant local Mach number for the suppression of the separation is 1.24. Karashima's measurements for t/c = 10% with a laminar boundary layer clearly show an instability for the Mach number range from $M_1 = 1.20$ to 1.24, in fair agreement with the present predictions.

These approximate predictions are well supported by McDevitt's[10] recent measurements of the flow instability on an 18% thick biconvex aerofoil at $R = 11 \times 10^6$. Thus Fig 13 (after Ref 10, Fig 25) shows the regions of type C flow instability[15], and the corresponding frequency parameter, as a function of free stream Mach number and angle of incidence. (In a type C flow instability a shock wave moves upstream along the aerofoil. The shock wave then leaves the aerofoil at the leading edge and propagates upstream against the incoming flow.) Fig 13 also includes values of local Mach number, M_1, upstream of the shock derived from Ref 11, Figs 27 and 28. When the free stream Mach number increases above the critical value (M = 0.71), M_1 increases until at about M = 0.75, with $M_1 = 1.20$, separation starts, together with the oscillatory flow. The mean shock position then moves forward until at a free stream Mach number of 0.76, M_1 falls to about 1.14 on the top surface (Fig 13a) and 1.10 on the lower surface (Fig 13b). With further increase in free stream Mach number, the mean shock moves downstream again, until when M = 0.78 steady flow is re-established with M_1 a little greater than 1.22 on the upper surface. A 'steady' separated flow then extends from the shock to the trailing edge. This region of steady separated flow is preceded by a small region of type A flow instability[15]. (In a type A flow instability a shock wave performs small oscillations about a mean position on an aerofoil.) Thus in this high Reynolds number experiments, with a natural turbulent boundary layer, the aerofoil provides the condition

$$1.13 < M_1 < 1.24 \quad ,$$

over the observed regime of instability. This condition is consistent with that inferred in Fig 12 from the present tests at low Reynolds numbers. The onset of the unsteady flow corresponds to the sudden forward movement of the mean shock position, which would traditionally be associated with severe flow separations. (See the discussion by Pearcey of Figs 32 and 38 in Ref 20.) Tentatively we may conclude that with a turbulent boundary layer a necessary (but certainly not a sufficient) condition for the instability to develop on biconvex aerofoils is that the local Mach number just upstream of the shock lies within the range from about

$$1.14 < M_1 < 1.24 \quad . \qquad (2)$$

This unstable range corresponds roughly with the range for the onset of significant separation on a wide range of aerofoils (Ref 20, section 3.2.1). However Figs 26 and 29 of Ref 10 give values of M_1 of 1.23 and 1.34 respectively, just below and just above the unsteady flow region. Hence the values of M_1 for the very unsteady flows represented in Figs 27 and 28 of Ref 10 (and used in Fig 13) could be a little misleading. Recent unpublished measurements[21] on a large 14% biconvex wing provide the condition:

$$1.23 < M_1 < 1.34 \quad .$$

The frequency of the shock oscillation is probably related to the time taken for disturbances to travel upstream over a length, [illegible], from the trailing edge to the mean shock position which will generally be in a region of fully separated flow. Fig 14a shows that the frequency measurements for the different t/c ratios with fixed transition are roughly correlated by this length and the free stream velocity, in terms of the transonic similarity parameter, K. The present measurements are in fair agreement with previous measurements covering t/c ratios from 10 to 20%, and [illegible] is inferred from those tests.

Many years ago Erickson and Stephenson[illegible] suggested a simple empirical formula for the aerodynamic frequency parameter, inversely proportional to the time taken for disturbances to travel from the trailing edge to the shock position:

$$\omega\ell/U = A = \pi(1 - M)/2M \quad . \tag{3}$$

Fig 14b shows that the measured frequency parameters are only about 70% of those predicted according to equation (3). However, despite the scatter, referencing these measurements to the predictions of equation (3) does reduce the wide variation which occurs with the transonic similarity parameter in Fig 13a. Hence the mechanism of the shock oscillation must be related with the wake oscillation, which starts at the trailing edge.

This hypothesis was confirmed by a special test made with the 14% thick aerofoil (with c = 50 mm) modified to incorporate a small trailing-edge flap, which could be freely hinged at 75% chord (Fig 15). A pair of heavy and light flaps of the same external geometry were provided to briefly investigate possible effects of the inertia of the flap. With the flap locked the instability was much the same as that measured previously, despite the rather severe three-dimensional disturbances provided by the flap 'stops'. With the flap unlocked there was a small mean flap deflection (determined by the aerodynamic hinge moment and the static moment of the flap) and small flap oscillations were allowed. These oscillations were not measured, but they must have significantly altered the boundary condition on the wake at the trailing edge, because the excitation in the Mach number range from M = 0.82 to 0.84 was severely reduced, with either flap. At somewhat higher Mach numbers, transonic 'buzz' was observed, with either flap oscillating, as indicated in the following table:

Flap	Range of instability (M)	Amplitude of buzz (°)
Heavy	0.88 to 0.90	at least ±10 (to stops)
Light	0.89 to 0.90	roughly ±5

The larger amplitude motion of the heavy flap during buzz may be readily explained. According to Lambourne[23] the buzz frequency at constant Mach number is given by:

$$\omega = \sqrt{(C_A + C_H)/I} \quad , \tag{4}$$

where C_A = aerodynamic hinge stiffness (identical for both flaps),
C_H = elastic hinge stiffness (in this test ≡ 0),
and I = moment of inertia of flap.

Hence the buzz frequency must be lower for the heavy flap. Now, in general, changes which lower the buzz frequency would be expected to increase the buzz amplitude, as in the present tests. This has been confirmed by experiments of Saito[24].

In contrast to the strong influence of the trailing-edge boundary condition on the aerodynamic instability, the leading-edge geometry has a comparatively weak influence. This was demonstrated with a 10 mm long × 100 mm wide piece of 30 grade carborundum paper was wrapped round the leading edge of the 18% thick aerofoil with c = 50 mm. The Mach number range for the instability and the frequency were essentially the same as with transition fixed with ballotini. However, the amplitude of the pressure fluctuations was reduced, consistent with an excessively thick turbulent boundary layer. Finke has also demonstrated[11] that the shock oscillation is relatively insensitive to changes in the leading edge geometry.

Finally it should be emphasised again that the instability boundaries (Fig 6) are not significantly influenced by tunnel interference, despite the high blockage ratio of the models (9% maximum for t/c = 18%, c = 50 mm). However, the frequency parameter measurements (Fig 7) may be subject to some interference, as discussed in section 3.3. Tunnel resonance frequencies were measured with the aerodynamic excitation provided by biconvex aerofoils over the Mach number range from M = 0.78 to 0.90 (Fig 16). These measurements at the first resonance mode are in good agreement with theoretical predictions and previous tests made with acoustic excitation. In particular, for this range of Mach number the resonance frequencies measured were unaffected by an increase in the depth of the plenum chamber from d = 0.67 to d = 4.00, as required by the theory for Mach numbers greater than about 0.6.

5 POSSIBLE INSTABILITIES ON SUPERCRITICAL AEROFOILS

Additional tests are needed to establish if instabilities in the structural frequency range occur on supercritical aerofoils within the flight envelopes of interest.

The narrow range of Mach number given by equation (2) is also associated with excitation on the 11% thick supercritical aerofoil tested by Ross[2] at $C_L = 0.55$, $R = 2 \times 10^6$, over a wide range of free stream Mach number. Hence the local Mach number criterion given by equation (2) may be also valid on supercritical aerofoils, although this single result is certainly not conclusive. For this aerofoil the mean pressure distributions and schlieren photographs suggest that any separations must be small. This is consistent with the low amplitude of the excitation and the monotonic downstream shift of the terminal shock wave as Mach number increases. The frequency parameter, $\omega\ell/U$, varies from about 0.32 at M = 0.75 to 0.10 at M = 0.87. This is only about 50% of that predicted according to equation (3). However, the pressure distribution on this aerofoil is completely different from that on the conventional aerofoils used to derive equation (3), or on the biconvex aerofoils.

6 CONCLUSIONS

Tests on a series of small biconvex aerofoil models suggest six main conclusions:

(1) A flow instability can develop at zero incidence at transonic speeds for thickness/chord ratios varying from 12 to 20% with both laminar and turbulent boundary layers. For a given aerofoil, the region of flow instability is restricted to a narrow range of Mach number (Fig 6) and is influenced by the state of the boundary layer.

(2) The origin of the flow instability is not yet fully explained. However, it is essentially a viscous phenomenon (Fig 10). A necessary (but not sufficient) condition for the onset of the instability is a local Mach number, M_1, just upstream of the terminal shock in the range from about:

$$1.14 < M_1 < 1.24 .$$

(3) The frequency parameter of the instability is displayed in Fig 7 and is probably determined primarily by the time taken for wake disturbances to pass upstream from the trailing edge to the shock (Fig 13).

(4) The unusual and sharply-defined (Figs 6 and 7) nature of this instability makes it a useful test for the methods of predicting unsteady viscous transonic flows now being developed, with particular reference to the Navier-Stokes equations.

(5) For instabilities at frequencies close to tunnel resonance the tunnel walls significantly alter the instabilities. This dynamic interference may be reduced by replacing the hard walls of the conventional working section with sound-absorbing walls (Figs 3 and 5).

(6) Tunnel resonance frequencies measured with the aerodynamic excitation provided by the flow instability are in good agreement with previous tests made with acoustic excitation, and also with theoretical predictions (Fig 16).

REFERENCES

No.	Author	Title, etc
1	N.C. Lambourne	A brief survey of the information on periodic fluctuations in the flow over wings at high subsonic Mach number. ARC 17304, January 1955
2	F.W. Roos D.W. Riddle	Measurements of surface-pressure and wake flow fluctuations in the flow field of a Whitcomb supercritical aerofoil. NASA TN-D 8443, August 1977
3	J.B. McDevitt L.L. Levy G.S. Deiwert	Transonic flow about a thick circular arc airfoil. AIAA Journal, Vol 14, No.5, pp 606-613, May 1976; or AIAA Paper 75-878, June 1975
4	L.L. Levy	An experimental and computational investigation of the steady and unsteady transonic flow fields about an aerofoil in a solid-wall test channel. AIAA Paper 77-678, June 1977
5	H.L. Seegmiller J.G. Marvin L.L. Levy	Steady and unsteady transonic flow. AIAA Paper 78-160, January 1978
6	D.G. Mabey	The use of sound-absorbing walls to reduce dynamic interference in wind tunnels. RAE Technical Report 76157 (1976); ARC R & M No.3831 (1976)
7	D.G. Mabey	The resonance frequencies of ventilated wind tunnels. RAE Technical Report 78038 (1978); ARC R & M No.3841 (1978)
8	D.G. Mabey	The reduction of dynamic interference by sound-absorbing walls in the RAE 3 ft wind tunnel. RAE Technical Report 77120; ARC R & M No.3837 (1977)
9	K. Karashima	Instability of shock waves on a thin aerofoil in high subsonic flow. Report No.363 (Vol 27, No.3) of Aeronautical Research Institute of Tokyo, March 1961
10	J.B. McDevitt	Supercritical flow about a thick circular arc airfoil. NASA TM 78549, January 1979
11	K. Finke	Shock oscillations in transonic flows. VDI Forschungsheft 580 (1977)
12	D.G. Mabey B.L. Welsh D.M. McOwat	Aerodynamic characteristics of moving trailing-edge controls at subsonic and transonic speeds. AGARD CP 262, Paper 20, May 1979

REFERENCES (concluded)

No.	Author	Title, etc
13	W. Eckhaus	On the theory of transonic aileron buzz. MIT-Fluid Dynamics Research Lab Report No.60-6, December 1960
14	R. Dvorak	On the unsteady boundary layer-shock wave interaction in the lower transonic region. Fluid Dynamics Transactions, Vol 2 (1965)
15	H. Tijdeman	Investigations of the transonic flow around oscillating aerofoils. NLR 77090U, October 1977
16	J.R. Spreiter A.Y. Alksne B.J. Hyett	Theoretical pressure distributions for several related nonlifting aerofoils at high subsonic speeds. NACA TN 4148, January 1958
17	S. Davis B. Satyanarayana	Two-dimensional transonic testing with splitter plates. NASA TP 1153, February 1978
18	E.D. Knechtel	Experimental investigation at transonic speeds of pressure distribution over wedge and circular arc aerofoil sections and evaluation of perforated wall interference. NASA TN D-15, August 1959
19	G.P. Wood P.B. Gooderum	Investigation with an interferometer of flow round a circular arc aerofoil at Mach numbers between 0.6 and 0.9. NACA TN 2801, October 1952
20	H.H. Pearcey	Shock induced separation and its prevention by design and boundary layer control. Boundary Layer and Flow Control, Vol 2, pp 1166-1344, Pergamon Press (1961)
21	D.G. Mabey	Oscillatory flows on a 14% thick biconvex wing at transonic speeds. RAE Technical Report in preparation
22	A.L. Erickson J.D. Stephenson	A suggested method of analysing for transonic flutter of control surfaces based on available experimental evidence. NACA TIB 1505 (1947)
23	N.C. Lambourne	Control surface buzz. ARC 23786, May 1962
24	H. Saito	On the aileron buzz in the transonic flow. Aeronautical Research Institute, University of Tokyo, Report 346 (1959)

Copyright ©, Controller HMSO, London 1980

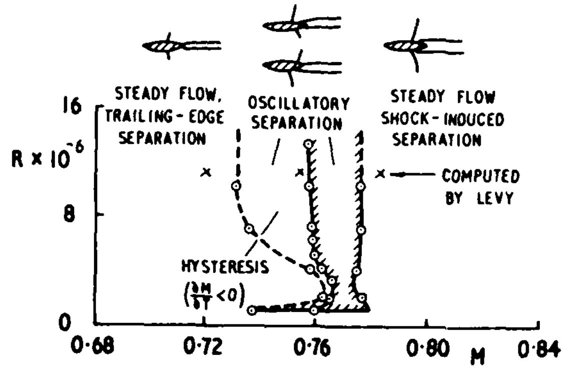

Fig 1 Flow domains for an 18% thick biconvex aerofoil (after Ref 3)

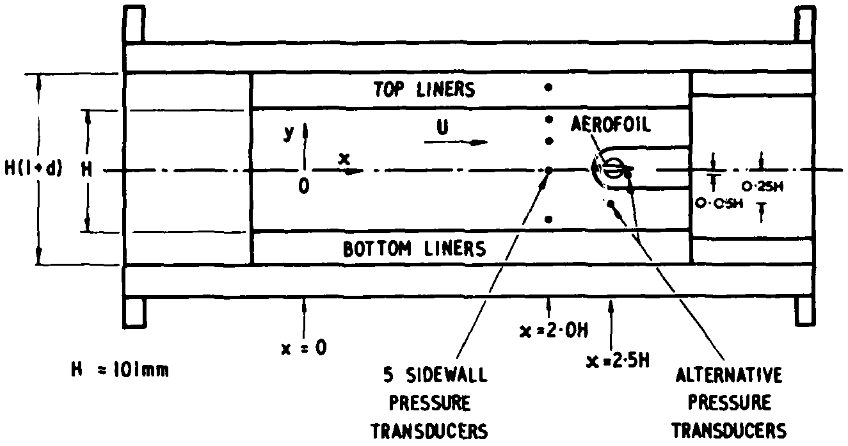
TOP LINERS
AEROFOIL
y
U
x
0
H(l+d)
H
0·25H
0·05H
BOTTOM LINERS
x = 0
x = 2·0H
x = 2·5H
H = 101mm
5 SIDEWALL PRESSURE TRANSDUCERS
ALTERNATIVE PRESSURE TRANSDUCERS

Fig 2 GA of aerofoils

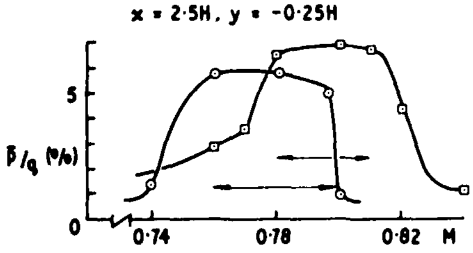

(a) RANGE OF FLOW INSTABILITY

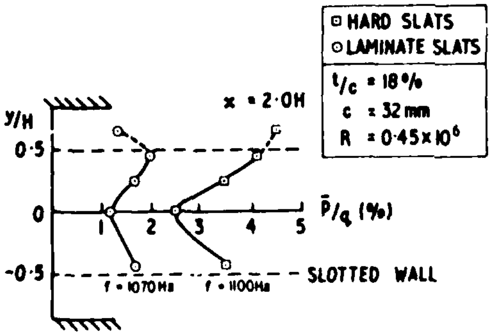

(b) STRONG RESONANCE M = 0·78

Fig 3 Typical results - transition free

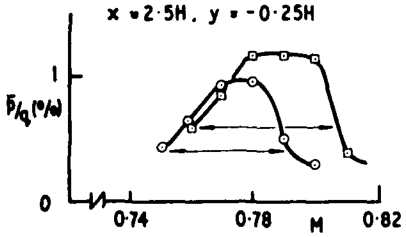

(a) RANGE OF INSTABILITY

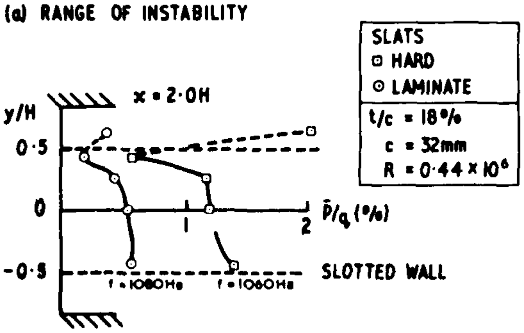

(b) UPSTREAM PRESSURE FLUCTUATIONS M = 0·78

Fig 4 Typical results - transition fixed

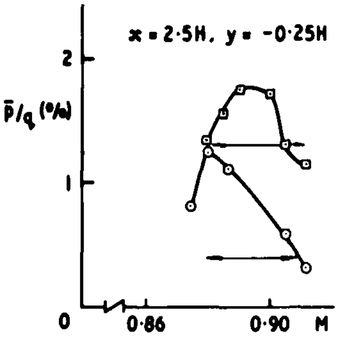

(a) RANGE OF INSTABILITY

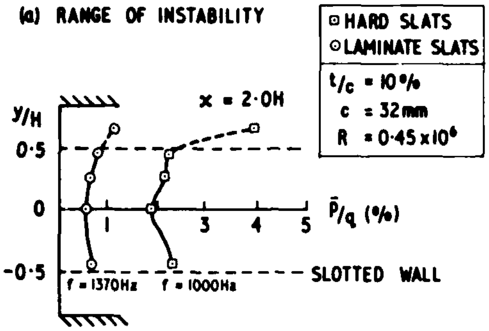

(b) RESONANCE MODE WITH HARD SLATS
M = 0·90

Fig 5 Forced oscillation with hard slats - transition free

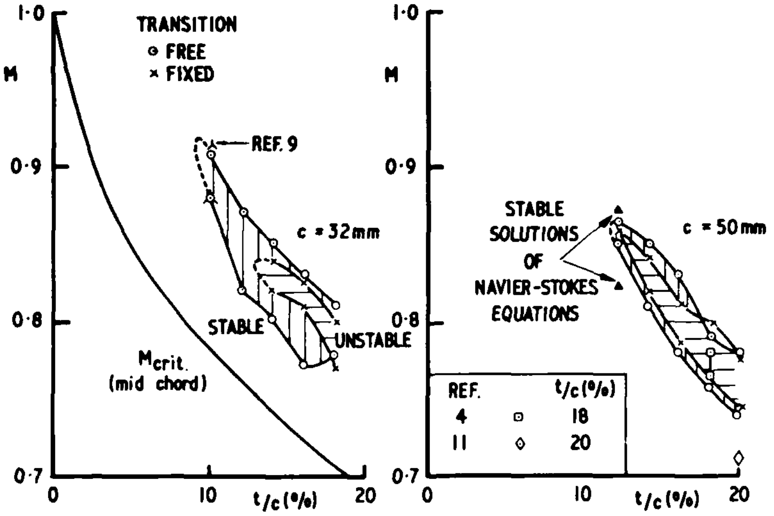

Fig 6 Instability boundaries for biconvex aerofoils (α = 0^0)

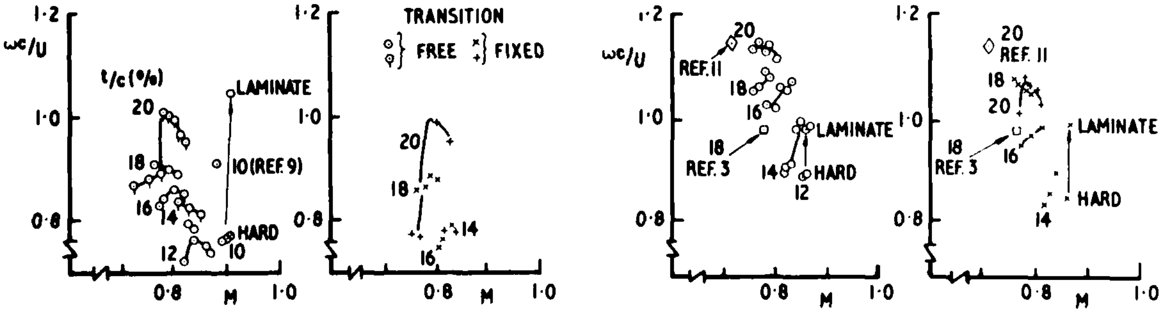

(a) c = 32mm

(b) c = 50mm

Fig 7 Frequency parameter for biconvex aerofoils (α = 0^0)

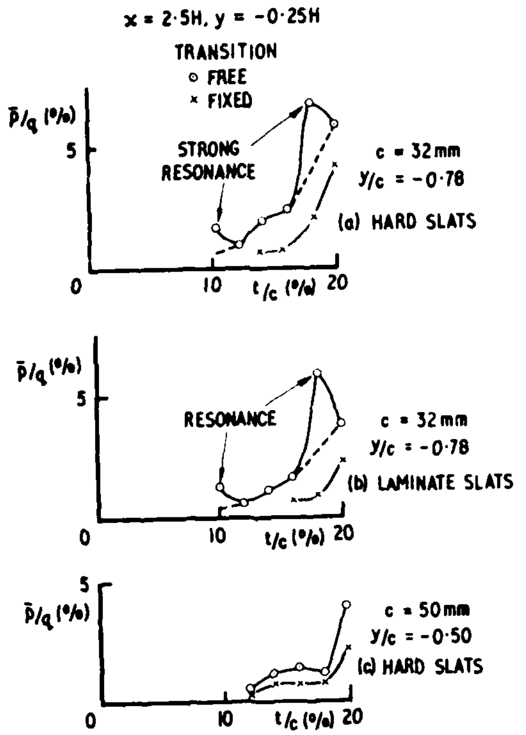

Fig 8 Maximum pressure fluctuations on sidewall

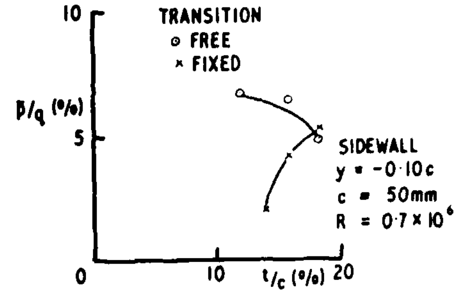

(a) VARIATION WITH THICKNESS/CHORD RATIO

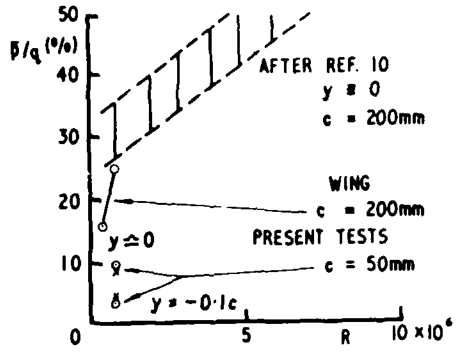

(b) VARIATION WITH REYNOLDS NUMBER $t/c = 18\%$, $M = 0.77$

Fig 9 Maximum pressure fluctuations ($x/c = 0.78$)

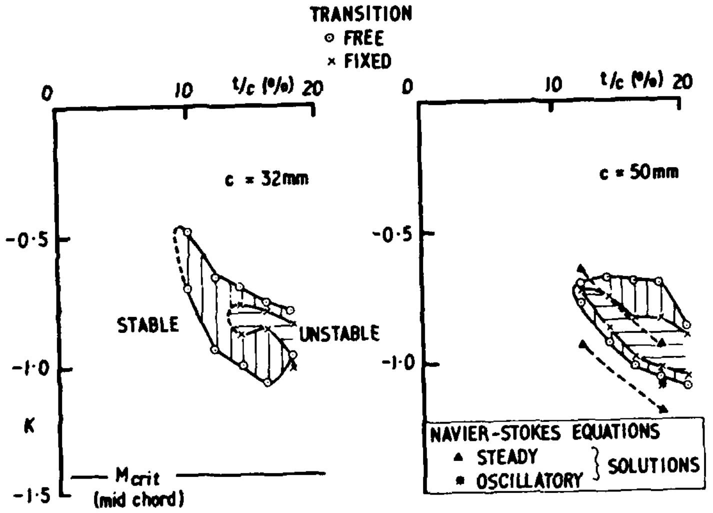

Fig 10 Instability boundaries for biconvex aerofoils - K against t/c

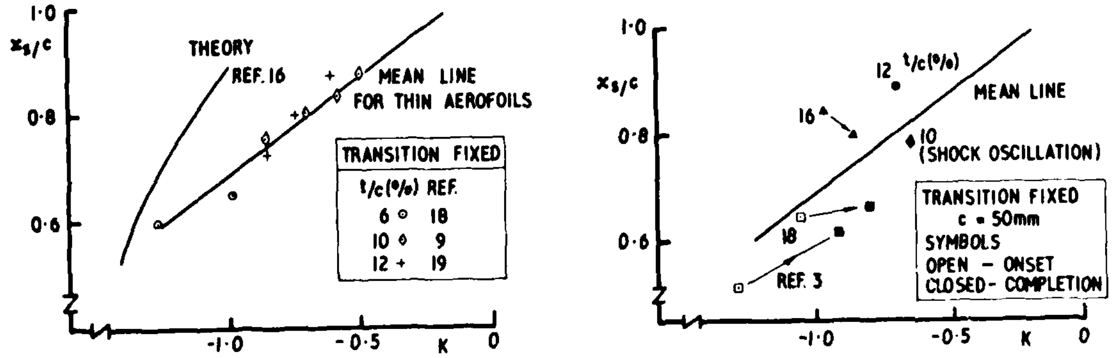

(a) FROM PRESSURE MEASUREMENTS (b) FROM OIL FLOW

Fig 11 Shock position vs transonic similarity parameter

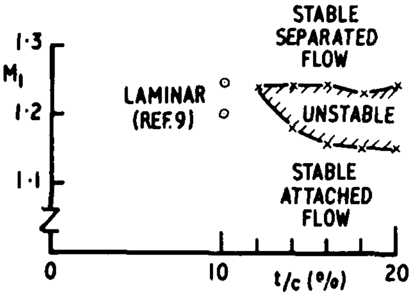

Fig 12 Mach numbers upstream of shock for instability (C = 50 mm)

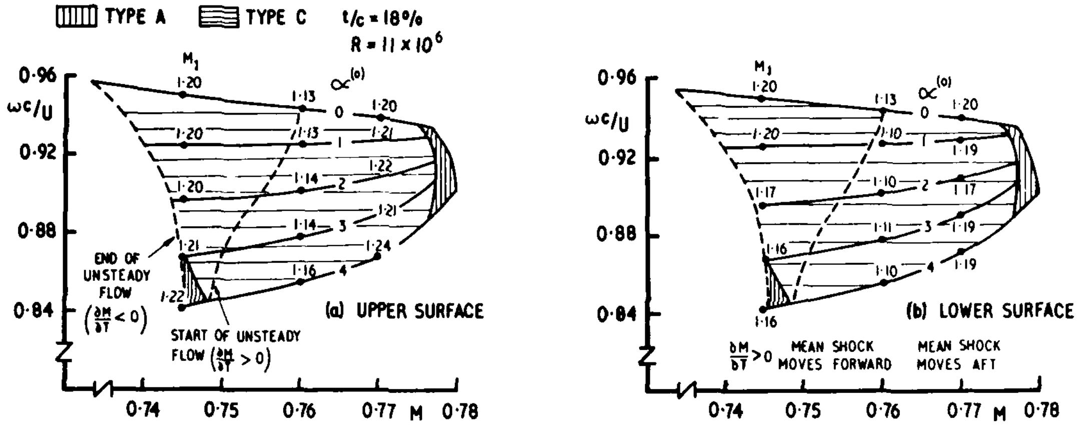

Fig 13 Boundaries for instability (after Ref 10, Fig 25)

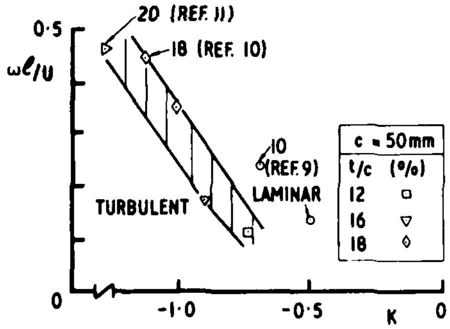

(a) EXPERIMENT

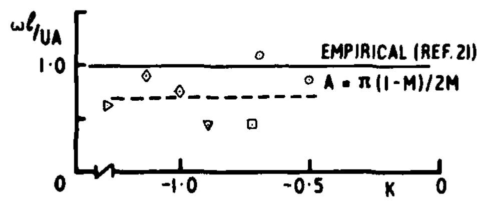

(b) CORRELATION

Fig 14 Frequency parameters based on distance from shock to trailing edge

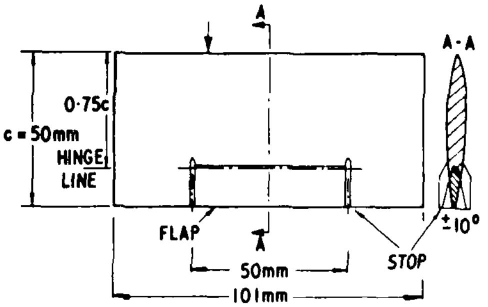
A
A-A
0·75c
c = 50mm
HINGE LINE
FLAP
STOP
±10°
50mm
101mm

Fig 15 Aerofoil with trailing-edge flap

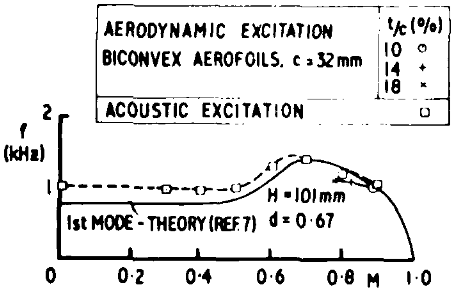

Fig 16 Resonance frequencies v Mach number for slotted walls

Experiments on a Turbulent Unsteady Boundary Layer with Separation.

Sergio De Ponte, Arturo Baron

Politecnico di Milano   Istituto di Ingegneria Aerospaziale
Via Golgi 40
20133 Milano, Italy

Abstract

Turbulent separation is an unsteady phenomenon in itself, even in steady external conditions. In this experiment a cyclic variation is produced in the "outstream" of a typical boundary layer wind tunnel with variable pressure gradient. Due to this cyclic variation, the point of separation in quasi-steady conditions is shifted in the streamwise direction approximately one third of the boundary layer length.

A hot-wire analysis of the velocity profiles, made by a sampling technique, shows no significant change in profile behaviour, except a lag in separation and reattachement. This result seems to be important in explaining some features of dynamic stall.

The experimental conditions (reduced frequency and Reynolds Number) are close, in order of magnitude, both to blade stall and stall flutter, as the frequency is about 4 Hz, the streamwise length is 1.5 m and the outstream velocity at the beginning of the deceleration is about 40 ms^{-1}.

The observed time lag in separation and reattachement is about 1/10 of the cycle, which agreeds with some oscillating airfoil tests.

Symbols

Cp	pressure coefficient
F	phase angle (degrees)
X	streamwise coordinate (mm)
Y	normal to wall coordinate (mm)
V	velocity (m/s)

1) Introduction

Cyclic separation of a laminar or turbulent boundary layer is governing many unsteady aerodynamic phenomena, such as stall flutter, rotating stall of compressors, rotor blade stall. This kind of phenomena may occurr at very low frequencies, where neither potential flow unsteadyness nor usual boundary layer unsteadyness are expected. It means that out-of phase forces and moments are possible and may excite vibrations.

The experiment here described, which is not yet completed, is an attempt to investigate on a separating boundary layer, perturbed in a cyclic way and in which the attached part shows no significant unsteady effect, while the separating part has a large time lag with respect to the corresponding steady condition.

The experiment started with some preliminary tests in order to define the frequency range in which a consistent time lag could be observed. It proceeded with an attempt to define what had to be measured to obtain significant data. This stage of the research is the scope of the present paper.

Of course, the usual unsteadyness of turbulent separation was found upon the cyclic separation which was introduced in the flow. In the present experimental conditions, this perturbation was not too large but caused the data scatter appearing in the results. It should be noticed that this scatter will be present in real life and is not only due to the inaccuracy of the experiment.

2) Experimental Facility

The experimental facility is a variable pressure gradient boundary layer wind tunnel. Its test section is shown in fig. 1

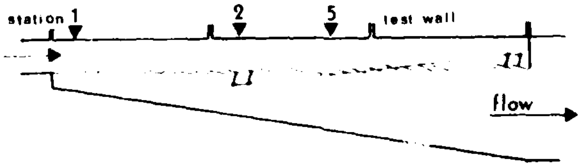

Fig. 1 Sketch of the test section of the wind tunnel.

The inlet cross-section is .1 x .3 m and the useful length is 1.5 m. The upper side of the tunnel is the test wall, while the lower side is a porous wall made by 29 adjustable vanes. Below this wall there is the suction duct, leading to a centrifugal blower (36 Hp). Four boundary layer suction slots are provided on each of the side walls, in order to obtain accurate two-dimensional conditions. In the present experiment side wall boundary layer control was not yet used.

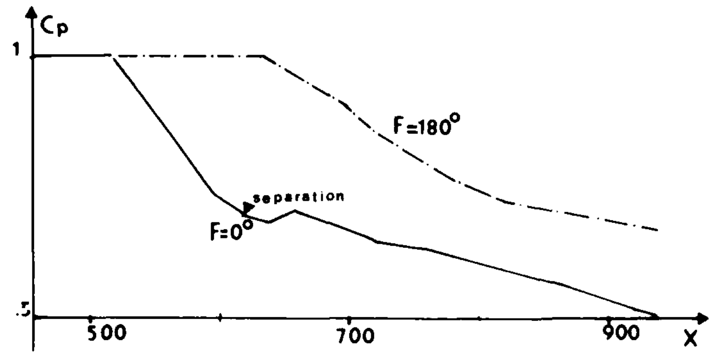

Fig. 2 Range of tested pressure coefficients.

Four of the adjustable vanes (number 12;13;28 and 29)are connected by a rod system to a mechanism driven by an electric motor, to produce a cyclic pressure gradient variation. The range of pressures obtainable in the present experiment is shown in fig. 2. The pressure is constant up to a certain point,where a weak or strong deceleration begins, causing eventually separation.The four vanes are moved in pairs in opposite directions and their lever arms are adjusted to obtain rather steady inlet flow conditions(1).

For simplicity of use, the test wall is divided into three sections (.5 x .3 m.)and ten of these sections are available, each one equipped with different instrumentation.In the present experiment three types of sections were used,one with streamwise pressure taps,one with pressure taps normal to the flow direction (for two-dimensionality checks) and one with a transversing mechanism for displacement of probes:65 mm was the maximum displacement.Tufts were provided on the whole test wall in preliminary tests, in order to observe separation.

Although the centrifugal blower is driven by a constant speed motor, the tunnel flow could be regulated bt choking the blower outlet.This regulation was not used in the present experiment as it was not necessary and to have a better repeatibility of tests.

3)Instrumentation

The instrumentation may be divided in two sections: the set for pressure measurement and the one for velocity profiles determination. Both are monitored by a data acquisition system.

The basic data acquisition system, originally intended only for strain-gauge measurements,is composed by a digital computer (HP 2114 B), its peripheral devices(Teletype,tape reader and puncher), a six digit voltmeter(integrating),a reed scanner and a reed relay card, the latter being the only available output device for data acquisition.The voltmeter can be used also as frequency meter on a time base of 1 second. The instrumentation is shown in fig. 3.

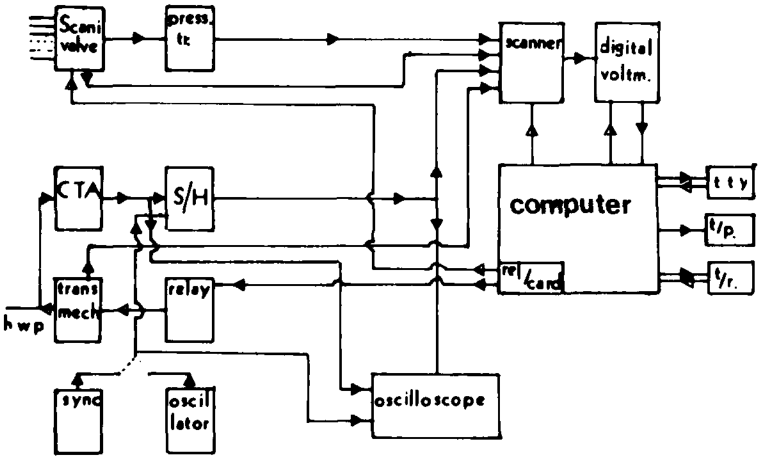

Fig. 3 Instrumentation

The basic instruments are a pressure transducer and a constant temperature hot-wire anemometer. For pressure measurement the interface is a Scanivalve with its control device. It allows also a check that the Scanivalve is in the right position at the end of a sequence,the computer enabling the data only if the check is positive.

The hot-wire anemometer signal has to be sampled at the proper phase and also in steady state measurement the same measuring chain is used, in order to have the same calibrations and response. The hot-wire signal is sent to a sample-and-hold amplifier and then to the scanner and digital voltmeter. The sampling pulse, properly timed and squared by a multivibrator, is supplied by a photoelectrical device placed near the puller of the vane control mechanism. the pulley is painted black and the proper phase is detected by the photoelectric **device** by means of a strip of reflecting tape,although it is now planned to use a counter and a fixed origin.For this pu**rpouse,** and to measure frequency, a second photoelectric device is placed in front of the teeth of the pulley. Due to the short time base of the frequency meter (1 second),the system resulted less accurate than the count of the pulley revolution by the aid of a stopwatch, [illegible] frequencies.

The transversing mechanism is [illegible], controlled by the relay card and equipped with [illegible].

A two-trace oscilloscope was connected in parallel to the [illegible], usually to read the original and sampled hot-wire signal and [illegible] the sampling pulse. **S**ometimes also original synchronization signal and its squared form were observe**d**. This allowed to monitor the whole test, in particular for the possible failure of the probe wire, and to check the flow. In this sense it was very useful in the determination of the end of the intermittent part of the flow, at the outer edge of the boundary layer.

4)Preliminary Tests

Preliminary tests were made in order to evaluate where unsteady effects were significant. For this purpouse, the hot-wire probe was placed close to the wall, while a second probe was placed in the same station , but in the outstream.As first, the signal was observed on an oscilloscope, in order to detect Lissajous figures.Turbulence was widely disturbing this detection and low-pass filtering caused some problem, due to the low frequencies. A good solution was to replace both oscilloscope and filters by an X-Y plotter. It was possible to observe in this way that the desired flow regime, in which only separation was strongly unsteady, could be in the range from 2 to 5 Hz for the tunnel Reynolds Numbers.In the present paper results at 3.66 Hz, corresponding to 220 rpm, are given.

In order to have a large enough cyclic shift for separation point,compared to the random fluctuation due to turbulence, the vanes placed between the two oscillating pairs were adjusted to obtain a rather strong pressure gradients, close to the maximum possible for an attached flow, observing tufts on the test wall and pressures on a multi-tube manometer. In unsteady conditions, of course, only tufts were observed. In this way it was possible to define a limited number of streamwise stations in which the overall behaviour of the flow could be observed, a larger number of stations being the scope of further developments of the research.

5)Experimental Procedure

For pressure measurements, only in steady conditions, a measuring wall, equipped with pressure taps each 20 mm was placed in any of the three possible positions and the pulley controlling the oscillating vanes was set by hand at the required angle. Pressures were red by the pressure transducer, via the Scanivalve. At each position the average value, the root mean square error on 20 samples were calculated, printed and punched. Any data reduction was (or will be) made by successive programs.

For velocity profile measurements, both the number of samples at each measuring point and the steps in the Y (normal to the wall) direction could be changed at any time during the tests, in order try the correct way of performing the experiments. At the first two measuring stations, for example, it was possible to extend measurements up to the end of intermittent turbulence for a good definition of the boundary layer edge. Furthermore steps were adjusted to the local boundary layer thickness and it was possible to have closer measurementsnear the wall. For each measuring point the Y coordinate, the average hot-wire signal and the root mean square error were printed and punched.Linearization of the signal was made by further programs. In this way the average process is made on the hot-wire signal and not on the true velocity value.This gives a small error close to the wall, where the response curve has its maximum curvature and the turbulence is large.

As the hot-wire signal is sampled at a given phase, in the unsteady case the average process gives the true ensemble average.

In the steady conditions the pulley is placed by hand in the right position and the syncronization system cannot give the sampling pulse, which is supplied by an external oscillator. In order to avoid to read twice the same sample,the computer enabled the voltmeter to measure at a frequency a bit lower than the sampling frequency.

6)Analysis Of Results

If we look at the shape of the velocity profiles upstream of the separation point, for example in station 2 (fig 4) we notice that there is no difference between steady and

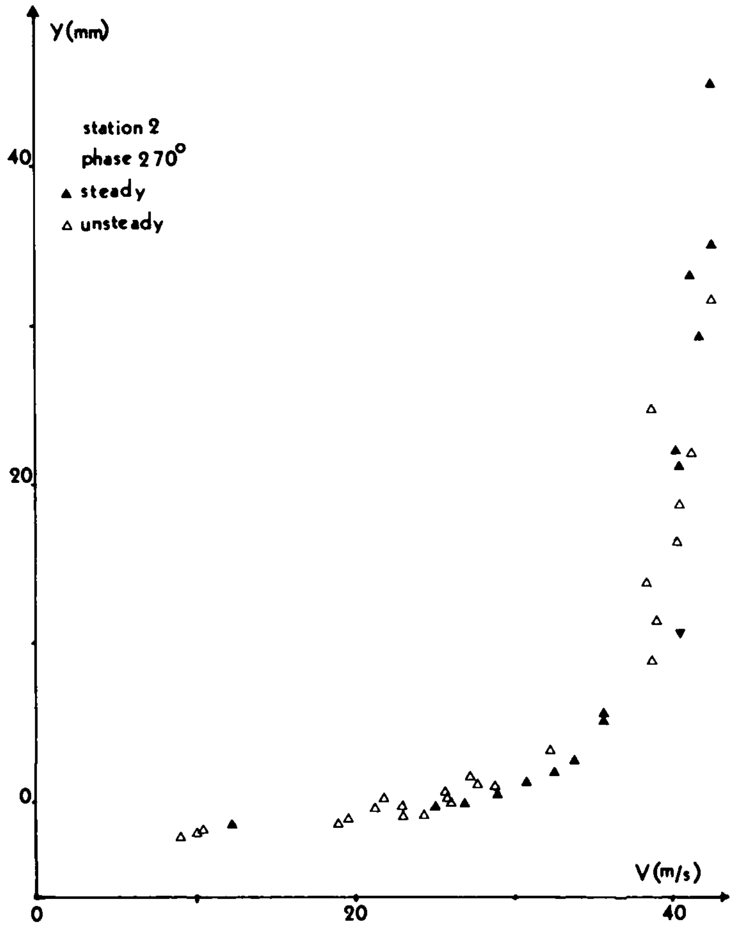

Fig. 5 Velocity profile upstream separation

unsteady velocity profiles,even in the conditions of maximum flow changes,as at the phase F=270°.Also the velocity at the outer edge of the boundary layer is the same. It means that the boundary layer itself and the external potential flow do not contain unsteady effects. Integral quantities will therefore coincide. Only the wall shear stress is not determined, as the boundary layer thickness is small and the dimensions of the wire, even when in contact to the wall,do not allow to go into the laminar sublayer. Approaching the wall, no significant reduction in turbulence was noticed on the oscilloscope.

When both flows, steady and unsteady, are attached, it is possible again to observe similar agreement between steady and unsteady velocity profiles, also in the region of cyclic separation, as in station 5, confirming that unsteadyness is not in the boundary layer behaviour (Fig. 5).

Before discussing separated flow results,we should observe thatwhen a turbulent fluctuation has a negative value, the average value of hot-wire signal is no more equal to the mean velocity,due to the non linear response of the instrument (even when the signal is linearized by analogical or numerical means). At the zero velocity value, for example, at the outer edge of the reversed flow, the average hot-wire signal is equal to the sum of its zero velocity value plus the root mean square error.This is a way to detect the upper edge of the reversed flow with hot-wires. In reversed flow the data presented are affected by this error and should be interpreted in this way.

The observation of the behaviour of the velocity profile at station 5 approaching separation, in the range between 270° and 330°, gives an example of what happens in the flow. At 270°(attached flow) and 330°(separated flow) both profiles are close together despite of the large data scatter. At 300°, on contrary,the flow is separated in steady conditions, while it is attached in the unsteady condition. The outer parts of the velocity profile, up to external flow, seem to coincide (Fig. 6)

The same happens in reattaching conditions, for example between 60° and 150°, at the same station (Fig 5). Reattachment retards with respect to the steady flow even in a larger way. Again, in attached (150°) and separated (60°) conditions, velocity profiles are close together.

7)Conclusions

Separation and reattachement show a time lag which is much more larger than the one appearing in attached boundary layers(2). The only way to explain this lag in separation and reattachement, when no other unsteady phenomena are present, is the time required to build up and destroy the reversed flow region. As in reversed flows velocities are small, compared to outstream velocities, time scales are larger.Furthermore, wakes will be more difficult to destroy than to build up, due to the different intensity of shearing stresses. This is also confirmed by the fact that the time lag seems to be larger in reattachement than in separation. In this sense, this lag is mainly matter of boundary layer-outstream

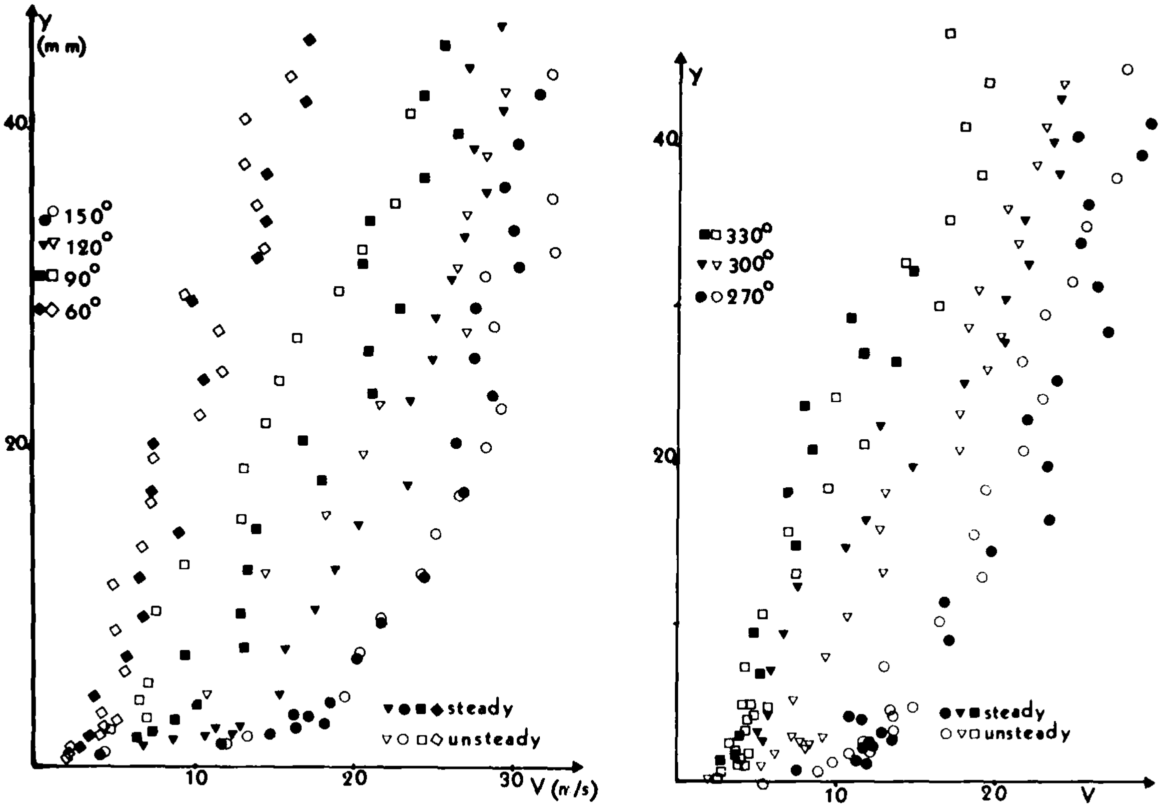

Fig. 5 Velocity profiles at station 5 (X = 810 mm)

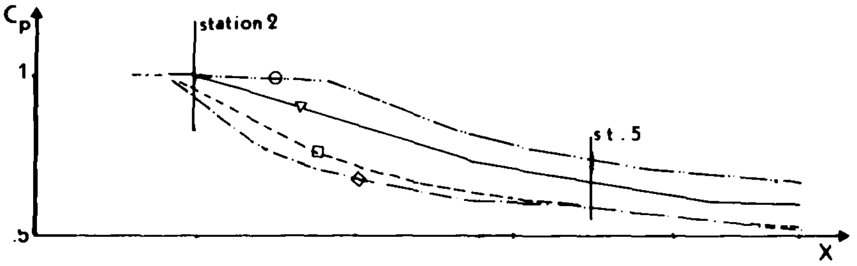

Fig. 6 Pressure gradients corresponding to fig.5

interaction. In order to predict this kind of phenomena, it seems therefore that,usual steady boundary layer calculation methods would be sufficient.It is therefore necessary to focus our attention in modelling separation and reversed flows.Incidentally, unsteadiness does not appear in subsonic potential flow equations, but in the boundary conditions, which represent the interaction mechanism in analytical form. At low frequencies, the approach to the dynamic stall problem would be simplyfied in this sense. [illegible] the trailing [illegible] allows the Kutta condition to be satisfied [illegible] separated on a wide part of the upper airfoil surface. [illegible] lift overshoot and large pitching moments ([illegible]).

[illegible] interesting feature is that, also when steady and unsteady velocity [illegible] not coincide, they have similar outer parts.It means that a very small variation [illegible] upstream is sufficient to produce separation.It is an aspect of the [illegible] of [illegible] which appears in separation flows. A better understanding of [illegible] this sensitivity is actually required, and will help not only [illegible] but also in planning new experiments.

The limitations of this experiment are not only due to the use of a single hot-wire [illegible], [illegible] a laser anemometer would give better information, [illegible] that [illegible] internal flows and not with airfoils. [illegible] In this experiment, for example, [illegible] gradient lengthwise [illegible], as shown in fig. [illegible]. [illegible]

References:

1) W. J. McCroskey - Personal communication

2) F. Brembati "An Investigation of an Unsteady Turbulent Boundary Layer" [illegible]-17

3) W. J. McCroskey "Introduction to Unsteady Aspects of Separation in Subsonic and Transonic Flow" AGARD LS 94

Aknowledgment:

The authors want to thank Mr McCroskey for important suggestions and DISA for having lent the second hot-wire anemometer for preliminary tests.

This work was partially supported by the Italian Research Council (CNR).

DISCUSSION SUMMARY

by
W.J.Mykytow, Consultant
Dayton, Ohio, US

The subject meeting consisted of three sessions and a round table discussion. Comments on each of the sessions were made by a session recorder and are repeated below. A resume' of the round table discussions then follows. The papers presented are listed in the meeting's proceedings report and in the following attachment.

1. SESSION I. PREDICTION METHODS AND COMPARISONS WITH EXPERIMENT, PART 1.

Recorder: Mr D G Mabey, U.K.

The paper presented by Prof Dowell gave a fine review of the problems of predicting attached, separated and transonic two-dimensional flows. One of his conclusions deserves to be quoted in full. "No transonic method can be expected to give useful information to the aeroelastician unless the mean steady flow it predicts and uses is accurate. Hence it is highly desirable to be able to input directly the best steady flow information which is available including that from experiment. The latter would include implicitly viscosity effects on the mean steady flow; in particular it would place the mean shock in the correct position."

The paper presented by Dr Yoshihara considered attached, transonic two-dimensional flows, using a viscous ramp method combined with a transonic small perturbation code.

The paper presented by M Javelle described a method of calculating three-dimensional time dependent turbulent boundary layers. The turbulence model used was similar to that in use at NASA Ames. The method looks promising, but needs to be combined with inviscid flow solutions for the prediction of loads.

Dr Geissler's paper covered a wide range of three-dimensional unsteady viscous flow problems, with considerable success. However, all the comparisons relate to subsonic flows.

(Additional comments were made by Mr Mabey in a letter to Dr J J Olsen as follows. "I think the most obvious common factor of the theoretical papers is that at transonic speeds the frequency parameter rapidly becomes comparatively unimportant (e.g. phase angle vs frequency parameter). Similarly the effect of non-linearities is confined to low frequency parameters.")

2. SESSION II. PREDICTION METHODS AND COMPARISONS WITH EXPERIMENTS, PART 2.

Recorder: Mr J Giesing, USA

The following comments are made on Houwink's paper on boundary layer effects on unsteady airloads.

Non Separated (Attached) Flow

A combination of experiments and theoretical calculations (NLR-LTRAN2+Boundary Layer Analysis) were done at NLR, on a NACA 64A006 airfoil with flap. The following points are made in the paper.

Viscous boundary layer effects produce a "de-cambering" of the airfoil with flap. The displacement thickness on the upper surface is greater than that on the lower surface resulting in a lower effective flap deflection. The viscous effects may be thought of as a sort of flap acting in opposition to the physical flap. Such a correction to the theoretical calculation greatly improves correlations with experimental data.

The viscous corrections diminish as frequency increases.

Wind tunnel wall corrections are important if accurate correlations of theory and experiment are to be obtained.

Using sophisticated thick body transonic theories can be less accurate than thin body theories if viscous effects are not accounted for. Viscous effects and thickness effects act in opposition to each other and in many cases if both are ignored errors will cancel. If just one of these effects is accounted for a loss in correlation may result.

Separated Flow

Separated flow can completely change the character and mechanism of shock wave motion. In the example presented the shock wave moved in the opposite direction to that for attached flow for flap motions.

Resonance appeared in some data which was not fully understood. The effects seen could be a wind tunnel resonance or a Buzz mechanism.

The paper by Messrs Couston, Angelini, Balleur and Girodreux-LaVigne concerned the effects of the unsteady boundary layer in a two-dimensional transonic calculation. This transonic calculation is done modeling viscous effects by "blowing" at the airfoil surface instead of physically adding the boundary layer displacement thickness. Such a method may have improved convergence characteristics over other methods.

The method includes a full unsteady Kutta condition for invicid flow but applies the condition at the airfoil surface and wake line. Some higher order viscous effects on the Kutta condition are not considered such as: (1) applying the Kutta condition at the boundary layer edge and (2) accounting for a pressure differential across the trailing edge due to streamline curvature effects. These higher order effects could explain the over estimate in the lift obtained.

Time step size governs whether iteration procedure will converge.

Including wake viscous effects seem to reduce correlation with test data.

Only nonseparated flows have been considered so far. Authors believe that the method will converge for separated flows due to the special properties of such flows.

These authors also concluded that wind tunnel wall corrections are important for accurate correlation of experiment and theory.

The paper by Garner, Payne and Baldock describes an experimental and theoretical approach to the understanding of transonic and viscous effects on the flutter of a conventional (non-supercritical) wing in three-dimensional flow.

An approximate theory which uses a two-dimensional steady transonic small perturbation method, with and without viscous effects, along with the linear three-dimensional method of Davis, is presented.

The experimental data for the simple swept and tapered wing flutter model shows a dip in flutter speed below that predicted by linear theory at M = .865 and a subsequent rise above it at M = .88. The dip in flutter speed is caused by an increase in lift curve slope due to transonic effects. The subsequent rise in flutter speed above that predicted by linear methods is caused by an aft shift in center of pressure due to transonic effects.

Viscous effects on flutter tended to reduce the transonic increase in lift curve slope and reduce the aft shift in center of pressure. Viscous effects, then, offset the transonic effects of thickness.

The paper showed that as the mean incident is increased, the flutter speed is increased.

Finally, wind tunnel wall effects were considered important in accurate correlation of theory and experiment.

In the paper by Shamroth and Gibeling the general Navier-Stokes equations are solved. The total temperature is held constant for two-dimensional unsteady separated flow. The method also considers compressible flow and has a turbulance flow model. Contoured coordinates are used for a noniterative, coupled, stable and consistently split method of computation.

The method is efficient requiring 15 seconds per time step on the CDC 7600 (using 3000 grid points). The author says this time will be cut in half in the future. The method requires 60-150 time steps for moderate incidence and about 250 time steps for high incidence.

The method was applied to airfoils with starting, time dependent, leading edge vortices. Good qualitative correlation with experimental data was observed at high angles of attack and at low Mach numbers. Major features were clearly shown such as starting vortex and secondary leading edge vortex and secondary leading edge vortex of negative sign.

In the future transonic calculations, including shock wave calculation, will be undertaken.

General Consensus

The following consensus seems to emerge from the papers of this Session II.

Thickness (and incidence) effects in transonic flow can not be considered without including viscous effects. Results of including only one effect may be more in error than including neither effect.

Wind tunnel wall effects are very important in transonic tests and calculations.

Quasi steady boundary layer effects are adequate for attached flow but not for separated flow.

General Comments

Linear theory along with "correction factors" will continue to be the backbone of the production methods in industry for some time to come. Correction factors are usually based on steady wind tunnel experiments or steady flow calculations using finite element transonic theory. Therefore, efforts in the areas of steady three-dimensional transonic flow calculation with viscous effects are needed to develop accurate correction factors. Also efforts should be extended to find out the effects of frequency on these correction factors.

3. SESSION III. EXPERIMENTAL STUDIES

Recorder: Ir R J Zwaan, Netherlands

All papers in this Session III reflected clearly the findings of a careful examination of experimental results. The papers contributed to the understanding of various real flow effects and included impulses to reliable flow modeling.

Davis discussed Reynolds number effects in unsteady transonic flow which have been dealt with rather poorly till now. Although not surprisingly, he concluded on the basis of results for conventional and supercritical airfoils with natural boundary layer transition that Reynolds number effects become strong in separated flow. This contains the warning that a straight-forward use of wind tunnel data may be dangerous and emphasises the need of using properly chosen transition strips. The extensive and systematic data base will be made available for long and will provide fine opportunities to comparisons with other data.

Försching presented in his paper experimental pressure distributions for an oscillating wing-flap system at low speeds, which showed almost unexplained large differences with flat plate theory for large mean flap angles and wing angles of attack. He discussed the role of the gap and the slot geometry. In the light of future active controls applications Försching's data possibly mark the beginning of more extensive studies covering theoretical work and higher speeds as well.

Mabey presented a very clear physical explanation of his work on unsteady separated flow about biconvex airfoils, concluded by a fascinating movie. He pointed to characteristics in the oscillating shock-induced separations (Mach number upstream of the shock, frequency parameter), which should also emerge in any modeling of the flow. The oscillations seem most pronounced in symmetric mean flow conditions. It would be worth investigating how the instability develops for practical airfoils. Possibly the data of Davis are able to provide further understanding.

de Ponte described an experimental study, the development of a boundary layer under a cyclically varying pressure gradient, of which the results show a remarkable lag in separation and reattachment. Also these results appear suitable as test data for theoretical verification and may be very useful in helicopter blade flow studies. Continuation of de Ponte's work deserves to be pursued with great interest.

4. ROUND TABLE DISCUSSION

Chairman: Dr J J Olsen, USA

The following paragraphs prepared by Mr W J Mykytow attempt to reconstruct and assemble some of the comments made during the round table discussion.

Airload Predictions

Very good progress has been made in the prediction of transonic unsteady airloads for unseparated flows and weaker shocks (some airfoils with extensive regions of supercritical flow are excepted) because of possible Reynolds number effects.

Inviscid Flow

Transonic small disturbance theory overpredicts airloads since shock movements are too large. The range of aerodynamic parameter linearity versus angle of attack increases with higher reduced frequency. However, flutter is critical at lower reduced frequencies. Inviscid three-dimensional methods should soon be available. Transonic small disturbance theory is likely to yield in time to the full potential method.

Viscous Flow

Viscous effects reduce airloads and are opposite to those from airfoil thickness. These effects decrease with increasing reduced frequency.

Predictions of the correct locations and strengths of the shock in three-dimensional flow are an essential prerequisite for accurate transonic unsteady airload estimates.

Calculations for two-dimensional flow with strong coupling between the outer inviscid flow and the inner viscous flow show that the shock strength and shock movements are reduced. These results produce better accord with experimental data. The viscous analyses for 2D require four times the computer effort for inviscid methods. The procedures appear to be extendable to 3D flow.

Several comments were made concerning strong shock-wave and boundary layer interactions, angle of attack effects and separated flow. The practical applicability of available mathematical-physical models was questioned as well as their likely high costs.

The general conclusion seemed to be that no reliable methods exist and, therefore, need to be developed based on fundamental theoretical and experimental research. This research is required since cruise speeds of future aircraft may be closer to separation boundaries. Also, transonic maneuvering for fighter aircraft will require operations at higher fixed and movable surface angles of attack.

Experimental data show that severe shock-boundary layer interactions produce shock motions opposite to those expected (i.e. forward shock motions for further increases in incidence at lower frequencies). Davis' paper discusses the balance between chordwise positive and negative pressure "lobes" for detached boundary layers and warns of the potential effect of Reynolds number on this balance of unsteady airloads.

Determination and simulation of the time dependent transition point are important factors.

Reattachment time scales since back flow velocities are lower.

Ways of adding viscous effects to Euler equation approaches should be investigated and could prove fruitful.

Both finite difference and integral methods for including boundary layer effects should be further investigated.

Navier-Stokes approaches will be useful but costly. They will not be employed for flutter calculations in the foreseeable future. Some broad qualitive agreements were shown for applications to high angle, lower speed separated flow. Other comments made about the utility of N-S approaches include:

a. Evaluate more economic methods.
b. Identify physical phenomena.
c. Understand factors affecting separation under adverse pressure gradients.
d. Identify methods to minimize shock induced separations and dynamic instabilities.
e. Define and guide experiments and equipment developments.

Control Surfaces

Design of transonic maneuvering fighters and active controls requires accurate methods for predicting unsteady aerodynamic airloads on LE and TE controls at high angles of attack or with gaps, slots, special devices, etc. These are lacking and require development. Experimental data at higher Reynolds numbers and Mach numbers is also a high priority research task.

An evaluation of sophisticated methods (including Reynolds number averaging in Navier-Stokes equation approaches) would be valuable to define potential prediction methods and to delineate applicability of less sophisticated methods.

Research is required for higher reduced frequencies where phenomena may not be quasi-steady.

Experimental Measurements

Transonic unsteady measurements have provided an extremely valuable foundation for analytical investigations and have revealed several important pehnomenological behaviors including buzz-like conditions.

Resonant wind tunnel effects were noticed during (unsteady) aerodynamic measurements on a rigid model and were reduced with acoustic linings.

Reference was made to calculations which show that the presence of viscous effects is necessary for the occurrence of severe oscillating shock-wake interactions. (See comments by Mr Zwaan on Mabey's paper above).

Wall effects at transonic speeds are not well known even for transonic steady flow. Even more severe difficulties exist in defining wall conditions and impedances for transonic unsteady flow. Tests, if practical, under conditions where wall effects are measurable, calculable, or minimized could be useful.

Additional experimental information is required for:

a. Higher Reynolds numbers.
b. Control surfaces.
c. Strong shock-boundary layer interactions and detached flows.
d. Practical 3D planforms.
e. Plunge motions.
f. Fundamental measurements via laser techniques on unsteady boundary layers, transition points, wakes, etc.

General

Further aircraft flutter applications are required to define the full stability boundary versus Mach number. Methods should be extended to cover the supersonic side of the boundary (including subsonic edges).

Design time limitations and costs of parameter variations will require development of dependable but economic transonic unsteady airload prediction methods for industrial use by the flutter engineer. Simpler phenomenological modeling of the viscous flow such as decambering and moving wedge-nosed ramps, etc should be valuable. Guideline recommendations from unsteady aerodynamic research scientists are welcome.

More extensive applications of unsteady aerodynamic methods in transonic flutter safety evaluations would also be most welcome. Results showing the effects from parameter variations which cause noticeable nonlinearities would provide useful guidance. Garner's paper was well received and shows a small effect from Reynolds number but a large effect from angle of attack variations.

Comparison of calculated results with measured model data (and/or flight data) are rare to date and much more are needed. Such comparisons should include frequencies, amplitude ratios and phases as well as velocity (Mach number, dynamic pressure). Discussion of causes of discrepancies would be useful.

Measurement of oscillating pressures on flutter models was recommended several times.

Pending accomplishment of some of the above developments, it was thought that flutter engineers would use the simplest analysis model (such as transonic small disturbance theory with simple boundary layer corrections, strip methods modified by 2D or 3D theory and measured data) in immediate future applications. Again, good definition of the steady flow field and shock characteristics was reemphasized.

5. SUMMARY COMMENTS

The AGARD SMI standard configurations should be employed in experimental and analytical investigations in so far as is practical. This will provide a valuable exchange of information and will accelerate the state-of-the-art.

The subject matter presented at this Specialist's meeting at first glance seems quite varied and even diverse. However, further evaluations will reveal many common threads and concerns, as well as different approaches and limitations.

The ensemble of papers certainly demonstrates the tremendous progress in the last few years made possible by more powerful computers, numerical analysis methods, special algorithms, individual interpretations of physical phenomena and the computer graphics display of physical flow characteristics.

Transonic unsteady pressure measurements in free flight may be economically feasible as pick-a-back measurements during extensive steady flow measurements on aircraft. Valuable information on Reynolds number and (lack of) wall effects could be revealed.

A brief resume or updated listing of wind tunnel and flight observed bending, torsional, control surface, and aerodynamic (rigid airfoil) buzz could be a useful scientific and industrial reference.

Flutter characteristics must be predicted withi[illegible]all fraction of specification flight safety margins. The challenge for development of an econo[illegible]d rapid method for accurate prediction of transonic unsteady airloads in industrial appl[illegible] therefore still exists. However, much progress has been accomplished in the last few years. [illegible]ally, [illegible]is objective will be achieved in the near future.

REPORT DOCUMENTATION PAGE

1. Recipient's Reference	2. Originator's Reference	3. Further Reference	4. Security Classification of Document
	AGARD-CP-296	ISBN 92-835-0281-7	UNCLASSIFIED

5. Originator Advisory Group for Aerospace Research and Development
North Atlantic Treaty Organization
7 rue Ancelle, 92200 Neuilly sur Seine, France

6. Title
BOUNDARY LAYER EFFECTS ON UNSTEADY AIRLOADS

7. Presented at
the 51st Meeting of the AGARD Structures and Materials Panel held in Aix-en-Provence, France on 14–19 September 1980.

8. Author(s)/Editor(s)	9. Date
Various	February 1981

10. Author's/Editor's Address	11. Pages
Various	180

12. Distribution Statement This document is distributed in accordance with AGARD policies and regulations, which are outlined on the Outside Back Covers of all AGARD publications.

13. Keywords/Descriptors

Boundary layer
Unsteady flow
Viscosity
Aeroelasticity
Aerodynamic loads

14. Abstract

The Meeting presented a survey of recent progress in the theoretical and experimental analysis of unsteady behaviour of the boundary layer. These improvements were presented as possible future tools for the introduction of viscous effects in classical aeroelastic applications. Some papers also dealt with actual means for coupling inviscid and viscous flow, and for deriving relatively simple models.

AGARD Conference Proceedings No.296
Advisory Group for Aerospace Research and Development, NATO
BOUNDARY LAYER EFFECTS ON UNSTEADY AIRLOADS
Published February 1981
180 pages

The Meeting presented a survey of recent progress in the theoretical and experimental analysis of unsteady behaviour of the boundary layer. These improvements were presented as possible future tools for the introduction of viscous effects in classical aeroelastic applications. Some papers also dealt with actual means for coupling inviscid and viscous flow, and for deriving relatively simple models.

P.T.O.

AGARD-CP-296

Boundary layer
Unsteady flow
Viscosity
Aeroelasticity
Aerodynamic loads

AGARD Conference Proceedings No.296
Advisory Group for Aerospace Research and Development, NATO
BOUNDARY LAYER EFFECTS ON UNSTEADY AIRLOADS
Published February 1981
180 pages

The Meeting presented a survey of recent progress in the theoretical and experimental analysis of unsteady behaviour of the boundary layer. These improvements were presented as possible future tools for the introduction of viscous effects in classical aeroelastic applications. Some papers also dealt with actual means for coupling inviscid and viscous flow, and for deriving relatively simple models.

P.T.O.

AGARD-CP-296

Boundary layer
Unsteady flow
Viscosity
Aeroelasticity
Aerodynamic loads

AGARD Conference Proceedings No.296
Advisory Group for Aerospace Research and Development, NATO
BOUNDARY LAYER EFFECTS ON UNSTEADY AIRLOADS
Published February 1981
180 pages

The Meeting presented a survey of recent progress in the theoretical and experimental analysis of unsteady behaviour of the boundary layer. These improvements were presented as possible future tools for the introduction of viscous effects in classical aeroelastic applications. Some papers also dealt with actual means for coupling inviscid and viscous flow, and for deriving relatively simple models.

P.T.O.

AGARD-CP-296

Boundary layer
Unsteady flow
Viscosity
Aeroelasticity
Aerodynamic loads

AGARD Conference Proceedings No.296
Advisory Group for Aerospace Research and Development, NATO
BOUNDARY LAYER EFFECTS ON UNSTEADY AIRLOADS
Published February 1981
180 pages

The Meeting presented a survey of recent progress in the theoretical and experimental analysis of unsteady behaviour of the boundary layer. These improvements were presented as possible future tools for the introduction of viscous effects in classical aeroelastic applications. Some papers also dealt with actual means for coupling inviscid and viscous flow, and for deriving relatively simple models.

P.T.O.

AGARD-CP-296

Boundary layer
Unsteady flow
Viscosity
Aeroelasticity
Aerodynamic loads

Papers presented at the 51st Meeting of the AGARD Structures and Materials Panel held in Aix-en-Provence, France on 14–19 September 1980.

ISBN 92-835-0281-7

Papers presented at the 51st Meeting of the AGARD Structures and Materials Panel held in Aix-en-Provence, France on 14–19 September 1980.

ISBN 92-835-0281-7

Papers presented at the 51st Meeting of the AGARD Structures and Materials Panel held in Aix-en-Provence, France on 14–19 September 1980.

ISBN 92-835-0281-7

Papers presented at the 51st Meeting of the AGARD Structures and Materials Panel held in Aix-en-Provence, France on 14–19 September 1980.

ISBN 92-835-0281-7

EN